Imperial College London

Coupled Point Neutron Kinetics and Thermal-Hydraulics Models of Transient Nuclear Criticality Excursions in Wetted Fissile Uranium Dioxide (UO_2) Powders

Academic Supervisors:
Dr Matthew Eaton
Dr Michael Bluck

Industrial Supervisors:
Dr Joanna Saxby
Mr Chris Ryden

Author:
Gregory Jones

Department of Mechanical Engineering

A thesis submitted in partial fulfilment of the requirements for the degree of Doctor of Philosophy in Nuclear Engineering of Imperial College London and the Diploma of Imperial College London

September 2022

Abstract

This thesis describes a phenomenologically based mathematical and computational methodology for the simulation of a postulated transient nuclear criticality excursion initiated by the incursion of water, from a fire-sprinkler system, into a bed of dry UO_2 powder. These potentially hazardous multi-phase dispersed particulate systems may form as a result of a fire or explosion in a nuclear fuel fabrication facility. The models proposed in this thesis aim to support nuclear criticality safety analysis and assessment. In addition, the development of these models aims to support emergency planning and preparedness.

The point neutron kinetics equations are coupled to phenomenological models of water infiltration, sedimentation, fluidisation, nuclear thermal hydraulics, radiolysis and boiling, through the use of multivariate reactivity feedback components. The spatial and temporal solution of this set of equations enables the modelling of postulated transient nuclear criticality excursions in highly dispersed three-phase particulate systems of UO_2 powder. The results indicate that there is the potential for large positive reactivities to be added to a UO_2 powder system as pores become filled with water. Generally, thermal expansion and Doppler broadening are insufficient to control the transient, leading to significant radiolysis and boiling on the surface of the UO_2 powder particles. Radiolytic gas and steam bubble induced fluidisation and sedimentation significantly alters the characteristics of a transient nuclear criticality excursion and should be carefully considered.

Research has also been undertaken examining transient nuclear criticality excursions in weak intrinsic neutron source UO_2 powder systems by solving the forward probability balance equation and using a Gamma probability distribution function to estimate mean wait-time probability distributions. Significant variations in the potential initial peak power are predicted for highly enriched, wetted, UO_2 powders as a function of the stochastic behaviour associated with criticality excursions in low neutron population systems.

Declaration of Originality

I hereby declare that the work contained in this thesis is my own unless stated otherwise. In such cases the work will be appropriately referenced.

Copyright Declaration

Acknowledgements

I would like to thank my principal academic supervisor Dr Matthew Eaton and my co-supervisor Dr Mike Bluck for their support and advice throughout the duration of my PhD studies. I would also like to thank Emeritus Professor M.M.R. Williams and Dr Christopher Cooling for the time they have spent helping me learn and develop throughout my PhD studies. I would also like to acknowledge the financial support of the Engineering and Physical Science Research Council (EPSRC) and AWE plc through the industrial CASE PhD programme (EPSRC Grant No.: EP/S513635/1). I would like to thank Mr Chris Ryden and Dr Joanna Saxby for their continued industrial support throughout the project. Finally, I am deeply grateful to my partner Priya for supporting me throughout this endeavour.

Contents

List of Figures

List of Tables

Nomenclature

Latin Symbols

$\mathbf{r}$ Position vector [cm]

$\mathbf{F}_{\mathrm{d}}$ Drag force vector on spherical particle [N]

$\mathbf{F}_{\mathrm{g}}$ Gravitational force vector on spherical particle [N]

$\mathbf{S}_1$ Sigmoid function [-]

$\mathbf{S}_2$ Reverse sigmoid function [-]

A_{cyl} Cross-sectional area of cylinder [m^2]

$A_{\mathrm{i,j,k}}$ Interfacial area between component, i, and component, j, in region, k [m^2]

$a_{\mathrm{I},0}$ Interfacial area concentration between gas and pure water [m^{-1}]

a_{I} Interfacial area concentration between gas and water in powder bed [m^{-1}]

a_{spline} Bivariate B-spline coefficients [-]

B_{g} Geometric buckling [cm^{-1}]

B_{m} Material buckling [cm^{-1}]

B_{x} One-dimensional B-spline basis function in x-direction [-]

B_{y} One-dimensional B-spline basis function in y-direction [-]

C_{D} Coefficient of drag [-]

$C_{\mathrm{H_2,equil}}$ Equilibrium concentration of $\mathrm{H_2}$ [mol m^{-3}]

C_{i} Delayed neutron precursor population for group, i [precursors]

c_{j} Specific heat capacity of component, j [J kg^{-1} K^{-1}]

D Neutron diffusion coefficient [cm]

d'_{b} Effective bubble diameter [m]

d_{agg} Size of agglomerated $\mathrm{UO_2}$ powder-water particle [m]

d_{b} Gas bubble diameter [m]

D_{k} Turbulent mixing coefficient of region, k [m^2 s^{-1}]

d_{p} $\mathrm{UO_2}$ powder particle diameter [m]

dV_{slump}/dt Volumetric deformation rate of wetted powder [m^3 s^{-1}]

E_{ψ} Modulus of elasticity for powder bed [Pa]

E_{fast} Fast neutron energy [eV]

E_{f} Energy generated per fission [J $\mathrm{fission}^{-1}$]

$E_{\mathrm{i,j}}$ Heat transfer rate for thermal process, i, for component, j [J s^{-1}]

$E_{\mathrm{net,j,k}}$ Net rate of heat transfer of component, j, in region, k [J s^{-1}]

E_{therm} Thermal neutron energy [eV]

$f_{1,2}$ Fractional occupancy of mesh cell either side of interface [-]

$f_{\mathrm{imm,0}}$ Bed immersion fraction if there were no slumping [-]

f_{imm} Powder bed immersion fraction [-]

f_{slump} Slumping fraction [-]

f_{util} Thermal utilisation factor [-]

f_{w} Volume fraction of bubble occupied by wake [-]

Fr Froude number [-]

g Gravitational acceleration [m s^{-2}]

g_{p} Fraction of fission fragment kinetic energy deposited in powder particle [-]

$G_{\mathrm{v}}(\mathrm{H_2O})$ Volumetric H_2O loss from radiolysis [m^3 J^{-1}]

$G_{\mathrm{v}}(H_2)$ Volumetric yield of hydrogen from radiolysis [m^3 J^{-1}]

h_{ψ} Hydraulic head due to matric suction [m]

H_{cyl} Height of cylinder [m]

$H_{\mathrm{H_2,sol}}$ Henry's constant for hydrogen [mol m^{-3} Pa^{-1}]

H_{k} Height of region, k [m]

$h_{\mathrm{l,v}}$ Latent heat of vapourisation [J kg^{-1}]

$h'_{\mathrm{l,v}}$ Adjusted latent heat of vapourisation [J kg^{-1}]

$h_{\mathrm{p,v}}$ Powder boiling heat transfer coefficient [W m^{-2} K^{-1}]

$h_{\mathrm{p,w}}$ Powder water convective heat transfer coefficient [W m^{-2} K^{-1}]

k Permeability of powder bed [m^2]

k_{∞} Infinite multiplication factor [-]

k_{b} Boltzmann constant [eV K^{-1}]

k_{eff} Effective multiplication factor [-]

$K_{\mathrm{sat,e}}$ Effective saturated hydraulic conductivity [m s^{-1}]

K_{sat} Saturated hydraulic conductivity [m s^{-1}]

k_{s} Sub-critical multiplication factor [-]

L_{neut} Neutron diffusion length [cm]

L_{t} Streaming operator

$M_{\mathrm{t}}^{\mathrm{i}}$ Delayed fission neutron production operator

$M_{\mathrm{t}}^{\mathrm{p}}$ Prompt fission neutron production operator

m_2^{s} Compressibility modulus of powder bed due to wetting [Pa^{-1}]

$M_{\mathrm{j,k}}$ Mass of component, j, in region, k [kg]

M_{t} Total fission neutron production operator

$M_{\mathrm{UO_2}}$ Mass of UO_2 powder in vessel [kg]

N Neutron population [neutrons]

N_{d} Number of data points used to construct bivariate B-spline [-]

N_{j} Number of components, j [-]

$N_{\mathrm{mol,j}}$ Number of moles of component, j [mol]

N_{thresh} Threshold neutron population [neutrons]

N_{x} Number of basis splines in the x-direction used to construct bivariate B-spline [-]

N_{y} Number of basis splines in the y-direction used to construct bivariate B-spline [-]

N_{z} Number of axially discretised mesh cells [-]

P Energy generation rate (fission power) [W]

$P_{\gamma,\mathrm{i}}$ Gamma probability distribution function for delayed neutron precursors [-]

$P_{\gamma,\mathrm{N}}$ Gamma probability distribution function for neutron population [-]

P_{abs} Absolute pressure [Pa]

P_{atm} Atmospheric pressure [Pa]

P_{gauge} Gauge pressure [Pa]

P_{j} Pressure of component, j [Pa]

p_{res} Resonance escape probability [-]

P_{wait} Gamma wait-time probability distribution function for the neutron population [-]

Pr Prandtl number [-]

Q Gamma wait-time cumulative distribution function for the neutron population [-]

Q_{i} Net flow of components from mesh cell, i [$\mathrm{m^3\ s^{-1}}$]

R Universal gas constant [$\mathrm{J\ mol^{-1}\ K^{-1}}$]

R_{cyl} Radius of cylinder [m]

R_{fiss} Range of fission fragments [m]

R_{i} Reactivity component, i [\$]

$R_{\mathrm{std,i}}$ Relative standard deviation of delayed neutron precursor population [-]

$R_{\mathrm{std,N}}$ Relative standard deviation of neutron population [-]

$Re_{d_{\mathrm{p}}}$ Reynolds number for flow around powder particle [-]

S_{A} Specific surface area of powder [$\mathrm{m^{-1}}$]

$S_{\mathrm{j,k}}$ Volumetric source/sink of component, j, in region, k [$\mathrm{m^3\ s^{-1}}$]

S_{n} Extraneous (fixed) neutron source [$\mathrm{neutrons\ s^{-1}}$]

s_{n} Intrinsic source density of neutrons [$\mathrm{neutrons\ s^{-1}\ (cm^{-3} \cdot UO_2)}$]

$S_{\mathrm{w,sat}}$ Maximum allowable saturation [-]

$S_{\mathrm{w,0}}$ Minimum allowable saturation [-]

S_{w} Saturation of powder bed pores [-]

T Reactor period [s]

t Time [s]

T_0 Reference temperature [K]

T_{I} UO_2 powder-water interface temperature [K]

$T_{\mathrm{j,k}}$ Temperature of component, j, in region, k [K]

T_{sat} Water boiling temperature [K]

U_{adj} Corrective adjustment velocity [$\mathrm{m\ s^{-1}}$]

u_{a} Pore air pressure [Pa]

$U_{\mathrm{g,crit}}$ Critical gas velocity for fluidisation [$\mathrm{m\ s^{-1}}$]

U_{j} Superficial velocity of component, j [$\mathrm{m\ s^{-1}}$]

$U_{\mathrm{net,j,k}}$ Net velocity of component, j, in region k [$\mathrm{m\ s^{-1}}$]

$U_{\mathrm{w,in}}$ Water surface infiltration rate [$\mathrm{m\ s^{-1}}$]

u_{w} Pore water pressure [Pa]

$v_{0,\mathrm{f,g,k}}$ Reference voidage in region, k [-]

$v_{\mathrm{f,j,k}}$ Volume fraction of component, j, in region, k [-]

$V_{\mathrm{j,k}}$ Volume of component, j, in region, k [$\mathrm{m^3}$]

v_{n} Neutron velocity [$\mathrm{cm\ s^{-1}}$]

$V_{\mathrm{UO_2}}$ Volume of UO_2 powder present in system

	$[m^3]$
y_{H_2}	Mole fraction of H_2 in bubble [-]
E	Neutron energy [eV]
F	Multivariate probability generating function [-]
f	Probability generating function for neutron emission probability [-]
Mo	Morton number [-]

Greek Symbols

$\bar{\nu}$	Average number of neutrons produced by fission [-]
β	Delayed neutron fraction [-]
β_{eff}	Adjoint-weighted effective delayed neutron fraction [-]
β_{i}	Delayed neutron fraction for group, i [-]
χ_{di}	Delayed neutron fission spectrum [-]
χ_{p}	Prompt neutron fission spectrum [-]
ϵ_{ff}	Fast fission factor [-]
ϵ_{k}	Porosity of region, k [-]
ϵ_{v}	Volumetric strain on powder bed [-]
η	Thermal expansion coefficient of water $[K^{-1}]$
η_{i}	Square inverse of relative standard deviation of delayed neutron precursor population [-]
η_{N}	Square inverse of relative standard deviation of neutron population [-]
η_{rep}	Reproduction factor [-]
γ	Enrichment of uranium by weight [-]
Γ_2	Diven factor [-]
$\hat{\Phi}$	Angular neutron flux shape function [-]
$\hat{\phi}$	Fundamental mode scalar neutron flux shape function $[cm^{-1}]$
κ_{j}	Thermal conductivity of component, j $[W\ m^{-1}\ K^{-1}]$
Λ	Mean prompt neutron generation time [s]
λ_{a}	Absorption transition rate $[s^{-1}]$
λ_{c}	Capture transition rate $[s^{-1}]$
Λ_{eff}	Effective mean prompt neutron generation time [s]
λ_{f}	Fission transition rate $[s^{-1}]$
λ_{i}	Decay constant for precursor group, i [s]
$\mathbf{\Omega}$	Neutron angular direction [-]
$\mu_{\text{eff,k}}$	Effective dynamic viscosity in region, k [Pa s]
μ_{ii}	2^{nd} partial derivative of generating function w.r.t. i-th delayed neutron precursor population
μ_{ij}	2^{nd} partial derivative of generating function w.r.t. i-th and j-th delayed neutron precursor population
μ_{j}	Dynamic viscosity of component, j [Pa s]
μ_{Ni}	2^{nd} partial derivative of generating function w.r.t. neutron population and i-th delayed neutron precursor population
μ_{NN}	2^{nd} partial derivative of generating function w.r.t. neutron population
ν	Number of neutrons born through fission [-]
ν_{max}	Maximum number of neutrons born through fission [-]
ν_{p}	Poisson's ratio for UO_2 powder bed [-]

Φ Angular neutron flux [neutrons cm^{-2} s^{-1}]

ϕ Scalar neutron flux [neutrons cm^{-2} s^{-1}]

$\Phi^{\dagger}$ Adjoint angular neutron flux [neutrons $cm^{-2}s^{-1}$]

$\Phi_0^{\dagger}$ Adjoint angular neutron flux [neutrons cm^{-2} s^{-1}]

ψ Matric suction [Pa]

ρ Reactivity [-]

ρ_{agg} Free air density [kg m^{-3}]

$\rho_{eff,k}$ Effective density in region, k [kg m^{-3}]

$\rho_{g,free}$ Free air density [kg m^{-3}]

$\rho_{j,bulk,k}$ Bulk density of component, j in region, k [kg m^{-3}]

$\rho_{j,th}$ Theoretical density of component, j [kg m^{-3}]

σ Surface tension of water [N m^{-1}]

Σ_a Macroscopic absorption neutron cross-section [cm^{-1}]

Σ_f Macroscopic fission neutron cross-section [cm^{-1}]

$\Sigma_{s,g' \rightarrow g}$ Macroscopic neutron scattering cross-section from energy group, g' to g [cm^{-1}]

$\sigma_{std,i}$ Standard deviation in delayed neutron precursor population

$\sigma_{std,N}$ Standard deviation in neutron population

$\sigma_{std,t}$ Standard deviation in mean wait-time [s]

Σ_s Macroscopic neutron scattering cross-section [cm^{-1}]

Σ_t Macroscopic total neutron cross-section [cm^{-1}]

τ Prompt neutron lifetime [s]

τ_{age} Neutron age [cm^2]

τ_{del} Average delayed neutron precursor lifetime [s]

ξ Bivariate B-spline smoothing parameter [-]

P_f Neutron emission probability [-]

Subscripts

boil Boiling

convec Inter-phase convection

dp Dry powder region

eject Ejection from vessel

gen Thermal energy generation

g Total gas

imm Water infiltration reactivity component

loss UO_2 powder loss reactivity component

pickup Pickup/fluidisation component for reactivity of advection

p Fissile powder

rg Radiolytic gas

slump Slumping component

sus Suspension/pooled water region

th Thermal reactivity component

t Total reactivity component

void Void reactivity component

v Water vapour

wp Wet powder region

w Water

Superscipts

$'$ Spatial derivative (variable per unit height) [m^{-1}]

$\bar{}$ Spatial average [-]

Acronyms

ADE Age Diffusion Equation

ADS Accelerator Driven System

ADU Ammonium Diuranate Carbonate

AGNES-P Accidentally Generated Nuclear Excursion Simulation-Powder

ALARP As Low As Reasonably Practicable

AUC Ammonium Uranyl Carbonate

BDF Backwards Differentiation Formula

BS British Standard

BTE Boltzmann Transport Equation

CDF Cumulative Distribution Function

CEA Commissariat à l'Energie Atomique et aux Énergies Alternatives

CFD Computational Fluid Dynamics

CFL Courant-Freidrichs-Lewy

DAS Data Acquisition System

DEM Discrete Element Method

DEM Discrete Element Method

DOE Department of Energy

EN European Norm

ERU Enriched Reprocessed Uranium

EURATOM European Union's European Atomic Energy Community

EVENT EVEn-parity Neutral particle Transport

FD Finite Difference

FEM Finite Element Modelling

FETCH Finite Element Transient Criticality

FV Finite Volume Method

G7 Group of Seven

GA Green-Ampt

GDF Geological Disposal Facility

GNF Global Nuclear Fuels

H/U Hydrogen to Uranium ratio

HEPA High Efficiency Particulate Air

HEU Highly Enriched Uranium

HLW High-Level Waste

HSE Health and Safety Executive

IAEA International Atomic Energy Agency

ICRP International Commission on Radiological Protection

ICSBEP International Criticality Safety Benchmark Evaluation Project

ILW Intermediate Level Waste

IPPE Institute of Physics and Power Engineering

IPSN Institut de Protection et Sûreté Nucléaire

IRSN Institut de Radioprotection et de Sûreté Nucléaire

ISL In-Situ Leaching

JAERI Japan Atomic Energy Research Institute

KEMA Keuring Van Electrotechnische Materialen

KSTR Keuring Van Electrotechnische Materialen Suspension Test Reactor

LBM Lattice-Boltzmann Method

LET Linear Energy Transfer

LEU Low-Enriched Uranium

MAGIC MERV Mass, Absorption, Geometry, Interaction, Concentration, Moderation, Enrichment, Reflection, and Volume

MCNP Monte Carlo N-Particle

MERMAIDS Mass, Enrichment, Reflection, Moderation, Absorption, Interaction, Density, and Shape

MEU Medium Enriched Uranium

MFP Mean Free Path

MOX Mixed OXide

NCE Neutron Continuity Equation

NCS Nuclear Criticality Safety

NDE Neutron Diffusion Equation

NEA Nuclear Energy Agency

NRC Nuclear Regulatory Commission

NSC National Security Complex

NTE Neutron Transport Equation

ODE Ordinary Differential Equation

ONE Office of Nuclear Energy

ONR Office for Nuclear Regulation

ORNL Oak Ridge National Laboratory

P_N Spherical harmonic basis function [-]

PCG Preconditioned Conjugate-Gradient

PDE Partial Differential Equation

PDF Probability Distribution Function

PIDE Partial-Integro-Differential Equation

PUREX Plutonium-Uranium Reduction EXtracton

RepU Reprocessed Uranium

SF Spontaneous Fission

SILENE Source d'Irradiation à Libre Evolution Neutronique

SKINATH-WP Simple KINetics And Thermal HydraulicsWetted Powder

SMR Small Modular Reactor

SNM Special Nuclear Material

SSG Specific Safety Guide

SUNDIALS SUite of Nonlinear and Differential/ALgebraic Solvers

TBP TriButyl Phosphate

TVD Total Variation Diminishing

U.K. United Kingdom

U.S. United States

UKAEA United Kingdom Atomic Energy Agency

WPNCS Working Party on Nuclear Criticality Safety

Chapter 1

Introduction

Since the early-mid twentieth century nuclear power has provided a low-carbon, energy dense source of power, that is capable of providing a near-continuous source of power to a nation's energy grid. Up to the year 2015, there have been over 500 civil nuclear reactors (Crossland, 2012), with 442 currently operating across 34 countries (IAEA, 2021). Figure 1.1 shows how nuclear power as a share of all electricity produced by a nation, has changed over the past 35 years. Also shown is the global share of electricity produced via nuclear energy, which currently stands at around 10%.

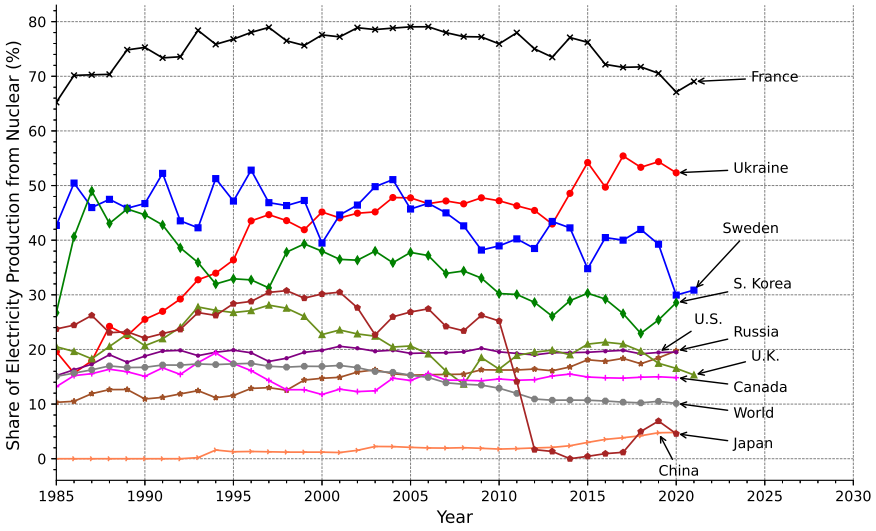

Figure 1.1: Global share of electricity generated from nuclear power (data from British Petroleum (2021)).

There are currently 52 further power reactors under construction globally, with 13 of those being constructed in China (IAEA, 2021), who have made nuclear power a key aspect of their drive to net-zero, as outlined in their most recent five-year plan (Xinhua News Agency, 2021). Other Group of Seven (G7) countries such as the United Kingdom (U.K.) have outlined their support for nuclear power in achieving net-zero by promising one new approved large-scale nuclear reactor project, as well

as continued support for Small Modular Reactors (SMRs) and Advanced Modular Reactors (AMRs) over subsequent years (Department for Business, Energy and Industrial Strategy, 2020). Furthermore, the United States (U.S.) Department of Energy (DOE) and Office of Nuclear Energy (ONE) have introduced a number of funding initiatives to support the successful demonstration of small-scale Generation IV nuclear reactors (Office of Nuclear Energy, 2022). Moreover, a European Commission strategic long-term plan has also signified the importance of using nuclear power alongside other renewable energy resources to transform Europe's electricity production (European Commission Communication, 2018).

An advantage of the renewed interest in nuclear power as a component of a diversified, carbon-neutral power grid, is the relative safety of the energy source when compared to other forms of energy. Markandya and Wilkinson (2007) have reported that when considering death rates from both accidents and air pollution, nuclear energy is safer than coal, biomass, and gas. Furthermore, the death rates per TWh of energy for nuclear are a similar order of magnitude to renewable energy resources such as wind and solar, although the financial impact of nuclear accidents are usually far greater (Sovacool et al., 2016). McLaughlin et al. (2000) describes how over recent years, the number of recorded nuclear accidents have dropped significantly. As a result, the overall financial impact of nuclear accidents has also reduced. The increasing safety of the nuclear industry may in part be attributable to the work of nuclear criticality safety (NCS) experts, whose responsibility it has been over the past 80 years, to prevent and minimise consequences of accidental nuclear criticality excursions.

1.1 Nuclear Criticality Safety

An accidental nuclear chain reaction may occur for a number of inter-related reasons, leading to the release of damaging ionising radiation, which can cause harm to those in the vicinity. The role of NCS experts is to mitigate the risks and understand the impact of inadvertent, self-sustaining, nuclear chain reactions, occurring outside nuclear reactors, preferably by eliminating any possibility for a nuclear criticality excursion (Clark, 1981). The state of criticality can be further expressed in terms of a multiplication factor, which conveys the ratio of neutrons from one generation to the next (Clayton, 2010). If there is a generational increase/decrease in neutrons, the system is super-critical/sub-critical. A constant neutron population corresponds to a critical system.

Two useful mnemonics used by NCS experts when trying to understand the likelihood of an accidental nuclear criticality excursion are MAGIC MERV (for Mass, Absorption, Geometry, Interaction, Concentration, Moderation, Enrichment, Reflection, and Volume) (Fernandez, 2020) and MERMAIDS (Mass, Enrichment, Reflection, Moderation, Absorption, Interaction, Density, and Shape) (Putman, 1999). These characteristics are used by NCS engineers to monitor the environment that nuclear material is in throughout the nuclear fuel cycle, with the aim of minimising the risk of accidental nuclear criticality excursions (Brown, 1981). The interdependency between each of these factors is strong, which highlights the nuanced complexity of NCS analysis. This is evidenced by (Clayton, 1974) who provides a wide-range of scenarios where conventional criticality safety concepts may not be appropriate.

The history of NCS dates back as early as 1940, before the availability of enriched uranium. At this time, Peierls (1940) used hand calculation methods to estimate the impact of a sustained nuclear criticality transient on people in the vicinity of a nuclear excursion. In the US, the field has been traced back by Paxton (1980) to the early days of the American nuclear industry, during World War II. The idea was conceived at an Oak Ridge National Laboratory (ORNL) Gaseous Diffusion Plant in 1943, that was rapidly built to produce enriched uranium to aid in the production of plutonium for the Manhattan Project. Early efforts of performing NCS calculations relied on relatively simple computations, using one- or two-energy groups and a mechanical calculator (Whitesides et al., 2010).

NCS of the ORNL plant was achieved through very conservative safety calculations, however, as more hypothetical accident scenarios were conceived, the need for critical experiments arose (Paxton, 1980). This led to what is believed to be the first critical assembly tests using ^{235}U to simulate deposits of fissionable material in gaseous diffusion enrichment facilities. Other notable early critical tests are discussed by Reider (1971). Subsequently, many critical and sub-critical tests have been performed. These have all been aimed at increasing the understanding of the critical nature of various configurations of fissile material to aid emergency planning and preparedness and NCS.

The associated international regulatory framework relating to radiological protection of workers and the public originates from the work of the International Commission on Radiological Protection (ICRP), whose role it is to investigate hazards associated with the release of ionizing radiation directed towards people, animals, and plants (ICRP, 1959). The first set of approved nuclear safety measures by the International Atomic Energy Agency (IAEA) in 1960, were based on recommendations from the ICRP, dating back to 1928 (IAEA, 1960). Over subsequent years, numerous regulatory requirement and guidance documents have been produced by the IAEA to encourage international collaboration in the field of nuclear safety. Although the IAEA standards provide an excellent resource for all aspects of nuclear safety, including both for regulators and organisations, regulation of safety remains a national responsibility (IAEA, 2006).

Within the UK, the Office for Nuclear Regulation (ONR) is the governing body that ensures regulations outlined by the Health and Safety Executive (HSE) are abided by when licensing nuclear facilities (ONR, 2017). Specific HSE regulatory documents that must be adhered to in the handling of nuclear material through the nuclear fuel cycle include the Health and Safety at Work etc. Act (1974), Nuclear Installations Act (1965) and The Ionising Radiations Regulations (2017). The latter document under Section 8 states that the radiation risk of any identifiable nuclear accident must be reduced as much as reasonably possible to limit the consequences or prevent such an accident from occurring. This regulatory requirement leads to the concept of ALARP (as low as reasonably practicable). ALARP is a cross-industry tool, applied to qualify and quantify cost-benefits associated with the risks of radiological or other accidents, ensuring that there is no unacceptable disproportionality between the two (IRPCG, 2012). ALARP measures include various methods such as conventional risk assessments, engineering design processes and probabilistic risk assessments. As part of the guidance on the demonstration of ALARP outlined in ONR (2020), it is necessary to give adequate weighting to the costs of accidents by understanding the radiation risks arising from foreseeable events. Therefore, in the remit of NCS, practising ALARP measures requires awareness of postulated nuclear criticality accidents throughout the nuclear fuel cycle.

1.2 Nuclear Criticality Safety of Fissile Powders in the Nuclear Fuel Cycle

Specific concern is given here to the role that fissile powders play in the nuclear fuel cycle and associated postulated nuclear criticality accidents involving fissile powder-based systems. An illustration of the nuclear fuel cycle is shown in Figure 1.2.

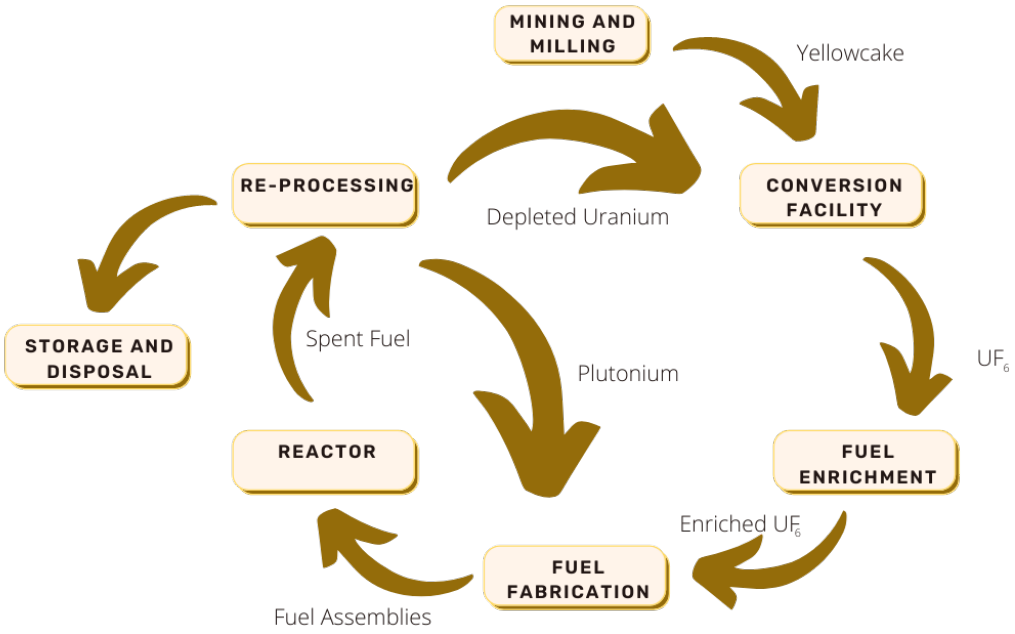

Figure 1.2: Closed nuclear fuel cycle.

Firstly, however, it is essential to describe the rheological properties of dispersed particulates, which may be categorised as colloidal suspensions, slurries, sludges and cakes. Andreotti et al. (2013) classifies colloids as particulates that are in the size range of 1 nm - 1 μm, whose stability depends on a balance between repulsive and attractive forces. Russel et al. (1989) describes how the dominant forces governing the stability of a colloid include, electrostatic forces, van der Waals forces, Brownian motion and viscous forces. The small characteristic size of these colloidal particles mean that the gravitational force, buoyancy and viscous force are less dominant. When the dispersed phase is larger, typically ≥ 1 μm, depending on the density of the particulate, the gravitational force on the particulate in the continuous phase liquid may become dominant, causing the colloidal suspension to sediment. As the volume fraction of particulates increases, a greater number of particle-particle interactions occur and the interaction force between particles becomes more dominant (Tadros, 2012). This marks the transition from a dilute suspension to a slurry. Two important characteristics of a slurry are its fluidity and that an apparent increase in effective viscosity (resistance to fluid flow) develops as the solid volume fraction of the dispersed phase increases (Komoda, 2019). In a laminar flow regime, where viscous effects dominate, the increase in effective medium viscosity requires a greater shear force to deform the fluid, resulting in a lower volumetric flow rate for a given shear stress (Wilson et al., 2006). At higher dispersed phase concentrations, the force applied on the mixture may be insufficient to continue its motion. In this case, the mixture will transition from being a free-flowing slurry to a sludge or cake (Griffith, 1991). Zafar et al. (2017) notes that forces relating to the contact

between particles, surface roughness as well as elastic and plastic deformation play an important role in characterising the behaviour of cakes or sludges.

The stages of the nuclear fuel cycle are typically classified as either front-end or back-end processes, with the demarcation between the two occurring when the nuclear fuel is in the nuclear power reactor. The first stage of the fuel cycle is the mining and milling of the orebody containing uranium, to produce Yellowcake. The production of uranium ore is concentrated to a small number of countries. Figure 1.3 shows the distribution of uranium production from both open pit and underground mining techniques. Most extracted uranium ore, which is found in a range of different mineral compounds, is formed of the compound uranium dioxide (UO_2), although oxidation may also result in the formation of tri-uranium oct-oxide (U_3O_8) (Dana, 1864; Janeczek et al., 1993).

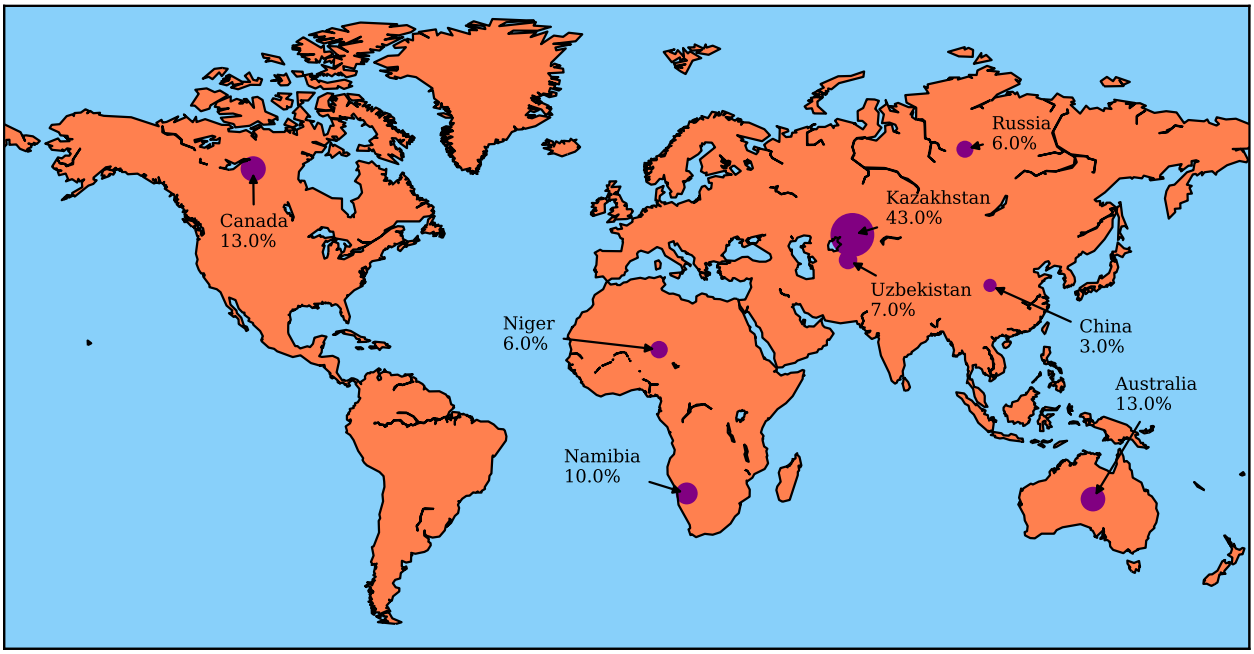

Figure 1.3: Global distribution of uranium mining in 2019 (data from NEA and IAEA (2020)).

Conventional mining methods involve extracting the mineral containing uranium from the ground and performing grinding and crushing operations in a mill to produce coarse mineral rocks. Most ore extraction methods involve breaking the ore off of the bulk orebody and collecting it to be sent to uranium mills. However, a slurry transport method may be used whereby ore extraction is achieved by firing high-pressure water jets onto the orebody, breaking it up and creating a slurry, which is then pumped to the surface (Narcy, 1994). This type of mineral recovery is still carried out in large amounts by countries such as Canada, Namibia, Australia, and Niger (NEA and IAEA, 2020). The powdered mineral containing uranium is put into the form of a slurry and transported to tanks where it is then leached in an acidic or alkaline solution and then purified using either ion exchange or solvent extraction techniques (Kim, 2018). Once purified, the uranium is precipitated, dried and calcined to form primarily Yellowcake (U_3O_8) (Edwards and Oliver, 2000). This concentrated uranium has purity of approximately 80% uranium (Choppin et al., 2013).

However, presently, 57% of uranium is extracted from the ground using an in-situ leaching method

(ISL) (NEA and IAEA, 2020). This process, depicted in Figure 1.4, involves recovering the uranium from the ground by passing an acidic or alkaline solution, usually along with an oxidant, through the porous rock structure, producing a uranium solution, which is then pumped to the surface level for further chemical treatment (Mudd, 2001). Some of the largest uranium producing countries in the world using this method include Kazakhstan, Uzbekistan, Australia, China, and Russia (NEA and IAEA, 2020). The uranium is then recovered to form Yellowcake in a similar way to the conventional methods used for ore extraction techniques. ISL is advantageous over conventional mining techniques as the uranium can be extracted from the ground without significant disturbance to the environment.

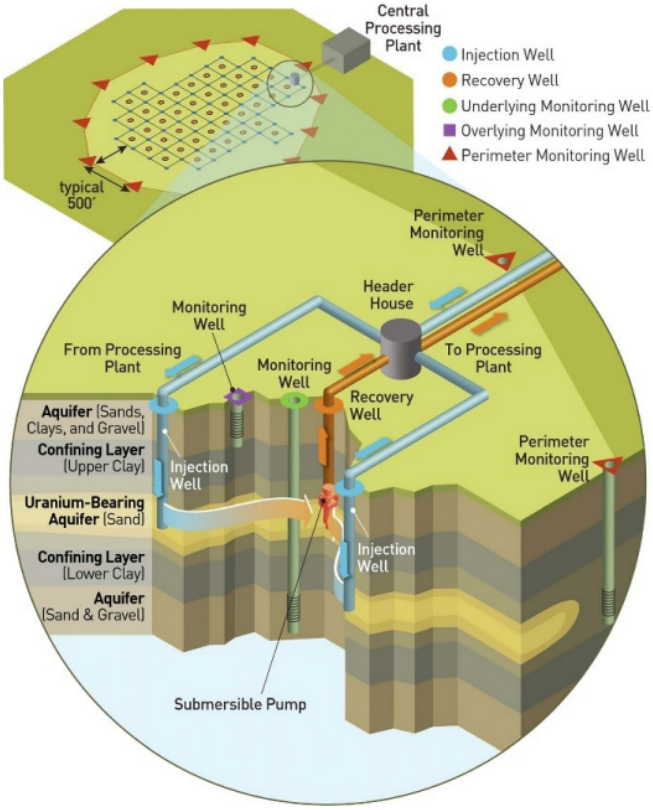

Figure 1.4: Isometric illustration of the ISL process [Photo: U.S. NRC (2016)].

Powdered uranium, or Yellowcake, shown in Figure 1.5 is the first form that a concentrated, dry, powdered nuclear material takes in the nuclear fuel cycle. IAEA (2014) notes that due to the current natural enrichment levels of Yellowcake being 0.072% ^{235}U, there is no credible risk of an accidental nuclear criticality excursion occurring before the uranium is enriched. However, radiological risks associated with uranium extraction techniques include alpha activity from the inhalation of airborne dust particles, radon exposure and gamma ray exposure from the ore or processed materials (Brown and Chambers, 2017).

Yellowcake is transported to conversion facilities where it is converted into uranium hexafluoride (UF_6) using a multistep chemical process, in preparation for isotope separation. The conversion process involves dissolving the Yellowcake in nitric acid (HNO_3) to form an impure uranyl nitrate solution ($UO_2(NO_3)_2$). The uranyl nitrate is then purified and may either be denitrated to form uranium trioxide (UO_3) powder or precipitated using ammonium hydroxide (NH_3) to produce an ammonium diuranate (ADU, $(NH_4)_2U_2O7$) precipitate which is then calcined to produce UO_3 powder

Figure 1.5: Concentrated natural uranium powder, known as Yellowcake [Photo: Calma and IAEA (2009)].

(Crossland, 2012). The UO_3 powder is then reduced using hydrogen (H_2) to produce UO_2 powder. Hydrofluorination of UO_2 particulates using hydrofluoric acid (HF) produces UF_4. The hydrofluorination process may use a counter-current gas-solid fluidised bed in order to efficiently execute the chemical process (Sutton et al., 1964). Efficiency is a fundamental advantage of chemically operating on a dispersed particulate system using fluidised bed methods because of the high specific surface area that can be achieved between the dispersed and continuous phase, increasing the rate at which the chemical process may be performed. Further fluorination using fluorine (F_2) produces the desired UF_6. Although powdered nuclear material exists throughout the conversion process, there remains no credible risk of an accidental transient nuclear criticality excursion due to the low natural enrichment of the uranium (IAEA, 2014). IAEA (2014) notes that the main risks associated with nuclear fuel conversion facilities, using natural uranium are the toxicological risks arising due to the release of HF and UF_6. Additional safety risks arise when handling the residues of nuclear materials.

The application of gaseous diffusion and the use of gas centrifuges constitute the two main enrichment methods used worldwide. These processes separate the ^{235}U and ^{238}U, increasing the concentration of the former in the gas, leading to higher levels of enrichment. In gaseous diffusion, UF_6 is supplied to the device using a high pressure feed. The gas is forced through a series of porous membranes, into a lower pressure region. Since ^{235}U is lighter than ^{238}U, the ^{235}U isotope permeates the membranes at a higher rate than ^{238}U, causing there to be a greater level of enrichment in the low pressure region, downstream of the porous membranes (Massignon, 1979). The remaining high pressure stream may now be considered depleted and may also be referred to as tails. In a gas centrifuge, a rotating drum containing the UF_6 gas is used to separate the isotopes that have different masses. The lighter ^{235}U will be located closer to the centre of rotation, whereas the centripetal force acting on the heavier ^{238}U isotope will cause it to be expelled radially further outwards, closer to the wall of the centrifuge (Olander, 1978).

The enriched UF_6 gas must be considered a nuclear criticality safety risk since the concentration of ^{235}U is greater than 1% (IAEA, 2014). However, it must also be noted that the probability of a

transient nuclear criticality excursion involving such low density gaseous fissile material is very remote (Paxton, 1980). This is due to the low probability of interaction between neutrons and target nuclei when UF_6 is gaseous. Postulated nuclear criticality safety risks may arise from the phase change of UF_6 into solid uranyl fluoride (UO_2F_2) in the presence of water or moist air. Significant accumulation of UO_2F_2 deposits may lead to concentrated masses of fissile material building up in the isotope separation devices, in excess of acceptable levels, therefore posing a nuclear criticality safety risk. Mitigating techniques typically include routine examination of enrichment facility equipment for any solids build-up, as well as routine instrumentation and measurement procedures of the efficiency of the enrichment facility (Taylor, 1973). Numerous nuclear criticality safety studies involving single and interacting arrays of UF_6 surrounded by hydrogenous moderator have been performed (Newlon and Mallett, 1966; Begue et al., 2013; O'Connor, 2013). These investigations have been specifically carried out for the storage and transport of large numbers of UF_6 cylinders between the enrichment and nuclear fuel fabrication facilities. The criticality safety of the containers used to transport UF_6 is ensured through the use of favourable geometry, fissile mass limits, fissile array spacing criteria and the application of moderating materials.

The conversion of the enriched UF_6 to enriched UO_2 powder and subsequently pellets in nuclear fuel fabrication facilities may pose the greatest front-end fuel cycle risk of accidental nuclear criticality excursions (Knief, 1985). Several processes have been implemented on an industrial scale to convert UF_6 into UO_2 powder. These methods may be classified as either 'dry' or 'wet' approaches. The ADU and ammonium-uranyl carbonate (AUC, $UO_2CO_3{\cdot}2(NH_4)_2CO_3$) methods are considered as 'wet' processes since they involve the precipitation of enriched uranium from aqueous solutions (Brandberg, 1973). In these 'wet' processes, gaseous UF_6 is dissolved in water, forming a UO_2F_2 slurry. Ammonia or ammonium carbonate ($(NH_3)_2CO_3$) is then added to form either an ADU or AUC precipitate slurry. Alternatively, AUC powders may also be produced via the addition of ammonium carbonate to a uranyl nitrate solution. These dispersed particulate slurries are then filtered, dried and heated in a reducing atmosphere, forming UO_2 powder particles. The morphological properties of the UO_2 powder particles are highly dependent on the intermediary steps from the gaseous UF_6 to the UO_2 powder (Janov et al., 1972).

For the 'dry' conversion of UF_6 to UO_2, gaseous UF_6 is hydrolysed with steam to produce UO_2F_2. The UO_2F_2 is then reduced using hydrogen gas to produce UO_2 (Brandberg, 1973). Two main methods are practised for the production of UO_2 powder using the 'dry' route. These are the rotating kiln method and the fluidised bed method with a particle coating technique. The fluidised bed method involves feeding a mixture of gaseous UF_6, gaseous H_2 and steam into a bed of dispersed UO_2 'seed' powder particles (Knudsen et al., 1964). The gas advection, introduced through a perforated plate produces enough pressure drop across the powder bed to introduce fluidisation. The turbulent motion of the powder particles and high specific surface area for the UO_2 result in efficient interfacial chemical processes on the surface of the UO_2 powder particles. The rotary kiln method outlined in Littlechild and Gillies (1974) is similar to the fluidised bed method, but uses an inclined rotating barrel with a mixture of UF_6 gas and dry steam. These two components react to produce uranyl fluoride powder which is then carried to the upper end of the kiln barrel. As the uranyl fluoride powder is transported down the rotating barrel, a counter-current flow of a hydrogen/steam mixture reacts with the uranyl

fluoride, producing UO_2 powder.

The specific IAEA regulatory guide associated with the nuclear criticality safety of uranium fuel fabrication facilities is SSG-6 (specific safety guide 6) (IAEA, 2010). This regulatory guidance document states that as part of the criticality control of the nuclear fuel fabrication facility, any unexpected changes to conditions that could result in an increase in the probability of a nuclear criticality accident should be taken into consideration for the criticality safety case. These unexpected changes may include the accumulation of dispersed fissile powder that has been aerosolised, any inadvertent change in neutron moderation or absorption and the re-distribution of fissile mass into a more critical configuration. Specific NCS consideration should be taken for the 'wet' process of UO_2 powder production due to the large number of process-related nuclear criticality accidents that have occurred in fissile solution based systems (McLaughlin et al., 2000).

A postulated nuclear criticality excursion may occur during the hydrolysation of UF_6 into a UO_2F_2 slurry if the concentration of UF_6 is above allowable limits or if the hydrolysing tank is of an unfavourable geometry. The incomplete formation of UO_2F_2 as a consequence of insufficient water present for the hydrolysation process, leads to the production of uranium oxy-tetrafluoride (UOF_4) (Wagner et al., 2015). Uncontrolled hydrolysation may also occur if the container holding UF_6 gas is ruptured and the UF_6 mixes with atmospheric moisture, present in surrounding air (Kips et al., 2007). Solid products of this reaction may then aggregate and sediment in air (Bostick et al., 1985), forming a critical configuration. Alternatively, inhalation of the aerosol may cause radiological harm to those in the nearby vicinity. The probability of a nuclear criticality excursion due to the hydrolysis and concentration of very fine UO_2F_2 particulates is low due to process controls that limit the mass of UF_6 used in transportation containers as well as in the hydrolysation process. Furthermore, due to the low density of gaseous UF_6, the concentration of uranium is expected to be sufficiently low that the dispersed particulate formed would not exceed a critical mass in the event that it agglomerated and sedimented. Of the 22 known process accidents that have occurred before the year 2000 and those that have occurred post 2000, none have been attributed to the hydrolysis of UF_6 during the fabrication of UO_2 powder (McLaughlin et al., 2000; Hodges and Sanders, 2014).

Once the UF_6 has been hydrolysed, ammonium carbonate or ammonium may be used to precipitate AUC or ADU. NCS risks may arise from the use of excess amounts of fissile material in the precipitation of the AUC and ADU particulates. Traditionally, AUC and ADU precipitation is performed in a geometrically favourable vessel of narrow width and rectangular shape (Keni et al., 1994). However, if precipitation is performed in a geometrically unfavourable vessel, this may contribute to the probability of an accidental nuclear criticality excursion. Of the reported nuclear criticality accidents outlined in McLaughlin et al. (2000) and Hodges and Sanders (2014), none have been as a direct result of the precipitation of AUC or ADU particulates.

Vacuum filtration may be carried out on the AUC or ADU slurry to produce a cake which is then dried and and heated in a reducing atmosphere to produce UO_2 powder particles (Yi-Ming et al., 1981). The process of vacuum filtration may also be carried out for the 'dry' UO_2 production process, once H_2 has been used to reduce the UO_2F_2 into UO_2 powder. No accidents have been recorded regarding the vacuum filtration of ADU and AUC precipitates. However, there has been a

recorded nuclear criticality accident at the Electrostal Machine Building Plant on the 3rd of November 1965 involving the vacuum transportation of uranium oxide in a slurry at 6.5-wt%, after a hydrogen reduction operation for the 'wet' UO_2 production route.

This accident, described in detail in McLaughlin et al. (2000), occurred when UF_6 was being converted to UO_2 in a dry conversion process. An illustration of the conversion facility is shown in Figure 1.6. UF_6 was burned in a hydrogen-air atmosphere to produce uranium oxides. A vacuum was then applied to transport these particulates to an accumulation hopper. During normal operation, the vacuum system would be turned off and the uranium oxides would accumulate via natural sedimentation in the 20 L vessel shown in Figure 1.6. During routine operation of the conversion system, a criticality accident alarm sounded. The cause of the alarm was a build-up of uranium in the vacuum supply vessel and other areas of the vacuum system due to a missing primary filter and incorrectly installed secondary filter. It is thought that the initiation of the nuclear criticality excursion was due to the settling of the uranium oxides to the bottom of the vacuum supply vessel during the failure. Termination of the transient nuclear criticality excursion was due to the re-distribution of fissile material to other areas of the vacuum supply vessel. There was no damage to equipment or harm to personnel. NCS controls that were in place included the use of favourable geometries, specifically for the accumulation hopper, as well as the use of the filtration system, preventing pollution of the vacuum system by fissile material.

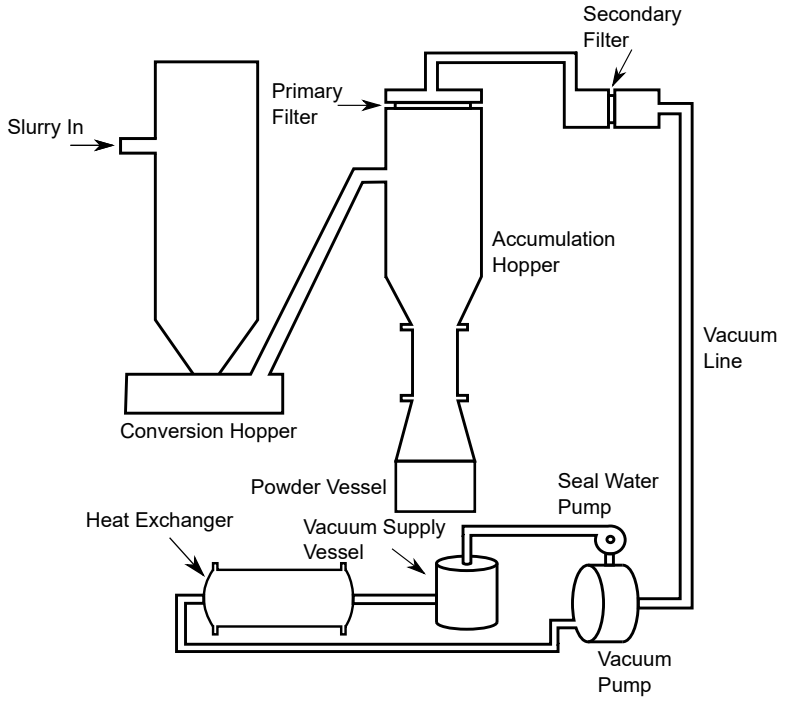

Figure 1.6: Schematic of the Electrostal Machine Building Plant facility used for 'dry' conversion of UF_6 to UO_2 (reproduction from McLaughlin et al. (2000)).

An additional accident (described extensively in McLaughlin et al. (2000)) involving a highly enriched uranium (HEU) (70-wt%) slurry occurred at the Novosibirsk Chemical Concentration Plant on the 15th May 1997. This accident arose in Building 17 where a chemical etching process was being used to remove defects on the surface of HEU fuel rods. An illustration of the components in operation are shown in Figure 1.7. Criticality safety controls included the implementation of optimal geometry

for all components that handled fissile material. The process used for chemical etching involved sequentially immersing the HEU rods in an alkali solution, water and acid solution. However, use of sodium hydroxide as the alkali caused leaching of UO_2 from the fuel rod. The leached products then sedimented on the bottom of the vessel. Once the etching process was complete on a batch of fuel rods, the alkali, water and acid vessels were drained into a collection vessel and subsequently pumped to receiving vessels. During routine inspection, a crust of UO_2 powder, found in the collection vessel, was dissolved gradually using nitric acid. However, the operators did not search for accumulation in the receiving vessels, as there were no requirements in criticality safety controls to do so. During subsequent operation, drainage of the etching solution caused a criticality alarm to sound. Attribution of the nuclear criticality excursion was assigned to the large volumes of solid UO_2 that were found crusted onto the receiver vessels. There were no significant exposures as a result of the accident.

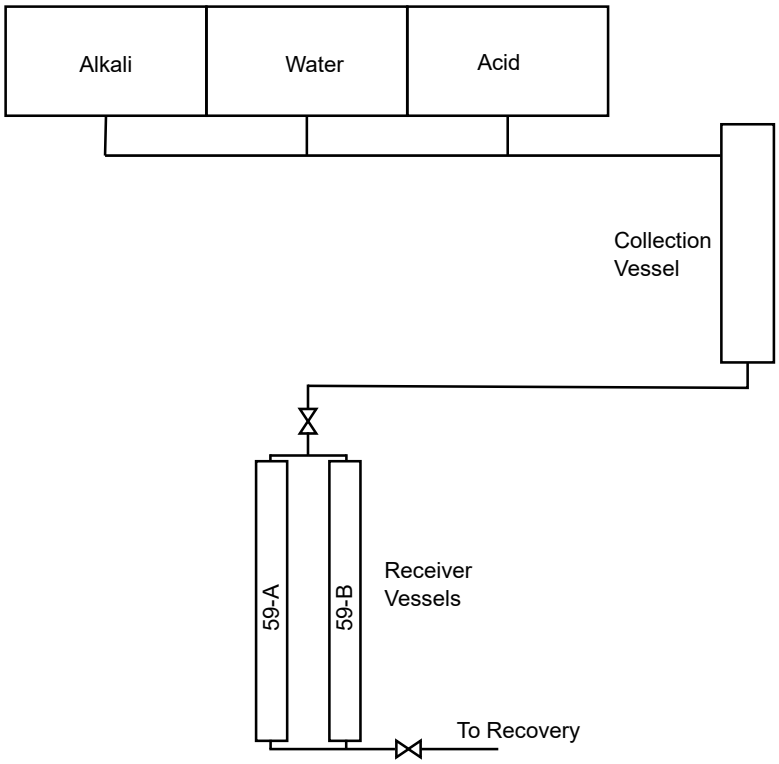

Figure 1.7: Schematic of the Novosibirsk facility used for chemical etching onto HEU fuel rod in preparation for adding cladding (reproduction from McLaughlin et al. (2000)).

Fire and explosion risk is an important nuclear safety case that must be accounted for in a uranium fuel fabrication facility. Any fire or explosion in a nuclear fuel fabrication facility may lead to the dispersion or aerosolisation of the dispersed particulates usually found in the facility such as, ADU, AUC, UO_2F_2 and UO_2 powders (IAEA, 2010). The use of hydrogen in these facilities for conversion, sintering and reduction processes should be carefully controlled since it poses a significant explosion risk (Sánchez and Williams, 2014). Additional fire and explosion risk arises from the presence of zircalloy which is a combustible metal, specifically in powdered form or as thin scrap (Datta, 1991). Other common industrial fire risks arise from the use of electrical cables, human error and the use of certain flammable products. Fire prevention techniques include the separation of hazardous materials, minimisation of fire load in process areas and the compartmentalisation of buildings to prevent spread (Holmes and McLaughlin, 1994). Fire tackling measures include the use of automated and manual

fire-suppression systems, which includes the use of sprinkler systems and manual fire-fighting. The risk of explosion should be mitigated by ensuring that the atmosphere surrounding particular operations is inert and by monitoring the presence of explosive materials throughout the facility. A more detailed description of NCS risks that are accompanied by a fire in a nuclear fuel fabrication facility is provided in Section 1.4.

DiPeso and Peterson (1998) postulated an NCS risk associated with a fire involving fissile material where the mixture of fissile material ash and water, from fire fighting, may lead to a nuclear criticality excursion. This type of excursion may occur due to the agglomeration of fissile ash with water (acting as moderator), causing a critical mass to form. Alternatively, water added to the fissile ash may cause mass re-distribution, leading to the formation of a critical geometry.

Prior to the UO_2 pellet fabrication, the UO_2 powder is homogenised in a conical blender (such as shown in Figure 1.8) by mixing the powder with some form of agitator. Doucet et al. (2003) postulated a NCS risk involving the incursion of water (acting as moderator), due to a burst pipe, into the conical blender. The ingression of water into the UO_2 powder bed may lead to an accidental transient nuclear criticality excursion. Instead of using a conical blender, a homogenisation machine may also be used. The machine achieves homogenisation of the powder by using a hydrogenous lubricant (acting as moderator) and applying a vibrating motion to achieve. The homogenised UO_2 powder is then pressed into a high density configuration and loaded into tubes in preparation for insertion into a nuclear power reactor. NCS controls in facilities that blend and compact UO_2 powder use geometry, mass, and moderation to achieve safety requirements Zurrón-Cifuentes et al. (2011). The blender is typically designed to be a favourable geometry that achieves acceptable amounts of neutron leakage. Furthermore, moderation is controlled by applying constraints on the H/U ratio that can be used. As well as the risk of water leaks, accidents may occur due to improper mixing of the UO_2 powder, leading to heterogeneous configurations, more than acceptable amounts of hydrogenous material or alternatively, non-optimal amounts of UO_2 powder.

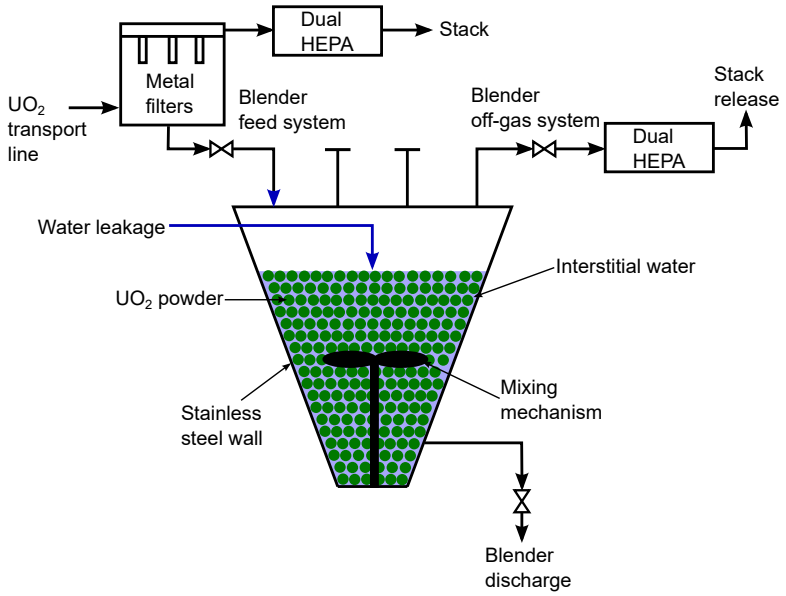

Figure 1.8: Schematic of a dry UO_2 powder blender used during the production of UO_2 pellets (reproduction from Basoglu et al. (1994)).

Once the UO_2 powder is pelletised and inserted into fuel rods, the fuel is transported to the nuclear power reactor and used in operation. This thesis does not address the risks of inadvertent nuclear criticality excursions during the operation of the nuclear power reactor. The fuel rods are usually sent to a reprocessing facility after a significant fuel burn-up. The purpose of nuclear fuel reprocessing is to maximise nuclear fuel utilisation. Spent or depleted nuclear fuel is reprocessed in order to achieve appropriate neutronic and physical characteristics for reuse in a nuclear power reactor. This is beneficial since it closes the fuel cycle. Borges Silverio and de Queiroz Lamas (2011) notes that up to 33 % of nuclear fuel is currently re-processed, leading to a significant increase in the fuel utilisation.

Nuclear fuel was first re-processed in the 1940s using pyrochemical and precipitation processes (Crossland, 2012). Modern nuclear fuel re-processing uses the plutonium-uranium reduction extraction (PUREX) process. This chemical process uses nitric acid to first dissolve the irradiated fuel slugs that are received from the power reactor (Starks, 1977). The solution that is produced contains a combination of ^{238}U, ^{235}U, plutonium isotopes as well as fission products, some of which are actinides. Before it is passed through a solvent extraction cycle, the solution may be further processed to remove certain components. Tributyl phosphate (TBP) is used in the solvent extraction cycle to separate the plutonium and uranium from fission products and chemical impurities. Separated plutonium from a second solvent extraction cycle is reduced to form a plutonium metal. The remaining solution is passed through a second uranium solvent extraction cycle. Extracted uranium is then denitrated to produce UO_3 (Baumgärtner and Ertel, 1980).

The processing rate of spent nuclear fuel assemblies through the PUREX process requires large solution flow rates of radiologically active fissile material. Consequently, associated nuclear criticality safety measures must be implemented to minimise the risk of an inadvertent self-sustaining nuclear chain reaction. Criticality safety is engineered into the PUREX process by ensuring that equipment is designed to be of favourable geometry (Herbst et al., 2011). The favourable geometric designs are used in conjunction with mass, concentration, and flow rate limits on fissile solutions to ensure the concept of 'always-safe' is satisfied (Boldt and Oberg, 1970). However, Boldt and Oberg (1970) notes a range of postulated nuclear criticality accident scenarios including an uncontrolled addition of fissile material above the prescribed safe limits, likely due to human error. Special process procedures are in place to ensure that additional fissile material is not added. Visual markers are also in place to ensure this is the case. Continuous monitoring of the activity of the solutions is achieved by sensors.

The formation of powdered or agglomerated deposits of concentrated fissile material in equipment, due to the addition of TBP or through precipitation, may also result in a nuclear criticality excursion. This is mitigated by prescribing limits on the amount of precipitated fissile material may be present in a vessel at any given time, ensuring that criticality will not be reached. Risks associated with other radiological and criticality related hazards in the PUREX process have been outlined in IAEA (2017) and summarised here. The risk of fire in these facilities is of the same origin as for nuclear fuel fabrication facilities, which includes the use of flammable materials such as solvents and reactive chemicals. A fire may introduce a credible risk of a nuclear criticality excursion by damaging or affecting mechanisms used to control the reactivity of the highly radioactive spent nuclear fuel. Furthermore, the use of fire-suppression systems, both automatic and manual, that involve the use

of water may, in some cases, alter the reactivity of the spent nuclear fuel by introducing significant moderation. Accidental nuclear criticality excursions as a result of fire are mitigated through careful fire hazard analysis and engineering controls. Similarly, there is a risk of explosions occurring in the re-processing facility through the use of highly flammable or explosive chemicals. The re-processing facility needs to be able to deal with loss of power or other support systems that may impact the processes used to control the reactivity of the spent nuclear fuel.

Once sufficient separation of individual fissile molecules is achieved, the products may be re-introduced into the nuclear fuel cycle in a variety of ways. Reprocessed uranium (RepU) may be further enriched in an enrichment facility, producing enriched reprocessed uranium (ERU) for subsequent fuel fabrication and usage. Furthermore, RepU may also be blended with HEU or medium enriched uranium (MEU) to produce a fuel with appropriate neutronic characteristics for use in certain types of nuclear power reactor (Combs, 2016). The plutonium may be mixed with depleted uranium from either a power reactor or enrichment facility to produce mixed oxide (MOX) fuel (Sakai et al., 2004). In a MOX fuel fabrication plant, UO_2 and PuO_2 are blended together in a conical blender in the presence of a lubricant, usually zinc stearate, to achieve homogenisation of the nuclear fuel (Provost et al., 2000). In Japan, the Nauta® mixer is used to blend the various nuclear fuels that constitute the MOX fuel pellet. An illustration of the blender shown in Figure 1.9a. The Nauta® conical mixing device utilises two rotational mixing mechanisms. One of these is an Archimedean screw that lifts and locally mixes the powder particles. The second mixing effect comes from the rotation of the Archimedean screw arm about the radial centre of the conical vessel. Figure y shows the mixing patterns that are produced as a result. The pressing and sintering of the MOX fuel pellets is performed in a similar way as for the production of UO_2 pellets from UO_2 powder, with additional shielding for operators to provide safety against spontaneous fission of ^{240}Pu (Haas, 1997).

The postulated risks of nuclear criticality excursions during the handling of enriched fissile powders in MOX fuel fabrication facilities are numerous. Similarities in the production of MOX fuel pellets compared with the fabrication of UO_2 fuel pellets, leads to similar postulated nuclear accident scenarios. Safety guidance outlined in IAEA (2010) highlights that the risks of fire and explosion, including the use of manual and automatic, water-based fire-suppression systems, pose a significant nuclear criticality safety risk. Additional safety consideration must be taken in the case of loss of support systems. This may result in a loss of cooling, ventilation or control systems through a loss of electricity, all of which may have significant consequences in a MOX fuel fabrication facility. Loss of cooling is particularly dangerous during the manufacture of MOX pellets since the MOX fuel has a high thermal load as it produces significant amounts of decay heat. Furthermore, the excess use of zinc stearate lubricant in concentrations that exceed the intended design within the blender should be taken into consideration since the lubricant acts as a moderator.

Uranium fuel in metallic form, found in the nuclear fuel cycle during intermediate process storage and as waste, presents certain NCS risks. Heat applied to uranium metal in the presence of oxygen causes hydriding (Burke and Smith, 1947). Formed uranium hydride is a fine, pyrophoric powder that may be susceptible to spontaneous combustion, or even explosion, when in the presence of oxygen (Stakebake, 1992). The NCS risks associated with pyrophoricity in nuclear powders have been well documented (Bannister, 1968; Orr et al., 2017). Typical measures to mitigate pyrophoricity concerns

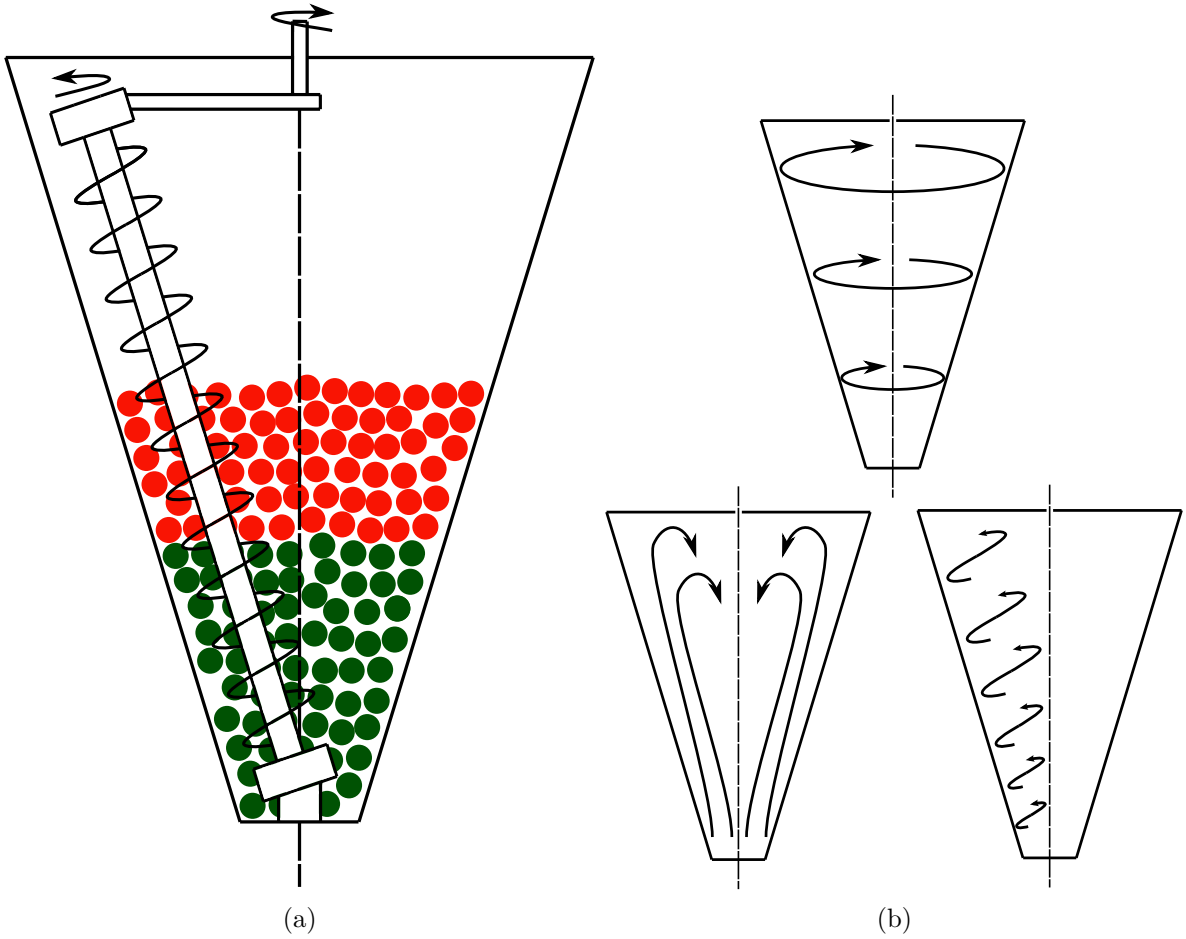

Figure 1.9: (a) Side elevation schematic of the Nauta® blender mixing MOX powder. (b) Three mixing patterns produced from MOX blender.

involves handling the nuclear fuel in an inert atmosphere, with low moisture content (Guyadec et al., 2010). A similar but potentially more severe NCS case occurs due to the hydriding of plutonium metal, which also exhibits pyrophoric behaviour once in fine, granulated form and exposed to air (Haschke and Stakebake, 2011). The severity is increased due to the potential for a combined auto-catalytic nuclear chain and chemical reaction in plutonium hydride, which contains the isotope ^{239}Pu. This is a result of the positive thermal reactivity feedback, which is caused by a low-lying energy resonance at 0.3 eV.

There is still no long-term spent nuclear fuel repository licensed to store high-level waste (HLW) for a period of time that exceeds 100 years (Crossland, 2012). Long-lived radionuclides that are generated through the nuclear fission process require very long-term storage. These radionuclides generate significant heat from radioactive decay. For the first 20 years, decay heat is predominantly the result of fission product β particles, rather than the decay of actinides. The generation of decay heat necessitates the use of cooling ponds, which act as a heat sink for the spent nuclear fuel whilst also providing radiological protection from the spent fuel (Federovich, 2007). Once the reactivity of the fissile material has dissipated, it may be sent to dry storage. There are a number of nuclear power producing countries that practice the dry storage of HLW (El-Samrah et al., 2021). IAEA (2020) outlines the associated IAEA SSG regarding the safety of spent nuclear fuel storage facilities.

Postulated NCS risks may stem from fire, explosion, and components that constitute acronym MAGIC MERV that are incorrectly controlled.

Although there is no active long-term storage scheme in place for intermediate level waste (ILW) and HLW, significant research efforts have been undertaken into the implementation of long-term geological disposal facilities (GDFs) and NCS risks associated with GDFs (Poirot-Delpech and Raineau, 2016). These GDFs are intended to be a means of storing very long term radioactive waste in a stable geological environment, deep underground. Active monitoring of the GDF would be planned for a short period of time, relative to the half-life of the contents of the GDF. Once active monitoring has ceased, the GDF would enter a post-closure stage. This storage phase may exist for hundreds of thousands of years. No containment mechanism can be proven to last over that long time frame; therefore, it is of importance from an NCS perspective that criticality risks be evaluated, in the event of loss of containment.

Although the original storage of the ILW and HLW will be sub-critical by controlling mass, geometry, and other characteristics affecting criticality. Over time, chemical or hydrological processes may cause the re-distribution of the nuclear waste into a critical configuration (Ahn, 2006). The degradation of waste packages over very long time-scales may be unavoidable, and so consideration must be taken to understand all the ways in which criticality may occur in the degraded package. Mason and Smith (2015) has postulated that waste packages may be susceptible to a nuclear criticality excursion in the event of flooding or groundwater flow in the post-closure GDF. This flooding may cause the material in the waste stacks to be carried away with the flow of water, leaving an unstable fissile structure that slumps into a more dense configuration, causing a nuclear criticality excursion. Alternatively, the flow of water may transport fissile material through the ground, leading to deposits that can form critical configurations (Mason et al., 2009). Of particular interest is how the Bowman-Venneri-Kastenburg autocatalytic phenomenon (Bowman and Venneri, 1996; Kastenberg et al., 1996) may cause highly energetic underground transient nuclear criticality excursions in the event of a nuclear criticality in HLW containing ^{239}Pu (Rechard, 2015).

A natural analogue to post-closure NCS studies in GDFs may be made with criticality in geologic formations, first studied by Kuroda (1956). One such natural nuclear reactor known as Oklo (Loss et al., 1988), located in Gabon, operated two billion years ago, when the natural enrichment of uranium was higher, at $\approx 3.7\%$ (Mason et al., 2012; Bentridi et al., 2011). The existence of this reactor was shown by Francis Perrin, who, in 1972, examined mined uranium deposits with less ^{235}U than should currently exist in natural uranium (Gil, 2018). Physical examination of the site led to the discovery of 16 lenticular zones interspersed within sandstone. Water infiltration through the porous sandstone, into the lenticular zone, led to long-term cyclical transient nuclear criticality excursions. The fundamental physics of the Oklo natural nuclear reactor were elucidated by Naudet (1991).

1.3 Sub-Critical and Approach-to-Critical Wetted Fissile Powder Experiments

The research presented in this thesis focuses on modelling transient nuclear criticality excursions in wetted fissile powders, specifically UO_2 powder. It is therefore necessary to outline the sub-critical, approach-to-critical and critical experiments historically performed on wetted or damp UO_2 powder systems.

As far as the author is aware, at the time of writing, there have been no super-critical experiments performed on fissile powders when wetted. NCS assessment of nuclear fuel facilities would be supported by such experiments, by giving NCS experts greater understanding of phenomena that affect transient nuclear criticality excursions in fissile powders. Moreover, experiments would support the validation of numerical codes, which can then be applied to a range of postulated NCS cases (Rouyer et al., 2003).

NCS engineers can perform steady-state calculations using codes previously verified against critical experiments. This increases process safety, equipment design and mitigates the risks to accidental transient nuclear criticality excursions.

The Nuclear Energy Agency (NEA) Working Party on Nuclear Criticality Safety (WPNCS), in a 2004 meeting, noted the requirement for integral benchmark studies, examining damp MOX powder systems (Patemoster et al., 1999). This led to the Institute of Physics and Power Engineering (IPPE) in the Russian Federation and the Commissariat à l'Energie Atomique et aux Énergies Alternatives (CEA) / Institut de Radioprotection et de Sûreté Nucléaire (IRSN) in France proposing damp MOX powder experiments. These experiments were proposed to model reflected and un-reflected, dry and damp MOX powders using weapons-grade and reactor-grade plutonium (NEA, 2005). Ivanova et al. (2009) accounts the results of the critical experiments performed at the BFS-1 experimental facility by the IPPE in the Russian Federation. Duhamel et al. (2005) lists other data from damp MOX powder critical experiments carried out by the CEA/IRSN.

Numerous critical experiments were designed and performed on damp uranium powder systems, using a split-table (a system for bringing two elements progressively closer to each other) approach. One such experiment, performed at the Rocky Flats Plant and documented by Rothe and Goebel (1982), used the split-table approach to model nuclear criticality in damp, 4.48 % enriched U_3O_8 powder with a hydrogen to uranium ratio, H/U = 2.03. Additional integral critical experiments were performed at this plant using U_3O_8 powder with a hydrogen to uranium ratio, H/U = 0.77, also in a split-table configuration (Tuck and Oh, 1979). For this experiment, a HEU ($\approx 93\%$ ^{235}U) solution, acting as a criticality driver, brought a large array of low-enriched U_3O_8, contained within cans, to criticality.

The Institut de Protection et Sûreté Nucléaire (IPSN), which is now the Institut de Radioprotection et de Sûreté Nucléaire (IRSN), also conducted approach-to-critical experiments, using a split-table configuration, from 1982 to 1986 at the Valduc research centre in France. The MARACAS experiment as it was known, shown in Figure 1.10, was able to contain up to six tonnes of nuclear material on two

tables, one of which was stationary, while the other was mobile. IRSN performed approach-to-critical experiments with 5 % low-enriched UO_2 powder that was moistened to reach variable moderation ratios (H/U = 2.0 to 3.0) (Maubert et al., 1999). Some of these investigations have been added to the International Criticality Safety Benchmark Evaluation Project (ICSBEP) which contains 2881 configurations of critical and near-critical assemblies for use as criticality safety benchmarks (Briggs et al., 2003).

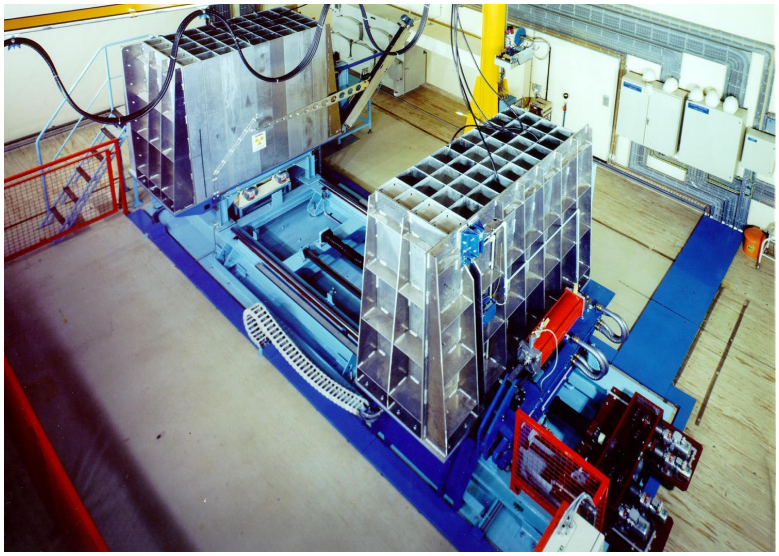

(a)

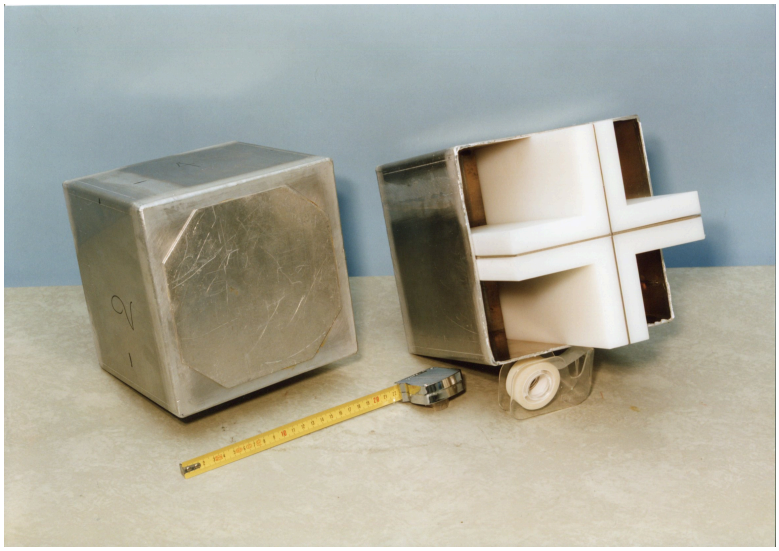

(b)

Figure 1.10: (a) MARACAS split-table experimental set-up showing static and moveable table [Photo: CEA/Valduc]. (b) Size of cubic units that contained the fissile material to be housed within MARACAS in an array formation [Photo: CEA/Valduc].

The CEA/IPSN performed the most extensive set of sub-critical experiments on UO_2 powder, at the Source d'Irradiation à Libre Evolution Neutronique (SILENE) experimental solution-based reactor facility located in Valduc, France. The United Kingdom Atomic Energy Agency (UKAEA) developed models, in conjunction with the CEA/IPSN, for modelling transient nuclear criticality excursions in wetted UO_2 powders which were calibrated using data and correlations from these experiments. These

numerical models were embodied within the POWDER transient nuclear criticality code (Bickley and Mather, 1991). SILENE was a homogeneous solution-based reactor that used HEU in a uranyl nitrate solution. A prescribed super-critical level could be obtained in the reactor by controlling the concentration of uranium present in the uranyl nitrate solution (Barbry, 1993). A control rod located in the core governed the initiation and termination of nuclear criticality excursions. The amount of reactivity change depended on the experiment being performed. A graphical illustration of the SILENE experimental reactor is shown in Figure 1.11 as well as an image of the reactor. Further images showing the scale of the test reactor, including the instrumentation surrounding the test reactor, as well as dummies with dosimetry equipment attached are shown in Figure 1.12. These images give an example of the wide-ranging extent of testing that was performed using the SILENE solution reactor.

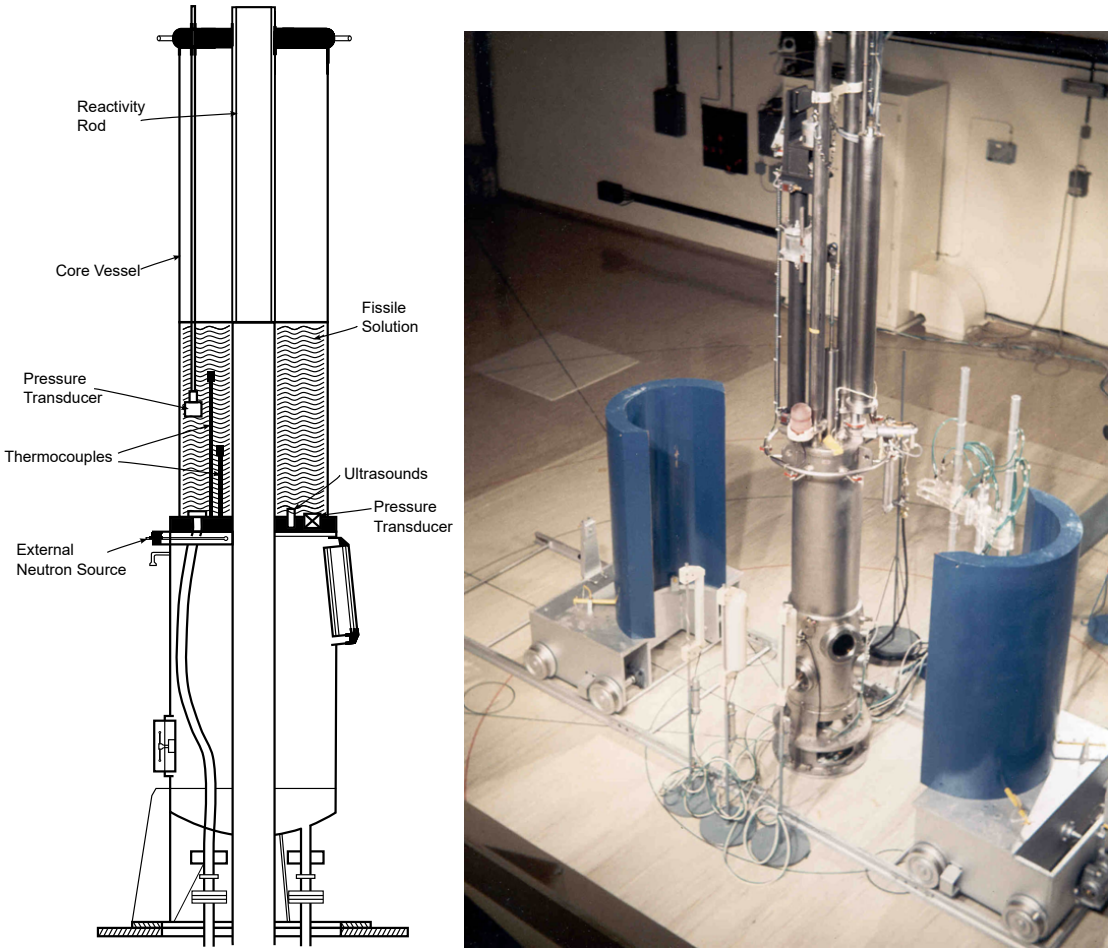

(a) (b)

Figure 1.11: (a) Side elevation view schematic of the SILENE uranyl nitrate experimental reactor. (b) Image of SILENE experimental reactor [Photo: CEA/Valduc].

Rozain et al. (1991) outlines three sub-critical experiments, including a water penetration study, a nuclear heating experiment and an electrical heating experiment. For the water penetration experiment, an experimental rig was created, capable of holding 500 kg of UO_2 powder. An illustration of the experimental setup is shown in Figure 1.13. A water jet, located axially above a cylindrical vessel, caused water to impinge upon the low-enriched (5-wt%) UO_2 powder at a rate of 0.5 L s^{-1}. Arrays of 16 humidity detectors were placed equidistantly throughout the height of the cylindrical vessel, such

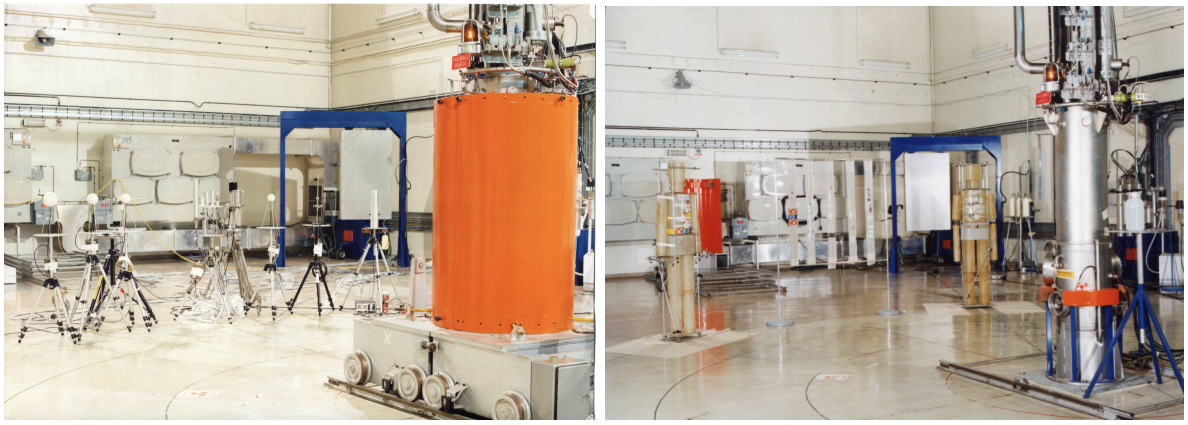

(a) (b)

Figure 1.12: (a) Equipment surrounding SILENE reactor [Photo: CEA/Valduc]. (b) Dummies with detectors placed around SILENE reactor for dosimetry study [Photo: CEA/Valduc].

that there were 8 detection planes. On the upper surface of the UO_2 powder bed, compaction sensors were used, capable of monitoring any collapse of the UO_2 powder bed that occurred throughout the water infiltration test. A data acquisition system (DAS) was used to convert the results into human-readable information. This experiment found that the penetration of water into the powder was approximately constant (2 cm min^{-1}) and the rate of powder bed collapse was 1 cm min^{-1}. Throughout the experiment, compaction caused the UO_2 powder bulk density increased from 1.0 g cm^{-3} to 2.2 g cm^{-3}. Assuming a theoretical density for UO_2 powder of $\rho_{p,th} = 10.95$ g cm^{-3}, the porosity variation was observed to be from 0.9087 to 0.7991. Information regarding the fraction of pores that remained dry throughout the water penetration study is not readily available.

The nuclear heating experiment was performed to gain an understanding of the thermal energy exchange characteristics of fissile UO_2 powder particles when dispersed in water. Samples were prepared and placed inside capsules similar to the one shown in Figure 1.14 and placed inside the SILENE reactor. The SILENE reactor was then pulsed and some incident neutrons on the fissile powder fissioned, generating fission energy, which subsequently led to thermal energy deposition in the UO_2 powder and surrounding water. These experiments found that there was a very high rate of thermal energy transfer between the powder particles and the surrounding liquid, leading to a local thermal equilibrium between the phases.

The final sub-critical experiment performed at the SILENE facility in Valduc, France, involved electrically heating a large sample of UO_2 powder dispersed in water up to the boiling point of the water. This experiment was performed to study geometric deformation of the UO_2 powder due to the formation of steam bubbles within UO_2 powder pore interstices. The results of this experiment indicated that small changes to the pressure of the vessel, due to the creation of steam bubbles, may produce a homogeneous displacement of the UO_2 powder and water. However, the dispersion may be a function of the doubling time, which for this experiment, was sufficiently low enough such that ejection of the UO_2 powder could not occur.

Two other sub-critical experiments carried out by Lichtenwalter (2008), at the Y-12 National Security Complex (Y-12 NSC) located in Oak Ridge, Tennessee, USA, involved the absorption of

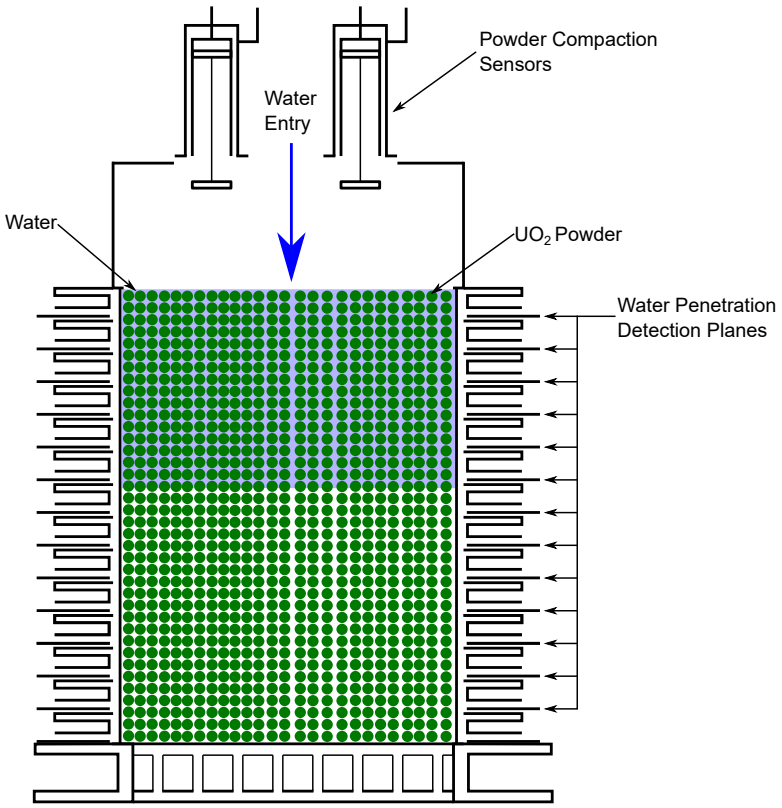

Figure 1.13: Side elevation view schematic of the SILENE water penetration into UO_2 powder experimental rig setup (reproduction from Rozain et al. (1991)).

water into depleted U_3O_8 powder. By slowly filling of a beaker of depleted U_3O_8 powder with water, the investigators observed a significant up-take of water ($> 78\%$) in the pore interstices, suggesting the majority of pores do not contain trapped air. For this experiment, the beaker was filled slowly to prevent disturbing the porous structure. The second experiment examined how the powder bed would disperse when impacted by a water jet that exceeded the Y-12 NSC sprinkler head's water flow rate. The flow rate prescribed was similar to if there was a water leak or manual fire fighting in the nuclear fuel fabrication facility. Results indicated that the jet of water impinging on the U_3O_8 powder bed disturbed the surface of the static powder bed, resulting in the formation of a suspension.

Dunn et al. (2013) performed wettability experiments as part of a Global Nuclear Fuels (GNF) sub-critical experiment. The objective of these experiments was to determine the water adsorption into various forms of UO_2 powder. They examined the wettability of UO_2 powder once converted from UF_6, granulated pre-compacted UO_2 powder, pellet shavings, U_3O_8 milled powder and UO_2 fuel pellets that were both sintered and un-sintered. Investigators used two wetting methods, one of which involved mixing the fissile powder and water in a conical beaker, before allowing the slurry/suspension to settle, examining the freestanding water. The other experiment involved pouring water onto a freestanding conical pile of powder that was not radially constrained. For the latter experiment, water adsorption into pore interstices was calculated by determining the volume of water run-off compared to water supplied to the powder bed. Dunn et al. (2013) found that unconstrained powders saw considerable run-off, with pore occupancies estimated at < 50 %. Furthermore, slurry formation generally required physical mixing of the fissile powder and water.

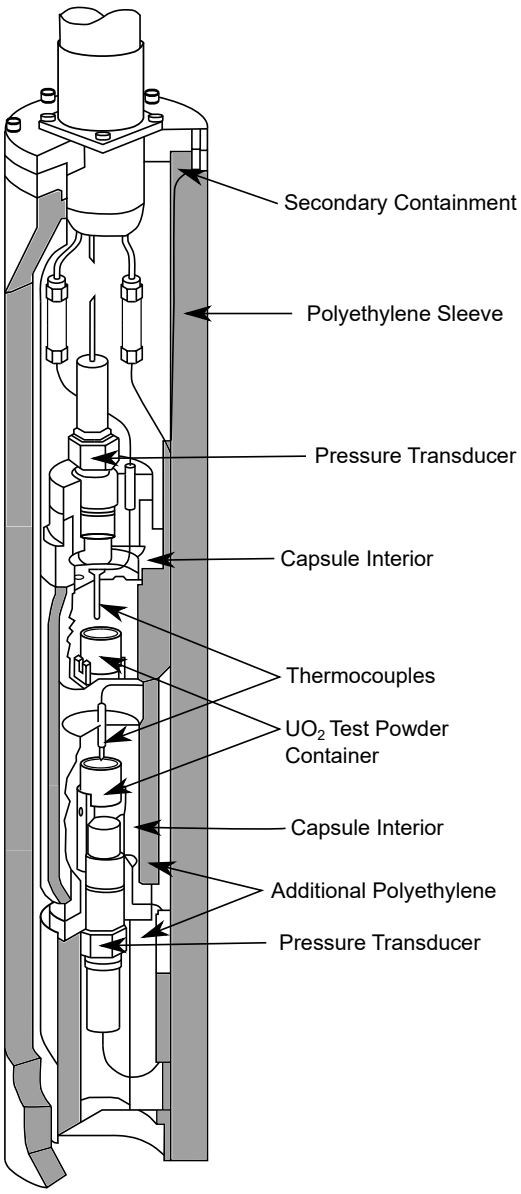

Figure 1.14: Isometric elevation cut-section view of capsule used to house UO_2 powder and water sample for placement in SILENE test reactor as part of the nuclear heating experiment examining thermal exchange between UO_2 powder dispersed in water (reproduction from Rozain et al. (1991)).

Significant research has also been dedicated to the use of fissile powders, specifically UO_2 (20-wt%), as a fuel for a suspension test reactor (Kersten, 1962). The Dutch company Keuring Van Electrotechnische Materialen (KEMA), in association with European Union's European Atomic Energy Community (EURATOM) designed and constructed one of the most well-known experimental sub-critical suspension test nuclear reactors, known as the KEMA suspension test reactor (KSTR). The reactor was built to examine the feasibility of suspension test reactors, as well as to study suitable suspension properties for such a reactor. Reactivity control of the KSTR was achieved by altering the concentration of the suspension dispersed in the water. This led to a varying H/U ratio and ultimately a change in reactivity. A simplified representation of the KSTR is shown in Figure 1.15. Researchers performed experiments on the chemical, radiochemical and mechanical properties of the dispersed UO_2 powder particles. The stability of the UO_2 powder was shown to be a function of the

surrounding de-mineralised water's pH level, with neutral water resulting in an unstable flocculation of UO_2 powder particles (Kalshoven, 1962). The critical concentration of UO_2 powder particles in the water was calculated through an extrapolation approach from a sub-critical state (Kersten, 1962). Kersten (1962) also found that by varying the upwards flow rate of the water through the KSTR vessel, the concentration could be adjusted, meaning that the effective multiplication factor, or reactivity, could also be controlled. Researchers showed that increasing the flow rate reduced the concentration of the suspension in the KSTR, with this effect being far more pronounced for flocculated (unstable) suspensions of UO_2 powder than for stable suspensions. Hermans (1959) studied the range of fission fragments in the suspension, showing that fission fragment ranges did not exceed 8 μm, which was less than the mean UO_2 powder size of 12 μm.

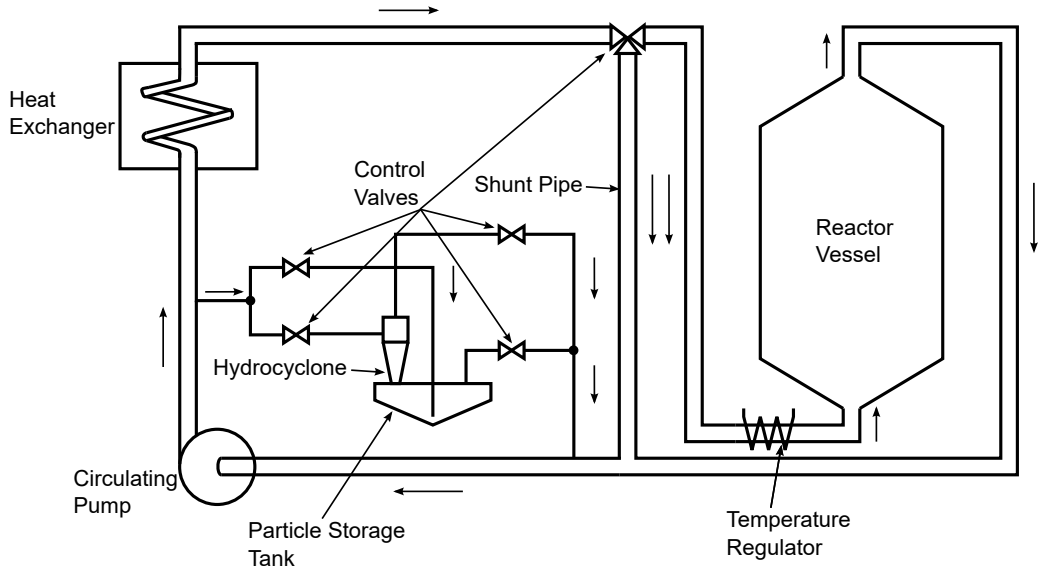

Figure 1.15: Simplified schematic of the sub-critical KSTR (reproduction from Went et al. (1964)).

Another UO_2 suspension or slurry based nuclear power reactor has been proposed recently by Laramore et al. (2018). Davidson et al. (1959) proposed a UO_2 powder-bismuth suspension reactor which could be controlled in a similar way to the KSTR, by forced circulation of the continuous liquid phase. Experiments were performed to examine the feasibility of suspending the UO_2 powder particles in the liquid metal (bismuth). Additional experiments documented by Ferguson (1957) examined the flowability of slurries through pipes as part of an aqueous suspension breeder reactor. This type of reactor uses a thorium dioxide ThO_2 dispersed phase in heavy water D_2O. This experiment was performed to investigate the chemical processing and flow of dispersed insoluble particulates that may build up as a result of reactor operation.

Although these experiments cannot be used to validate the super-critical states modelled in this thesis, they may provide validation for individual components of the neutron kinetics and phenomenological model. These experiments may also ensure that certain parts of the physics compare to experimentally derived data. This is specifically the case for the percolation sub-critical experiment carried out at the SILENE facility.

1.4 Proposed Nuclear Criticality Safety Case

Manual or automated fire fighting related criticality accident scenarios, as a consequence of a fire or explosion in a nuclear fuel fabrication facility, have already been emphasised. Specific interest in this thesis is applied to the inadvertent addition of water (acting as a moderator), from an automated fire-suppression system or manual fire-fighting, into a cylindrical barrel containing enriched UO_2 powder (Raap et al., 2014). This may occur in a single fissile unit, or during array storage and transportation of fissile material in the nuclear fuel cycle, as noted by Yearwood et al. (1993). Other than fire-suppression systems, additional sources of water (acting as moderation), may include tsunamis or burst water pipes in the facility housing the fissile powder. This postulated transient nuclear criticality excursion is the subject of this thesis.

Carter et al. (1968) extensively discusses the importance of preventing nuclear criticality accidents as a consequence of automated or manual fire-fighting. The author also explains that the consequences of a fire in a nuclear fuel fabrication facility, such as the aerosolisation of alpha emitting fissile material, may be worse than the NCS risk associated with water-based fire fighting. Therefore, it may be preferential to apply automated or manual water-based fire fighting techniques to combat a fire.

Datta (1991) notes that one of the primary risks of fire in a nuclear fuel fabrication facility comes from the storage, handling, and process use of hydrogen and flammable solvents. Fine particulate off-cuts, produced during the grinding of UO_2 fuel pellets, also pose a risk of fire and explosion. Guyadec et al. (2010) describes the potentially pyrophoric behaviour that these off-cuts may exhibit if spread in a non-inert atmosphere. This poses a significant risk, since the consequence of spontaneous ignition of aerosolised UO_2 particulates may be quite severe. Zircalloy is typically electrically arc welded in these facilities in an inert atmosphere, however, if fine powdered forms of this combustible metal escape the inert atmosphere, pyrophoric behaviour may be witnessed. Glovebox related fires are also considered a credible threat, even though operations are usually performed in an inert atmosphere under negative pressure (Datta, 1991). The handling of ordinary combustible materials such as fuel oils, liquified fuel gases and natural gas also pose a fire risk (IAEA, 2014). Other conventional manufacturing facility risks of fire are present, such as electrical cabling and human-error (IAEA, 2010).

The double contingency principle ensures that two independent failures must occur in the handling of the UO_2 powder for there to be an accidental transient nuclear criticality excursion. Double contingency measures include the specification of sub-critical packaging limits and the use of neutron absorbing inserts (IAEA, 2010). There is also a lid on the barrels containing UO_2 powder, likely preventing direct impingement of water from above the barrel. The sub-critical packaging limit is prescribed such that the mass of UO_2 powder, when optimally moderated, does not reach a critical state, by some prescribed factor of safety. Steady-state analytical or numerical methods using deterministic and Monte Carlo methods may be used to predict the effective multiplication factor, k_{eff}, of an optimally moderated UO_2 powder bed.

One of the most fundamental fire prevention techniques comes from the design of the nuclear fuel fabrication facility process areas. These areas are typically large open rooms, up to 45 feet in height (Datta, 1991). Process environments in the rooms of these facilities are usually compartmentalised,

to prevent the fast spreading of the fire and to allow for different fire hazard analyses in different process environments (Kwon et al., 2018). The French fire prevention scheme described in Savornin et al. (1989) cites containment as of the utmost importance in a fire prevention and mitigation plan. Containment is usually attained through the use of 8-inch cement block walls and cement concrete floors and roofs (Datta, 1991). Ventilation and air-conditioning systems between the compartmentalised rooms in nuclear fuel fabrication facilities are designed such that air flow travels from an area of lower contamination to one of higher contamination. This is achieved by controlling the pressures of each room, through the adjustment of air handling rates and dampers in the duct systems. Effluents are filtered from a fire in one of these compartmentalised zones by using high efficiency particulate air (HEPA) filters.

Fire drills are also a vital component of fire safety in these facilities, ensuring all personnel are aware of their responsibilities. Carter et al. (1968) describes a methodology for compartmentalisation, showing that a consistent graded fire-fighting scheme can be derived by assigning each process environment a category. The categorisation is based on several variables, but of particular importance is the risk of a criticality occurring due to the addition of a water-based fire suppression system in the process environment. Category A environments are reserved for ones where there is no risk of a criticality occurring, whereas, category B, C and D process environments correspond to a minimal, finite and high risk of criticality due to water-based fire fighting methods.

Carter et al. (1968) posits that the first three minutes of the fire is the most effective time to extinguish it. Common active fire fighting and protection equipment in nuclear fuel fabrication facilities include the use of flammable liquid storages, provision of fire pumps, hoses, hydrants, portable extinguishers, and the use of automatic fire-suppression systems (Datta, 1991). The specific type of fire suppression system that should be installed in a compartmentalised zone of a nuclear fuel fabrication facility should take into consideration the speed of response, type of combustible material present and items important to safety (AERB, 2009). The three main water-based fire suppression techniques include the use of water jets, firing streams of water droplets, a water fog system and a high-expansion water-based foam. Each of these may be used depending on the risk of criticality due to moderation in the specific process environment (Carter et al., 1968).

There are a large number of British Standard (BS) and European Norm (EN) documents that govern everything related to fire fighting as mitigation in domestic, commercial and industrial facilities. British Standards Institute (2015) outlines the design, installation, and maintenance requirements of automated fire sprinkler systems within the U.K. This extensive document governs every aspect of an automated fire suppression systems design and maintenance. Also described is a hazard classification scheme for fires on industrial sites. Of specific interest from a NCS modelling perspective is the automated sprinkler type, sprinkler discharge density, spray patterns, temperatures, water source, spacing, and height from the floor. These factors govern the rate at which water penetrates the fissile powder bed. Some of this information is provided for automated fire sprinkler systems in Table 1.1. The sprinkler discharge density corresponds to the discharge flow rate from the sprinkler in litres per minute, divided by the area that the sprinkler water spans. It must be noted that in many high-risk process areas, the use of a water-based fire suppression system may be prohibited. Gas-, powder- or chemical foam-based fire extinguishers may be used if water is prohibited.

Table 1.1: Sprinkler types and flow rates as a function of hazard class.

Hazard class	Sprinkler type	Sprinkler discharge density [mm min^{-1}]
Light hazard	Conventional, spray, ceiling, flush, flat spray, recessed, concealed, and sidewall	2.25
Ordinary hazard	Conventional, spray, ceiling, flush, flat spray, recessed, concealed, and sidewall	5.0
High hazard	Conventional, spray	7.5 to 12.5

Water mist systems may also be used to combat fires. These work by spraying very fine droplets of water at high pressure through nozzles that break up the water into micro droplets. These systems are effective in smaller process areas, where the bulk density of the mist in the air can limit the oxygen that the fire receives. British Standards Institute (2020) describes the design, installation, and maintenance requirements and guidance for fixed water mist and deluge systems.

Water-based fire fighting methods may pose risks of criticality when used in certain process environments. A water film thickness study on non-fissile material has been performed by Ross et al. (1991), examining the impingement characteristics of automated fire suppression systems in nuclear fuel fabrication facilities. Ross et al. (1991) also performed a steady-state criticality study, finding that criticality may occur under certain conditions. This criticality risk is specifically pertinent for water jet-based fire sprinkler systems used in process areas that contain arrays of fissile material (Yearwood et al., 1993). Steady-state nuclear criticality studies of water-mist systems, indicated that there could be a risk of criticality if uncontrolled use of water mist is permitted in some process environments (McCaughey and Bidinger, 1988).

No nuclear criticality accidents have been reported due to the addition of water (acting as moderator) into UO_2 powder, held in cylindrical barrels whilst awaiting pelletisation (McLaughlin et al., 2000). However, Hodges and Sanders (2014) reported a near-miss accident associated with the storage of UO_2 powder in cylindrical vessels. This near-miss accident, described in U.S. NRC (2002), occurred at the Framatome ANP facility in Richland, Washington on the 3rd of April 2002. The facility used 45-gallon drums that contain a neutron absorbing spider assembly for handling UO_2 powder. The absorbing insert is designed such that a nuclear criticality excursion will be avoided, even if optimal moderation of the UO_2 powder drum is achieved through the addition of water. However, at the end of drum life, the absorbing insert is usually removed and re-used. During the near-miss event, an operator prepared a blend of UO_2 powder for dissolution using an old drum that no longer contained a neutron absorbing insert. This failure of one of the double contingency measures meant that if there was an accidental incursion of water into the drum, a transient nuclear criticality excursion may have occurred. An operator in an enclosure down-stream of this opened the container, observed that there was no insert present, and acted according to protocol, preventing the situation from getting worse.

The prevalence of fissile powders throughout the nuclear fuel cycle and the associated risks of wetting-induced transient nuclear criticality excursions in fissile powders, predominantly due to fire and explosion related water-based fire fighting, has been outlined. NCS experts are obliged to ensure that the risks of accidental nuclear criticalities are reduced to ALARP in nuclear fuel process environments. This is achieved in nuclear fuel fabrication facilities by using the double contingency principle when handling UO_2 powder. However, if these measures fail, the potential characteristics of a wetting-induced nuclear criticality excursion in a UO_2 powder drum must be known.

The motivation of this thesis is to examine the consequences of such an accident, by considering neutron kinetics, nuclear thermal hydraulics, water infiltration, radiolysis and boiling processes in wetted UO_2 powder beds under delayed and prompt super-critical conditions. The models proposed in this thesis aim to enhance emergency planning and preparedness methodology by providing insight into the potential characteristics of such an accident.

An illustration of the UO_2 powder drum that is modelled throughout this thesis is shown in Figure 1.16. The infiltration of water from an automated fire suppression sprinkler impinges on the UO_2 powder bed from above. At high sprinkler flow-rates, water begins to pool on top of the UO_2 powder bed, creating a top reflector region. The domain is separated into three regions, each distinguished by a sharp interface. During the infiltration of water, the UO_2 powder bed is separated by a sharp wetting front that distinguishes the dry, unsaturated UO_2 powder bed from the wetted part of the UO_2 powder bed. The geometric, material mass and thermophysical properties of the system are described in greater detail in Section 3.4, but are taken from the data described for the SILENE sub-critical wetting experiment in Rozain et al. (1991). Although a selection of mean UO_2 powder particle sizes are studied in various chapters of this thesis, a mono-disperse approximation is used throughout. The effects that poly-dispersivity may have on the UO_2 powder packing, permeability and other thermophysical properties of the system are not considered. This approximation is discussed further in Section 3.4.2.

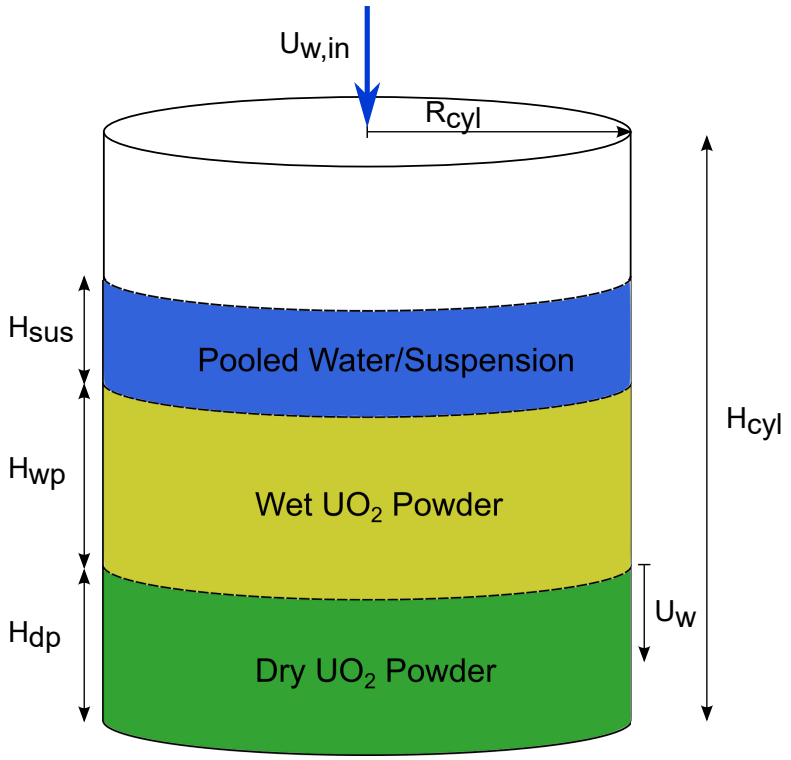

Figure 1.16: Representation of three-region UO_2 powder bed with region interfaces separating dry powder region, wet powder region and pooled water region.

1.5 Project Scope

The aim of this project is to propose and utilise neutron kinetics equations, coupled with the multi-group steady-state neutron diffusion and phenomenological models of three-phase flow, to simulate transient nuclear criticality excursions in UO_2 powder beds undergoing water infiltration. The proposed model simulates a postulated NCS case, where the incursion of water into a cylindrical vessel housing UO_2 powder initiates a transient nuclear criticality excursion by adding moderation. The source of the water (acting as moderator) may either be from a fire-sprinkler system, manual firefighting or water pipe leakages/bursts.

The novel parts of this thesis are as follows:

1. Coupled point neutron kinetic, two-group neutron diffusion and three-phase phenomenological model of continuity and thermal energy for modelling transient nuclear criticality excursions in UO_2 powder beds undergoing water infiltration.
2. Application of a model for the wetting-induced collapse of a UO_2 powder bed, applied to a piston-like infiltration model. The subsequent effect this phenomenon has on a wetting-induced transient nuclear criticality excursion is examined through a sensitivity study.
3. Gas-induced UO_2 powder bed fluidisation, turbulent mixing and sedimentation models are developed for agglomerated UO_2 powder particles. The subsequent effect this phenomenon has on a wetting-induced transient nuclear criticality excursion is examined.
4. Wait-time distribution study of HEU UO_2 powder systems undergoing a wetting-induced nuclear criticality excursion that satisfy low-source criterion and the impact that this has on the peak fission rate and integrated fissions.

1.6 Thesis Structure

The chapters of this thesis are as follows. Chapter 2 discusses various methods that may be used for NCS analysis. A detailed review of existing mathematical and numerical models for simulating transient nuclear criticality excursions in wetted fissile powder systems are presented. Lastly, the spatial and temporal numerical methods applied in this thesis are described. Chapter 3 outlines all aspects relating to the base model used to simulate wetting-induced transient nuclear criticality excursions in static UO_2 powder beds with point neutron kinetics, multi-group neutron diffusion, nuclear thermal hydraulics, radiolytic gas and steam equations. The proposed model is applied to two different cases, distinguished by their mean powder particle size. Fission power, energy and the importance of particular components of reactivity are calculated as well as other key parameters. The phenomenological approach used to represent water infiltration into the UO_2 powder is compared to experimentally derived settling rates outlined by Rozain et al. (1991). Chapter 4 is an extension of the model derived in the previous chapter, adding processes for the wetting-induced collapse of the UO_2 powder bed. An alternative method is used to evaluate macroscopic neutron cross-section data, and an additional reactivity feedback component has been derived. Once again, the effect that these extensions have on a wetting-induced transient nuclear criticality excursion is examined. In Chapter 5 a number of extensions are added to the model. These include modelling gas-bubble induced

fluidisation and turbulent mixing, which results in the formation of a three-phase suspension above the settled wet UO_2 powder bed. Additionally, a phenomenological model is given for sedimentation, with the sedimentation rate of agglomerated UO_2 powder particles derived directly from experimental observations. A method using bi-variate B-spline interpolations is used to evaluate bi-variate reactivity feedback components. Chapter 6 uses the forward stochastic balance equation to determine the mean neutron population and associated variance in a HEU UO_2 powder that is in a low-source regime. Reactivity is added to the system through the infiltration of water, similar to previous chapters. The Gamma distribution is used to estimate the mean wait-time. Deterministic simulations are performed using the model proposed throughout this thesis on HEU systems, starting from the transition between the stochastic and deterministic regimes. The effect that the wait-time distribution has on the peak power of a wetted highly enriched UO_2 powder system is examined. Finally, Chapter 7 proposes some avenues for future work, as well as providing a summary of work in this thesis.

Chapter 2

Mathematical and Computational Modelling for Nuclear Criticality Safety Analysis and Assessment of Fissile Powders

2.1 Introduction

IAEA guidance states in IAEA (2010) that several methods may be used to perform NCS analysis in nuclear fuel fabrication facilities. These include the use of experimental data, hand calculational methods and deterministic or Monte Carlo computational techniques. This thesis predominantly uses deterministic methods to evaluate the consequences of transient nuclear criticality excursions in wetted UO_2 powders. However, existing Monte Carlo codes are used throughout to obtain reactivity component profiles and macroscopic nuclear cross-section data. This chapter describes some of the methods that may be used for NCS evaluation, and also goes into greater detail about the spatial and temporal discretisation scheme used in this thesis.

2.2 Hand Calculational Methods

Hand calculational methods provide a means of analysing the state of criticality of fissile systems without the complexity overhead that may usually be associated with deterministic or Monte Carlo criticality safety codes. Due to the generally simpler nature of hand calculation methods, sensitivity analysis or perturbation techniques may be employed. This provides NCS experts with knowledge of how varying system parameters (in accordance with MAGIC MERV or MERMAIDS) may affect a system's criticality.

Examining the worst-case scenario and calculating the infinite multiplication factor (k_∞) are some basic concepts that may be used when performing hand calculational methods. The k_∞ value refers to

the neutron multiplication factor of a fissile system when there is no leakage of neutrons. If the hand calculational method indicates that the value of k_∞ is less than unity for the worst-case scenario, one may then posit that under no circumstance will a nuclear criticality excursion occur.

Hand-calculation methods of NCS for single fissile units, described in Bowen and Busch (2006), use one-group and modified one-group neutron diffusion theory, buckling conversions and core-density conversions. The neutron diffusion approximation, which assumes linear anisotropy in the angular neutron flux, is an appropriate approximation for large, homogenous nuclear systems that are highly scattering. This approximation is not strictly valid near vacuum boundaries, strongly absorbing materials, localised anisotropic neutron sources or when the time variation of the neutron current density is comparable to the mean collision time.

The neutron diffusion equation (NDE) can be heuristically derived by using Fick's law within the neutron continuity equation (NCE) to relate the neutron current to the scalar neutron flux. Alternatively, it can be derived in a mathematically rigorous manner by first angularly discretising the neutron transport equation (NTE) using spherical harmonic (P_N) basis functions and then truncating this expansion after two terms. This yields the P_1 equations which can be reduced to the NDE by solving for the scalar neutron flux. This spherical harmonic (P_N) derivation has the advantage of rigorously deriving an expression for neutron diffusion coefficient. The steady-state neutron diffusion and P_1 equations are mathematically equivalent. However, the time-dependent P_1 equations, which can be reduced to a single telegrapher equation (Dulla and Ravetto, 2008), is not in general equivalent to the time-dependent NDE (Duderstadt and Hamilton, 1976).

The NDE is presented and discussed further in Section 2.4. A buckling conversion technique may be applied to convert the neutron leakage properties of a fissile system from one geometry into another simple geometry. This is a powerful technique that gives the NCS expert a means of analytically modelling a range of simple geometries, evaluating which minimises the effective multiplication factor, denoted k_{eff}. Core-density conversion techniques may also be used to examine uniform density changes to fissile systems. Various hand calculation methods also exist for NCS analysis of arrays of fissile material; however, these are out of the scope of this thesis and are therefore not described in more detail. Further information regarding array NCS can be found within Knief (1985) and Bowen and Busch (2006).

The one-speed, steady-state NDE is a balance equation that accounts for neutron leakage, absorption, and production. Re-arrangement of the one-speed, steady-state NDE in a homogeneous, one-dimensional slab yields the following:

$$\nabla^2\phi + \frac{\bar{\nu}\Sigma_{\text{f}} - \Sigma_{\text{a}}}{D}\phi = 0 \tag{2.1}$$

where $\bar{\nu}$ [-] is the average number of neutrons produced by fission, Σ_{f} [cm^{-1}] and Σ_{a} [cm^{-1}] are the macroscopic fission and absorption neutron cross-sections, D [cm] is the neutron diffusion coefficient and ϕ [neutrons cm^{-2} s^{-1}] is the scalar neutron flux.

The material buckling, denoted B_{m} [cm^{-1}], may be defined as:

$$B_{\mathrm{m}}^2 = \frac{\bar{\nu}\Sigma_{\mathrm{f}} - \Sigma_{\mathrm{a}}}{D} \tag{2.2}$$

Substitution of Equation (2.2) into Equation (2.1) yields the following:

$$\nabla^2\phi + B_{\mathrm{m}}^2\phi = 0 \tag{2.3}$$

The corresponding analytical solution may be found by prescribing boundary conditions at the end of each slab and letting the general solution of Equation (2.1) be given by:

$$\phi(x) = A\cos(B_{\mathrm{g}}x) + C\sin(B_{\mathrm{g}}x) \tag{2.4}$$

where A and C correspond to the amplitude of the scalar neutron flux and are obtained through suitable boundary conditions and B_{g} [cm^{-1}] is the geometric buckling, which is dependent on the geometrical properties of the system.

If the geometric and material buckling are equal, the fissile system is critical. If material buckling exceeds that of geometric buckling then the system is super-critical, and sub-critical if vice-versa. From hand calculational methods of the one-speed NDE, it is possible to determine the critical dimensions of a reactor using material properties and the appropriate geometric buckling relation. The geometric buckling is found by solving the Helmholtz eigenvalue problem for different geometries.

As previously stated, the infinite multiplication factor, denoted k_∞, may be introduced to determine the maximum neutron multiplicity in a fissile system when there is no neutron leakage. Since this models an 'infinite' fissile system, the value of k_∞ is given by the ratio of production in one neutron generation over absorption in the previous generation:

$$k_\infty = \frac{\bar{\nu}\Sigma_{\mathrm{f}}}{\Sigma_{\mathrm{a}}} \tag{2.5}$$

When applying thermal corrections to the one-speed NDE to consider two-group effects, k_∞ may also be defined by the following four-factor relation:

$$k_\infty = \eta_{\mathrm{rep}}\epsilon_{\mathrm{ff}}p_{\mathrm{res}}f_{\mathrm{util}} \tag{2.6}$$

with:

$$\eta_{\mathrm{rep}}f_{\mathrm{util}} = \frac{\bar{\nu}\Sigma_{\mathrm{f}}}{\Sigma_{\mathrm{a}}} \tag{2.7}$$

where η_{rep} [-] is the reproduction factor, which corresponds to the ratio of the number of fast

neutrons produced by thermal fission to the number of thermal neutrons absorbed. The variable, ϵ_{ff} [-], is the fast fission factor, which is the ratio of the number of fast neutrons born by fission at all energies to the number of fast neutrons born through thermal fission. The resonance escape probability, p_{res} [-], is the probability that a slowing down neutron will not be captured in the energy resonance regions before becoming thermalised. The thermal utilisation factor, denoted f_{util} [-], is the fraction of neutrons that are absorbed in the fuel, compared to the total number of neutrons that are absorbed or leak from the core.

NCS experts may use this four-factor formula to evaluate the multiplication factor of an infinite fissile system, thus gaining information about whether it is feasible that an accidental transient nuclear criticality excursion may occur. The formula may also be directly used in a 'corrected' version of the steady-state, one-speed NDE:

$$\nabla^2\phi + \frac{\Sigma_{\text{a}}}{D}(k_\infty - 1)\phi = 0 \tag{2.8}$$

Letting the neutron diffusion length, $L_{\text{neut}} = \sqrt{D/\Sigma_{\text{a}}}$ [cm], the following may be written:

$$\nabla^2\phi + \frac{(k_\infty - 1)}{L^2_{\text{neut}}}\phi = 0 \tag{2.9}$$

where now the material buckling $B^2_{\text{m}} = (k_\infty - 1)/L^2_{\text{neut}}$. By equating the material and geometric buckling, NCS experts can gain an understanding of the critical dimensions in certain simple geometries, giving them the ability to design out most risks of criticality.

A more detailed modified version of one-group neutron diffusion theory exists that uses a six-factor formula, which accounts for neutron slowing down distance and non-thermal neutron leakage. In this formula, the material buckling is given by:

$$B^2_{\text{m}} = (k_\infty - 1)/(L^2_{\text{neut}} + \tau_{\text{age}}) \tag{2.10}$$

where τ_{age} [cm^2] is the neutron age.

One may use buckling conversion techniques to perform parametric NCS studies, examining the critical dimensions of a system in a range of different simple geometries (Paxton, 1972). This may aid NCS by giving an expert approximate knowledge of spatial dimensions that cause fissile systems to be critical. Critical size-density relationships may also be introduced according to Paxton and Pruvost (1986) to quickly estimate alterations to critical dimensions due to changes in density of uniform, homogeneous fissile systems.

Bowen and Busch (2006) found agreement between analytical modified one-group neutron diffusion theory and Monte Carlo and deterministic neutron transport codes, when estimating critical dimensions for certain fissile systems. The comparison of the results presented in Bowen and Busch (2006) show the importance of applying factors of safety if the predominant NCS calculation technique

is via hand calculation methods. Experiments may also be used to understand the accuracy of the hand calculation method for the particular fissile system under consideration.

Analytical analysis of time-dependent point neutron kinetics models also provide a powerful, yet simple means of analysing power distributions for a given fissile system's effective multiplication factor. Starting from the point kinetics equation, neglecting the effect of delayed neutron precursors, the change in the neutron population is given in Shultis and Faw (2016) as:

$$\frac{dN(t)}{dt} = \left(\frac{k_{\text{eff}} - 1}{k_{\text{eff}}\Lambda}\right) N(t) \tag{2.11}$$

whose solution is the following exponential function:

$$N(t) = N(0) \exp\left[\left(\frac{k_{\text{eff}} - 1}{k_{\text{eff}}\Lambda}\right) t\right] \tag{2.12}$$

where N [neutrons] is the neutron population at time, t [s], and Λ [s] is the mean prompt neutron generation time, which is typically $\Lambda \approx 10^{-4}$ s.

However, this analytical approach does not take delayed neutron precursors into account, which are the primary reason that nuclear reactors can be controlled. The presence of delayed neutron precursors that over time decay, releasing neutrons, increases the effective period of the fissile system. The concept of an effective mean prompt neutron generation time, denoted Λ_{eff} [s], may be introduced to attempt to account for these delayed effects.

$$\Lambda_{\text{eff}} = (1 - \beta_{\text{eff}})\Lambda + \beta_{\text{eff}}(\Lambda + \bar{\tau}_{\text{del}}) \tag{2.13}$$

where β_{eff} [-] is the adjoint-weighted effective delayed neutron fraction (which is usually very small, at around 0.65 % for a uranium system) and $\bar{\tau}_{\text{del}}$ [s] is the average delayed neutron precursor lifetime.

The neutron population as a function of time may then be given as:

$$N(t) = N(0) \exp\left[\frac{k_{\text{eff}} - 1}{k_{\text{eff}}\Lambda_{\text{eff}}} t\right] \tag{2.14}$$

The period of the fissile system, denoted T [s], which gives information regarding the time required for the system, in its present state, to increase in power by a factor of e, is given as:

$$T = \frac{k_{\text{eff}}\Lambda_{\text{eff}}}{k_{\text{eff}} - 1} \tag{2.15}$$

This information may be used by NCS experts to understand the kinetics of an accidental transient nuclear criticality excursion up to the point where reactivity feedback components begin to significantly affect the fissile system's reactivity.

2.3 Previous Modelling Efforts of NCS in Fissile Powder Beds

Numerous approaches to modelling accidental transient nuclear criticality excursions in wetted powders have been proposed in the literature. These typically range from the more simple spatially independent, phenomenological models, to high fidelity coupled computational fluid dynamics (CFD) and neutron transport models. A review of the existing methods for modelling UO_2 powders, as well as other fissile powders (such as MOX) is summarised here.

The POWDER code (Mather et al., 2004; Bickley and Mather, 1991), developed by the UKAEA in conjunction with the CEA, was one of the first codes developed to simulate the infiltration of water into a bed of initially unsaturated, enriched UO_2 powder. The CEA performed companion experiments at the SILENE reactor (Rozain et al., 1991) in Southern France. Water impingement and collapse (or slumping) of the UO_2 powder bed were the initiating phenomena behind an accidental transient nuclear criticality excursion in the UO_2 powder beds modelled using the POWDER code. The POWDER code did not directly model mass transfer of these phases, instead accounting for geometric changes to the fissile system solely in the neutronics, through the specification of a reactivity insertion component in the point neutron kinetics equations. Negative reactivity components included those due to Doppler broadening, thermal expansion and vapour formation. For the nuclear thermal hydraulics, a representative particle surrounded by a sphere of water, was modelled in each axial mesh cell. Thermal conduction and fission energy deposition were modelled using a finite difference (FD) scheme in a spherical co-ordinate system. The effects of forced and free thermal convection are neglected. The POWDER code also employed a model of nucleate boiling.

A similar code, presented in Basoglu (1992); Basoglu et al. (1994), named Simple Kinetics and Thermal HydraulicsWetted Powder (SKINATH-WP), was developed for modelling transient nuclear criticality excursion characteristics in a cylindrical blender of homogeneously mixed UO_2 powder and water. This code coupled point neutron kinetics with a lumped thermal feedback model. Reactivity addition was modelled by the homogeneous addition of water to the cylindrical blender. Nuclear thermal hydraulics was modelled using a thermal energy balance that took into consideration two scenarios, one with zero heat transfer between the UO_2 powder and water, and another with infinite heat transfer between the two phases. Steam produced for the infinite heat transfer case was assumed to leave the system instantaneously.

DiPeso and Peterson (1998) proposed another methodology for modelling transient nuclear criticality excursions in wetted fissile ash, or slurries, that may occur due to burning of fissile material and subsequent automated or manual fire fighting in a nuclear fuel fabrication facilities. This model coupled the point neutron kinetics equations to hydrodynamic and nuclear thermal hydraulic equations through the use of lumped parameter feedbacks. Reactivity was added to the system by the addition of water to a sump that contained fissile ash. Corresponding reactivity feedback mechanisms include thermal expansion and void production. The nuclear thermal hydraulics sub-model included components for fission energy deposition in the slurry, radiative and convective interfacial heat transfer between the water and fissile powder, as well as vapourisation around particulates. The mass transfer of water was modelled through a mass and momentum conservation equation.

The Finite Element Transient Criticality (FETCH) code has been applied to granular MOX fuel, contained within a conical blender, housed in nuclear fuel fabrication facilities (Gomes et al., 2008; Pain et al., 2009; Gomes et al., 2011). Although the original intent of the code was for solution-based systems, it has also found applicability to high-fidelity multiphase flows in fissile powders, contaminated soils, fluidised beds and other fissile porous media (Pain et al., 1998). FETCH uses the Fluidity FEM CFD code, coupled with the EVEn-parity Neutral particle Transport (EVENT) code. EVENT solves the linearised form of the non-linear Boltzmann transport equation, otherwise known as the NTE, in phase-space using an even-parity principle. The discretisation is FEM in space, multi-energy group and uses spherical harmonics to discretise the angle. Fluidity solves the Navier-Stokes equations for mass, momentum, and energy using a FEM discretisation scheme. This high-fidelity model has been applied to a layered MOX powder system in a conical blender, lubricated using zinc stearate. The complex nature of this type of multi-physics model makes it challenging to evaluate the importance of particular parameters on the model. Furthermore, this type of high-fidelity model may be computationally demanding and therefore, short timescales are usually considered when applying the model to simulating transient nuclear criticality excursions.

The Japan Atomic Energy Research Institute (JAERI) developed three codes for use on fissile powder systems, named the Accidentally Generated Nuclear Excursion Simulation-Powder (AGNES-P) code, the DOCTRINE code and the FEDEX-P code. Neutronic and nuclear thermal hydraulic modelling varies in level of complexity between these codes. AGNES-P is a point model with similar characteristics to SKINATH-WP. DOCTRINE considers more complicated geometry than AGNES-P whilst still using point kinetics. FEDEX-P solves the time and spatially dependent NDE alongside the NavierStokes equations using 3D FEM (Yamane et al., 2003a). Sakai et al. (2005) used the discrete element method (DEM) to model the dynamics of MOX powder particles during the agitation process. This was coupled with a continuous energy Monte Carlo neutron transport code to study how particle dynamics affect the criticality of the MOX powder as it was stirred in an agitation tank (Sakai et al., 2004).

A recent study by Laramore et al. (2018) modelled the chemical stability of UO_2 powder suspensions, to investigate the feasibility and potential characteristics of colloidal suspension reactors. They posited that by controlling the stability and separation distance of the UO_2 powder particles in the suspension, the reactivity of the system could be controlled. The effect that the solid particle packing factor in the suspension has on the parameters that constitute the four-factor model of the infinite multiplication factor, k_∞ was also examined.

2.4 Neutron Transport, Neutron Diffusion and the Point Neutron Kinetics Equations

The NTE was first derived in the late 1930s by Ornstein and Uhlenbeck (1937) in the context of studying the kinetic properties of neutrons within paraffin (Flugge, 1959; Amaldi, 1984). The NTE is a linearised form of the full non-linear Boltzmann transport equation (BTE), which describes the non-equilibrium average statistical behaviour of a gas of atoms or molecules (Boltzmann, 1970). The linearised form neglects neutron-neutron interactions, which is an appropriate assumption since the

density of neutrons in the system is very small. The NTE is a hyperbolic partial-integro-differential equation (PIDE), which is a function of a seven-dimensional phase space of solution variables: position (x, y, z); energy (E); angular direction ($\mathbf{\Omega}$); and time (t). The time-dependent NTE with delayed neutron precursors is given as:

$$\frac{1}{v_{\mathrm{n}}(E)}\frac{\partial}{\partial t}\Phi(\mathbf{r},E,\mathbf{\Omega},t) = \left(L_{\mathrm{t}} + M_{\mathrm{t}}^{\mathrm{p}}\right)\Phi(\mathbf{r},E,\mathbf{\Omega},t) + \sum_{i=1}^{6}\lambda_{\mathrm{i}}\left(\frac{\chi_{\mathrm{di}}(E)}{4\pi}C_{\mathrm{i}}\right) + S_{\mathrm{n}}(\mathbf{r},E,\mathbf{\Omega},t) \tag{2.16}$$

and for the delayed neutron precursors:

$$\frac{\chi_{\mathrm{di}}(E)}{4\pi}\frac{\partial C_{\mathrm{i}}(\mathbf{r},t)}{\partial t} = M_{\mathrm{t}}^{\mathrm{i}}\Phi(\mathbf{r},E,\mathbf{\Omega},t) - \lambda_{\mathrm{i}}\left(\frac{\chi_{\mathrm{di}}(E)}{4\pi}C_{\mathrm{i}}\right) \tag{2.17}$$

where $\mathbf{r}$ [cm] is the position vector of the differential volume, dV in phase space, t [s], v_{n} is the neutron velocity, L_{t} and $M_{\mathrm{t}}^{\mathrm{p}}$ are the streaming and prompt fission operators, respectively. The variable Φ [neutrons cm^{-2} s^{-1}] is the angular neutron flux, $\chi_{\mathrm{di}}(E)$ [-] is the delayed neutron spectrum, S_{n} [neutrons s^{-1}] is the extraneous (fixed) neutron source, $M_{\mathrm{t}}^{\mathrm{i}}$ is the delayed fission neutron production operator, λ_{i} [s^{-1}] is the i-th delayed neutron precursor decay constants and C_{i} [precursors] is the i-th delayed neutron precursor population.

The streaming operator, denoted L_{t}, is given by:

$$L_{\mathrm{t}}\cdot = -\mathbf{\Omega}\cdot\nabla\cdot - \Sigma_{\mathrm{t}}(\mathbf{r},E,t)\cdot + \int_0^{4\pi} d\Omega' \int_0^{\infty} dE' \Sigma_{\mathrm{s}}(\mathbf{r},E'\rightarrow E,\mathbf{\Omega}'\rightarrow\mathbf{\Omega},t)\cdot \tag{2.18}$$

where Σ_{t} [cm^{-1}] is the macroscopic total neutron cross-section and Σ_{s} [cm^{-1}] is the macroscopic neutron scattering cross-section.

The prompt fission neutron production operator, denoted $M_{\mathrm{t}}^{\mathrm{p}}$, is given by:

$$M_{\mathrm{t}}^{\mathrm{p}}\cdot = \frac{1}{4\pi}(1-\beta)\chi_{\mathrm{p}}(E)\int_0^{\infty} dE' \int_0^{4\pi} d\mathbf{\Omega}' E'\bar{\nu}\Sigma_{\mathrm{f}}(\mathbf{r},E',t)\cdot \tag{2.19}$$

where $\chi_{\mathrm{p}}(E)$ [-] is the prompt neutron fission spectrum and β is the delayed neutron fraction.

The delayed fission neutron production operator, denoted $M_{\mathrm{t}}^{\mathrm{i}}$, is given by:

$$M_{\mathrm{t}}^{\mathrm{i}}\cdot = \frac{1}{4\pi}\beta_{\mathrm{i}}\chi_{\mathrm{di}}(E)\int_0^{\infty} dE' \int_0^{4\pi} d\mathbf{\Omega}' E'\bar{\nu}\Sigma_{\mathrm{f}}(\mathbf{r},E',t)\cdot \tag{2.20}$$

where β_{i} [-] are the fraction of neutrons from the i-th delayed neutron precursor group.

The total fission neutron production operator, denoted M_{t}, is then given as the sum of the prompt

and delayed neutron contributions such that:

$$M_{\mathrm{t}}\cdot = M_{\mathrm{t}}^{\mathrm{p}}\cdot + \sum_{\mathrm{i}=1}^{6} M_{\mathrm{t}}^{\mathrm{i}}\cdot \tag{2.21}$$

In general, the NTE can be computationally challenging to solve for large scale, general geometry, nuclear reactor physics and shielding problems. Therefore, a mathematical approximation to the NTE is often used in whole-core nuclear reactor physics simulations, which is the NDE. The NDE was first elucidated to in Amaldi and Fermi (1936), and has since become one of the most popular tools for radiation transport and shielding calculations. The NDE is an elliptic PIDE and is derived from the NTE by first expanding the angular variation of the NTE in a basis of spherical harmonic functions (Jeans, 1917). Truncation of the expansion yields an assumption that the angular variation of neutrons is, at most, linearly anisotropic. The NDE also assumes that the extraneous neutron source and neutron scattering are isotropic (Stacey, 2018). The angularly independent, scalar neutron flux is defined as:

$$\phi(\mathbf{r}, E, t) = \int_0^{4\pi} d\Omega \Phi(\mathbf{r}, E, \mathbf{\Omega}, t) \tag{2.22}$$

The resulting time and energy-dependent NDE, which is now a five-dimensional (5D) equation, may be given as:

$$\begin{aligned}\frac{1}{v_{\mathrm{n}}(E)}\frac{\partial\phi(\mathbf{r},E,t)}{\partial t} + \nabla\cdot D(\mathbf{r},E,t)\nabla\phi(\mathbf{r},E,t) + \Sigma_{\mathrm{t}}(\mathbf{r},E,t)\phi(\mathbf{r},E,t) = \\ + \int_0^{\infty} dE'\Sigma_{\mathrm{s}}(\mathbf{r},E'\rightarrow E,t)\phi(\mathbf{r},E',t) + (1-\beta_{\mathrm{eff}})\chi_{\mathrm{p}}(E)\int_0^{\infty} dE'\bar{\nu}\Sigma_{\mathrm{f}}(\mathbf{r},E',t)\phi(\mathbf{r},E',t) \\ + \sum_{i=1}^{6}\chi_{\mathrm{di}}(E)\lambda_{\mathrm{i}}C_{\mathrm{i}}(\mathbf{r},t) + S_{\mathrm{n}}(\mathbf{r},E,t)\end{aligned} \tag{2.23}$$

with associated delayed neutron precursors given by:

$$\frac{\partial C_{\mathrm{i}}(\mathbf{r},t)}{\partial t} = -\lambda_{\mathrm{i}}C_{\mathrm{i}}(\mathbf{r},t) + \beta_{\mathrm{i}}\int_0^{\infty} dE\nu\Sigma_{\mathrm{f}}(\mathbf{r},E,t)\phi(\mathbf{r},E,t) \tag{2.24}$$

The NDE can also be considered as an asymptotic approximation of the NTE, which has important implications for the numerical solution of the NTE in host materials that are highly scattering (Larsen and Keller, 1974; Larsen, 1992). It can be demonstrated mathematically that the NDE is a reasonable lower-order approximation to the NTE for the migration of neutrons in weakly absorbing media, several mean-free paths (MFPs) away from isolated sources, physical boundaries and heterogeneous-material interfaces (Hebert, 2020).

The energy dependence of the NDE can be discretised by the multi-group approximation, which

decomposes the energy dependence into a sequence of discrete energy intervals with prescribed upper and lower energy bounds. Within these discrete energy intervals, the macroscopic neutron cross-sections are averaged with respect to a prescribed energy dependent scalar neutron flux (Hebert, 2020). In its modern form, the multi-group approximation was first derived by Hurwitz and Ehrlich in the early 1950s. In their research, they reduced the age diffusion equations (ADE) to a finite set of coupled linear differential equations called the multi-group equations (Hurwitz and Ehrlich, 1953). The multi-group approximation has since found widespread use in the numerical solution of the energy-dependent NTE and NDE. Using the multi-group approximation, the energy-dependent NDE can be reduced to a system of weakly coupled partial differential equations (PDEs), which can then be spatially discretised.

If information regarding how the macroscopic neutron cross-sections vary as a function of the physical properties of the fissile system, such as UO_2 powder packing fraction, water content, voidage and temperature, then Equations (2.16) and (2.23) may be solved with appropriate boundary conditions, to model transient nuclear criticality excursions in fissile powder systems. However, due to the high dimensionality of the problem, the numerical solution of this equation when coupled to a multi-physics code, is computationally challenging.

However, for the purposes of NCS it is common to reduce the complexity of the problem even further, to a 'lumped parameter', or point representation. The point neutron kinetics approximation has been successfully used for modelling fissile powder and solution-based systems for NCS applications (Rozain et al., 1991; Basoglu et al., 1994; Cooling et al., 2014; Winter et al., 2018).

One of the first written forms of the point neutron kinetics equations can be found within Wigner (1942). However, more general developments of the point neutron kinetics equations were reported at similar times by Ussachoff (1955) and Henry (1955). The point neutron kinetics equations may be arrived at from the one-speed NDE (Dorning, 2010) or more generally from the time-dependent NTE (Akcasu et al., 1971).

The derivation from the NTE involves decomposition of the neutron number density into a shape function (still containing time dependency) and a time function. In the case where the shape function does not change with time, the time function simply becomes the neutron population. A representation of the separation of variables in the case where the shape function does not change over time is given as:

$$\Phi(\mathbf{r}, \mathbf{\Omega}, E, t) = \hat{\Phi}(\mathbf{r}, \mathbf{\Omega}, E)N(t) \tag{2.25}$$

and:

$$\frac{1}{4\pi}\chi_{\mathrm{i}}(E)C_{\mathrm{i}}(\mathbf{r}, t) = \int_0^{4\pi} \hat{\Phi}(\mathbf{r}, \mathbf{\Omega})C_{\mathrm{i}}(t)d\mathbf{\Omega} \tag{2.26}$$

where $\hat{\Phi}$ [-] is the angular neutron flux shape function (Dorning, 2010).

Fundamental to the derivation is the introduction of a 'steady-state reference reactor', that is in a critical condition. It has been shown that by using the adjoint NTE, the neutron importance in the critical reference reactor is proportional to the time function (point representation of the neutron population). The time function may be interpreted as the total neutron importance for sustaining the chain reaction, in the reactor under consideration. After some mathematical manipulation, the following point kinetics equation may be arrived at:

$$\frac{dN(t)}{dt} = \left(\frac{\rho(t) - \beta_{\text{eff}}}{\Lambda}\right) N(t) + \sum_{\text{i}}^{6} \lambda_{\text{i}} C_{\text{i}}(t) + S_{\text{n}}(t) \tag{2.27}$$

with the associated delayed neutron precursor populations for the point approach are given by:

$$\frac{dC_{\text{i}}(t)}{dt} = \left(\frac{\beta_{\text{i}}}{\Lambda}\right) N(t) - \lambda_{\text{i}} C_{\text{i}}(t) \tag{2.28}$$

where N [neutrons] is the neutron population and ρ [-] is the reactivity of the system.

In this derivation, the neutron kinetics parameters such as ρ, β_{i} and Λ are determined by weighting the shape function by the neutron importance (adjoint angular neutron flux) of the 'steady-state reference reactor'. The formulation of these adjoint weighted parameters can be found in numerous nuclear reactor physics textbooks (Hebert, 2020; Bell and Glasstone, 1970; Dorning, 2010) and may be summarised as:

$$\rho(t) = \frac{\langle \Phi_0^{\dagger}, (H_{\text{t}} - H_0)\hat{\Phi} \rangle}{\langle \Phi_0^{\dagger}, M_{\text{t}} \hat{\Phi} \rangle} \tag{2.29}$$

where $\Phi_0^{\dagger}$ [neutrons cm^{-2} s^{-1}] is the adjoint angular neutron flux of the 'steady-state reference reactor', $H_{\text{t}} = L_{\text{t}} + M_{\text{t}}$ and H_0 is the summation of the 'steady-state reference reactor' streaming and fission operator.

$$\beta_{\text{i}} = \frac{\langle \Phi_0^{\dagger}, M_{\text{t}}^{\text{i}} \hat{\Phi} \rangle}{\langle \Phi_0^{\dagger}, M_{\text{t}} \hat{\Phi} \rangle} \tag{2.30}$$

$$\beta_{\text{eff}} = \sum_{\text{i}=1}^{6} \beta_{\text{i}} \tag{2.31}$$

$$\Lambda = \frac{\langle \Phi_0^{\dagger}, \hat{\Phi}/v_{\text{n}} \rangle}{\langle \Phi_0^{\dagger}, M_{\text{t}} \hat{\Phi} \rangle} \tag{2.32}$$

Alternatively, the kinetics parameters may be determined through the use of Monte Carlo codes such as MCNP (Werner et al., 2018). Coupling of the point neutron kinetics model to the physical

properties of the system such as temperature and void fraction are achieved through reactivity feedback coefficients. These are determined through the use of Monte Carlo codes.

2.5 Spatial Finite Volume Discretisation Method

The Finite Volume (FV) method is one of the most common numerical schemes for solving problems involving mass flows (Versteeg and Malalasekera, 2007), since it is conservative in nature. The scheme presents a methodology for solving PDEs, such as the advection-dispersion equation, as well as PIDEs, such as the NDE. Average values for solution variables such as water volume, radiolytic gas and steam volumes, as well as thermal energies are obtained across each cell. Gauss' theorem changes divergence operators in continuity equations to surface integrals, enabling for the determination of mesh cell face fluxes. This method ensures that one cell's loss is another's gain. For a general property, ϕ, the convection-diffusion equation is given as (Versteeg and Malalasekera, 2007):

$$\frac{\mathrm{d}\phi}{\mathrm{d}t} = -\nabla \cdot (\rho \mathbf{u}\phi) + \nabla \cdot (D\nabla\phi) + S_\phi \tag{2.33}$$

Formal integration over the control volume (CV), applying Gauss' theorem yields the continuity equation in the form required for the FV method:

$$\int_{CV} \frac{\mathrm{d}\phi}{\mathrm{d}t}\mathrm{d}V = -\int_A (\rho \mathbf{u}\phi) \cdot \mathbf{n}\mathrm{d}A + \int_A (D\nabla\phi) \cdot \mathbf{n}\mathrm{d}A + \int_{CV} S_\phi \mathrm{d}V \tag{2.34}$$

where the advective velocity vector is $\mathbf{u}$, the dispersion coefficient is represented by D, and the source/sink term is expressed by S_ϕ.

This thesis utilises a radially and azimuthally symmetric Eulerian FV spatial discretisation scheme in a cylindrical co-ordinate system. An illustration of the discretised domain showing the cylindrical FV slices as well as the three discrete regions is provided in Figure 2.1. Advective terms are spatially discretised using the first-order upwind differencing scheme described in Tu et al. (2013), where the direction of information travel is determined by the sign of each component constituting the net advective flow on the interface. The details of higher order methods with unconditional stability that utilise total variation diminishing (TVD) schemes are provided in Versteeg and Malalasekera (2007), but are not used here. The dispersive and diffusive terms are discretised using a second-order approximation. Simulations are performed with axial cell numbers ranging from 1000 to 5000.

The work presented in this thesis assumes that sharp interfaces exist between the dry and wet UO_2 powder regions, between the wet UO_2 powder and pooled water regions and at the free surface located at the top of the pooled water region. The suitability of a sharp wetting-front assumption is discussed later in this thesis. There are three interface locations that can be determined explicitly through the prescription of interface conditions at each interface. The Eulerian FV mesh cell that contains the interface between two regions is split into two sub-cells, using a cut-cell method similar to that of Ingram et al. (2003), ensuring that the exact location of the interface can be tracked. However, a limitation of using the cut-cell method alone exists when the region interfaces move dynamically

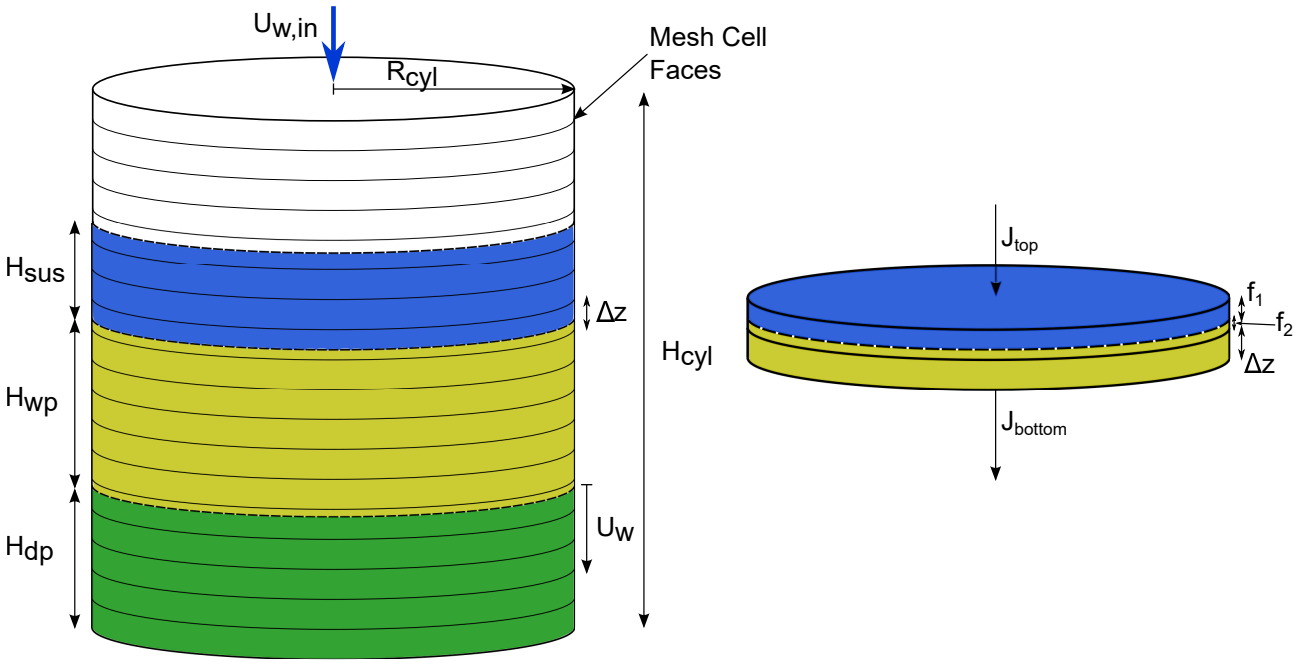

Figure 2.1: Representation of three-region UO_2 powder bed with Eulerian FV mesh shown on top, alongside a close-up representation of FV mesh showing cut-cells between the wetted UO_2 powder and pooled water/suspension regions.

through the static Eulerian mesh. As the region interface moves through a mesh cell, there will be a case where an infinitesimal differential height is brought about as a result of the discretisation of the cut-cell whose boundary approaches a Eulerian mesh cell, leading to a singularity. To account for this singularity, Ingram et al. (2003) uses a cell split-and-merge technique that merges the mass and energy of a cut-cell with an adjacent cell, creating an effectively larger cell. When the region interface has moved into the adjacent Eulerian FV mesh cell, a split operation is performed, re-producing the original mesh structure. An illustration of the method is shown in Figure 2.2. The following conditions are applied for the merge and split operations, respectively:

$$f_{1,2} < 0.4 \tag{2.35}$$

and:

$$f_{1,2} \geq 0.4 \tag{2.36}$$

where $f_{1,2}$ [-] is the ratio of the size of the sub-cells created using the cut-cell method, to the size of the base FV Eulerian mesh cell.

The split-and-merge limit, $f_{1,2}$, is prescribed a value of 0.4 to ensure that cut-cells remain a relatively similar size throughout the simulation. This allows the time integrator to maintain a similar step size to if there were no cut-cells (Ingram et al., 2003). This feature of the PDE solver is expressed mathematically through the Courant-Friedrichs-Lewy (CFL) stability criterion. The condition in one-

dimension (1D) is given by:

$$\frac{u\Delta t}{\Delta z f_{1,2}} < C_{\max} \tag{2.37}$$

where u [m s^{-1}] is the magnitude of the velocity or speed at which information travels across the spatial grid, Δt [s] is the time-step, $\Delta z f_{1,2}$ [m] is the size of a cut-cell which is less than the nominal mesh cell size, Δz [m], and $C_{\max}$ [-] is the maximum Courant number for stability.

Clearly, from Equation (2.37), larger time-steps are possible for cases where the size of the cut-cell are of similar order of magnitude to the nominal size of the mesh cell; hence the limits prescribed for the cell split-and-merge in Equations (2.35) and (2.36). Equation (2.37) also suggests that in cases where the advective or dispersive magnitudes of the flow are large, a highly refined spatial mesh may require a correspondingly large number of time-steps to produce a stable solution. The value of $C_{\max}$ may be increased by using an implicit time-integrator.

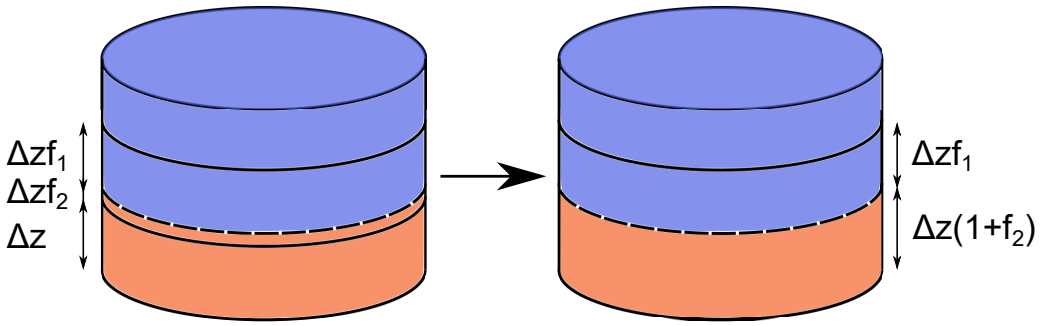

Figure 2.2: Representation of three-region UO_2 powder bed with Eulerian FV mesh super-imposed, alongside close-up representation of FV mesh.

2.6 Temporal Backwards Differentiation Formula Method

The solution in time is found using the CVODE solver from the suite of nonlinear and differential/algebraic solvers (SUNDIALS) library, written in C, but with interface modules developed in modern Fortran (Hindmarsh et al., 2005). The CVODE solver uses a variable-order, variable-step, multistep backward differentiation formula (BDF) method, in fixed-leading coefficient form, for the solution of stiff ordinary differential equations (ODEs) that are of the form:

$$\sum_{i=0}^{K_1} \alpha_{n,i} y^{n-i} + h_n \beta_{n,0} \dot{y}^{n-i} = 0 \tag{2.38}$$

where K_1 [-] is the order of the BDF method, $\alpha_{n,i}$ [-] and $\beta_{n,0}$ [-] are coefficients that depend on the method order, step size history and the normalisation $\alpha_{n,0} = -1$, with n referring to the present time-step which is being solved for. The time-step size is given by h_n [s]. The variable being solved for, and its derivative, are denoted respectively by the terms y and $\dot{y}$.

SUNDIALS employs a version of the variable time-step BDF method derived by Brayton et al.

(1972). This method is in turn an advanced version of the uniform time-step method first proposed by Nordsieck (1962) and Gear (1971). For orders $K_1 = 1$ and $K_1 = 2$, the BDF method is A-stable, meaning that as long as all modes in the system are stable, the method will be stable for any step size. However, at higher orders, the BDF method cannot be A-stable. This requires the CVODE solver to carefully calculate a step size that ensures the solution remains in the region of stability (Hindmarsh et al., 2005).

The discretised non-linear temporal ODE is solved using a fixed-point iteration method. The initial guess of the fixed-point iteration method is an explicitly predicted value of y, based on previous solutions. The SUNDIALS library has numerous methods for ensuring that an appropriate step size is chosen, ensuring the error local absolute and relative error of the solution are adequately minimised (Byrne and Hindmarsh, 1975).

Chapter 3

Nuclear Criticality Excursion Models for Wetted UO_2 Powder Beds with Water Infiltration

3.1 Introduction

The majority of work presented in this chapter is reproduced from Jones et al. (2022b).

This chapter introduces the fundamental models used throughout this thesis for point neutron kinetics, nuclear thermal hydraulics, radiolytic gas production and boiling. Three-phase, three-region continuity and thermal energy equations are proposed and solved numerically for modelling wetting-induced transient nuclear criticality excursions in wetted UO_2 powder systems. Coupling of the mass transfer and nuclear thermal hydraulics equations to the neutronics of the system is achieved through bi-variate polynomial reactivity feedback correlations. The steady-state multi-group neutron diffusion equation has been solved in a cylindrical system for regular changes in reactivity, to obtain radially averaged, axially normalised scalar neutron flux shape functions. The aim of this chapter is to outline a methodology for modelling wetting-induced transient nuclear criticality excursions in UO_2 powder beds, presenting peak power and fission energy yield over a period of simulation time.

3.2 Model Phenomenology

3.2.1 Point Kinetics

The point kinetics equations have been described in Section 2.4, and are outlined here in an alternative form (Duderstadt and Hamilton, 1976):

$$\frac{dN(t)}{dt} = \frac{\beta_{\text{eff}} N(t)}{\Lambda} \left(R_{\text{t}}(t) - 1\right) + \sum_{\text{i}=1}^{6} \lambda_{\text{i}} C_{\text{i}}(t) + S_{\text{n}} \tag{3.1}$$

$$\frac{dC_{\mathrm{i}}(t)}{dt} = -\lambda_{\mathrm{i}} C_{\mathrm{i}}(t) + \frac{\beta_{\mathrm{i}}}{\Lambda} N(t) \tag{3.2}$$

$$\begin{aligned} R_{\mathrm{t}}(t) = R_{\mathrm{imm}}(f_{\mathrm{imm}}) + \Delta R_{\mathrm{th,p,dp}}(\bar{T}_{\mathrm{p,dp}}, f_{\mathrm{imm}}) + \Delta R_{\mathrm{th,p,wp}}(\bar{T}_{\mathrm{p,wp}}, f_{\mathrm{imm}}) \\ + \Delta R_{\mathrm{th,w,wp}}(\bar{T}_{\mathrm{w,wp}}, f_{\mathrm{imm}}) + \Delta R_{\mathrm{void,wp}}(\bar{v}_{\mathrm{f,g,wp}}, f_{\mathrm{imm}}) + \Delta R_{\mathrm{void,sus}}(\bar{v}_{\mathrm{f,g,sus}}, f_{\mathrm{imm}}) \end{aligned} \tag{3.3}$$

The total reactivity of the system, R_{t}, measured in dollars (\$), is defined as the sum of individual components where R_{imm} is the wetting-induced reactivity (usually positive reactivity effect), $\Delta R_{\mathrm{th,p,dp}}$, $\Delta R_{\mathrm{th,p,wp}}$ and $\Delta R_{\mathrm{th,w,wp}}$ represent thermal reactivity feedbacks due to temperature changes in the dry powder, wet powder and pore water respectively. Void reactivity feedback is modelled in the pores and pooled water by the variables $\Delta R_{\mathrm{void,wp}}$ and $\Delta R_{\mathrm{void,sus}}$ respectively. The bed immersion fraction, f_{imm}, is defined in Equation (3.5) as the ratio of the height of the wetted powder region to the total height of the powder bed.

The reactivity of the system in dollars is related to the effective multiplication factor, k_{eff} through the following:

$$R = \frac{k_{\mathrm{eff}} - 1}{k_{\mathrm{eff}} \beta_{\mathrm{eff}}} \tag{3.4}$$

$$f_{\mathrm{imm}}(t) = \frac{H_{\mathrm{wp}}(t)}{H_{\mathrm{dp}}(t) + H_{\mathrm{wp}}(t)} = 1 - \frac{H_{\mathrm{dp}}(t)}{H_{\mathrm{dp}}(t) + H_{\mathrm{wp}}(t)} \tag{3.5}$$

where H_{dp} [m], H_{wp} [m] are the heights of the dry powder and wetted powder regions respectively.

The source term, denoted S_{n} is given by:

$$S_{\mathrm{n}} = s_{\mathrm{n}} V_{\mathrm{UO_2}} \tag{3.6}$$

where s_{n} [neutrons s^{-1} ($\mathrm{cm}^{-3} \cdot \mathrm{UO_2}$)] is the intrinsic source density of neutrons, discussed further in Section 3.2.2. The term, $V_{\mathrm{UO_2}}$ [m^3], corresponds to the volume of UO_2 powder present in the system, which for a static UO_2 powder bed, remains unchanged.

3.2.2 Neutron Source for the Point Kinetics Equations

In point kinetics calculations, for nuclear reactor physics and nuclear criticality safety applications, there are usually either distributed intrinsic (or inherent) neutrons sources, localised extrinsic (or installed) neutron sources or combinations of both of these sources (Radkowsky, 1964). There are a number of physical processes that lead to distributed intrinsic neutron source such as spontaneous fission (Flerov and Petrjak, 1940; Scharff-Goldhaber and Klaiber, 1946), (α,n) nuclear reactions (Kudryavtsev et al., 2020), cosmic ray induced spallation neutron sources (Rossi, 1933) and also (γ,n) nuclear

reactions (Bernstein et al., 1947). In general, spallation neutron sources and (γ,n) nuclear reactions are not important for nuclear criticality excursion analysis. However, spallation neutrons sources are important for accelerator driven systems (ADS) (Pyeon, 2021; Verma and Katovsky, 2018). Photo-neutron or (γ,n) nuclear reactions are important for the analysis of heavy water (D_2O) moderated reactors such as the CANDU (Canadian Deuterium-Uranium) reactor (Colomb, 1960). In this case the point kinetics equations are modified by the inclusion of additional delayed neutron groups to represent the effect of the photo-neutron sources (Cohn, 1959). Moreover, it is important to account for photo-neutrons as not accounting for these neutron sources may lead to inaccuracies in the determination of the reactivity of the system (Cohn, 1959).

In general, the most important neutron sources in nuclear criticality excursion problems are usually spontaneous fission and (α,n) nuclear reactions and these have been measured for fissile liquids such as uranyl nitrate and uranyl flouride (Hankins, 1966; Seale and Anderson, 1991). The (α,n) neutron source occurs through interaction of the α particles, emitted in natural radioactivity of uranium, with light nuclei (Kudryavtsev et al., 2020). The relative strengths and importance of spontaneous fission and (α,n) nuclear reactions depends upon the uranium enrichment of the fuel (Radkowsky, 1964). For sub-critical systems with weak neutron sources it may be important to model the stochastic fluctuations of the neutron field and this can be achieved using either Monte Carlo methods (Cooling et al., 2016) or the Pál-Bell equations (Pál, 1958; Bell, 1963). Hansen developed a criterion for determining whether systems were in the weak neutron source regime where stochastic effects dominate (Hansen, 1960). This weak neutron source regime is important in the start-up of nuclear reactors with highly enriched nuclear fuels (Williams and Eaton, 2016). This is the reason why primary and secondary extrinsic neutron sources are installed within nuclear reactors to avoid potential blind nuclear reactor start-up scenarios (Shaw, 1969). Such blind nuclear reactor start-up scenarios can lead to overheating and damage of the nuclear fuel within the nuclear reactor core (Lewis, 1977).

In nuclear criticality safety analysis the presence of weak neutron sources can lead to issues in measuring neutron fluxes as well as the degree of sub-criticality (Iwamoto et al., 2017). Moreover, it may lead to significant variations in burst wait times should a nuclear criticality excursion occur (Williams, 2016; Winter et al., 2018). Therefore, in general, for accurately modelling nuclear criticality excursions, it is useful to know whether the system is in the weak neutron source regime (Hansen, 1960) and the magnitudes of the distributed intrinsic (or inherent) and any localised extrinsic (or installed) neutron sources to ensure that appropriate initial conditions are prescribed for the problem being analysed. These prescribed initial conditions for the nuclear criticality excursions analysed in this Chapter are derived by assuming the initially sub-critical systems have achieved some steady-state prior to the nuclear criticality excursion (Lewis, 1977; Kerlin and Upadhyaya, 2019). This assumption leads to the following prescribed initial neutron and delayed neutron precursor populations (Lewis, 1977; Kerlin and Upadhyaya, 2019):

$$N(0) = -\frac{s_{\mathrm{n}}\Lambda}{R_{\mathrm{t}}(0)\beta_{\mathrm{eff}}}V_{\mathrm{UO_2}} \tag{3.7}$$

and:

$$C_{\mathrm{i}}(0) = -\frac{\beta_{\mathrm{i}} s_{\mathrm{n}}}{\lambda_{\mathrm{i}} R_{\mathrm{t}}(0) \beta_{\mathrm{eff}}} V_{\mathrm{UO_2}} \tag{3.8}$$

where $N(0)$ and $C_{\mathrm{i}}(0)$ are the initial sub-critical neutron population and i-th group delayed neutron precursor population, respectively.

However, the averaging of the neutron sources over the system domain is itself a non-trivial task in order to develop a rigorous averaging procedure in order to account for any spatial, energy, angular and temporal variation of the neutron sources. In general, for point kinetics calculations, an appropriately adjoint weighted fundamental mode neutron source must be derived to account for the relative spatial, angular, energy and temporal variation of the neutron sources (Spriggs et al., 1999). The magnitude of the intrinsic neutron source can be determined using either the deterministic code SOURCES-4C (Wilson et al., 2002, 2005) or an appropriate Monte Carlo code such as MC21 (Griesheimer et al., 2015). SOURCES-4C and MC21 can evaluate both the spontaneous fission and (α,n) neutron sources. Recent research has indicated that the intrinsic neutron source values predicted by SOURCES-4C and MC21 are broadly in agreement for systems such as 2.4 % enriched uranium dioxide (UO_2) (Griesheimer et al., 2017).

The nuclear criticality excursions that are presented in this chapter involve a 500 kg powder bed made of 5 % enriched uranium dioxide (UO_2) powder which is in an environment where there are no extrinsic neutron sources present. Therefore, it is assumed that the only neutron sources are the intrinsic (or inherent) neutron sources from spontaneous fission and (α,n) nuclear reactions. In general, either SOURCES-4C or an ancillary Monte Carlo simulation would have to be performed in order to determine an appropriate magnitude for the intrinsic neutron sources. However, for the purposes of this chapter and for all the nuclear criticality excursions simulations performed, the spontaneous fission and (α,n) neutron source determined by Griesheimer et al. (2017) will be utilised. The reason for using the 2.4 % enriched UO_2 intrinsic neutron source value from the Griesheimer et al. (2017) paper is because the magnitude, or strength, of this neutron source will not differ substantially to the value for the 5 % enriched UO_2 case. Sensitivity analysis of the intrinsic neutron source strength, outlined in Section 3.6.3, has shown that nuclear criticality transients in the present system are not sensitive to the prescribed variations of the intrinsic neutron source strength. Griesheimer et al. (2017) determined a value for 2.4 % enriched uranium dioxide (UO_2) of 6.248×10^{-4} (α,n) neutrons s^{-1} ($g^{-1} \cdot UO_2$) and 1.172×10^{-2} spontaneous fission (SF) neutrons s^{-1} ($g^{-1} \cdot UO_2$) using SOURCES-4C. For the MC21 Monte Carlo simulations Griesheimer et al. (2017) determined a value of 6.248×10^{-4} (α,n) neutrons s^{-1} ($g^{-1} \cdot UO_2$) and 1.168×10^{-2} neutrons s^{-1} ($g^{-1} \cdot UO_2$). The agreement between the SOURCES-4C values and the MC21 values for the neutron sources is approximately 2 %. In addition the spontaneous fission (SF) process is by far the most dominate process involved in producing the intrinsic neutron source as expected. Given that the theoretical density of UO_2 powder is 10.95 g cm^{-3}, the corresponding total neutron source due to (α, n) interactions and spontaneous fission is $s_{\mathrm{n}} = 0.135$ neutrons s^{-1} ($cm^{-3} \cdot UO_2$).

In order to determine whether the 5 % enriched uranium dioxide (UO_2) powder systems studied in this Chapter is in the stochastic regime it is important to apply the Hansen criterion (Hansen,

1960). If the system obeys Hansen's criterion then the system is in a regime where stochastic effects in the neutron kinetics become important. Hansen (1960) stated that weak neutron limit criterion was given by:

$$\frac{2S_{\mathrm{n}}\tau}{\bar{\nu}\Gamma_2} << 1 \tag{3.9}$$

where τ [s] is the prompt neutron lifetime and Γ_2 [-] is the Diven factor, which can be expressed as:

$$\Gamma_2 = \frac{\overline{\nu(\nu-1)}}{\bar{\nu}^2} \tag{3.10}$$

Basoglu (1992) noted that generally for 5 % enriched UO_2 powder systems the value of $2/\bar{\nu}\Gamma_2 \approx 1$, given that the Diven factor, $\Gamma_2 \approx 0.8$ (Hansen, 1960; Diven et al., 1956; Okajima et al., 2000). This yields Hansen's criterion as:

$$S_{\mathrm{n}}\tau << 1 \tag{3.11}$$

The intrinsic neutron source density determined by Griesheimer et al. (2017) is used as an approximation for the 5 % enriched UO_2 powder system analysed in this Chapter. Given the powder bed mass of 500 kg and approximate density of UO_2 of 0.01095 kg cm^{-3}, the total distributed intrinsic neutron source is calculated to be $S_{\mathrm{n}} = 6172$ neutrons s^{-1}. The mean neutron lifetime near criticality has been described in Section 3.4.7 as $\tau = 5.33 \times 10^{-5}$ s. Using the Hansen (1960) criterion:

$$S_{\mathrm{n}}\tau = 0.329 \tag{3.12}$$

This value only marginally satisfies the condition specified in Equation (3.11) (Spriggs et al., 1999). However, in reality the system will largely be deterministic in its behaviour even with this marginal value (Spriggs et al., 1999). Therefore, for the system analysed in this Chapter, the effects of stochastic neutron kinetics effects do not need to be considered any further.

3.2.3 Governing Equation for Water, Radiolytic Gas and Steam Components

The generalised form of the equations governing component and region mass transfer in a three-phase UO_2 powder bed, contained within a cylindrical vessel, where only the water and gas phases are mobile may be represented by the following advection-dispersion equation with a volumetric source/sink term (Bear, 1972; Cova, 1966):

$$\frac{\partial V'_{\mathrm{j,k}}(t,z)}{\partial t} = \frac{\partial}{\partial z}\left(D_{\mathrm{k}}(t,z)\frac{\partial V'_{\mathrm{j,k}}(t,z)}{\partial z} + U_{\mathrm{net,j,k}}(t,z)V'_{\mathrm{j,k}}(t,z)\right) + S'_{\mathrm{j,k}}(t,z) \tag{3.13}$$

where $V'_{\mathrm{j,k}}(t,z)$ [m^2] corresponds to the volume per unit height of component, j, in region, k. It

should be noted that the present model is applied to a cylindrical domain with a constant radius axially throughout the domain. The variable, $U_{\mathrm{net,j,k}}(t,z)$ [m s^{-1}], is the net component advective velocity, which takes a different form depending on the phase and region in question. The dispersive coefficient, $D_{\mathrm{k}}(t,z)$ [m^2 s^{-1}] varies only spatially and is the same regardless of the component, j, in question for a given region, k. The variable $S'_{\mathrm{j,k}}(t,z)$ [m^2 s^{-1}] corresponds to the net source/sink per unit height, for component, j, in region, k. The component index, denoted j = w, rg, v, corresponds to the water, radiolytic gas and steam components, respectively. The region index, denoted k = dp, wp, sus, corresponds to the dry powder, wet powder and pooled water/suspension regions, respectively.

The powder particle number density, or volume fraction, in the settled wet powder region and dry powder region do not vary spatially and are instead prescribed a constant value. This physically corresponds to a static UO_2 powder bed which may essentially act as a porous immoveable solid. Therefore, Equation (3.13) does not apply to the powder held within either the dry powder or settled wet powder regions. The following condition applies to the total continuity of each dynamic component in the cylindrical domain (j = w, rg, v):

$$v_{\mathrm{f,w,k}}(t,z) + v_{\mathrm{f,rg,k}}(t,z) + v_{\mathrm{f,v,k}}(t,z) = 1 \tag{3.14}$$

where $v_{\mathrm{f,j,k}}(t,z) = V'_{\mathrm{j,k}}(t,z)/A_{\mathrm{cyl}}$ corresponds to the volume fraction of component, j, in region, k. Here, the term $A_{\mathrm{cyl}} = \pi R^2_{\mathrm{cyl}}$ [m^2] corresponds to the cross-sectional area of the cylindrical domain.

The dispersive term in Equation (3.13) is discretised using a second order centred-difference approach around mesh cell faces. Advective components in Equation (3.13) are resolved using a first order upwind scheme, where the direction of upwinding depends dynamically on the sign of each component comprising the net advective term, $U_{\mathrm{net,j,k}}(t,z)$.

Table 3.1 describes how the net advective velocity may be calculated for each region and component. Mathematical relations for the rate of water infiltration into the UO_2 powder bed, denoted U_{w} [m s^{-1}] is described in more detail in Section 3.2.4. The gas bubble advection rate, U_{g} [m s^{-1}] is described in more detail in Section 3.2.6. The term ΔS_{w} corresponds to the change in saturation from the dry to the wetted case for the UO_2 powder bed and is also described further in Section 3.2.4.

The term $S'_{\mathrm{j,k}}(t,z)$ is the volumetric rate of change of sources and sinks per unit height, for a given component, j, in a region, k. Table 3.2 indicates the terms that this parameter is prescribed for each component in each region. Section 3.2.7 describes the terms $S'_{\mathrm{boil,w}}$ [m^2 s^{-1}] and $S'_{\mathrm{boil,v}}$ [m^2 s^{-1}] which correspond to a volumetric sink and source, respectively, that represent the break-up of water molecules and the creation of steam, due to latent heat supplied to vapourise water. Radiolytic gas sink and source terms used in Table 3.2 denoted by $S'_{\mathrm{H_2O}}$ [m^2 s^{-1}] and $S'_{\mathrm{H_2}}$ [m^2 s^{-1}], respectively, are described in more detail in Section 3.2.5.

To ensure continuity in the proposed model, the sources and sinks present in the component and region-specific continuity equations, denoted by, $S'_{\mathrm{j,k}}(t,z)$, introduce an advective component on the flow. Additionally, the slip velocities that exist between phases, represented by phase specific advective components such as the gas velocity, $U_{\mathrm{g}}(t,z)$ [m s^{-1}] in Table 3.1 also require the application

Table 3.1: Net advective mass transfer for each component in each region with advective term in continuity equation.

Region, k	Component, j	$U_{\mathrm{net,j,k}}(t,z)$ [m s^{-1}]
Settled wet powder	Water	$-U_{\mathrm{w}}(t) + U_{\mathrm{adj}}(t,z)$
Settled wet powder	Radiolytic gas	$-U_{\mathrm{w}}(t) + U_{\mathrm{g}}(t,z) + U_{\mathrm{adj}}(t,z)$
Settled wet powder	Steam	$-U_{\mathrm{w}}(t) + U_{\mathrm{g}}(t,z) + U_{\mathrm{adj}}(t,z)$
Pooled Water/Suspension	Water	$-U_{\mathrm{w}}(t)\,(1 - v_{\mathrm{f,p,wp}})\,\Delta S_{\mathrm{w}} + U_{\mathrm{adj}}(t,z)$
Pooled Water/Suspension	Radiolytic gas	$-U_{\mathrm{w}}(t)\,(1 - v_{\mathrm{f,p,wp}})\,\Delta S_{\mathrm{w}} + U_{\mathrm{g}}(t,z) + U_{\mathrm{adj}}(t,z)$
Pooled Water/Suspension	Steam	$-U_{\mathrm{w}}(t)\,(1 - v_{\mathrm{f,p,wp}})\,\Delta S_{\mathrm{w}} + U_{\mathrm{g}}(t,z) + U_{\mathrm{adj}}(t,z)$

of a corrective advective component to ensure that mass conservation is satisfied. This component, denoted in Table 3.1 by the term $U_{\mathrm{adj}}(t,z)$ [m s^{-1}], applies equally at spatial location, z, across all non-stationary components. Evaluation of this parameter for the present problem is performed by considering the following condition that takes into consideration the effect of volumetric sources/sinks on the flow of each component over a differential height, dz, across a discretised mesh cell denoted by index, i:

$$\int_{dz} \sum_{\mathrm{j}=1}^{N_{\mathrm{j}}} \left(\frac{\partial}{\partial z} \left(D_{\mathrm{k}}(t,z) \frac{\partial V'_{\mathrm{j,k}}(t,z)}{\partial z} + U_{\mathrm{net,j,k}}(t,z) V'_{\mathrm{j,k}}(t,z) \right) + S'_{\mathrm{j,k}}(t,z) \right) dz = Q_{\mathrm{i}}(t) \tag{3.15}$$

where $N_{\mathrm{j}} = 3$ is the number of non-stationary components. The variable $Q_{\mathrm{i}}(t)$ [m^3 s^{-1}] corresponds to the net flow of all components into or out of a discretised mesh cell. The subscript, i, corresponds to the index of the FV discretised mesh cell. The value, $Q_{\mathrm{i}}(t)$, is zero for intermediate cells, but takes a non-zero value for cells that are located on interfaces between regions or at boundaries, where the boundary or interface itself may move due to some net flow into or out of the discretised mesh cell. Using boundary or interface conditions and prescribed values of $Q_i(t)$, the term $U_{\mathrm{adj}}(t,z)$ may be calculated, ensuring continuity when solving Equation (3.13) numerically for each component in each region.

Table 3.2: Source and sinks for each component in each region in the continuity equation.

Region, k	Component, j	$S'_{\mathrm{j,k}}(t,z)$ [m^2 s^{-1}]
Settled wet powder	Water	$-S'_{\mathrm{boil,w}}(t,z) - S'_{\mathrm{H_2O}}(t,z)$
Settled wet powder	Radiolytic gas	$S'_{\mathrm{H_2}}(t,z)$
Settled wet powder	Steam	$S'_{\mathrm{boil,v}}(t,z)$

Discretisation of the problem using an FV spatial discretisation scheme leads to two $U_{\mathrm{adj}}(t,z)$ terms for each cylindrical discretised mesh cell, one at the upper and another at the lower face. This yields a set of N_{z} equations per component, per region, where N_{z} is the number of discretised cells containing a non-zero mass of components. Using this method, there are $N_{\mathrm{z}} + 1$ unknown advective components, denoted $U_{\mathrm{adj}}(t,z)$. By prescribing Equation (3.16) at the wetting front ($z = H_{\mathrm{dp}}$), the term, $U_{\mathrm{adj}}(t,z)$ may be readily determined at the upper face of the cell containing the wetting front. From here, the corrective advective term that ensures continuity may be determined at each cell face

from the wetting front to the free surface, located at the top of the domain, ensuring that interface conditions are satisfied as interface cell faces are encountered in the discretisation. As previously described in Section 2.5, the region interfaces are tracked through the use of a cell merge and split technique. This combined with the numerical schemes applied in this thesis ensure that sharp interfaces remain intact throughout the numerical simulation.

$$D_{\mathrm{wp}}(t, H_{\mathrm{dp}})\frac{\partial V'_{\mathrm{j,wp}}(t, H_{\mathrm{dp}})}{\partial z} + U_{\mathrm{net,j,wp}}(t, H_{\mathrm{dp}})V'_{\mathrm{j,wp}}(t, H_{\mathrm{dp}}) = 0 \tag{3.16}$$

The corresponding expression for $Q_{\mathrm{i}}(t)$ at the mesh cell containing the wetting front models the pores of the interface cell filling with water and gas products that advect downwards due to the continuous phase flow potential:

$$Q_i(t) = \pi R^2 U_{\mathrm{w}}(t)(1 - v_{\mathrm{f,p,dp}}) \tag{3.17}$$

The interface between the settled wet powder and pooled water regions is prescribed a Robin condition that is applied to ensure that there is a continuity of flow across the face, with no axial movement of the interface itself. The interface condition for components, j = w, rg, v, is given by:

$$\begin{aligned} D_{\mathrm{wp}}(t, H_{\mathrm{dp+wp}})\frac{\partial V'_{\mathrm{j,wp}}(t, H_{\mathrm{dp+wp}})}{\partial z} + U_{\mathrm{net,j,wp}}(t, H_{\mathrm{dp+wp}})V'_{\mathrm{j,wp}}(t, H_{\mathrm{dp+wp}}) = \\ D_{\mathrm{sus}}(t, H_{\mathrm{dp+wp}})\frac{\partial V'_{\mathrm{j,sus}}(t, H_{\mathrm{dp+wp}})}{\partial z} + U_{\mathrm{net,j,sus}}(t, H_{\mathrm{dp+wp}})V'_{\mathrm{j,sus}}(t, H_{\mathrm{dp+wp}}) \end{aligned} \tag{3.18}$$

The corresponding expressions for $Q_{\mathrm{i}}(t)$, used to calculate $U_{\mathrm{net,j,wp}}(t, H_{\mathrm{dp+wp}})$ in Equation (3.18), yielding continuity and no net exchange of products across the interface is:

$$Q_{\mathrm{i}}(t) = 0 \tag{3.19}$$

At the top of the domain the following boundary condition is prescribed to the gaseous components, j = rg, v:

$$\begin{aligned} D_{\mathrm{sus}}(t, H_{\mathrm{dp+wp+sus}})\frac{\partial V'_{\mathrm{j,sus}}(t, H_{\mathrm{dp+wp+sus}})}{\partial z} + U_{\mathrm{net,j,sus}}(t, H_{\mathrm{dp+wp+sus}})V'_{\mathrm{j,sus}}(t, H_{\mathrm{dp+wp+sus}}) \\ = U_{\mathrm{g}}(t, H_{\mathrm{dp+wp+sus}})V'_{\mathrm{j,sus}}(t, H_{\mathrm{dp+wp+sus}}) \end{aligned} \tag{3.20}$$

and for the water component (j = w), the following boundary condition is prescribed:

$$D_{\text{sus}}(t, H_{\text{dp+wp+sus}}) \frac{\partial V'_{\text{w,sus}}(t, H_{\text{dp+wp+sus}})}{\partial z} + U_{\text{net,w,sus}}(t, H_{\text{dp+wp+sus}}) V'_{\text{w,sus}}(t, H_{\text{dp+wp+sus}}) = -U_{\text{w,in}} \pi R^2 \quad (3.21)$$

where $U_{\text{w,in}}$ [m s^{-1}] is the flow rate of water into the domain.

The value of $U_{\text{adj,N}_\text{z}}(t)$ at the bottom of the discretised mesh cell containing the free surface (cell N_z), located at, $H_{\text{dp+wp+sus}}$, is used to adjust the height of the free surface. The full expression for the height of the free surface and each other region is described in Section 3.2.4.

The presence of the static UO_2 powder is simply modelled by prescribing a constant UO_2 powder bulk density throughout static powder bed.

3.2.4 Water Infiltration

Once water has entered the system, it fills the interstitial voids between the powder particles, increasing the total system bulk density. Therefore, the infiltration of the water into the powder bed will yield a system with an overall increased macroscopic neutron scattering cross-section. Fast neutrons born through fission events are now more likely to be thermalised or moderated, through the scattering of neutrons with the hydrogen atoms of the water molecules within the interstitial voids. This neutron thermalisation, or moderation effect, leads to an increased probability of subsequent thermal neutron fission occurring within the fissile material in the powder bed. The resulting increased rate of fission corresponds to a positive reactivity effect on the system.

An accurate model of unsteady infiltration into a bed of initially dry, or partially saturated fissile powder is required to model the effect water has on the system reactivity. Water infiltration may be considered as a reactivity insertion and is the predominant driving force behind the initial nuclear criticality excursions simulated in this thesis. Prior research on the modelling of fissile powder systems assumed wetting caused a constant ramp reactivity insertion (Rozain et al., 1991; Basoglu, 1992; Basoglu et al., 1994; Yamane et al., 2003b). However, without modelling the infiltration phenomenon, the variation in the reactivity over time as a direct result of wetting is unknown. Knowledge of the spatial water content during a nuclear criticality excursion is essential when analysing mechanisms that may quench the transient, such as thermal expansion, Doppler broadening, radiolysis and boiling. These factors affect the nuclear criticality assessment and safety case by limiting the fission power and determining the magnitude of negative reactivity feedback.

Infiltration phenomenon have been extensively studied within the fields of geology and soil mechanics. This has led to the development of various numerical modelling techniques (Marsily, 1986; Bear, 1972; Fredlund et al., 2012). One such method defined by Bear (1972) uses constitutive closure relations to solve two-phase porous media flow equations for phase saturations and pressures. Experiments to empirically determine necessary values for these closure correlations have not been carried out for fissile powder systems, posing a challenge when implementing this model.

An alternative approach proposed by Richards (1931) assumes that the non-wetting phase is

passive, thus reducing the complexity of the system to a single-phase (Farthing and Ogden, 2017). Therefore, this approach assures that the gaseous phase remains at atmospheric pressure and does not influence the flow of water. This assumption is valid when the air can move freely to the atmosphere. Richards' equation assumes that the wetting phase fluid is incompressible. A constitutive relation is also required when implementing this method, which typically takes a non-linear form (Brooks and Corey, 1964).

Another approach, first described by Green and Ampt (1911) (GA), that does not require the use of empirical correlations, is used in this thesis. This model considers there to be a sharp interface between the two immiscible fluids (non-wetting and wetting phases), creating a fully saturated region, and a dry region. The GA equation also assumes that the air phase is passive and free to escape from the domain. Figure 1.16 shows how the domain may be separated using the GA infiltration model approach. The location of the planes separating individual regions changes as water percolates through the domain.

In an experimental study looking at the infiltration of water into earthen liners, Albrecht and Cartwright (1989) found that the GA method was able to successfully model the propagation of the wetting front. A study comparing the wetting front propagation using the GA model and Richards' equation by Govindaraju et al. (1992) supports this finding.

Preliminary results have shown that when water infiltrates a fissile powder bed, a significant amount of radiolytic gas and water vapour may be produced. Therefore, the downward flow of water through the domain must be retarded to model the resistance to flow induced by the generation and advection of gas bubbles within the wetted fissile powder. The original GA equation may be found within the research literature (Green and Ampt, 1911; Warrick, 2003). The proposed adjustment which accounts for the impedance to flow due to the presence of gas is:

$$U_{\mathrm{w}}(t) = \frac{K_{\mathrm{sat,e}}(1 - \bar{v}_{\mathrm{f,g,wp}}(t))}{(1 - v_{\mathrm{f,p,wp}})\Delta S_{\mathrm{w}}} \left(\frac{H_{\mathrm{sus}}(t) + h_{\psi} + H_{\mathrm{wp}}(t)}{H_{\mathrm{wp}}(t)} \right) \tag{3.22}$$

where:

$$\Delta S_{\mathrm{w}} = S_{\mathrm{w,sat}} - S_{\mathrm{w,0}} \tag{3.23}$$

where H_{sus} [m] is the height of the pooled water region, h_{ψ} [m] is the hydraulic head due to matric suction. To prevent a singularity arising in Equation (3.22), the wetted region height, H_{wp} [m], starts at a very small positive value. The variable $K_{\mathrm{sat,e}}$ [m s^{-1}] represents the effective saturated hydraulic conductivity, $S_{\mathrm{w,sat}}$ [-] is the saturation level in the saturated case which may be less than one if there is residual air within the interstices of the pores and $S_{\mathrm{w,0}}$ [-] is the initial uniform saturation which may be greater than zero if there is any initial natural saturation of the porous medium due to hygroscopic effects. The present model assumes that all pores are completely filled with water, $S_{\mathrm{w,sat}} = 1$, and that unsaturated pores are fully dry, $S_{\mathrm{w,0}} = 0$.

The porosity may be found by first relating the solid volume fraction when k = dp, wp, to the bulk density of the UO_2 powder:

$$v_{\mathrm{f,p,k}} = \frac{\rho_{\mathrm{p,bulk,k}}}{\rho_{\mathrm{p,th}}} \tag{3.24}$$

where $\rho_{\mathrm{p,bulk,k}}$ [kg m^{-3}] is the UO_2 powder bulk density in region, k, and $\rho_{\mathrm{p,th}}$ [kg m^{-3}] is the density of solid UO_2. The bulk powder density may also be defined as:

$$\rho_{\mathrm{p,bulk,k}} dV = \rho_{\mathrm{p,th}} dV_{\mathrm{p}} \tag{3.25}$$

where dV_{p} [m^3] is the volume of powder within the volume element (dV [m^3]) under consideration.

The porosity of region, k, ϵ_{k} [-], is then given by:

$$\epsilon_{\mathrm{k}} = 1 - v_{\mathrm{f,p,k}} \tag{3.26}$$

The hydraulic conductivity, which defines the ease at which water percolates through the system, is considered on the saturated side of the sharp wetting front. For saturated flows, the hydraulic conductivity may be characterised using the following equation (Marsily, 1986):

$$K_{\mathrm{sat}} = \frac{k \rho_{\mathrm{w,th}} g}{\mu_{\mathrm{w}}} \tag{3.27}$$

where k [m^2] is the permeability at full saturation, g [m s^{-2}] is the acceleration due to gravity, $\rho_{\mathrm{w,th}}$ [kg m^{-3}] is the density of water and μ_{w} [Pa s] is the water dynamic viscosity.

Experiments investigating the measurement of hydraulic conductivity were performed by Bouwer (1966). These experiments suggested that an adjustment to the saturated hydraulic conductivity of water was required in the unsaturated case, to account for the impedance to the flow of water in porous media due to the presence of entrapped air. This adjustment to the hydraulic conductivity led to an improved agreement between models and experiments of water ingress into unsaturated porous media (Bouwer, 1966). Using this approach, the effective saturated hydraulic conductivity ($K_{\mathrm{sat,e}}$ [m s^{-1}]) used in Equation (3.22) may be expressed as:

$$K_{\mathrm{sat,e}} = \frac{1}{2} K_{\mathrm{sat}} \tag{3.28}$$

A comprehensive comparison regarding the various empirical and semi-empirical measures of saturated permeability carried out by Odong (2007), indicated that the Koseny-Carman formula produced reliable results for particles sizes up to 300 μm. The anticipated particle size range for UO_2 powder produced using various manufacturing methods is from 1 μm to 100 μm distributed log-normally

(Clayton and Aronson, 1958; Andreev et al., 2009). Therefore, the Koseny-Carman relation has been considered appropriate for determining the saturated permeability. The equation to represent this is (Marsily, 1986; Carman, 1956):

$$k = \frac{\epsilon^3}{5S_{\mathrm{A}}^2(1-\epsilon)^2} \tag{3.29}$$

where S_{A} [m^{-1}] is the specific surface area which is evaluated as the surface area exposed to the fluid per unit volume of the solid.

UO_2 powders have different powder particle size distributions and levels of sphericity depending on the manufacturing method utilised Clayton and Aronson (1958). Changes to the powder drum specific surface area arise because of differences in the orientation and packing structure of powders. For this investigation, the fissile porous medium is assumed to contain spherical, mono-dispersed powder particles with surfaces that are fully exposed to the wetting phase fluid. As a result, the specific surface area may be described as:

$$S_{\mathrm{A}} = \frac{6}{d_{\mathrm{p}}} \tag{3.30}$$

where d_{p} [m] is the mean powder particle diameter.

3.2.5 Radiolytic Gas Production

Ionising radiation causes molecules within the water to break into smaller molecules through a process known as radiolysis. Fission fragments are known to be the main cause of radiolysis in Aqueous Homogeneous Reactors (AHRs) (Lane et al., 1958). The problem of water decomposition within slurry reactors has been proposed to be similar to that of AHRs (Steele et al., 1963b). During primary radiolysis, these ionised particles dissociate into free radicals H· and ·OH. Many free radicals combine before they diffuse apart, forming more stable molecules. The yields of the primary species depend strongly on the linear energy transfer (LET) parameter. The LET is the energy that is transferred to the water per unit length along the fission track. Yields of H_2 and H_2O_2 are highest for radiations with high LET, whilst yields of free radicals such as H and OH are largest for radiations with low LET. Free radicals re-combine in dense fission tracks very quickly and are therefore neglected in this thesis (Lane et al., 1958). The effect of hydrogen peroxide (H_2O_2) which decomposes in water is not considered in this thesis.

Small pockets of gas get trapped in the interstices of the powder particles throughout water infiltration. These small pockets of gas are in dynamic equilibrium with the dissolved gasses in the pore water. The decomposition of water due to radiolysis leads to the production of small bubbles along the fission tracks. These small bubbles will collapse if the dissolved gas concentration is below their dynamic equilibrium concentration ($C_{\mathrm{H_2,equil}}$ [mol m^{-3}]). If the dissolved gas concentration rises above the equilibrium concentration, the direction of mass transfer reverses, now going from the dissolved to the gaseous phase. The theory of gas bubble formation is described in more detail by Spiegler et al. (1962). The following condition expresses the equilibrium concentration of gas within

the pores of the porous medium:

$$C_{\mathrm{H_2,equil}} = \left(P_w + \frac{4\sigma}{d_\mathrm{b}} \right) H_{\mathrm{H_2,sol}} y_{\mathrm{H_2}} \tag{3.31}$$

where P_w [Pa] is the water pressure, $H_{\mathrm{H_2,sol}}$ [mol m^{-3} Pa^{-1}] is Henry's constant for hydrogen, σ [N m^{-1}] is the surface tension of water and $y_{\mathrm{H_2}}$ [-] is the mole fraction of hydrogen gas in the trapped bubble. The diameter of the gas bubble, d_b [m], can play a significant role in the determination of the equilibrium concentration. For fast transients in fissile solution systems bubble nucleation typically occurs on fission track bubbles where the bubble size is on the order of 10^{-8} m (Winter, 2019). However, bubble nucleation within porous media is expected to be different due to the presence of a large number of solid particles in the water. Direct numerical simulation using microscopic pore-network models by Li and Yortsos (1995) indicated that the radius of the porous cavity where the trapped air is located will govern the equilibrium concentration. Mean particle sizes of UO_2 powders indicate that gas trapped within a porous cavity may have a radius on the order of 10^{-7} m to 10^{-5} m. Therefore, the gas held within porous cavities provides better nucleation sites at a lower concentration than on fission track bubbles. Consequently, mass transfer of radiolysis products to the gaseous phase is modelled at the porous cavity as opposed to across the surface of the fission track bubbles.

The present model assumes that hydrogen produced via radiolysis is instantaneously present within the gaseous phase. The low hydrogen content of atmospheric air means that only small amounts of dissolved hydrogen would be required for mass transfer into the gaseous phase. For this reason, the assumption has been considered appropriate. Oxygen is produced via secondary reactions and is not a product of the initial break-up of water. The fission yield, typically governed by the magnitude of the initial power spike after the system reaches a critical state, is not affected by the presence of oxygen since it forms much later in the transient. Therefore, the production of oxygen as a by-product of radiolysis has not been considered in the proposed model.

The number of molecules produced of a given species X per 100 eV of fission energy absorbed by the water is denoted $G(X)$. In the proposed model the hydrogen yield must be converted to a volumetric hydrogen yield through the use of the ideal gas law:

$$V_\mathrm{rg} = \frac{N_\mathrm{mol,rg} R T_\mathrm{rg}}{P_\mathrm{rg}} \tag{3.32}$$

where $R = 8.31$ J mol^{-1} K^{-1} is the universal gas constant, $N_\mathrm{mol,rg}$ [mol] is the number of moles of gas, T_rg [K] and P_rg [Pa] is the gas temperature and pressure respectively.

As noted by Steele et al. (1963b), a fraction of the energy (defined as g_p [-] in Equations (3.56) and (3.57)) from fission recoil fragments are deposited in the water, the remaining energy is deposited in the powder. An additional multiplier that accounts for the fractional occupation of the pores surrounding the particle by water must also be included. This leads to the following definition for the volumetric generation of H_2 per unit height, $V'_\mathrm{rg}(t,z)$ [m^2], in region k, interstitially around wetted UO_2 powder particles:

$$S'_{\mathrm{H_2}}(t,z) = (1-g_{\mathrm{p}})(1-v_{\mathrm{f,g,k}}(t,z))G_{\mathrm{v}}(\mathrm{H_2})P'(t,z) \tag{3.33}$$

where $G_{\mathrm{v}}(\mathrm{H_2})$ [$\mathrm{m^3\ J^{-1}}$] is the volumetric yield of hydrogen from radiolysis due to fission recoil fragments and P' [$\mathrm{W\ m^{-1}}$] is the linear energy generation rate within the system.

The corresponding sink term corresponding to the volumetric loss of water in region k, is given by:

$$S'_{\mathrm{H_2O}}(t,z) = (1-g_{\mathrm{p}})(1-v_{\mathrm{f,g,k}}(t,z))G_{\mathrm{v}}(\mathrm{H_2O})P'(t,z) \tag{3.34}$$

where $G_{\mathrm{v}}(\mathrm{H_2O})$ [$\mathrm{m^3\ J^{-1}}$] is the volumetric dissociation of water per Joule of energy deposited by fission fragments.

3.2.6 Bubble Size and Advection Velocity

The advective velocity of the bubbles through the domain will ultimately govern the rate of loss of gas from the system and will form an important component in determining the variation in reactivity feedback due to voidage. In order to estimate this value, an understanding of bubble size and flow regimes is required. The following section describes the evaluation of the gas bubble advection rate, U_{g} [$\mathrm{m\ s^{-1}}$], which is valid when the spatial location, z, that is in question, is located within the wet UO_2 powder or pooled water region (k = wp, sus).

Gas bubble sizes in the wetted fissile powder may be compared to those observed in three-phase fluidised bed systems due to their geometric similarities. For systems with small solid particles ≈ 88 μm in size, the Sauter mean diameter of bubbles were found to be similar to that of a two-phase system with no solid phase (Luewisutthichat et al., 1997). This is supported by experiments conducted by Quicker et al. (1984) where bubble characteristics for low solid volume was similar to that of a two-phase system. The proposed model expresses the three-phase powder bed as a two-phase system by using an effective medium viscosity approach (Fan, 1989).

The interfacial area concentration may be used to determine the Sauter mean gas bubble diameter. Comprehensive reviews of existing correlations may be found in Beenackers and Van Swaaij (1993), and Jo (2016). Due to disparities in three-phase fluidised bed systems, large variations in the interfacial area concentration correlation exists in the cited literature. A number of correlations, based on experimental data, are only valid for the system which they were developed for Quicker et al. (1984); Sun et al. (1988). However, a correlation that has been shown to be valid for a wider range of solid volume fractions and particle sizes has been defined in Beenackers and Van Swaaij (1993) as:

$$a_{\mathrm{I}}(t,z) = a_{\mathrm{I,0}}(t,z)\left(\frac{\mu_{\mathrm{w}}}{\mu_{\mathrm{eff}}}\right)^{0.21}\left(\frac{\rho_{\mathrm{eff}}(t,z)}{\rho_{\mathrm{w,th}}}\right)^{0.1} \tag{3.35}$$

where a_{I} [$\mathrm{m^{-1}}$] is the interfacial area concentration for radiolytic gas and steam in the wet powder and pooled water regions (k = wp, sus), $a_{\mathrm{I,0}}$ [$\mathrm{m^{-1}}$] is the interfacial area concentration in pure water,

and ρ_{eff} [kg m^{-3}] and μ_{eff} [Pa s] are the effective medium density and effective medium viscosity in region, k. These are defined respectively as:

$$\rho_{\text{eff,k}}(t,z) = \rho_{\text{p,th}} v_{\text{f,p,k}} + \rho_{\text{w,th}} v_{\text{f,w,k}}(t,z) + \rho_{\text{g,th}} v_{\text{f,g,k}}(t,z) \tag{3.36}$$

$$\mu_{\text{eff,k}} = \mu_{\text{w}}(1 - v_{\text{f,p,k}})^{-2.8} \tag{3.37}$$

Research carried out by Zeitoun et al. (1994) investigating interfacial area concentration in the bubbly flow regime for two-phase systems is shown in Equation (3.38).

$$a_{\text{I,0}} = 556.4 v_{\text{f,g,k}}(t,z)^{0.74} \tag{3.38}$$

The Sauter mean diameter of a bubble is defined as:

$$d_{\text{b}}(t,z) = \frac{6 v_{\text{f,g,k}}(t,z)}{a_{\text{I}}} \tag{3.39}$$

Substitution of Equations (3.35) and (3.38) into Equation (3.39) yields the following relation for the bubble diameter as a function of the void fraction:

$$d_{\text{b}}(t,z) = 1.0784 \times 10^{-2} v_{\text{f,g,k}}^{0.26} \left(\frac{\mu_{\text{w}}}{\mu_{\text{eff}}}\right)^{-0.21} \left(\frac{\rho_{\text{eff}}(t,z)}{\rho_{\text{w,th}}}\right)^{-0.1} \tag{3.40}$$

where the constant 1.0784×10^{-2} has units of metres, yielding d_{b} in units of metre.

A correlation may now be found to calculate the velocity of gas bubbles in the pore and pooled water. Experimental correlations developed by Zuber and Findlay (1965) concerning vertical gas flow in pipes may be used for a porous medium model if considering the system as a bundle of tubules. Later work by Roosevelt and Corapcioglu (1998) found that although gas transport in porous media may on occasion be modelled using a bundle of capillary tubes, actual gas transport in porous media deviates significantly from this idealised flow model. This could be due to the tortuosity of the porous medium causing significant lateral movement of bubbles.

For high slurry flows ($< 5\%$ powder by volume) Yang et al. (2007) found that the gas advection velocity may be correlated to solid volume fraction within the porous medium. A review of gas advection velocities for slurries with higher volume fractions may be found in the cited literature (Cheng et al., 2011). Work by Cheng et al. (2011) highlighted the importance of using a correlation that is valid for the expected mean particle size. It was found that smaller sized powders were easier to displace, meaning that less force was required for bubbles to push to the surface. At larger powder diameters, bubbles were more likely to becomes trapped (Ji et al., 1993). For some porous media considered by Roosevelt and Corapcioglu (1998), it was observed that bubbles below a critical size

would never reach the surface and they would either become entrapped or coalesce into larger bubbles. A model for bubble breakup and coalescence within the bubbly flow regime has been described by Jo and Revankar (2011) but is out of the scope of this investigation.

The present model assumes that gas flows are predicted to be solely within the bubbly flow regime. Although the actual gas flow will vary between different flow regimes, this approximation enables the implementation of the correlation developed by Tsuchiya et al. (1997), which applies to fluidised beds. This correlation models the fluidised bed using effective medium properties. Experimental analysis by Li and Prakash (2000) found that this correlation correctly predicted the bubble rise velocity for slurry concentrations from 15 % to 40 % by volume. At higher solid particle concentrations this correlation fails because the granular flow of the powder becomes more dominant than fluid dynamic flow (Gibilaro et al., 2007). Using this model, the dimensionless bubble velocity, $U'_{b,k}$, in region, k, may be represented as:

$$U'_b(t,z) = \left[\left(\frac{\mathrm{Mo}^{-0.25}(t,z)}{K_\mathrm{b}(t,z)} (d'_\mathrm{b}(t,z))^2 \right)^{-n} + \left(\frac{2c}{d'_\mathrm{b}(t,z)} + \frac{d'_\mathrm{b}(t,z)}{2} \right)^{-0.5n} \right]^{-1/n} \tag{3.41}$$

where n [-], c [-] and K_b [-] are empirically determined parameters, Mo [-] is the Morton number and d'_b [m] is the effective bubble diameter. The regions in which this correlation is valid is when k = wp, sus. The empirical constant, c, ranges from 1.2 to 1.4 for mono-component and multi-component liquids respectively. The variable, n, ranges from 1.6 to 0.8 for purified to contaminated liquids respectively. K_b may be found from:

$$K_\mathrm{b}(t,z) = \max(K_{b,0}\mathrm{Mo}^{-0.038}(t,z), 12) \tag{3.42}$$

where $K_{b,0}$ [-] varies from 14.7 to 10.2 for aqueous solutions (including water) to organic solvents (mixtures) respectively. The Morton number of the may be defined as:

$$\mathrm{Mo}(t,z) = \frac{g\mu^4_{\mathrm{eff,k}}}{\rho_{\mathrm{eff,k}}(t,z)\sigma^3} \tag{3.43}$$

The effective bubble diameter may be found using:

$$d'_\mathrm{b}(t,z) = d_\mathrm{b}(t,z) \left(\frac{\rho_\mathrm{eff}(t,z)g}{\sigma} \right)^{0.5} \tag{3.44}$$

where the bubble diameter is given in Equation (3.40).

The gas bubble velocity may then be defined as:

$$U_\mathrm{g}(t,z) = U'_\mathrm{b}(t,z) \left(\frac{\sigma g}{\rho_\mathrm{eff}(t,z)} \right)^{0.25} \tag{3.45}$$

3.2.7 Governing Equations for Nuclear Thermal Hydraulics

The generalised form of the equations governing component and region nuclear thermal hydraulics in a three-phase UO_2 powder bed take a similar form to thermal energy equations outlined within the cited literature (Kuznetsov, 1994; Ingham and Pop, 2005; Alazmi and Vafai, 1999; Williams, 2019). The governing equation includes terms for intra-phase thermal conduction, thermal convection (constituting both advection and diffusion) as well as phase-dependent thermal energy sources and sinks. Inter-phase thermal coupling that models phenomenon such as convection and boiling are modelled through the component dependent sources and sinks. The equation governing the nuclear thermal hydraulics of the static UO_2 powder (j = p and k = dp, wp) is:

$$M'_{\mathrm{p,k}} c_{\mathrm{p}} \frac{\partial T_{\mathrm{p,k}}(t,z)}{\partial t} = \frac{\partial}{\partial z}\left(\kappa_{\mathrm{p}}(T_{\mathrm{p,k}}) A_{\mathrm{cyl}} v_{\mathrm{f,p,k}} \frac{\partial T_{\mathrm{p,k}}(t,z)}{\partial z}\right) + E'_{\mathrm{net,p,k}}(t,z) \tag{3.46}$$

where $M'_{\mathrm{j,k}}$ [kg m^{-1}] is the mass per unit height of component, j, in region, k. The variable c_{j} [J kg^{-1} K^{-1}] corresponds to the specific heat capacity of component, j. $T_{\mathrm{j,k}}$ [K] is the temperature of component, j, in region, k. The net phase and component dependent thermal energy source/sink is given by $E'_{\mathrm{net,j,k}}(t,z)$ [W m-1]. The thermal conductivity of the stationary powder is given by $\kappa_{\mathrm{p}}(T_{\mathrm{p,k}})$ [W m^{-1} K^{-1}].

The mass per unit height of the component, j, in region, k, may be defined as:

$$M'_{\mathrm{j,k}} = \rho_{\mathrm{j,th}} A_{\mathrm{cyl}} v_{\mathrm{f,j,k}} \tag{3.47}$$

The governing equation used to model the nuclear thermal hydraulics of the pore and pooled water (j = w and k = wp, sus) is:

$$c_{\mathrm{j}}\left[\frac{\partial}{\partial t}\left(M'_{\mathrm{j,k}}(t,z) T_{\mathrm{j,k}}(t,z)\right) - \frac{\partial}{\partial z}\left(D_{\mathrm{k}}(t,z)\frac{\partial}{\partial z}\left(M'_{\mathrm{j,k}}(t,z) T_{\mathrm{j,k}}(t,z)\right)\right.\right.$$
$$\left.\left. + U_{\mathrm{net,j,k}}(t,z) M'_{\mathrm{j,k}}(t,z) T_{\mathrm{j,k}}(t,z)\right)\right] = E'_{\mathrm{net,j,k}}(t,z) \tag{3.48}$$

where the expression for $U_{\mathrm{net,j,k}}(t,z)$ is given in Table 3.1. The turbulent mixing coefficient, $D_{\mathrm{k}}(t,z)$, is identical to the one defined in Equation (3.13). The thermal energy source/sink term, $E'_{\mathrm{net,j,k}}(t,z)$ [W m^{-1}], is described for each component, in each region, in Table 3.3. The deposition of thermal energy from fission in the powder and water is represented by the terms $E'_{\mathrm{gen,p}}(t,z)$ [W m^{-1}] and $E'_{\mathrm{gen,w}}(t,z)$ [W m^{-1}], respectively, whereas inter-phase convection is modelled through the term denoted $E'_{\mathrm{convec,p}}(t,z)$ [W m^{-1}] in Table 3.3. Section 3.2.8 describes the approaches used to model the thermal energy sources and sinks.

The interface and boundary conditions take a similar form to those for the mass continuity equations. At the wetting front, where $z = H_{\mathrm{dp}}$, the powder thermal energy interface condition is given

Table 3.3: Source and sinks for each component in each region in the thermal energy equations.

Region, k	Component, j	$E'_{\mathrm{net,j,k}}(t,z)$ [J m^{-1} s^{-1}]
Dry powder	UO_2 powder	$E'_{\mathrm{gen,p}}(t,z)$
Settled wet powder	UO_2 powder	$E'_{\mathrm{gen,p}}(t,z) - E'_{\mathrm{convec,p}}(t,z) - E'_{\mathrm{boil,p}}(t,z)$
Settled wet powder	Water	$E'_{\mathrm{gen,w}}(t,z) + E'_{\mathrm{convec,p}}(t,z)$

by a continuity across the face such that the following is satisfied:

$$\kappa_{\mathrm{p}}(T_{\mathrm{p,dp}})v_{\mathrm{f,p,dp}}\frac{\partial T_{\mathrm{p,dp}}(t,H_{\mathrm{dp}})}{\partial z} + U_{\mathrm{w}}(t,H_{\mathrm{dp}})v_{\mathrm{f,p,dp}}c_p rho_{\mathrm{p,th}}T_{\mathrm{p,dp}}(t,H_{\mathrm{dp}}) = \kappa_{\mathrm{p}}(T_{\mathrm{p,wp}})v_{\mathrm{f,p,wp}}\frac{\partial T_{\mathrm{p,wp}}(t,H_{\mathrm{dp}})}{\partial z} \quad (3.49)$$

The following interface condition is prescribed at the wetting front ($z = H_{\mathrm{dp}}$) for the pore water:

$$D_{\mathrm{wp}}(t,H_{\mathrm{dp}})\frac{\partial}{\partial z}\left(M'_{\mathrm{w,wp}}(t,H_{\mathrm{dp}})T_{\mathrm{w,wp}}(t,H_{\mathrm{dp}})\right) + U_{\mathrm{net,w,wp}}(t,H_{\mathrm{dp}})M'_{\mathrm{w,wp}}(t,H_{\mathrm{dp}})T_{\mathrm{w,wp}}(t,H_{\mathrm{dp}}) = 0 \quad (3.50)$$

Since there is no UO_2 powder present in the pooled water region (k=sus), there is no thermal energy transfer in the UO_2 across the interface at $z = H_{\mathrm{dp+wp}}$, therefore, the following interface condition may be prescribed:

$$\frac{\partial T_{\mathrm{p,wp}}(t,H_{\mathrm{dp+wp}})}{\partial z} = 0 \quad (3.51)$$

A continuity of thermal energy across the interface between the pore and pooled water yields the following interface condition:

$$\begin{aligned} D_{\mathrm{wp}}(t,H_{\mathrm{dp+wp}})\frac{\partial}{\partial z}&\left(M'_{\mathrm{w,wp}}(t,H_{\mathrm{dp+wp}})T_{\mathrm{w,wp}}(t,H_{\mathrm{dp+wp}})\right) \\ &+ U_{\mathrm{net,w,wp}}(t,H_{\mathrm{dp+wp}})M'_{\mathrm{w,wp}}(t,H_{\mathrm{dp+wp}})T_{\mathrm{w,wp}}(t,H_{\mathrm{dp+wp}}) \\ &= D_{\mathrm{sus}}(t,H_{\mathrm{dp+wp}})\frac{\partial}{\partial z}\left(M'_{\mathrm{w,sus}}(t,H_{\mathrm{dp+wp}})T_{\mathrm{w,sus}}(t,H_{\mathrm{dp+wp}})\right) \\ &\quad + U_{\mathrm{net,w,sus}}(t,H_{\mathrm{dp+wp}})M'_{\mathrm{w,sus}}(t,H_{\mathrm{dp+wp}})T_{\mathrm{w,sus}}(t,H_{\mathrm{dp+wp}}) \end{aligned} \quad (3.52)$$

At the top of the domain, the infiltration of water from a fire-suppression system, introduces thermal energy into the system. This is represented in the thermal energy equation by the following boundary condition:

$$D_{\text{sus}}(t, H_{\text{dp+wp+sus}})\frac{\partial}{\partial z}\left(M'_{\text{w,sus}}(t, H_{\text{dp+wp+sus}})T_{\text{w,sus}}(t, H_{\text{dp+wp+sus}})\right)$$
$$+ U_{\text{net,w,sus}}(t, H_{\text{dp+wp+sus}})M'_{\text{w,sus}}(t, H_{\text{dp+wp+sus}})T_{\text{w,sus}}(t, H_{\text{dp+wp+sus}}) = -U_{\text{w,in}}\pi R^2\rho_{\text{w,th}}T_{\text{w,in}} \quad (3.53)$$

3.2.8 Nuclear Thermal Hydraulic Sources/Sinks

The generation of energy due to the deposition of fission products within the powder and water has been defined as (Williams, 2019):

$$E'_{\text{gen,p}}(t, z) = (g_{\text{p}} + (1 - g_{\text{p}})v_{\text{f,g,wp}}(t, z))P'(t, z) \quad (3.54)$$

$$E'_{\text{gen,w}}(t, z) = (1 - g_{\text{p}})(1 - v_{\text{f,g,wp}}(t, z))P'(t, z) \quad (3.55)$$

The fraction of kinetic energy held by a fission fragment that is deposited in the particle, g_{p}, depends on both the relative magnitudes of the range of fission products and the size of the fissile powder particle in water. Theoretical considerations of this parameter by Gardner (1959) indicated that for homogeneous slurry systems, the kinetic energy of fission fragments may be deposited within both the solid phase and the surrounding aqueous phase. For particle sizes over ≈ 20 μm, g_{p} does not depend on powder particle concentration and may be defined as (Gardner, 1959; Steele et al., 1963a):

$$g_{\text{p}} = \frac{3d_{\text{p}}}{8R_{\text{fiss}}} \; ; \; d_{\text{p}} < R_{\text{fiss}} \quad (3.56)$$

$$g_{\text{p}} = 1 - \frac{3R_{\text{fiss}}}{4d_{\text{p}}} + \frac{R^3_{\text{fiss}}}{8d^3_{\text{p}}} \; ; \; d_{\text{p}} > R_{\text{fiss}} \quad (3.57)$$

where R_{fiss} [m] is the range of fission fragments in solid UO_2.

The linear energy generation rate or fission power, P' at an instant in time, t, and at a position z is given by:

$$P'(t, z) = E_{\text{f}}\int_0^{\infty}\Sigma_{\text{f}}(t, z, E)N(t)\hat{\phi}(z, E)v(E)dE \quad (3.58)$$

where E_{f} [J fission^{-1}] is the average energy released from a fission reaction. The velocity of the neutrons, v_{n} [cm s^{-1}], is approximately 2.2×10^5 cm s^{-1} and 1.4×10^9 cm s^{-1} for thermal and fast neutrons respectively. The variable E_{f} represents the average energy released from fission, which for ^{235}U is $E_{\text{f}} = 3.2 \times 10^{-11}$ J. The normalised, energy dependent, radially averaged, scalar neutron flux, $\hat{\phi}$ at position z with energy E, is modelled using the steady-state NDE; this is discussed further in Section 3.2.10. The macroscopic fission cross-section is determined using the Monte Carlo code

Serpent; this is discussed further in Section 3.4.11.

The main mechanism of thermal energy transfer between the UO_2 powder and surrounding water is via convection. Heat transfer by thermal radiation between the fissile powder and surrounding water is small in comparison. Inter-phase conduction is considered only through the process of boiling. The following equation defines the specific rate of transfer of thermal energy from the powder to the surrounding water:

$$E'_{\text{convec}}(t,z) = h_{\text{p,w}}(t,z) v_{\text{f,w,wp}}(t,z) A'_{\text{p,w,wp}} \left(T_{\text{p,wp}}(t,z) - T_{\text{w,wp}}(t,z)\right) \tag{3.59}$$

where $A'_{\text{p,w,wp}}$ [m] is the interfacial area between the powder and water per unit height and $h_{\text{p,w}}$ [W m^{-2} K^{-1}] is the convective heat transfer coefficient between the powder and water.

When assuming spherical, mono-disperse particles, the interfacial area per unit height may be readily defined as:

$$A'_{\text{p,w,wp}} = \frac{6\pi R^2 v_{\text{f,p,wp}}}{d_{\text{p}}} \tag{3.60}$$

A correlation by Wakao and Kaguei (1983) accurately predicted the interfacial convective heat transfer coefficient in packed beds with wide-ranging properties. An investigation by Kuwahara et al. (2001) used microscopic pore-scale analysis to develop a correlation that corroborates the results of the correlation outlined in Wakao and Kaguei (1983). The correlation in Wakao and Kaguei (1983), shown in Equation (3.61) has been implemented in this thesis to model the interphase convective heat transfer coefficient.

$$h_{\text{p,w}}(t,z) = \frac{\kappa_{\text{w}}(T_{\text{w,wp}})}{d_{\text{p}}} \left[2 + 1.1 Pr^{1/3}(T_{\text{w,wp}}) Re_{d_{\text{p}}}^{0.6}(t,z)\right] \tag{3.61}$$

where κ_{w} [W m^{-1} K^{-1}] is the fluid thermal conductivity, $Re_{d_{\text{p}}}$ [-] represents the Reynolds number where the characteristic length is the powder diameter, and Pr [-] is the fluid Prandtl number. The Reynolds number may be defined as:

$$Re_{d_{\text{p}}}(t,z) = \frac{\rho_{\text{w,th}} U_{\text{w}}(t,z) d_{\text{p}}}{\mu_{\text{w}}} \tag{3.62}$$

The Prandtl number may be defined as:

$$Pr = \frac{c_{\text{w}} \mu_{\text{w}}}{\kappa_{\text{w}}(T_{\text{w,wp}})} \tag{3.63}$$

Small variations in the convective heat transfer coefficient, through the selection of different correlations, are not expected to affect the rate of heat transfer between the powder and water. This is

because the interfacial area between the powder and water is so great for small particles (see Equation (3.60)), that the overall rate of heat transfer is relatively high.

When the system becomes supercritical, the increased rate of energy generation causes a corresponding increase in the rate of thermal energy deposited in the system. If the thermal reactivity feedback due to Doppler broadening and thermal expansion does not sufficiently decrease the energy generation rate of the system, the temperature of the water may increase up to the boiling point. At the boiling point, any further heat transfer into the water will lead to vapourisation. The increased voidage due to the presence of vapour in the system will act as negative reactivity feedback. In this case, the production of vapour will strongly affect the fission rate, which is directly proportional to the energy generation rate. This is expected to be the main mechanism for heat loss from the powder and water. Therefore, this is an important phenomenon to consider when modelling such systems.

Once the edge of the powder particle reaches the boiling temperature of the surrounding water, any additional heat transferred to the water phase provides energy to vaporise the water. The proposed film boiling model, described within Faghri and Zhang (2006), is shown in Equation (3.64). Using this model, energy is transferred from the powder, into the film and bulk liquid. This correlation is valid when the full surface area of an immersed sphere is in contact with water. Although this may not be directly comparable to the geometry being considered, the high porosities simulated ensure that most of a single UO_2 powder particle is surrounded by water.

$$E'_{\text{boil}}(t,z) = h_{\text{p,v}}(t,z) A'_{\text{p,w}} v_{\text{f,w,k}}(t,z) \max\left[0, (T_{\text{I}}(t,z) - T_{\text{sat}})\right] \tag{3.64}$$

where k = wp, corresponding to the wetted powder region. In Chapter 5, k = wp, sus.

where $h_{\text{p,v}}$ [W m^{-2} K^{-1}] is the boiling heat transfer coefficient, T_{sat} [K] is the boiling point of water at atmospheric pressure and T_{I} [K] is the interface temperature between the powder particle wall and surrounding liquid. The interface temperature is defined as the average between the powder and water temperature:

$$T_{\text{I}}(t,z) = \frac{1}{2}\left(T_{\text{p,wp}}(t,z) + T_{\text{w,wp}}(t,z)\right) \tag{3.65}$$

The proposed model does not consider condensation phenomena. The high rate of heat transfer between the powder and water means that both phases are expected to reach the boiling point of water at the same time. The corresponding generation of gas and reduction in the volume of liquid water, per unit height, due to this latent heat transfer may be represented respectively as follows:

$$S'_{\text{boil,v}} = \frac{E'_{\text{boil}}(t,z)}{\rho_{\text{v,th}} h_{\text{l,v}}} \tag{3.66}$$

and:

$$S'_{\text{boil,w}} = -\frac{E'_{\text{boil}}(t,z)}{\rho_{\text{w,th}} h_{\text{l,v}}} \tag{3.67}$$

where ρ_v [kg m^{-3}] and $h_{\text{l,v}}$ [J kg^{-1}] are the vapour density and latent heat of vaporisation, respectively. These values are specified at atmospheric pressure and the boiling point of water.

Research by Leinhard and Dhir (1973) found a correlation, shown in Equation (3.68), for the film boiling heat transfer coefficient on the surface of an immersed sphere. The full surface area of the spherical particle is assumed to be in contact with the surrounding liquid, making the heat transfer coefficient similar to the case of a fully immersed sphere.

$$h_{\text{p,v}}(t,z) = 0.67 \left[\frac{\kappa_{\text{v}}^3 \rho_{\text{v,th}} g (\rho_{\text{w,th}} - \rho_{\text{v,th}}) h'_{\text{l,v}}(t,z)}{\mu_{\text{v}} d_{\text{p}} (T_{\text{I}}(t,z) - T_{\text{sat}})} \right]^{0.25} \tag{3.68}$$

where κ_{v} [W m^{-1} K^{-1}] is the vapour thermal conductivity and μ_{v} [Pa s] is the dynamic viscosity of the vapour. The adjusted latent heat of vaporisation, $h'_{\text{l,v}}$ [J kg^{-1}], may be defined as:

$$h'_{\text{l,v}}(t,z) = h_{\text{l,v}} + 0.4 c_{\text{v}} (T_{\text{I}}(t,z) - T_{\text{sat}}) \tag{3.69}$$

3.2.9 Region Height Change

The GA approach models the system as a three region problem, where the increase in height of the wet powder region is expressed as:

$$\frac{dH_{\text{wp}}}{dt} = U_{\text{w}}(t) \tag{3.70}$$

The change in the height of the dry powder region may be described respectively as:

$$\frac{dH_{\text{dp}}}{dt} = -U_{\text{w}}(t) \tag{3.71}$$

The change in height of the pooled water region that contains the free surface may be expressed as:

$$\frac{dH_{\text{sus}}}{dt} = U_{\text{w,in}}(t) - U_{\text{w}}(t) \frac{\epsilon \Delta S_{\text{w}}}{(1 - \bar{v}_{\text{f,g,wp}}(t))} + U_{\text{adj,N}}(t) \tag{3.72}$$

where $U_{\text{adj,N}}(t)$ [m s^{-1}] is the rate at which the free surface height changes in the top discretised mesh cell of the pooled water region.

3.2.10 The Neutron Diffusion Equation and the Scalar Neutron Flux Distribution

An axial representation for the distribution of fission power in the system is required for the 1D nuclear thermal hydraulics and radiolytic gas equations. The model described in this thesis separates out the

spatial flux shape from the neutron population by using a lumped parameter method, as described by Duderstadt and Hamilton (1976). The radially averaged, axially normalised, scalar neutron flux shape, $\hat{\phi}_{\mathrm{g}}(z)$ [m^{-1}], is determined by solving the steady-state two-group NDE. The steady-state two-group neutron diffusion equation is solved for the cylindrical geometry with r-z spatial variation and may be defined as (Duderstadt and Hamilton, 1976):

$$-\nabla \cdot D_{\mathrm{g}}(r,z)\nabla\phi_{\mathrm{g}}(r,z) + \Sigma_{\mathrm{t,g}}(r,z)\phi_{\mathrm{g}}(r,z) = \sum_{g'=1}^{2} \Sigma_{s,g'\rightarrow g}(r,z)\phi_{\mathrm{g'}}(r,z) + \frac{\chi_{\mathrm{p,g}}}{k_{\mathrm{eff}}} \sum_{g'=1}^{2} \bar{\nu}_{\mathrm{g'}}\Sigma_{\mathrm{f,g'}}(r,z)\phi_{\mathrm{g'}}(r,z) \quad (3.73)$$

where $D_{\mathrm{g}} = 1/3\Sigma_{\mathrm{t,g}}$ [cm] is the energy group-dependent neutron diffusion coefficient and $\Sigma_{\mathrm{s,g'}\rightarrow\mathrm{g}}$ [cm^{-1}] is the macroscopic neutron scattering cross-section from group, g', to the present group under consideration, g.

The radially averaged, normalised, axial and energy-dependent spatial flux shape, $\hat{\phi}_{\mathrm{g}}(z)$, is calculated directly from the solution of the two-group NDE using the following:

$$\hat{\phi}_{\mathrm{g}}(z) = \frac{\int_0^R r dr \phi_{\mathrm{g}}(r,z)}{\int_0^{H_{\mathrm{dp+wp+sus}}} dz \int_0^R r dr \sum_{\mathrm{g}=1}^{2} \phi_{\mathrm{g}}(r,z)} \quad (3.74)$$

The two-group scalar neutron flux is normalised such that the resulting spatial flux shape satisfies the following:

$$\int_0^{H_{\mathrm{dp+wp+sus}}} dz \sum_{\mathrm{g}=1}^{2} \hat{\phi}_{\mathrm{g}}(z) = 1 \quad (3.75)$$

The solution of the two-group NDE is found using a power iteration method for the effective multiplication factor (k_{eff}), or eigenvalue, in conjunction with a preconditioned conjugate-gradient (PCG) solver for the scalar neutron flux. The geometry is modelled as a right-circular-cylinder, with a reflective boundary condition prescribed at $r = 0$ for all z, which may be defined as:

$$-D_{\mathrm{g}}(0,z)\frac{\phi_{\mathrm{g}}(0,z)}{dr} = 0 \quad (3.76)$$

At $r = R_{\mathrm{cyl}}$, the following vacuum boundary condition is prescribed for all z:

$$\frac{1}{4}\phi_{\mathrm{g}}(R_{\mathrm{cyl}},z) + \frac{1}{2}D_{\mathrm{g}}(R_{\mathrm{cyl}},z)\frac{\phi_{\mathrm{g}}(R_{\mathrm{cyl}},z)}{dr} = 0 \quad (3.77)$$

At $z = 0$ and $z = H_{\text{dp+wp+sus}}$, for all r, the following vacuum boundary condition is prescribed:

$$\frac{1}{4}\phi_{\text{g}}(r,z) + \frac{1}{2}D_{\text{g}}(r,z)\frac{\phi_{\text{g}}(r,z)}{dz} = 0 \tag{3.78}$$

The dominant eigenvalue, also known as the effective multiplication factor, k_{eff} [-], that is found when solving the eigenvalue problem outlined by Equation (3.73), is not used directly in the proposed model. The purpose of the two-group NDE is solely to determine the spatial neutron flux shape, $\hat{\phi}_{\text{g}}$. The two-group NDE is solved for every 0.5 \$ change in the wetting-induced reactivity component, R_{imm}.

Energy condensed (or group-collapsed) and resonance self-shielded macroscopic neutron cross-sections have been determined using the results of neutron transport simulations performed using the Monte Carlo code Serpent at different bed immersion fractions. These energy condensed and resonance self-shielded macroscopic neutron cross-sections are specified using a two-group structure. The thermal neutron energy group was prescribed using the following lower and upper energy range boundaries:

$$0 \text{ eV} < E_{\text{therm}} < 0.625 \text{ eV} \tag{3.79}$$

where E_{therm} [eV] is the thermal neutron energy group. The fast neutron energy group was prescribed using the following lower and upper energy range boundaries:

$$0.625 \text{ eV} < E_{\text{fast}} \tag{3.80}$$

where E_{fast} [eV] is the fast neutron energy group.

All prompt neutrons born through fission are assumed to be fast such that $\chi_{\text{p}}(E_{\text{fast}}) = 1$ and $\chi_{\text{p}}(E_{\text{therm}}) = 0$.

3.3 Infiltration Model Comparison to Experiment

The infiltration ODEs defined by Equations (3.22), (3.71) and (3.72) may be solved in isolation to examine the accuracy of modelling infiltration into UO_2 powder using the Green and Ampt model. Data to perform this comparison is obtained from a paper by Rozain et al. (1991) which describes an infiltration experiment carried out by the CEA. In this experiment, a jet of fine droplets was directed to impinge upon and wet the surface of a UO_2 powder contained within a cylindrical drum. Humidity sensors placed at equidistant points throughout the vessel were used to monitor the rate of infiltration into the powder bed. The experimental data required to investigate the accuracy of the infiltration model is documented in Table 3.4.

Data from the CEA experiment indicated that the powder density increased from 1000 kg m^{-3} to 2200 kg m^{-3} (Rozain et al., 1991). Since the proposed model does not consider the variable powder densities at this stage, an average density of 1600 kg m^{-3} has been used. Furthermore, the size

distribution of the powder used in the CEA experiment was not reported. Therefore, to compare the results of the simulation to the experiment, the infiltration characteristics were obtained for several mean powder particle sizes. This was then compared to mean UO_2 powder particle sizes found during the manufacture of UO_2 powders.

Table 3.4: Infiltration simulation parameters.

Property	Symbol	Value
Drum height	H_{cyl}	1.0 m
Initial dry powder height	H_{dp}	0.6217 m
Initial wet powder height	H_{wp}	0 m
Initial water height	H_{sus}	0 m
Powder mass	$M_{\text{p,dp}} + M_{\text{p,wp}}$	500 kg
Surface flow rate	$U_{\text{w,in}}$	9.947×10^{-4} m s^{-1}
Drum radius	R_{cyl}	0.4 m
UO_2 dry powder bulk density	$\rho_{\text{p,bulk,dp}}$	1600 kg m^{-3}
UO_2 wet powder bulk density	$\rho_{\text{p,bulk,wp}}$	1600 kg m^{-3}
Solid UO_2 powder density	$\rho_{\text{p,th}}$	10950 kg m^{-3}

Experimental results reported by Rozain et al. (1991) indicated that water was detected at the lowest humidity sensors at a time of approximately 1850 s. The constant rate of penetration into the powder described by Rozain et al. (1991) has been derived from experimental results as 1/3 mm s^{-1}. The geometry of the system at time $t = 0$ s in Figure 3.1 refers to the initial conditions specified in Table 3.4. The infiltration time into the powder bed may also be calculated using this constant infiltration rate and the estimated mean powder bulk density defined in Table 3.4. This value, calculated to be 1865 s, indicates that the mean powder bulk density chosen reflects the infiltration time estimated by Rozain et al. (1991) to within approximately 1 %. The mean powder bulk density specified in the model (1600 kg m^{-3}) has therefore been considered appropriate.

The simulated size of the wetted powder region is shown as a function of time in Figure 3.1, for several mean powder particle sizes. Also documented is the constant speed of penetration defined by Rozain et al. (1991), determined from experimental data. The GA infiltration model found that for all mean powder particle sizes considered, the speed of penetration into the powder was slightly non-linear. As the mean powder particle size decreased, the permeability of the powder also decreased, leading to lower infiltration rates. The simulated speed of penetration satisfies experimental results when the mean powder particle size is between 9 μm and 10 μm. These mean powder particle sizes are similar to the range of UO_2 powder particle sizes observed in the cited literature (Kersten, 1962; Andreev et al., 2009; Clayton and Aronson, 1958).

3.4 Case Study Parameters

3.4.1 System Geometry & Bed Characteristics

The geometric properties of the vessel that is modelled throughout this thesis are described here. The vessel was 1.0 m in height with a radius of 0.4 m. The unsaturated UO_2 powder bed porosity was 0.8540, and total mass of UO_2 powder in the domain was 500 kg. This yielded a corresponding powder

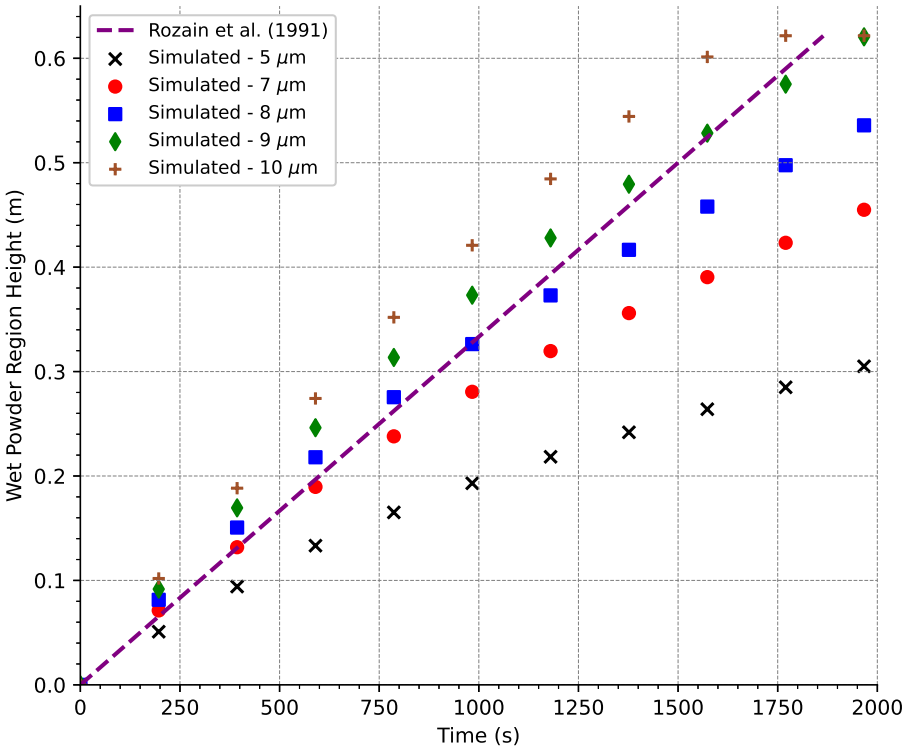

Figure 3.1: The propagation of the wetted powder region is shown for a number of different mean powder diameters. The dashed line represents the constant rate of infiltration that was assumed by Rozain et al. (1991) having conducted an infiltration experiment on a UO_2 powder drum.

bed height of 0.6217 m, based on a theoretical density of 5-wt% enriched UO_2 of $\rho_{p,th} = 10950$ kg m^{-3}.

An activated sprinkler system, producing a uniform sheet of water, entered the domain through the top of the vessel at a speed of $U_{w,in} = 9.947 \times 10^{-4}$ m s^{-1} ($= 0.5$ L s^{-1}) and temperature of $T_{in} = 293.15$ K. The speed of the water hitting the surface of the powder is assumed to be low enough such that the powder is not disturbed. If at any point in the transient, the height of the pooled water went above the maximum system height, the appropriate volume of water/gas was removed from the top of the domain.

3.4.2 Mean Powder Particle Sizes

Experimental work by Andreev et al. (2009), and Clayton and Aronson (1958), indicate that log-normal powder particle size distributions are commonly found for UO_2 powders manufactured using various techniques. This corresponds well with many other powder systems whose mean powder particle size are distributed log-normally (Bear, 1972). The present model does not consider the poly-dispersion of powder particle sizes. To see the effect of the mean powder particle size on the nuclear criticality transient, a large and a small powder particle size of 100 μm and 10 μm were simulated.

3.4.3 Thermophysical Properties

UO_2 Powder

Excellent resources outlining the thermophysical properties of uranium dioxide can be found in Belle (1961) and Haase et al. (1986). Further information regarding the theoretical density of UO_2 may be found within the cited literature (WPNCS, 2006). Correlations for the specific heat capacity of UO_2 as a function of temperature were found by Fink et al. (1981). The variation of the specific heat capacity as a function of temperature for 5 % enriched uranium is shown in Figure 3.2. A constant value for the specific heat capacity was calculated by averaging the value over the expected temperature range of the UO_2 powder. The expected range of the UO_2 powder temperature was predicted to be between 293.15 K to 610 K, yielding an average UO_2 specific heat capacity of $c_p = 274$ J kg^{-1} K^{-1}. Analysis shown in Figure 3.20b indicate that local UO_2 powder temperatures do not exceed 610 K.

The change in UO_2 powder density as a function of temperature is accounted for by the thermal feedback equations, but is neglected in the multiphysics part of the model. Figure 3.2 shows that by using a correlation defined by Ronchi et al. (2004), the density does not change significantly over the expected temperature range.

The thermal conductivity of solid UO_2 powder (κ_p) may be modelled as a function of temperature using a correlation presented in Fink et al. (1981). Figure 3.2 highlights that over a temperature range of approximately 600 K, the thermal conductivity doubles. The correlation defined by Fink et al. (1981) incorporated into the this model for the case where the region, k = dp, wp, may be seen in Equation (3.81).

$$\kappa_p = \left[0.068337 + 1.6693 \times 10^{-4} T_{p,k} + 3.1886 \times 10^{-8} T_{p,k}^2\right]^{-1} + 0.12783 T_{p,k} e^{-1.1608/k_b T_{p,k}} \tag{3.81}$$

where $k_b = 8.6144 \times 10^{-5}$ eV K^{-1} is the Boltzmann constant.

A summary of the thermophysical data for the UO_2 powder particles can be seen in Table 3.5.

Table 3.5: Thermophysical properties of UO_2 powder.

Property	Symbol	Value
Specific heat capacity	c_p	274 J kg^{-1} K^{-1}
Thermal conductivity	κ_p	see Equation (3.81)
Bulk density of dry powder	$\rho_{p,bulk,dp}$	1600 kg m^{-3}
Bulk density of wet powder	$\rho_{p,bulk,wp}$	1600 kg m^{-3}
Theoretical density	$\rho_{p,th}$	10950 kg m^{-3}

Water

The specific heat capacity of water does not depend strongly on temperature, therefore a value of $c_w = 4.2 \times 10^3$ J kg^{-1} K^{-1} was used for the case study. By applying the Boussinesq approximation to the free convection equation, the effect of water temperature was modelled using the water thermal expansion coefficient. The density of water is specified at the initial system temperature of 293.15 K.

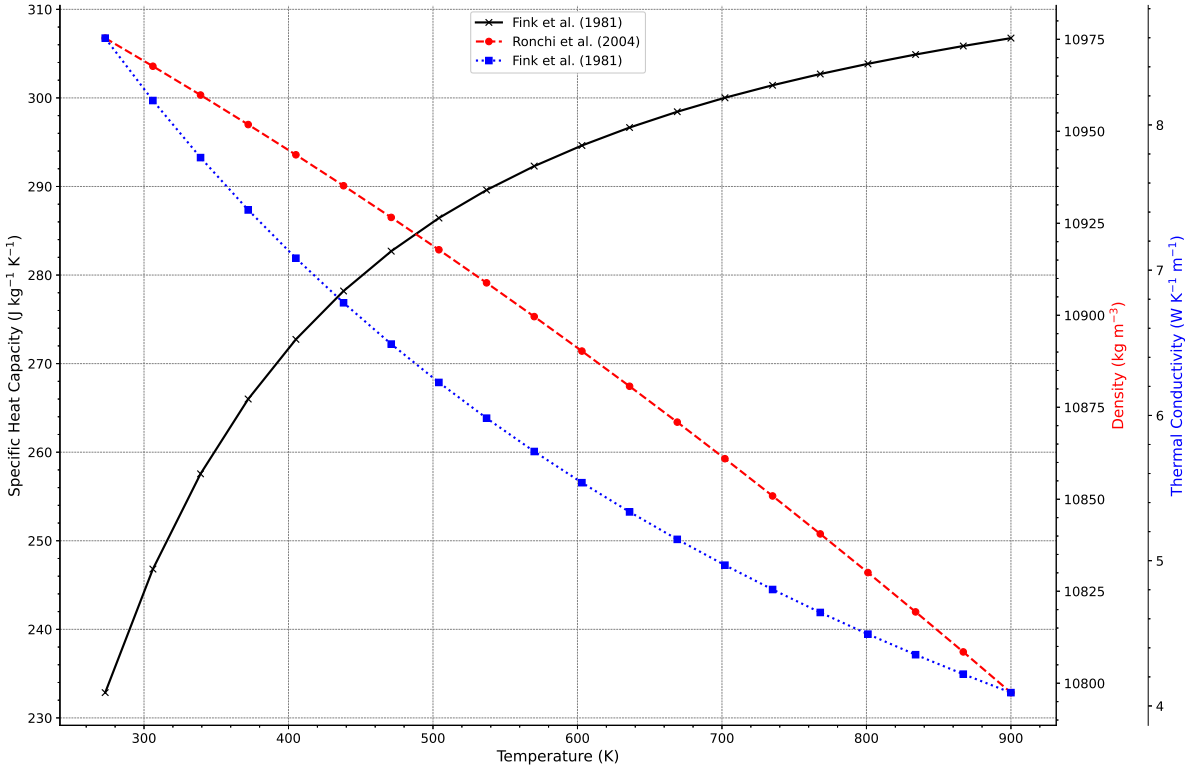

Figure 3.2: The thermophysical data for UO_2 powder at 5-wt% enrichment for the range of expected powder temperatures.

The dynamic viscosity was determined using the correlation described by Pátek et al. (2009) and is given as:

$$\mu_w(T_\mathrm{w}) = \left[280.68\left(\frac{T_\mathrm{w}}{300}\right)^{-1.9} + 511.45\left(\frac{T_\mathrm{w}}{300}\right)^{-7.7} + 61.131\left(\frac{T_\mathrm{w}}{300}\right)^{-19.6} + 0.45903\left(\frac{T_\mathrm{w}}{300}\right)^{-40}\right] \times 10^{-6} \quad (3.82)$$

A summary of the thermophysical properties of water is given in Table 3.6.

Table 3.6: Thermophysical properties of water.

Property	Symbol	Value
Specific heat capacity	c_w	4.2×10^3 J kg^{-1} K^{-1}
Boiling point	T_sat	373.15 K
Thermal expansion coefficient	η	2.14×10^{-4} K^{-1}
Dynamic viscosity	μ_w	see Equation (3.82)
Density	$\rho_\mathrm{w,th}$	998.1 kg m^{-3}

Steam

The steam temperature was treated to be in equilibrium with the surrounding liquid. Therefore, the thermophysical properties may be interpreted from steam tables contained in Faghri and Zhang (2006) at a temperature of approximately 373 K. Table 3.7 outlines the constant thermophysical properties of steam used in this case study.

Table 3.7: Thermophysical properties of water vapour at boiling.

Property	Symbol	Value
Specific heat capacity	c_{v}	2.060×10^{3} J kg^{-1} K^{-1}
Latent heat of vaporisation	$h_{\mathrm{l,v}}$	2.2512×10^{6} J kg^{-1}
Thermal conductivity	κ_{v}	2.46×10^{-2} W m^{-1} K^{-1}
Dynamic viscosity	μ_{v}	1.271×10^{-5} Pa s
Density	$\rho_{\mathrm{v,th}}$	5.863×10^{-1} kg m^{-3}

3.4.4 Turbulent Mixing Coefficient

Turbulence occurs when chaotic changes in flow velocity occur around a mean value (Coussot, 1997). This process manifests itself through the generation of turbulent eddies throughout the liquid medium. The varying shape of turbulent eddies may be understood to form via an energy cascade (Friedlander, 1957). The phenomena of an energy cascade refers to the energy transfer between eddies as they go from the largest possible size, to the smallest. The varying eddy length and velocity scales observed during this energy cascade may be characterised by a mean length and velocity scale (Csanady, 1973).

Full turbulence models are complex, computationally demanding and beyond the scope of the proposed model. Cooling et al. (2014) models turbulent diffusion in fissile solutions as a Fickian diffusive process driven by the turbulence caused by gas bubble advection. The following equation described the turbulent mixing coefficient used in the proposed model based on Cooling et al. (2014):

$$D = \frac{v_{\mathrm{eddy}} r_{\mathrm{eddy}}}{\pi} \tag{3.83}$$

where v_{eddy} [m s^{-1}] and r_{eddy} [m] are the velocity and radius of the largest eddies that are predicted to be in the system.

Turbulent mixing is expected to occur throughout all regions where advecting gas bubbles are present. The size and velocity of turbulent eddies are expected to vary depending on whether they are present in the wet powder region of pooled water. The proposed model estimates the turbulent mixing coefficient using a constant value for each region, where $D_{\mathrm{wp}} = 0.0001$ m^2 s^{-1} and $D_{\mathrm{sus}} = 0.001$ m^2 s^{-1} respectively. Sensitivity analysis has been performed on the values to examine their importance in determining the peak power, energy released and time to boiling for the nuclear criticality transient.

3.4.5 Radiolytic Gas Generation Coefficient

Experiments to evaluate $G(X)$ for uranium-thorium slurry systems due to fission recoil particles have been carried out by Steele et al. (1963b). The fraction of the total fission energy deposited in the surrounding water was found to depend on particle size and concentration. The number of hydrogen molecules produced through the break-up of water per 100 eV of fission energy was found to be

2.1 ± 0.2 molecules per 100 eV, near the maximum value of 2.35 molecules per 100 eV expected for water. This is contrary to the work in Lane et al. (1958) which states that the maximum value of $G(H_2)$ for pure water is 1.8 molecules per 100 eV. In the proposed model the more conservative value that minimises radiolytic gas production has been chosen, $G(H_2) = 1.8$ molecules per 100 eV. The proposed model considers constant vapour properties of 1 atm and 373.15 K, leading to a volumetric generation coefficient of $G_v(H_2) = 5.37 \times 10^{-9}$ m^3 J^{-1}. For the range of radiolytic gas temperatures expected (273.15 K to 373.15 K), $G_v(H_2)$ varies from 4.2×10^{-9} m^3 J^{-1} to 5.37×10^{-9} m^3 J^{-1}.

3.4.6 Range of UO_2 Fission Fragments

The average range of fission fragments in UO_2 varies depending on the mass of the fission fragment considered and the initial kinetic energy of fission fragments. Experimental data produced by Eichenberg et al. (1957) indicates that there is a linear relationship between the atomic mass of the fission fragment and its range in UO_2. The fission fragment range varied from approximately 8 μm for lighter fragments, down to approximately 5 μm for heavier fragments. Based on this data, the mean fission fragment range is prescribed as $R_{fiss} = 7$ μm.

3.4.7 Delayed Neutron Data and Generation Time

The fraction of neutrons born via delayed neutron precursors and the decay constant of delayed neutron precursors were determined through a series of neutron transport simulations using the Monte Carlo code MCNP (Werner et al., 2018), ranging in bed immersion fraction, f_{imm}, from 0 to 1. The results for each of the six delayed neutron precursor groups are shown in Table 3.8. The fraction of neutrons born via delayed neutron precursors and decay constant of delayed neutron precursors did not vary widely for the range of bed immersion fractions considered. The mean prompt neutron generation time was found to be $\Lambda = (5.32959 \pm 0.0094) \times 10^{-5}$ s. The total fraction of neutrons born via delayed neutron precursors was found to be $\beta_{eff} = (733 \times \pm 8) \times 10^{-5}$.

Table 3.8: Delayed neutron precursor group data.

Group, i	β_i ($\times 10^{-5}$)	λ_i (s^{-1})
1	25 ± 1	0.01335 ± 0.00000
2	129 ± 4	0.03264 ± 0.00000
3	122 ± 3	0.12099 ± 0.00000
4	279 ± 5	0.30482 ± 0.00001
5	125 ± 4	0.85704 ± 0.00003
6	53 ± 2	2.87888 ± 0.00015

3.4.8 Wetting-Induced Reactivity Insertion

The ingress of water into the interstices between the UO_2 powder particles has been modelled in dollars (\$) as a reactivity insertion, denoted R_{imm}. MCNP was used to determine the effective multiplication factor (k_{eff}) at a range of bed immersion fractions. The reactivity was calculated using:

$$R_{imm} = \frac{k_{eff} - 1}{k_{eff}\beta_{eff}} \tag{3.84}$$

The polynomial best-fit line described by Equation (3.85) and shown in Figure 3.3 has been used

to describe the reactivity insertion due to wetting between known values found using MCNP.

$$R_{\text{imm}}(f_{\text{imm}}) = \sum_{i=0}^{n} C_i f_{\text{imm}}^i \tag{3.85}$$

where $f_{\text{imm}} = H_{\text{wp}}/H_{\text{dp+wp}}$ is the bed immersion fraction, $n = 4$ is the polynomial order, the coefficients of the polynomial C_{i} are defined in Table 3.9.

Table 3.9: Bed immersion feedback coefficients.

i	0	1	2	3	4
C_i	-90.8692	531.7354	-973.8299	832.3316	-270.8543

At low bed immersion fractions the system is deeply sub-critical and no significant variations to the fission rate is predicted. It is therefore possible to begin the simulation from a bed immersion fraction that corresponds to a near- delayed critical point. The system configuration that corresponds to this near delayed critical point is given in Table 3.10, which corresponds to a bed saturation of $f_{\text{imm}} = 0.29$ and initial reactivity of -0.179 \$.

Table 3.10: Initial region heights, neutron density and delayed neutron precursor concentrations.

Property	Symbol	Value
Initial dry powder height	H_{dp}	0.4414 m
Initial water height	H_{pooled}	0.3783 m
Initial wet powder height	H_{wp}	0.1803 m

3.4.9 Thermal Reactivity Feedback

Powder and water thermal expansion, and the associated density changes of the powder bed, occurring as a result of increasing system temperatures, leads to a decreased probability of interactions between neutrons and target nuclei. This usually reduces the reactivity of the system. Increasing temperatures also leads to Doppler broadening, which broadens microscopic nuclear cross-sections, increasing the probability of interaction between neutrons and ^{238}U nuclei. For UO_2 powder systems moderated by water, this decreases the system reactivity. A thermal reactivity feedback term incorporated into the point kinetics equation (see Equation (3.1)) has been used to model these effects. The proposed model has separated thermal reactivity feedbacks by phase and region. The change in reactivity due to temperature variations, denoted $\Delta R_{\text{th,j,k}}(\bar{T}_{\text{j,k}}, f_{\text{imm}})$, is a function of both temperature and the bed immersion fraction. Here, the subscript relating to the component of interest, j = p, and the region, k = dp, wp.

The effects of Doppler broadening and thermal expansion on the system reactivity were determined using the Monte Carlo code MCNP. For each bed immersion fraction considered, the effective multiplication factor (k_{eff}) was calculated for all expected region/phase specific temperatures. Room temperature (293.15 K) was the lower temperature limit for the MCNP simulations. Preliminary analysis indicated that the powder temperature would not rise above 800 K, therefore this was set as the upper limit. The upper temperature limit for the water was set just above the boiling point (383.15 K), given atmospheric conditions. These values represent the range of validity for the reactivity feedback correlations created using the results of MCNP simulation data. The ENDF/B-VII

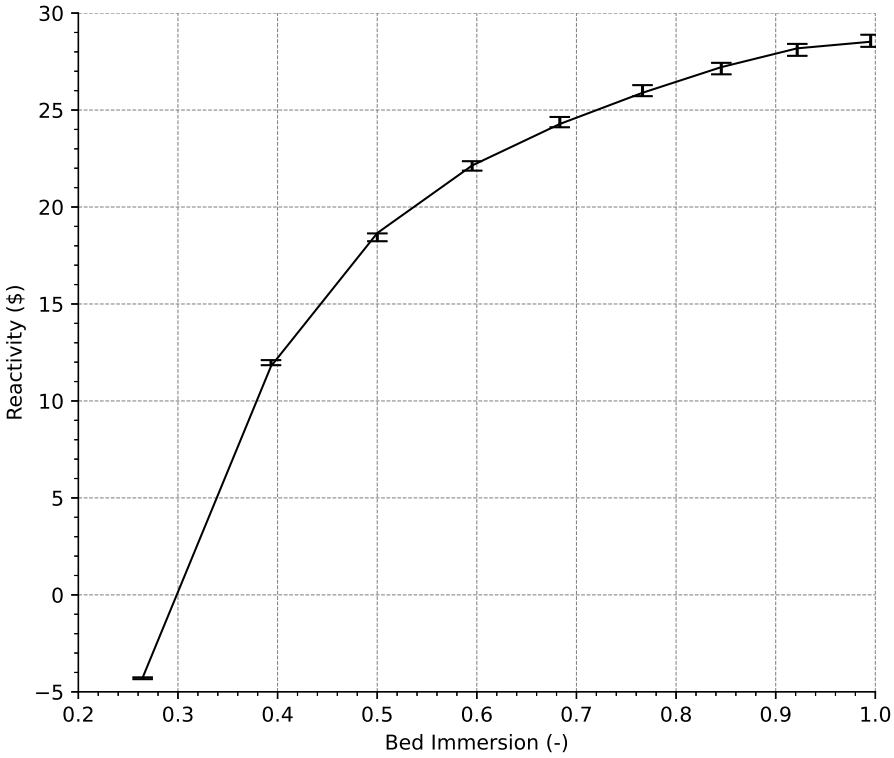

Figure 3.3: The reactivity inserted due to the infiltration of water into the dry powder calculated using $\beta_{\text{eff}} = (733 \pm 8) \times 10^{-5}$. The line represents the correlation specified by Equation (3.85).

nuclear data library was used to obtain temperature adjusted nuclear cross-sections for MCNP simulations. The method of stochastic mixing described in Donnelly (2011) was used to evaluate thermal feedback effects at temperatures not explicitly tabulated in the ENDF/B-VII nuclear data library.

The results of the MCNP simulations are shown in Figures 3.4 to 3.6. A line of best-fit that is a function of both temperature and bed immersion has also been shown.

For water in the pore space between fissile powder particles, the reactivity was found to be a linear function of temperature and a second order polynomial function of bed immersion. In the wet powder, the thermal reactivity feedback was found to be a linear function of both temperature and bed immersion. Doppler broadening in the dry powder region decreased the reactivity. Thermal expansion of the dry powder due to increased temperatures caused a fraction of the dry powder to penetrate the wetting front and become surrounded by water. Although the wetting front location did not change, the greater mass of fissile powder in the wet powder region due to this expansion introduced a positive reactivity feedback. The effect of this can be seen in Figure 3.6 which shows that the reactivity due to a combination of Doppler broadening and thermal expansion resulted in a net positive reactivity feedback. The following equation defines the general thermal reactivity feedback for a given phase/region:

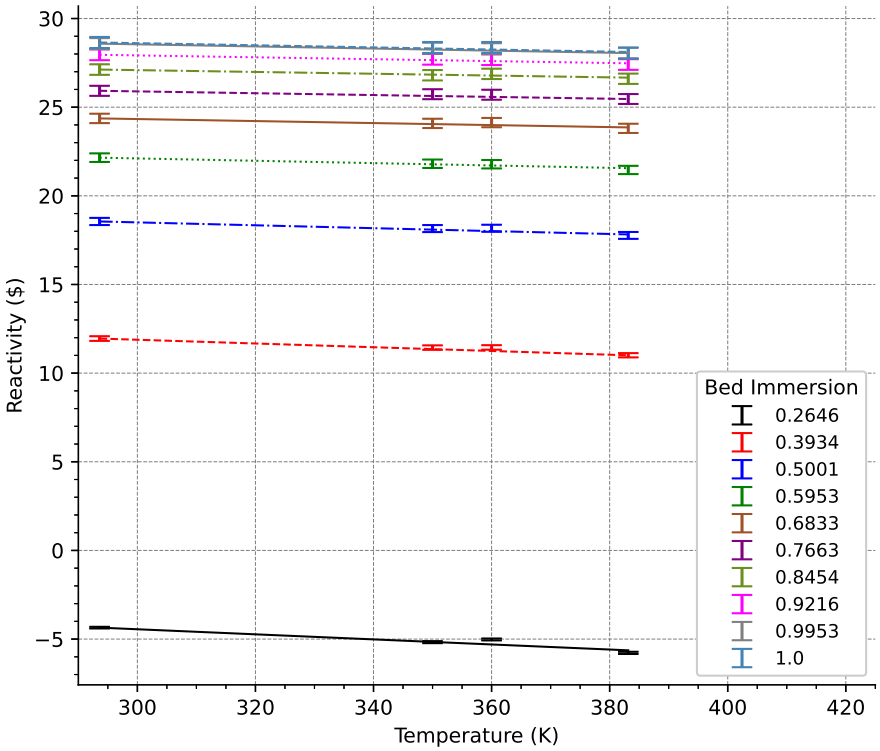

Figure 3.4: The points represent the reactivity calculated using MCNP due to variations in temperature from Doppler broadening and expansion of pore water. The lines represents the correlation described by Equation (3.87).

$$\Delta R_{\mathrm{th,j,k}}(\bar{T}_{\mathrm{j,k}}, f_{\mathrm{imm}}) = R_{\mathrm{th,j,k}}(\bar{T}_{\mathrm{j,k}}, f_{\mathrm{imm}}) - R_{\mathrm{th,j,k}}(T_0, f_{\mathrm{imm}}) \tag{3.86}$$

where T_0 [K] is the reference temperature at the start of the simulation, which is prescribed $T_0 = 293.15$ K, for all regions and components present in the system initially. The correlations are of the form:

$$R_{\mathrm{th,j,k}}(\bar{T}_{\mathrm{j,k}}, f_{\mathrm{imm}}) = \left(C_0 f_{\mathrm{imm}}^2 + C_1 f_{\mathrm{imm}} + C_2\right) \bar{T}_{\mathrm{j,k}}(t) \tag{3.87}$$

where $\bar{T}_{\mathrm{j,k}}$ is the average temperature of component, j, in region, k. Substituting Equation (3.87) into Equation (3.86), the following may be found:

$$\Delta R_{\mathrm{th,j,k}}(\bar{T}_{\mathrm{j,k}}, f_{\mathrm{imm}}) = \left(C_0 + C_1 f_{\mathrm{imm}} + C_2 f_{\mathrm{imm}}^2\right) \left(\bar{T}_{\mathrm{j,k}}(t) - T_0\right) \tag{3.88}$$

Table 3.11 shows the coefficients for each of the regions and phases used to describe the thermal reactivity feedback correlation, along with the R-squared value.

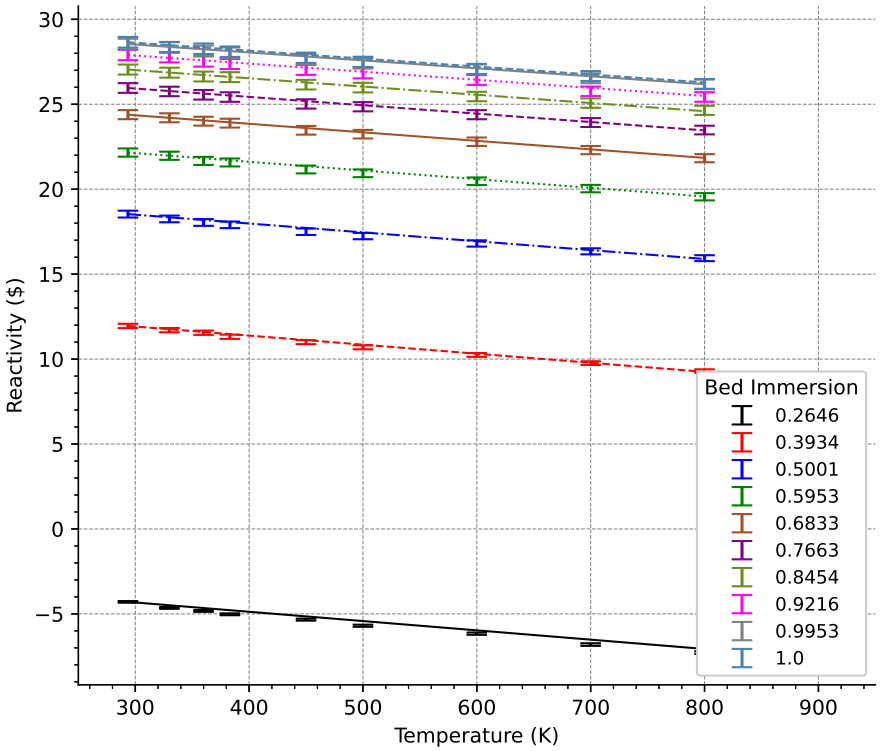

Figure 3.5: MCNP data points are shown alongside the correlation used for temperature variations in the wet powder.

Table 3.11: Thermal feedback coefficients and R-squared for correlation.

Region	C_0 ($\times 10^{-2}$)	C_1 ($\times 10^{-2}$)	C_2 ($\times 10^{-2}$)	R^2
dry powder	0.4219	−0.8590	0.4700	0.99994
wet powder	−0.5759	0.1086	0.0000	0.99986
pore water	−2.5051	4.8433	−2.9357	0.99992

3.4.10 Void Reactivity Feedback

Void reactivity feedback has been separated into pore water and pooled water components. This is because voids in the interstices between fissile powder particles are expected to have a much larger effect on system reactivity than voids located in the pooled water, which does not contain fissile material. Voids present in the system provide pathways for neutrons to travel with a very low probability of collision, increasing neutron leakage and usually decreasing the macroscopic absorption neutron cross-section.

Using MCNP, a series of simulations were carried out to investigate the reactivity of the system at various void fractions and bed immersion fractions. Voids in MCNP were modelled by decreasing the density of water in the appropriate region, any excess volume of water was moved upwards. The maximum system height was 1 m, meaning that in some cases water left the system.

Figure 3.7 highlights that within the wet powder region there is a non-linear relationship between

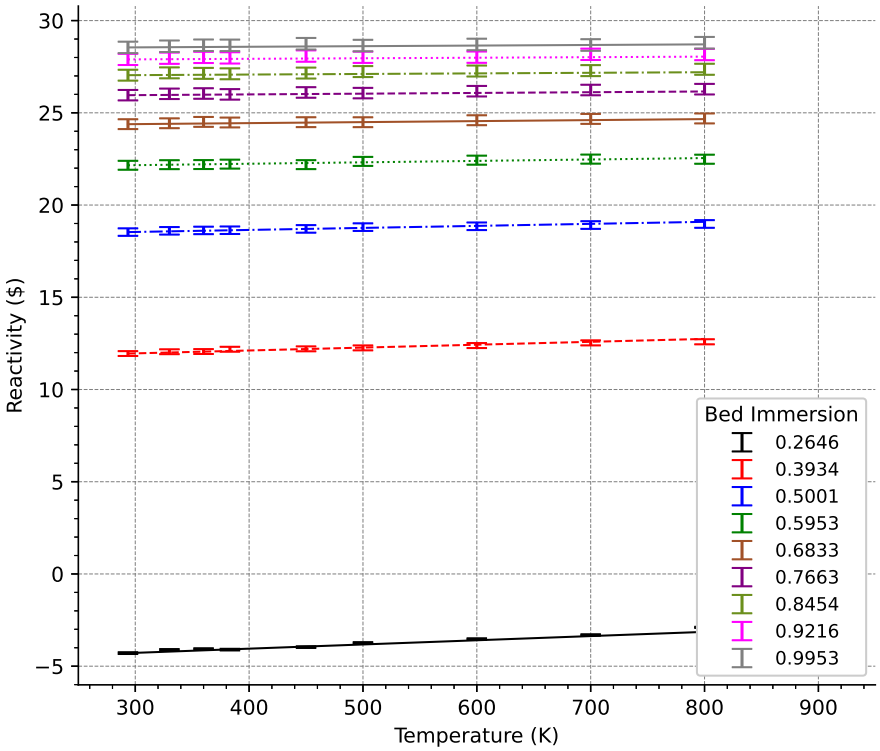

Figure 3.6: MCNP data points are shown alongside the correlation used for temperature variations in the dry powder.

the reactivity, voidage and bed immersion fraction. This differs from data for the pooled water region, shown in Figure 3.8, which shows a linear relationship between reactivity and voidage, and a non-linear relationship between reactivity and bed immersion fraction. These graphs confirm that voids present in the pores have a greater effect on the reactivity of the system than voids present in the pooled water.

The reactivity feedback due to the presence of voids in regions, k = wp, sus, is:

$$\Delta R_{\text{void,k}}(\bar{v}_{\text{f,g,k}}, f_{\text{imm}}) = R_{\text{void,k}}(\bar{v}_{\text{f,g,k}}, f_{\text{imm}}) - R_{\text{void,k}}(v_{0,\text{f,g,k}}, f_{\text{imm}}) \tag{3.89}$$

where $v_{0,\text{f,g,k}} = 0.0$ is the reference or initial voidage in the region, k, being considered.

The correlation for the reactivity as a function of bed immersion fraction and voidage within the pores takes the following form:

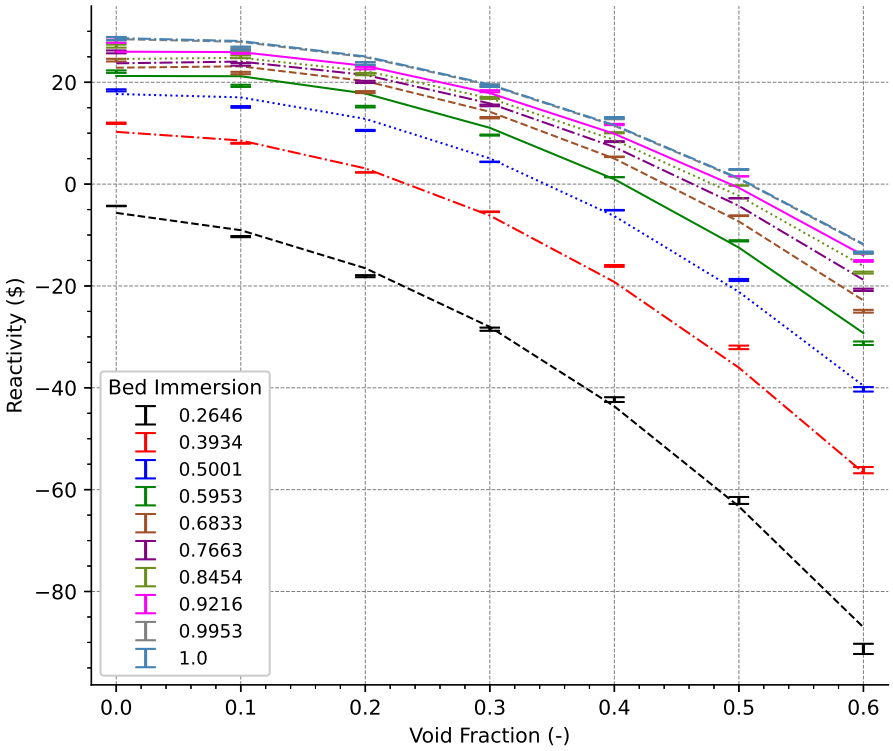

Figure 3.7: The reactivity due to the presence of voids located in the pores around the wet powder. The lines represent the correlation described by Equation (3.90).

$$R_{\text{void,wp}}(\bar{v}_{\text{f,g,wp}}, f_{\text{imm}}) = C_0 + C_1 f_{\text{imm}}(t) + C_2 \bar{v}_{\text{f,g,wp}}(t) + C_3 f^2_{\text{imm}}(t) + C_4 \bar{v}_{\text{f,g,wp}}(t) f_{\text{imm}}(t) + C_5 \bar{v}^2_{\text{f,g,wp}}(t) + C_6 f^3_{\text{imm}}(t) + C_7 f^2_{\text{imm}}(t) \bar{v}_{\text{f,g,wp}}(t) + C_8 f_{\text{imm}} \bar{v}^2_{\text{f,g,wp}}(t) \quad (3.90)$$

The coefficients for Equation (3.90), which are described in Table 3.12, give a close fit to MCNP simulated data ($R^2 = 0.99556$).

Table 3.12: Void feedback coefficients for voids present within pores.

i	0	1	2	3	4	5	6	7	8
C_i	-72.72	362.1	-62.1	-464.4	224.1	-232.0	203.7	-155.4	108.7

Reactivity as a result of voids present in the pooled water region has been defined by the following correlation:

$$R_{\text{void,sus}}(\bar{v}_{\text{f,g,sus}}, f_{\text{imm}}) = \left(C_0 f^2_{\text{imm}}(t) + C_1 f_{\text{imm}}(t) + C_2\right) \bar{v}_{\text{f,g,sus}}(t) \quad (3.91)$$

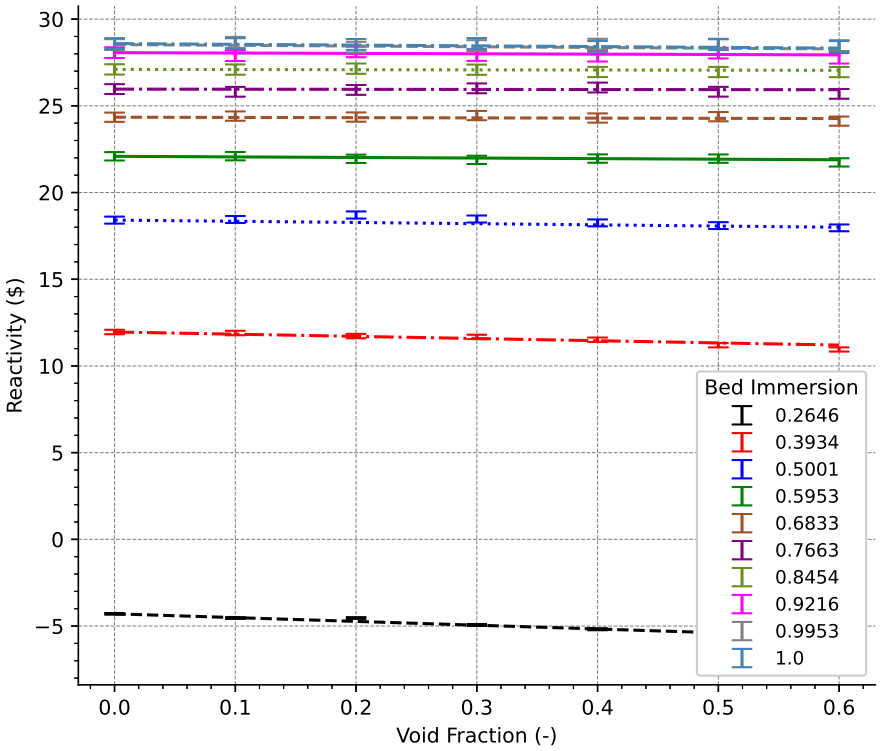

Figure 3.8: The reactivity due to the presence of voids within the pooled water. The lines represent the correlation described by Equation (3.91).

The coefficients for Equation (3.91), which are described in Table 3.13, give a close fit to MCNP simulated data ($R^2 = 0.99972$).

Table 3.13: Void feedback coefficients for voids present within pooled water.

i	0	1	2
C_i	-4.929841	12.476281	-7.983281

3.4.11 Energy Condensed and Resonance Self-Shielded Macroscopic Neutron Cross-Section and Associated Correlations as a Function of Immersion Fraction

Group condensed and resonance self-shielded macroscopic cross-sections were determined using the Monte Carlo neutron transport code Serpent (Leppänen et al., 2015) for the two-group macroscopic neutron cross-sections required by the neutron diffusion code. The bed immersion fraction was varied to investigate the functional dependence of the macroscopic cross-sections on the height of the wet powder region.

A homogenised three region approach was used as an approximate geometry for the Monte Carlo neutron transport simulations. This neglects the effect of double heterogeneity spatial self-shielding which causes nuclear cross-sections to vary radially through an individual powder particle as well as in space overall (Sanchez and Pomraning, 1991). Research on ^{239}Pu systems by Shmakov et al. (2000) showed that typically the homogenisation of dispersed particulates in a continuous moderator produces

appropriate values for nuclear cross-sections when the mean free path of thermal neutrons is greater than the size of the particulates (Shmakov, 1999). Similar conclusions were made by Yamamoto et al. (2006) investigating Mixed OXide (MOX) fuel pellets. In this case, double heterogeneity spatial self-shielding effects do not significantly affect the nuclear cross-sections. Furthermore, increasing the number density of UO_2 powder particles in the continuous water phase decreases the impact of the double heterogeneity on the macroscopic nuclear cross-sections (Williams, 1974). However, there is still spatial self-shielding effects associated with the natural spatial variation of the energy-dependent scalar neutron flux within the homogeneous material regions. Using MCNP, Laramore et al. (2018) showed that a homogeneous approach was appropriate for the range of UO_2 powder sizes used in this Chapter. This was further supported by the Working Group on Nuclear Criticality Safety Data at JAERI (JAERI, 2001) who showed that the change in the infinite multiplication factor for particles of size $d_p = 200$ μm was less than 0.3 % for 5 % enriched UO_2 powder at a bulk density of 2.0 g cm^{-3}. Using a homogenised region approximation significantly reduces the computing complexity of the Monte Carlo simulations of the solution domain. If one was to use Monte Carlo methods to model the problem as a heterogeneous dispersed particulate multiphase material (Delgado and de Lima, 2018), where all the individual UO_2 particles or grains are modelled, would be computational very challenging (Brown and Martin, 2004).

Another factor to consider is the agglomeration, or clumping, of dispersed particulates which would lead to particles that are effectively larger than their constituents. Large particles may be formed by a process known as soft agglomeration, where smaller primary particles are loosely bound by Van der Waals forces (Hartley et al., 1985; Balakrishna et al., 2009). There may be a case where the size of the agglomerate becomes large enough that the double heterogeneity spatial self-shielding effects become significant. In this case, the heterogeneity of the system must be taken into account. The present model does not consider the agglomeration of powder particles. Statistical methods for modelling the agglomeration of the powder particles in a continuous medium may be found within the cited literature (Williams, 1974; Randall, 1963).

Figure 3.9 shows the variation of the macroscopic neutron cross-sections as a function of bed immersion. Thermal group fission and absorption neutron cross-sections in the dry powder region vary non-linearly as a function bed immersion. All other group and region cross-sections are considered to be independent of the bed immersion fraction. Figure 3.10 represents the two-group neutron scattering cross-sections for the dry powder, wet powder and pooled water regions respectively.

The correlation, as a function of immersion fraction, defining the thermal fission and absorption macroscopic neutron cross-sections within the dry powder region are of the following form:

$$\Sigma_X = C_0 + C_1 f_{\text{imm}}(t) + C_2 f_{\text{imm}}^2(t) \tag{3.92}$$

where Σ_X may be the macroscopic absorption cross-section (Σ_a), the macroscopic fission cross-section (Σ_f) or the average number of neutrons born through fission multiplied by the macroscopic fission cross-section ($\bar{\nu}\Sigma_f$). Table 3.14 highlights the coefficients used in the correlation.

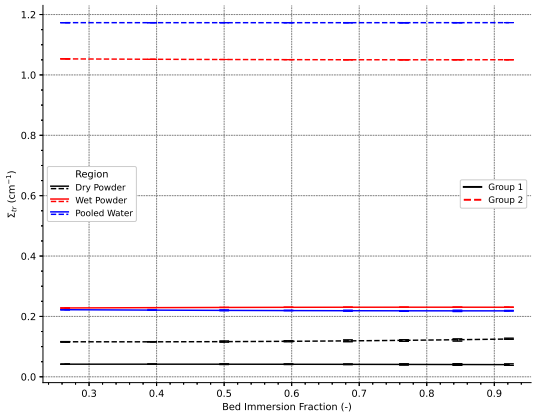

(a) Σ_{tr}.

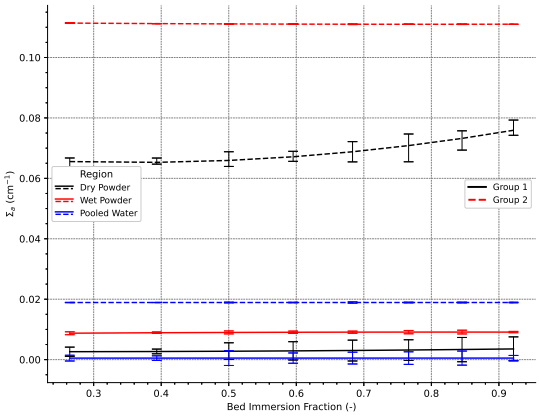

(b) Σ_{a}.

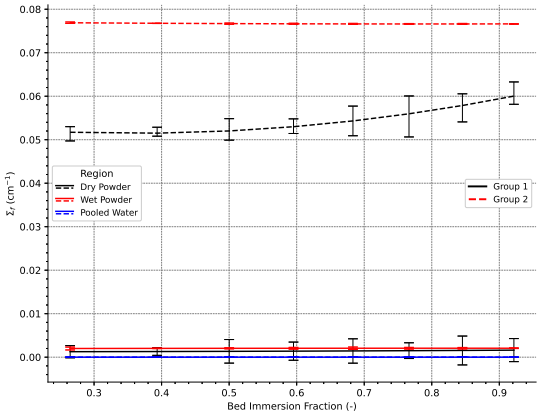

(c) Σ_{f}.

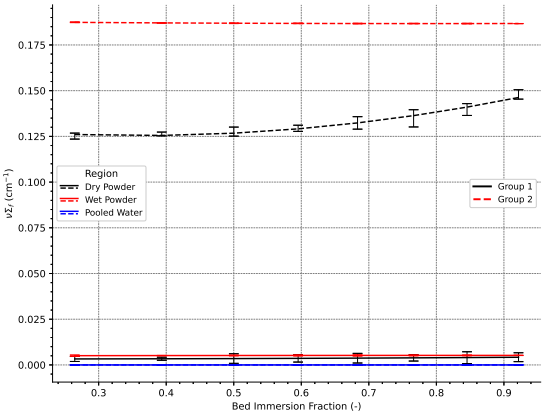

(d) $\bar{\nu}\Sigma_{\mathrm{f}}$.

Figure 3.9: The fast and thermal macroscopic neutron cross-sections for each region is shown. The points represent data calculated using Serpent, the lines represent the values/correlations used in the proposed model.

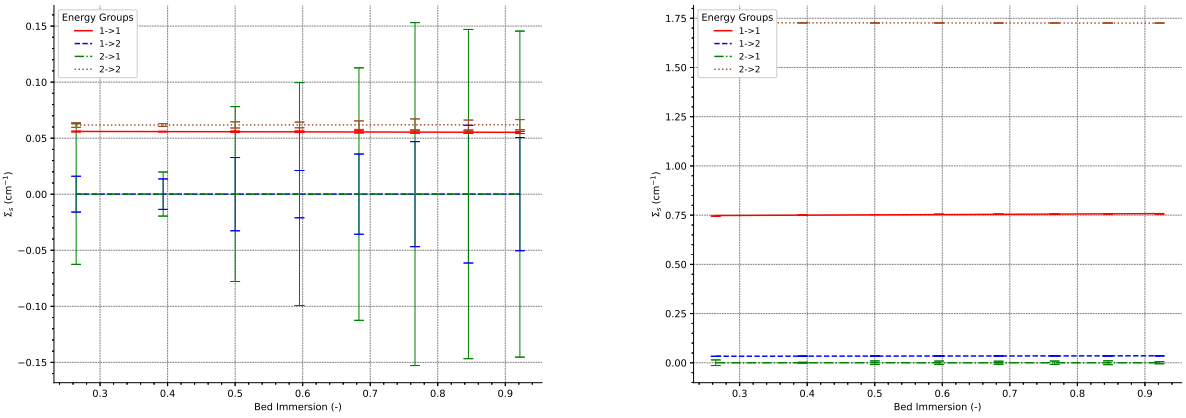

(a) Dry powder.

(b) Wet powder.

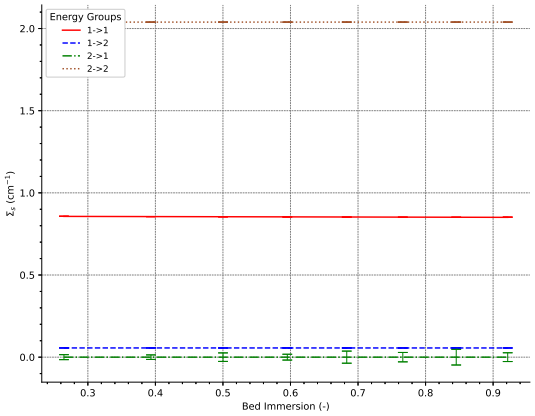

(c) Pooled water.

Figure 3.10: The macroscopic neutron scattering cross-sections for each region. The lines represent the values defined to model these cross-sections in the neutron diffusion code.

Table 3.14: Dry powder region thermal fission and absorption macroscopic neutron cross-section correlation coefficients.

Cross-Section (cm^{-1})	C_0	C_1	C_2
$\bar{\nu}\Sigma_f$	0.14448371	−0.09262251	0.10812776
Σ_a	0.07504803	−0.04757275	0.0554874
Σ_f	0.05929682	−0.03801429	0.0443752

The remaining data for the macroscopic neutron cross-sections have been considered independent of bed immersion, and are shown in Table 3.15.

Table 3.15: Region specific two-group macroscopic neutron cross-sections. Subscripts 1 and 2 correspond to fast and thermal groups respectively.

Region	Dry Powder		Wet Powder		Pore Water	
g	1	2	1	2	1	2
$\bar{\nu}\Sigma_{f,g}$	0.00343	see eqn 3.92	0.00490	0.18813	0.00000	0.00000
$\Sigma_{a,g}$	0.00363	see eqn 3.92	0.00835	0.11183	0.00049	0.01890
$\Sigma_{f,g}$	0.00132	see eqn 3.92	0.00193	0.07717	0.00000	0.00000
$\Sigma_{s,1->g}$	0.05598	0.00003	0.74489	0.03248	0.85863	0.05621
$\Sigma_{s,2->g}$	0.00018	0.06079	0.00032	1.72766	0.00007	2.03920
$\Sigma_{tr,g}$	0.04073	0.12236	0.22794	1.05325	0.22295	1.17310

All neutrons born through fission are assumed to be fast neutrons, i.e. $\chi_p(E_{fast}) = 1$ and $\chi_p(E_{therm}) = 0$.

Correlation Example Results

The macroscopic neutron cross-section correlations may now be used within the two-group, three region neutron diffusion code to evaluate the scalar neutron flux distribution and the effective multiplication factor (k_{eff}). To verify the neutron diffusion code and correlations, the results have been compared to values calculated using Serpent. In the case of the effective multiplication factor (k_{eff}) results from MCNP were also used. Figure 3.11 highlights how the effective multiplication factor (k_{eff}) varies as a function of bed immersion fraction. As expected, MCNP and Serpent predict similar effective multiplication factors. The neutron diffusion approach under-predicts the effective multiplication factor. Differences between the Monte Carlo neutron transport codes and the diffusion code are expected for several reasons. The diffusion approximation is not well suited to evaluate the scalar neutron flux at interfaces well. Given that there are three interfaces present within the model, this may be the main source of error. Furthermore, the diffusion model implemented reduces the continuous energy group structure in the Monte Carlo code to a two-group approximation. Using a coarsely discretised energy group structure will inherently introduce some error when compared to the continuous energy approach implemented by Serpent and MCNP.

Discrepancies in the effective multiplication factor, k_{eff}, between the neutron diffusion code and Monte Carlo codes will not affect the nuclear criticality transient as this data is not directly used by the proposed model. Instead, the reactivity components described in the previous sections by the derived correlations are used to determine the total reactivity of the system at a given time, t. This approach eliminates computational complexity by having simple polynomial approximations of the reactivity

rather than having to solve the time-dependent neutron diffusion equation at every time step. Solving the neutron diffusion equation solely for the axial scalar neutron flux distribution enables the use of a quasi-static approach for the neutron diffusion equation, which has much less computational requirements than the time-dependent neutron diffusion equation. Furthermore, employing the time-dependent neutron diffusion equation to model the system's reactivity would require correlations for the macroscopic nuclear cross-sections as functions of both voidage and temperature. This would produce a single reactivity value, making it hard to evaluate individual effects of each reactivity component, whereas the point kinetics approach can directly model the effects of each reactivity component on the fission power of the system.

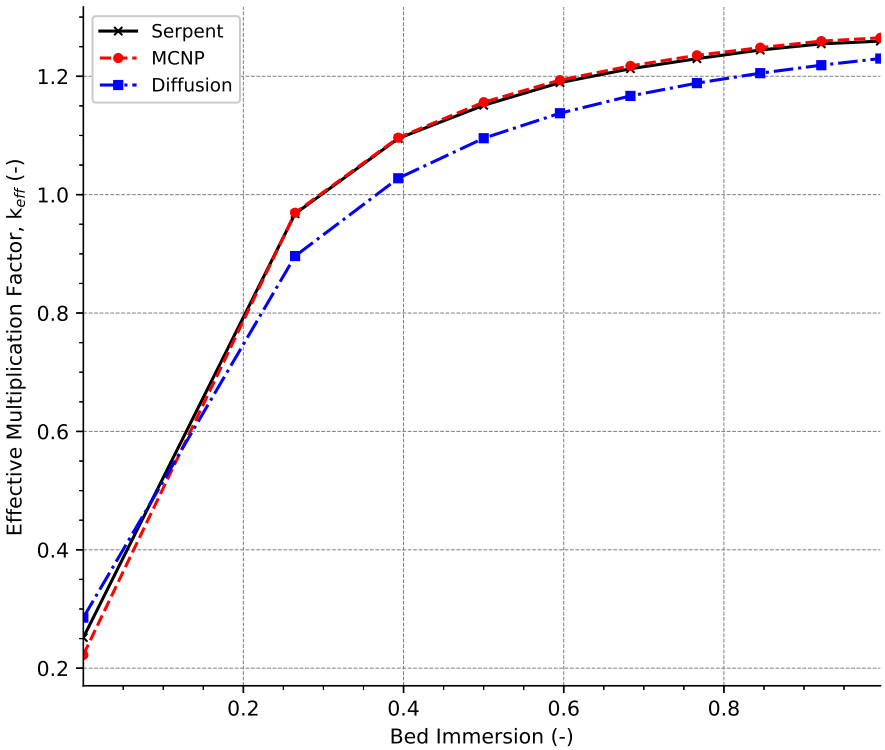

Figure 3.11: The effective multiplication factor (k_{eff}) as a function of bed immersion calculated with the three codes used throughout this study. The two transport codes produce very similar results, whereas the neutron diffusion code differs.

The normalised scalar neutron flux distribution calculated using Serpent and the neutron diffusion model are shown in Figure 3.12. The peak of the flux distribution can always be seen in the wet powder region. As the bed becomes more saturated, the peak moves down the drum and spreads out. The dry powder region appears to show a non-linear increase in neutron flux from the base to the interface with the wet powder region. A secondary bump can be seen in the pooled water region due to the effect of thermal neutrons in the neutron diffusion model. Good agreement between the scalar neutron flux profiles for the two models indicate that the correlations used for the macroscopic neutron cross-sections are appropriate.

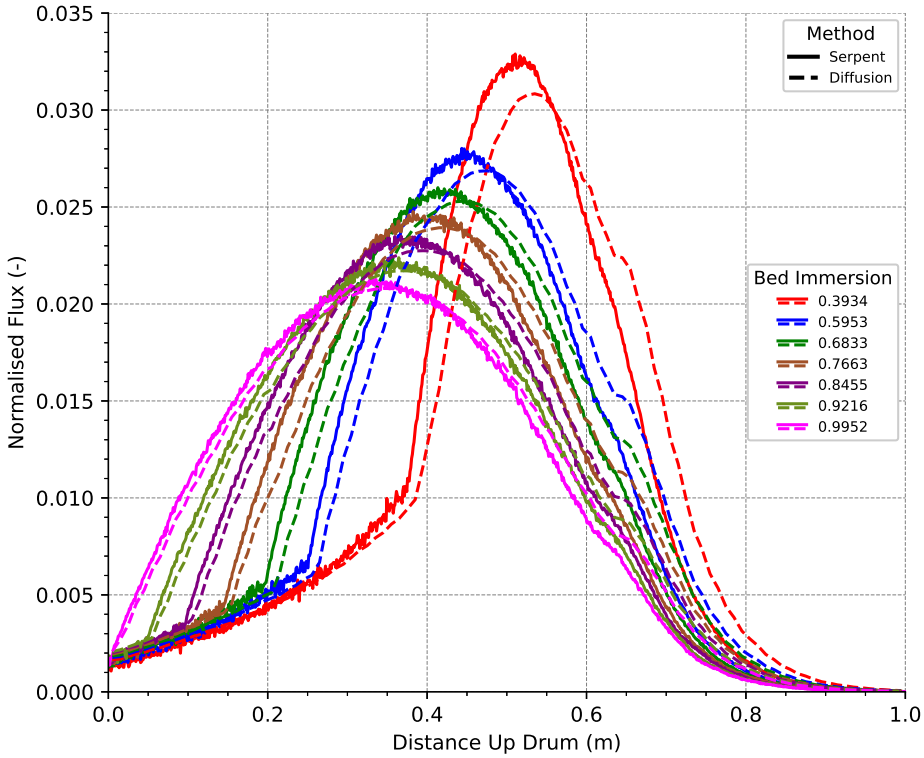

Figure 3.12: The normalised flux distribution computed at various bed immersion fractions using the Serpent Monte Carlo code and the developed deterministic neutron diffusion code.

For the case studies considered, the neutron flux distribution was re-calculated every 0.5 \$ of wetting-induced reactivity insertion.

3.5 Initial Conditions and Input Parameters

3.5.1 Summary of Initial Conditions

The sub-critical system is assumed to be in thermodynamic equilibrium at a temperature of 293.15 K. The reference temperature used to evaluate the thermal reactivity feedback is therefore set at 293.15 K. No gas is present in the system at the start of the simulation. The initial neutron and delayed neutron precursor densities are calculated from Equations (3.7) and (3.8) using an initial reactivity of, $R_{\mathrm{t}} = -0.179$ \$, initial source density of $s_{\mathrm{n}} = 0.135$ neutrons s^{-1} ($\mathrm{cm}^{-3} \cdot \mathrm{UO_2}$) and delayed neutron data and generation time described in Section 3.4.7. The initial reactivity, $R_{\mathrm{t}} = -0.179$ \$, has been found using the near-critical geometry of the powder bed, outlined in Section 3.4.8. These calculated initial conditions are specified alongside the other prescribed conditions in Tables 3.16 and 3.17.

Table 3.16: Group-wise initial delayed neutron precursor populations.

Group, i	1	2	3	4	5	6
C_{i} (precursors)	88127.85	185844.75	47488.58	42922.37	6849.32	913.24

Table 3.17: Initial conditions for sub-critical partially wetted UO_2 powder bed.

Property	Symbol	Value	Discussed
Dry powder height	H_{dp}	0.4414 m	Section 3.4.8
Wet powder height	H_{wp}	0.1803 m	Section 3.4.8
Water height	H_{sus}	0.3783 m	Section 3.4.8
Neutron population	N	251.14 neutrons	Section 3.2.1
Intrinsic source	s_n	0.135 neutrons s^{-1} ($cm^{-3} \cdot UO_2$)	Section 3.2.1
Initial dry powder region saturation	$S_{w,0}$	0	-
Reference temperature	T_0	293.15 K	-
All-region and component water temperature	T_w	293.15 K	-
All-region and component void fraction	$v_{f,g}$	0	-

3.5.2 Summary of Inputs Parameters

A summary of the input parameters for simulating the nuclear criticality in the wetted UO_2 powder bed are shown in Table 3.18.

Table 3.18: Summary of input parameters for sub-critical partially wetted UO_2 powder.

Property	Symbol	Value	Discussed
UO_2 specific heat capacity	c_p	274 J kg^{-1} K^{-1}	Section 3.4.3
Vapour specific heat capacity	c_v	2.060×10^3 J kg^{-1} K^{-1}	Section 3.4.3
Water specific heat capacity	c_w	4.2×10^3 J kg^{-1} K^{-1}	Section 3.4.3
UO_2 mean powder particle size	$d_{p,1}$, $d_{p,2}$	10 μm, 100 μm	Section 3.4.2
Pooled water turbulent mixing coefficient	D_{sus}	10^{-3} m^2 s^{-1}	Section 3.4.4
Pore water turbulent mixing coefficient	D_{wp}	10^{-4} m^2 s^{-1}	Section 3.4.4
Radiolytic gas generation coefficient	$G_v(H_2)$	5.36777×10^{-9} m^3 J^{-1}	Section 3.4.5
Drum height	H_{cyl}	1.0 m	Section 3.4.1
Latent heat of vaporisation	$h_{l,v}$	2.2512×10^6 J kg^{-1}	Section 3.4.3
Surface water flow rate	$U_{w,in}$	9.947×10^{-4} m s^{-1}	Section 3.4.1
Drum radius	R_{cyl}	0.4 m	Section 3.4.1
UO_2 fission fragment range	R_{fiss}	7 μm	Section 3.4.6
Water boiling point	T_{sat}	373.15 K	Section 3.4.3
Water input temperature	T_{in}	293.15 K	Section 3.4.1
UO_2 powder enrichment	γ	5 %	Section 3.4.1
UO_2 powder porosity	ϵ	0.8540	Section 3.4.1
Water thermal expansion coefficient	η	2.14×10^{-4} K^{-1}	Section 3.4.3
UO_2 thermal conductivity	κ_p	Equation (3.81)	Section 3.4.3
Vapour thermal conductivity	κ_v	2.46×10^{-2} W m^{-1} K^{-1}	Section 3.4.3
Solid UO_2 powder particle density	$\rho_{p,th}$	10.95×10^3 kg m^{-3}	Section 3.4.1
Vapour dynamic viscosity	μ_v	1.271×10^{-5} Pa s	Section 3.4.3
Water dynamic viscosity	μ_w	see Equation (3.82)	Section 3.4.3
Vapour density	$\rho_{v,th}$	5.863×10^{-1} kg m^{-3}	Section 3.4.3
Water density	$\rho_{w,th}$	998.1 kg m^{-3}	Section 3.4.3

3.6 Results

3.6.1 Large Particle Size

Results are displayed as functions of time from the start of the simulation as opposed to the start of water infiltration. For the 100 μm mean powder particle size considered here, criticality occurs approximately 150 seconds after water infiltration begins. The simulation has begun at a point just before criticality, this is reflected in the results by stating $t = T - 150$ seconds where t and T represent the time since wetting began and the time since the simulation began respectively. Data is shown logarithmically in time due to the short timescales over which the nuclear criticality transient occurs for the 100 μm mean powder particle size case. This is contrary to the 10 μm powder size case which is not shown logarithmically due to the fission power fluctuations occurring on the order of tens of seconds (see Figure 3.17a).

The variation in the fission power and total fission energy generated 300 s after the initial nuclear criticality excursion is shown in Figure 3.13a. The initial super-criticality causes the fission power to reach a magnitude of 2.7169×10^8 W (271.69 MW). The system briefly reaches prompt super-critical, with the total reactivity going above unity at approximately $t = 0.3$ s after the first wetting induced criticality is reached. Figures 3.13b and 3.15a show that the initial fission power spike leads to the production of radiolytic gas which subsequently causes the system to go sub-critical and then plateau. The plateau in system reactivity and fission power is predicted until boiling occurs as the wetting-induced reactivity matches the reactivity due to the presence of radiolytic gas voids. The reactivity effect of temperature at such high positive reactivity insertions has been shown to not affect the system reactivity as much as voidage in the wet powder. The same may be predicted for voids in the pooled water which do not develop a large negative reactivity feedback, even at high voidage.

Figure 3.13b shows that the infiltration of water adds approximately 15 \$ over 5 seconds of time since the initial criticality. Over this time-frame the majority of fissions occur, producing 3.1×10^7 J (31 MJ) out of the total 9.79×10^7 J (97.98 MJ) of fission energy over the duration of the simulation. Figure 3.13a also shows that the nuclear criticality transient does not terminate once the simulation ends at $t = 300$ s. Instead, the system reaches a new equilibrium at a fission power of 1.8×10^5 W (180 kW). For a direct comparison of the energy released by systems of different particle sizes, the smaller particle size simulation was also limited to 300 s.

The high rate of reactivity insertion causes a sharp increase in the UO_2 powder and pore water temperature, this can be seen in Figure 3.16a. The increase in temperature leads to boiling in the water filled interstices between powder particles at approximately 2.6 s after the wetting-induced criticality is first reached (see Figure 3.15a). Due to the large surface area between the powder and water, large volumes of steam were created over a short timescale. This resulted in lower interaction cross-sections in the regions with high voidage, causing the system to go deeply sub-critical. Due to the presence of delayed neutron precursors, boiling did not cause the fission power of the system to decrease below 2.5×10^5 W (250 kW).

The region heights and species' mass, shown in Figure 3.14, indicate that at the onset of boiling

there is a decrease in the mass of water in the system. This is predominantly due to the overflowing of the containment vessel as large volumes of gas are generated in the wet powder region. Over longer timescales the water varies a small amount due to a balance between the incoming water from the sprinkler system and the vaporisation of water on the particle surface as well as radiolysis.

As gas passes into the pooled water region and out of the system, the void reactivity feedback decreases, leading to an increased total system reactivity. The spatial variation in the void fraction at $t = 300$ s is shown in Figure 3.15.

The axial temperature distribution for the saturated UO_2 powder is shown in Figure 3.16b. The temperature of the powder bed tends to decrease further up the drum. Pooled water remained under the boiling point for the duration of the simulation. As predicted, the local powder and water temperatures in the wet powder region were almost the same, as a result of the high interfacial area between the phases.

3.6.2 Small Particle Size

When $d_p = 10$ μm, criticality occurred approximately 410 seconds after infiltration began. The simulation was started at a point just before criticality, this is reflected in the results by stating $t = T - 410$ seconds. The presence of gas within the system impeded the progression of the wetting front.

The variation in various reactivity components is shown in Figure 3.17b. The rate of increase in the wetting-induced reactivity is less for the 10 μm than the 100 μm case. Figure 3.17a shows that the initial criticality excursion causes the fission power to spike at 3.1×10^6 W (3.1 MW). The subsequent steady power rise increases the power to 3.6×10^6 W (3.5 MW) before boiling occurs. Subsequent fission power oscillations that occur after the onset of boiling do not exceed the initial fission power spike. The total energy released over the 300 s of simulated time is 6.5×10^7 J (65 MJ).

The system reaches prompt critical at a later time than for the larger particle size (approximately $t = 12$ s) because of the lower rate of water infiltration caused by a lower powder bed permeability. During the initial delayed super-critical stage of the transient, the concentration of delayed neutron precursors begins to build and the fission power rises at a lower rate than in the prompt super-critical stage. Once the system reaches prompt super-critical the fission power is limited by the production of radiolytic gas and to a lesser extent, Doppler broadening. A plateau can be seen with steadily increasing fission power until boiling occurs.

Figure 3.19 shows a sharp increase in the volume of radiolytic gas in the pores around the powder particles at the time of prompt super-criticality. This gas advects into the pooled water region and eventually leaves the system. Figures 3.18a and 3.18b show that the production of radiolytic gas pushes water out of the top of the container. Significant volumes of radiolytic gas cease to be produced when boiling occurs due to the large volumes of steam that take up space between the powder particles.

A significant reduction in the fission power is predicted at $t = 28$ s as steam generated in the wetted powder adds approximately 7 \$ of negative reactivity into the system. After this time, the power decreases to an order of magnitude of 10^5 W. Advection of the steam from the domain (see Figure 3.19) causes the system reactivity to slowly approach critical again. A cyclical fission power

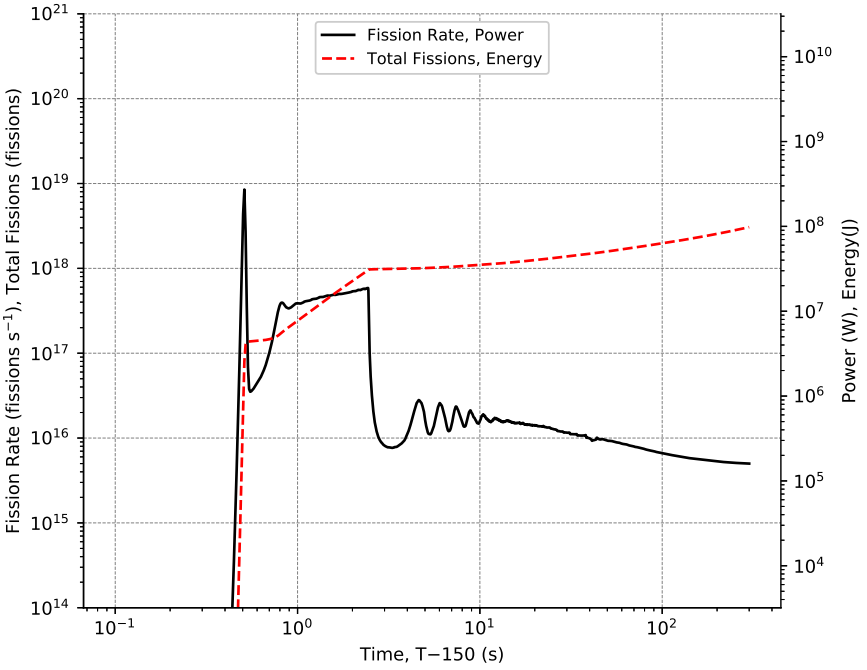

(a)

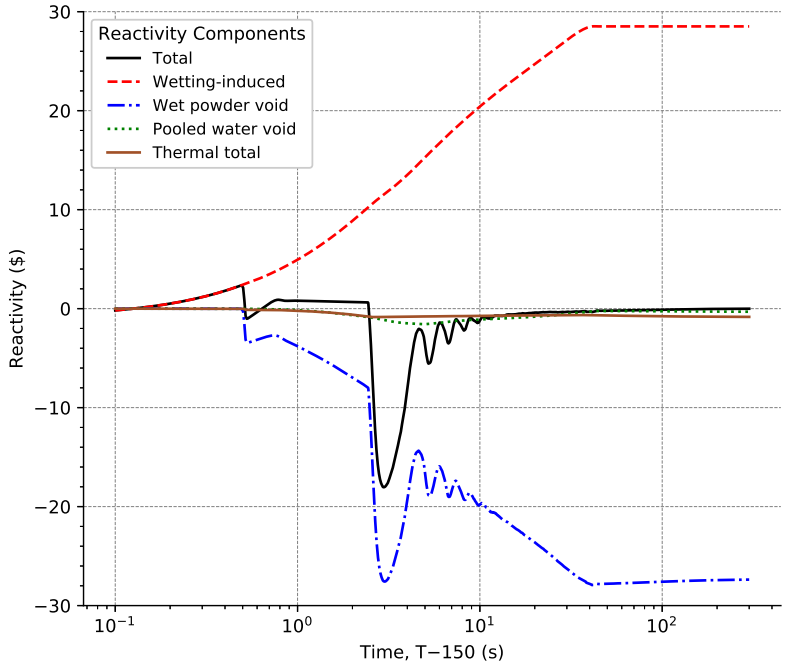

(b)

Figure 3.13: (a) The variation in fission power and fission energy over time. (b) Variation of each reactivity component as well as total system reactivity. Both for the case where $d_{\mathrm{p}} = 100$ μm.

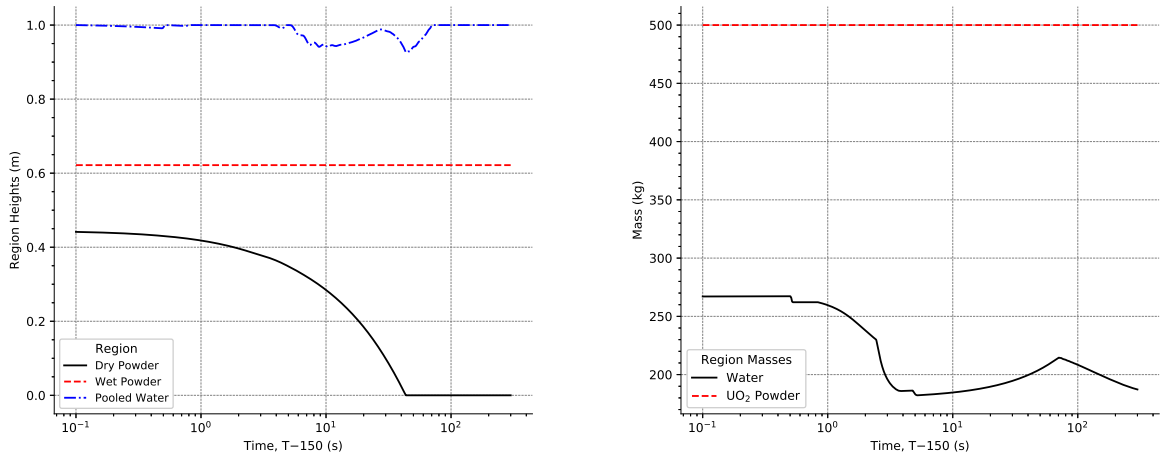

(a) (b)

Figure 3.14: (a) The variation in region height shows the infiltration of water into the domain. (b) Variation in the total UO_2 powder and water mass over time. Both for the case where $d_p = 100$ μm.

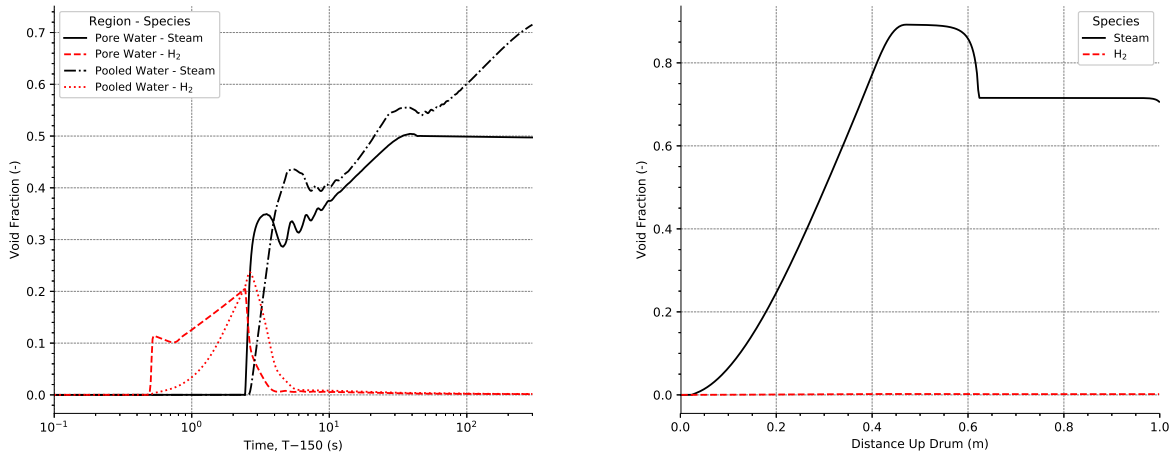

(a) (b)

Figure 3.15: Voidage data for the case where $d_p = 100$ μm. (a) The variation in void fraction over time. (b) The spatial variation in void fraction throughout the domain at $t = 300$ s.

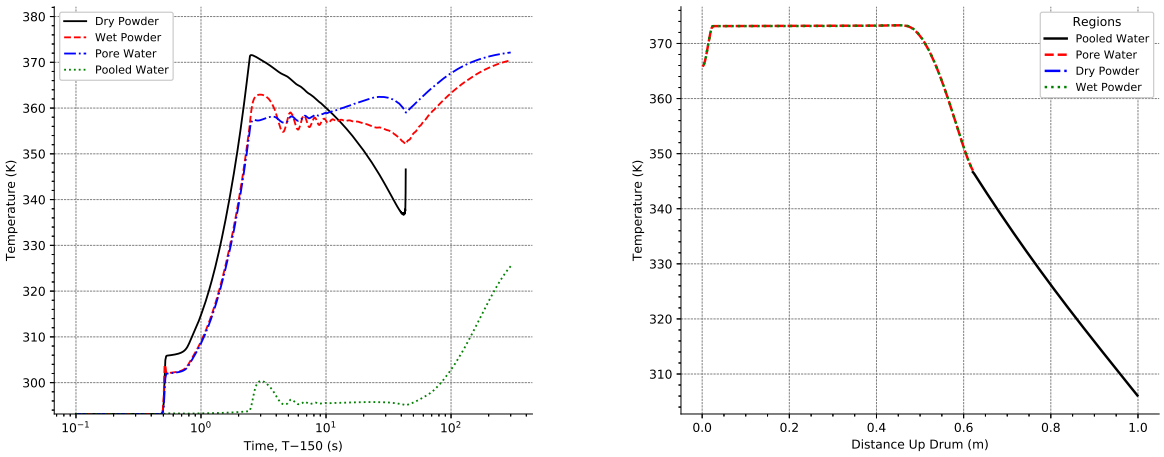

(a) (b)

Figure 3.16: Temperature data for the case where $d_p = 100$ μm. (a) The variation in region and species temperatures over time. (b) The spatial variation in temperature throughout the domain at $t = 300$ s.

response with small amplitude is predicted as water hits highly superheated dry powder at the wetting front. This causes violent boiling, adding negative reactivity, preventing further boiling until the gas advects from the region around the wetting front and the process repeats.

The steep gradient between the dry and wet powder shown in Figure 3.20b may be attributed to a number of reasons. A combination of efficient convection between the wet powder and pore water, as well as the high heat capacity of the pore water, means that significantly more energy is required to raise the wet powder temperature than the dry powder. Also, the production of steam adds a cooling effect in the wet powder region, this is not present in the dry powder. The result is a dry powder region that heats up quickly when compared to the wetted powder. The low thermal conductivity of UO_2 combined with the high porosity prevents a significant exchange of thermal energy between the dry and wet powder.

3.6.3 Sensitivity of Turbulent Mixing Coefficient and Intrinsic Neutron Source

The turbulent mixing coefficient is a complex parameter to correctly determine due to the chaotic nature of turbulent flows caused by the generation and advection of gas bubbles in the pore and pooled water. By altering the turbulent mixing coefficient for each region by an order of magnitude, the effect that this parameter has on the initial fission power spike, total energy released and time to boiling may be evaluated. Table 3.19 shows that over the 300 s of simulated time, the primary fission power spike that occurs after the initial criticality excursion has a strong dependence on powder particle size and not the turbulent mixing coefficient. Similarly, the time to boiling did not vary widely by changing the turbulent mixing coefficient by an order of magnitude in each region. Small variations in the fission energy released 300 s after the initial criticality excursion are predicted as the turbulent mixing coefficient varies. The particle size is predicted to strongly affect the fission energy released over the first 300 s of the nuclear criticality excursion. Decreasing the turbulent mixing coefficient in the wet powder region prevented energy and voids from diffusing through the system.

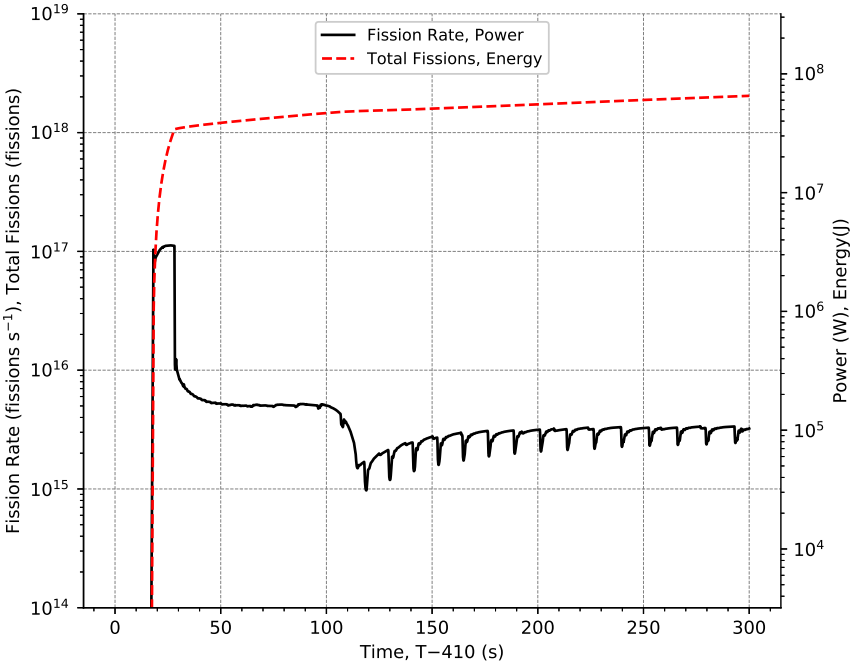

(a)

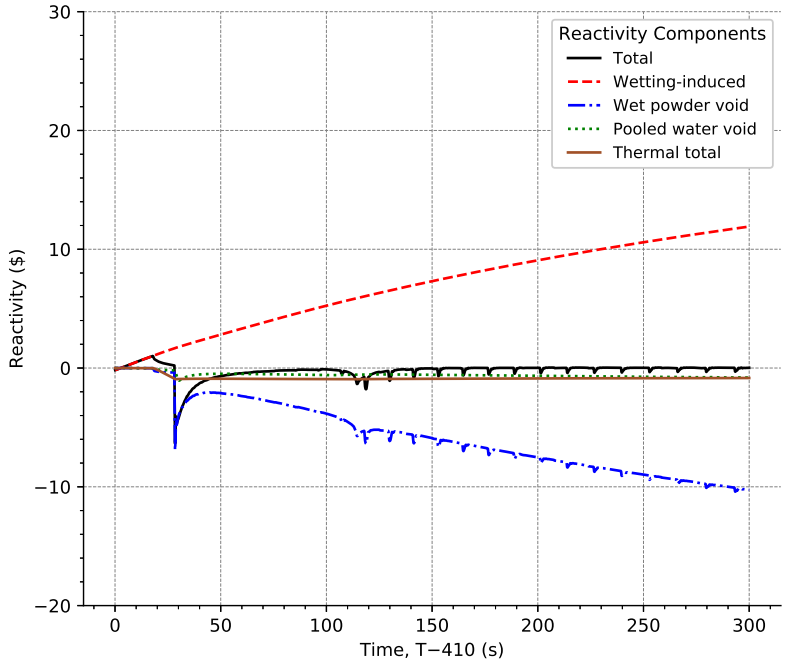

(b)

Figure 3.17: (a) The variation in fission power and fission energy over time. (b) Variation of each reactivity component as well as total system reactivity. Both for the case where $d_{\mathrm{p}} = 10$ μm.

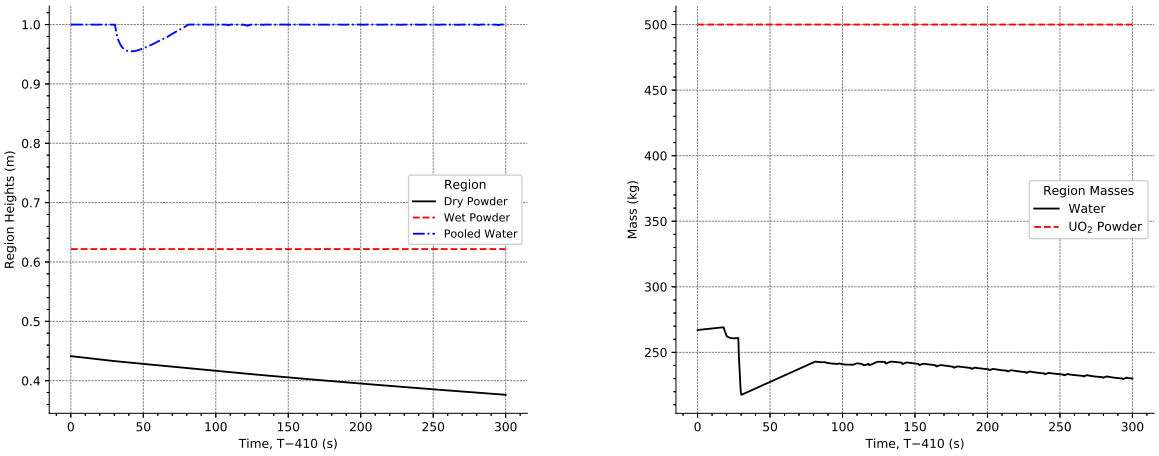

(a) (b)

Figure 3.18: (a) The variation in region height shows the infiltration of water into the domain. (b) Variation in the total UO_2 powder and water mass over time. Both for the case where $d_p = 10$ μm.

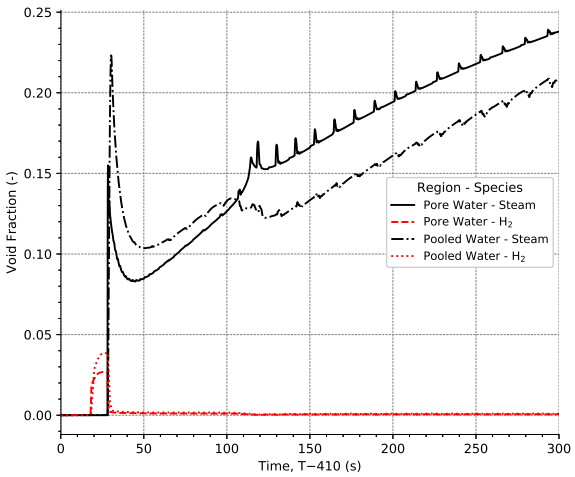

Figure 3.19: The region and species specific void fraction for the case where $d_p = 10$ μm.

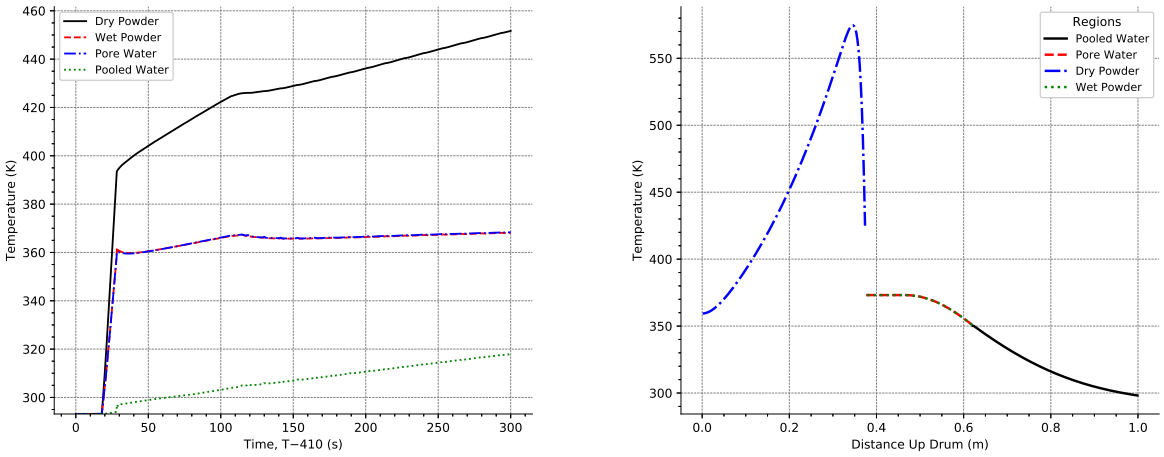

(a) (b)

Figure 3.20: Temperature data for the case where $d_p = 10$ μm. (a) The variation in region and species temperatures over time. (b) The spatial variation in temperature throughout the domain at $t = 300$ s.

For the small powder size case this suppressed the subsequent fission power spikes. The effect on the energy released for the larger powder size was less pronounced. Fission energy release for the 100 μm powder particles were similar in magnitude regardless of the turbulent mixing coefficient.

Table 3.19: Sensitivity of initial peak fission power, energy and boiling time to mean powder particle size and turbulent mixing coefficients.

Case	d_p (μm)	$D_{t,wp}$ (m^2 s^{-1})	$D_{t,pooled}$ (m^2 s^{-1})	Primary fission power Spike (MW)	Fission Energy (MJ)	Time to Boiling (s)
1	10	10^{-4}	10^{-3}	3.60	65.30	28.12
2	100	10^{-4}	10^{-3}	271.69	97.98	2.46
3	10	10^{-5}	10^{-3}	3.59	65.09	28.13
4	100	10^{-5}	10^{-3}	271.66	97.94	2.46
5	10	10^{-4}	10^{-4}	3.60	65.28	28.12
6	100	10^{-4}	10^{-4}	271.69	97.98	2.46
7	10	10^{-3}	10^{-3}	3.56	65.14	28.22
8	100	10^{-3}	10^{-3}	272.06	97.99	2.47
9	10	10^{-4}	10^{-2}	3.60	65.28	28.12
10	100	10^{-4}	10^{-2}	271.69	97.98	2.46

The intrinsic neutron source was varied by 50 % above and below the nominal value of $s_n = 0.135$ neutrons s^{-1} ($cm^{-3} \cdot UO_2$) and the effect on the initial peak fission power and energy released 300 s after the initial nuclear criticality excursion for the case where $d_p = 100$ μm was studied. Corresponding new neutron density and delayed neutron precursor initial conditions were calculated. Results shown in Figure 3.21 indicate that there is a small dependence on the initial peak fission power due to the intrinsic neutron source density. This amounts to initial peak fission power variations no greater than 2.85 %. A larger intrinsic source density led to a decreased peak fission power because reactivity feedback's were able to be greater in magnitude before the prompt super-critical state was reached.

The total energy released from fission 300 s after the initial nuclear criticality excursion did not differ by more than 0.005 % relative to the energy produced from fission for the nominal neutron source density case. This is expected since the energy produced from fission of neutrons from intrinsic sources is very low compared to the energy produced from neutrons born through fission during the transient.

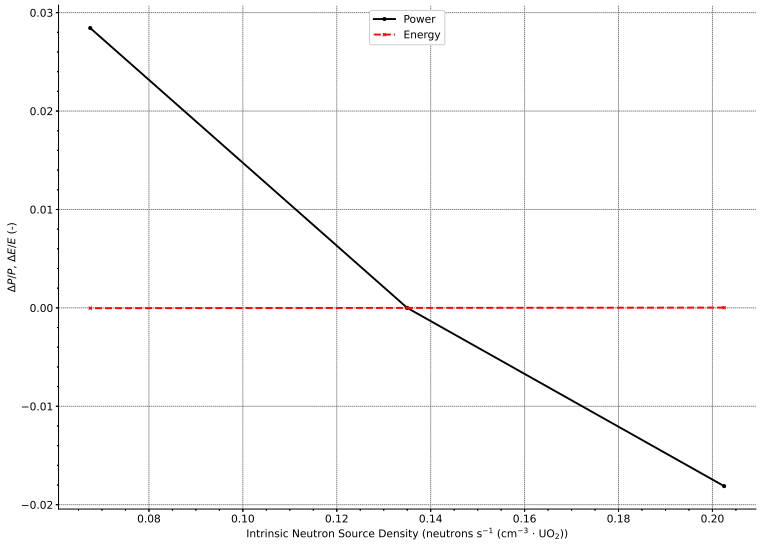

Figure 3.21: The relative variation of fission power and energy as a function of the intrinsic neutron source density.

3.7 Conclusions

This chapter proposed a novel model coupling point nuclear reactor kinetics with phenomenologically based models of powder bed wetting and nuclear thermal hydraulics, including models for the generation and advection of steam and radiolytic gas, for the analysis of nuclear criticality excursions in fissile powder bed systems under wetting conditions. The point nuclear reactor kinetics model used non-linear multi-dimensional reactivity components that are dependent on the powder bed immersion fraction, temperature and system voidage. These types of systems can be found in nuclear fuel production and fabrication facilities around the world. Understanding potential nuclear criticality excursions, under processing and storage conditions, is an important aspect of nuclear criticality safety assessment. Using this model, the initial fission power spike and fission yield, over the 300 s of simulated time, could be quantified.

A comparative study found good agreement between the proposed Green and Ampt infiltration model and experimental data by Rozain et al. (1991), for UO_2 mean powder particle sizes observed in the literature.

The first fission power spike was predominantly limited by the production of radiolytic gas. Due to the presence of water in the system, which has a high specific heat capacity, the powder temperature could not increase enough to counter the significant positive reactivity insertion due to water infiltration. As a result, the system remained in a delayed super-critical state until enough energy had been deposited in the powder-water mixture for boiling to occur and for steam to be produced. The decreased rate of wetting due to the variation in the powder bed size caused the geometry of the system to change less rapidly around the point of criticality. This may be the reason for the varying neutron kinetic response predicted by the simulations of the powder beds.

For both powder beds considered, boiling caused the system to become significantly sub-critical due to the negative void reactivity effect caused by the presence of large volumes of steam in the pore interstices. The larger mean powder particle sized bed reached a new delayed critical state at a lower fission rate. Although powder motion has not been modelled, the large volumes of gas generated over these short timescales are likely to provide enough force to overcome the weight of gravity of the powder, resulting in powder motion. This corresponds well with the study performed by Rozain et al. (1991) who also noted that the production of gas was likely to result in significant motion of the powder bed.

The fission power response and peak fission power was found to vary depending on the powder particle size. A maximum fission power of 272 MW was predicted for the larger powder particles compared to 3.60 MW for the smaller sized powder particles, indicating that the initial release of neutrons is far greater for the UO_2 powder bed consisting of larger particles. The fission energy released during the first 300 s of the transient nuclear criticality excursion was predicted to be a strong function of the mean powder particle size at 65 MJ and 98 MJ for the small and larger powder particle sized cases, respectively. In the absence of experimental data, one may note that the total yield was similar in order of magnitude to previous simulations of powder bed systems by Rozain et al. (1991) and Basoglu et al. (1994).

Although the peak fission power and time to boiling was found to be almost independent of the range of turbulent mixing coefficient, they depended strongly on the mean powder particle size used. Similarly, the fission energy released over the duration of the simulation was a strong function of mean powder particle size and to a lesser extent, the turbulent mixing coefficient. The energy was found to be independent of the intrinsic neutron source density used in the investigation. A weak dependence was predicted for the initial peak fission power reached after the initial nuclear criticality excursion and the intrinsic neutron source density.

Chapter 4

Nuclear Criticality Excursion Models for Slumping of Wetted UO_2 Powder Beds

4.1 Introduction

The majority of work presented in this chapter is reproduced from Jones et al. (2022a).

This chapter extends the models of the previous chapter to include wetting-induced volumetric collapse of the UO_2 powder bed. In high porosity meta-stable fissile powder beds, wetting-induced volumetric collapse may lead to a significant re-distribution of fissile material and moderator in the powder bed. The re-distribution of fissile mass may affect the initiation and characteristics of a wetting-induced transient nuclear criticality excursion in a UO_2 powder bed. Here, numerous cases are examined that investigate how differing degrees of wetting-induced volumetric collapse of a UO_2 powder bed may affect a transient nuclear criticality excursion.

4.2 Extensions to Model

4.2.1 Powder Bed Volumetric Collapse

Slumping occurs when there is an alteration to the pore-scale forces acting on the fissile powder bed. Susceptible powder beds are those that form meta-stable, low bulk density configurations. A comprehensive review of the different slumping mechanisms may be found in Al-Rawas (2000). Fredlund and Morgenstern (1976) introduced a framework for modelling volumetric slumping through the use of constitutive relations based upon the linearity of the stress-strain relationship for a powder bed. In this model, local variations in porosity are not considered. This approach has successfully been used by Pereira and Fredlund (2000), Li et al. (2016) and Houston et al. (1993) investigating slumping in porous media systems. Tadepalli and Fredlund (1991) showed that this solid mechanics model of porous bed slumping could be validated by experimental data. Rao and Revanasiddappa

(2000) successfully used this methodology on porous media with wide range of mean particle sizes. This framework has also been applied by Cho and Lee (2001) and Sun et al. (2016) who simulated wetting-induced slumping of three-phase porous media.

In a fissile powder bed, two components of stress comprise this volumetric stress-strain relationship. The first arises as water percolates through the powder bed, where a balance of cohesive and adhesive forces between the water and powder particles alters the effective stress on powder particles (Bresson and Moran, 2004). This may lead to local shear failure between the powder grains, causing the powder bed to slump, forming a more dense configuration (Tadepalli et al., 1992). Swelling may also occur, whereby the fissile powder bed expands upon water infiltration (Fredlund and Morgenstern, 1976). The second component of stress occurs due to variations in axial pressure on the fissile powder bed from direct contact forces on the powder particles. Together, these factors form a stress-strain state surface, which can be seen in Figure 4.1. Here, a path from one state point to another identifies the volumetric changes experienced by the powder bed as a result of pressure variations. Typically, these state surface compression/expansion paths exhibit hysteresis, which is not considered in the present study (Fredlund et al., 2012). This work is concentrated solely on the wetting-induced component of slumping and how this affects a wetting-induced transient nuclear criticality excursion within a UO_2 powder bed.

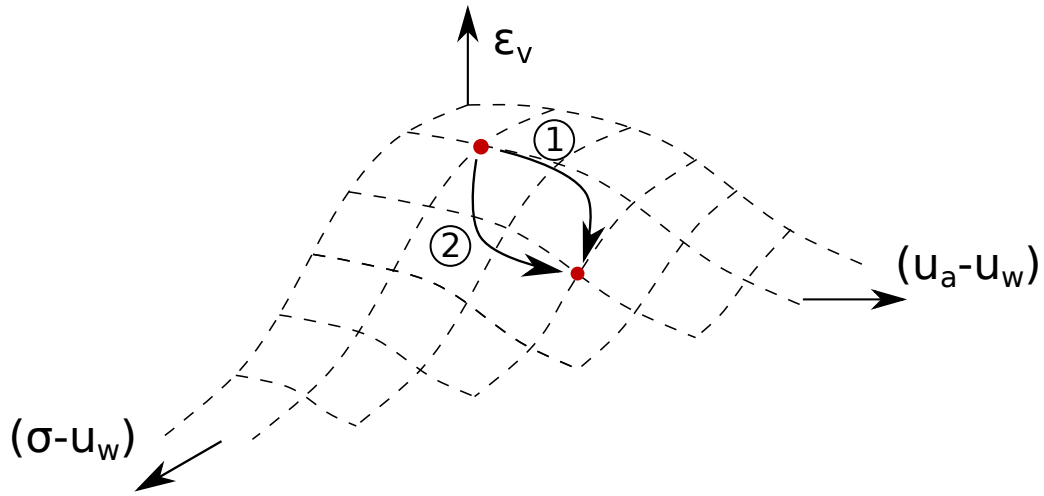

Figure 4.1: A state surface for a given porous media collapse phenomenon indicating the initial and final states connected by lines 1 and 2 indicating various ways in which slumping may occur (reproduction from Fredlund et al. (2012)).

The matric suction, ψ [Pa], may be defined as the difference between the pore-air, u_a [Pa] and pore-water, u_w [Pa] pressures:

$$\psi = u_\mathrm{a} - u_\mathrm{w} \tag{4.1}$$

The matric potential varies from its maximum value in the unsaturated region to zero in the saturated region (Brooks and Corey, 1964). Using the sharp wetting front model described in the previous chapter, it follows that the matric potential behaves as a step function at the wetting front, where the saturation changes from the minimum to maximum value. Slumping caused by changes

to the matric potential is therefore expected to occur as the dry fissile powder becomes wetted. The equation describing how alterations to the matric potential lead to volumetric strain in the wetted powder, denoted $\epsilon_{\mathrm{v}}(t)$ [-], may be given as (Fredlund and Morgenstern, 1976):

$$\epsilon_{\mathrm{v}}(t) = \frac{1}{\pi R^2 U_{\mathrm{w}}(t)} \frac{dV_{\mathrm{slump}}(t)}{dt} = m_2^{\mathrm{s}} \Delta\psi \tag{4.2}$$

where dV_{slump}/dt [m^3 s^{-1}] represents the rate of volumetric deformation of the wetted powder and m_2^{s} [Pa^{-1}] is an empirically determined compressibility modulus describing the gradient of the UO_2 powder bed effective stress-strain curve.

The fissile powder beds considered in this thesis are contained within cylindrical vessels which prevent radial expansion. This scheme, known as K_0 loading, yields the following relation for the compressibility modulus due to wetting (Fredlund et al., 2012):

$$m_2^{\mathrm{s}} = \frac{1 + \nu_{\mathrm{p}}}{E_{\psi}(1 - \nu_{\mathrm{p}})} \tag{4.3}$$

where E_{ψ} [Pa] is the modulus of elasticity for the powder bed with respect to changes in matric potential, and ν_{p} [-] is Poisson's ratio for the UO_2 powder bed.

For a step change in matric potential across the wetting front, Equation (4.2) may be written as:

$$U_{\mathrm{slump}}(t) = U_{\mathrm{w}}(t) m_2^{\mathrm{s}} \Delta\psi \tag{4.4}$$

where $U_{\mathrm{slump}}(t)$ [m s^{-1}] is the rate of collapse of the wet powder, pooled water interface.

Since the compressibility due to wetting, m_2^{s} and the change in matric potential across the wetting front, $\Delta\psi$ for a UO_2 powder bed is unknown, one may define a combined parameter which is varied to capture different levels of volumetric collapse. The slumping fraction, f_{slump} [-], due to wetting may then be defined as:

$$U_{\mathrm{slump}}(t) = U_{\mathrm{w}}(t) f_{\mathrm{slump}} \tag{4.5}$$

where $f_{\mathrm{slump}} = m_2^{\mathrm{s}} \Delta\psi$ is the term used to describe the fraction of volumetric collapse of the newly wetted powder over a differential time, dt.

4.2.2 Powder Particle Number Density in Slumping Porous Medium

In Chapter 3, the solid volume fraction, or packing, of the dry and wetted regions of the UO_2 powder bed were prescribed a constant value, reflecting the scenario where the powder bed remained static. In this chapter, however, volumetric collapse (slumping) on the wetted side of the sharp wetting front at the spatial location, $z = H_{\mathrm{dp}}$, results in a varying UO_2 powder solid volume fraction across the wetting front. The exchange of UO_2 powder between the dry and wetted region in a slumping powder

bed, due to wetting and volumetric collapse, may be expressed as:

$$(U_{\mathrm{w}}(t) - U_{\mathrm{slump}}(t))V'_{\mathrm{p,wp}} = U_{\mathrm{w}}(t)V'_{\mathrm{p,dp}} \tag{4.6}$$

Substituting Equation (4.5) into Equation (4.6) yields the wetted powder region linear volume density of UO_2 powder particles in terms of the dry powder solid volume fraction and the rate of powder bed collapse:

$$V'_{\mathrm{p,wp}} = \frac{V'_{\mathrm{p,dp}}}{1 - f_{\mathrm{slump}}} \tag{4.7}$$

4.2.3 Region Height Change

The previous expressions outlined in Section 3.2.9, representing the change in height of the wetted powder and pooled water/suspension regions, must be re-considered to account for the effects of volumetric collapse of the UO_2 powder bed. The change in height of the dry powder region as a function of time remains unchanged, since wetting-induced volumetric collapse does not affect the dry UO_2 powder bed structure. Therefore, the wet powder region and pooled water region height change as a function of time may be respectively defined as:

$$\frac{dH_{\mathrm{wp}}(t)}{dt} = U_{\mathrm{w}}(t) - U_{\mathrm{slump}}(t) \tag{4.8}$$

$$\frac{dH_{\mathrm{sus}}(t)}{dt} = U_{\mathrm{w,in}}(t) - (U_{\mathrm{w}}(t) - U_{\mathrm{slump}}(t))\,(1 - v_{\mathrm{f,p,wp}})\,\Delta S_{\mathrm{w}} + U_{\mathrm{adj,N}}(t) \tag{4.9}$$

4.2.4 Alterations to Mass Transfer Governing Equations and Nuclear Thermal Hydraulics

The governing equations for water, radiolytic gas and steam in this chapter remains identical to those stated in Equation (3.13). However, an additional advection term, $U_{\mathrm{slump}}(t)v_{\mathrm{f,p,wp}}$, must be specified in the pooled water region, that captures the effects the wetting-induced volumetric collapse of the UO_2 powder bed. The resulting region and component advective terms are prescribed in Table 4.1. No alterations are required for the sources/sinks in Equation (3.13).

Furthermore, the interface condition between the settled wet powder and pooled water regions must be altered to account for the moving interface corresponding to the downward collapse of the UO_2 powder as it transitions into a more dense configuration. The condition for water, steam and radiolytic gas continuity at $z = H_{\mathrm{dp+wp}}$ is given as:

Table 4.1: Net advective mass transfer for each component in each region with advective term in continuity equation.

Region, k	Component, j	$U_{\mathrm{net,j,k}}(t,z)$ [m s^{-1}]
Settled wet powder	Water	$-U_{\mathrm{w}}(t)+U_{\mathrm{adj}}(t,z)$
Settled wet powder	Radiolytic gas	$-U_{\mathrm{w}}(t)+U_{\mathrm{g}}(t,z)+U_{\mathrm{adj}}(t,z)$
Settled wet powder	Steam	$-U_{\mathrm{w}}(t)+U_{\mathrm{g}}(t,z)+U_{\mathrm{adj}}(t,z)$
Pooled Water/Suspension	Water	$-U_{\mathrm{w}}(t)\,(1-v_{\mathrm{f,p,wp}})\,\Delta S_{\mathrm{w}}-U_{\mathrm{slump}}(t)v_{\mathrm{f,p,wp}}$ $+U_{\mathrm{adj}}(t,z)$
Pooled Water/Suspension	Radiolytic gas	$-U_{\mathrm{w}}(t)\,(1-v_{\mathrm{f,p,wp}})\,\Delta S_{\mathrm{w}}-U_{\mathrm{slump}}(t)v_{\mathrm{f,p,wp}}$ $+U_{\mathrm{g}}(t,z)+U_{\mathrm{adj}}(t,z)$
Pooled Water/Suspension	Steam	$-U_{\mathrm{w}}(t)\,(1-v_{\mathrm{f,p,wp}})\,\Delta S_{\mathrm{w}}-U_{\mathrm{slump}}(t)v_{\mathrm{f,p,wp}}$ $+U_{\mathrm{g}}(t,z)+U_{\mathrm{adj}}(t,z)$

$$D_{\mathrm{wp}}(t,H_{\mathrm{dp+wp}})\frac{\partial V'_{\mathrm{j,wp}}(t,H_{\mathrm{dp+wp}})}{\partial z}+U_{\mathrm{net,j,wp}}(t,H_{\mathrm{dp+wp}})V'_{\mathrm{j,wp}}(t,H_{\mathrm{dp+wp}})= D_{\mathrm{sus}}(t,H_{\mathrm{dp+wp}})\frac{\partial V'_{\mathrm{j,sus}}(t,H_{\mathrm{dp+wp}})}{\partial z}+U_{\mathrm{net,j,sus}}(t,H_{\mathrm{dp+wp}})V'_{\mathrm{j,sus}}(t,H_{\mathrm{dp+wp}}) \quad (4.10)$$

The following expression described the net flow out of the discretised mesh cell on the wetted powder side of the interface at $z=H_{\mathrm{dp+wp}}$:

$$Q_{\mathrm{i}}(t)=-A^2_{\mathrm{cyl}}U_{\mathrm{slump}}(1-v_{\mathrm{f,p,wp}}) \quad (4.11)$$

The corresponding expression for the net flow of flow components into the discretised mesh cell in the pooled water region, just above the interface at $z=H_{\mathrm{dp+wp}}$ is:

$$Q_{\mathrm{i}}(t)=A^2_{\mathrm{cyl}}U_{\mathrm{slump}} \quad (4.12)$$

Applying these two conditions in the regions either side of the interface enables the determination of $U_{\mathrm{net,j,wp}}(t,H_{\mathrm{dp+wp}})$ and $U_{\mathrm{net,j,sus}}(t,H_{\mathrm{dp+wp}})$ in Equation (4.10), ensuring that a moving interface condition is satisfied. All other boundary and interface conditions are identical to those prescribed in Chapter 3. Moreover, the governing equations and boundary/interface conditions for nuclear thermal hydraulics outlined in Section 3.2.7 and associated constitutive relations outlined in Section 3.2.7 may be used here to model the nuclear thermal hydraulics in a UO_2 powder bed with wetting-induced collapse, without alteration.

4.2.5 Pressure Drop Through Porous Bed

The water infiltration method outlined by Green and Ampt (1911), used to model water infiltration into porous media, assumes a laminar Darcian type flow, driven solely by hydrostatic head (Marsily, 1986). Other components of pressure that otherwise contribute to flow are not directly modelled. Furthermore, the flow is assumed to be incompressible, implying that continuous phase local pressure

variations introduced by phenomenon such as shocks are neglected. A simple relation for hydrostatic head in the present model employs a homogenisation approach for calculating effective densities of the water and gas phases present. Furthermore, the dispersed gas bubbles are assumed to be in a pressure equilibrium with the surrounding continuous phase liquid. The resulting gauge pressure, taking the top of the pooled water as reference point, may be determined using the following expression:

$$P_{\text{gauge}}(t,z) = \int_{z}^{H_{\text{dp+wp+sus}}} \left(\rho_{\text{w,th}} \frac{V'_{\text{w,k}}(t,z)}{V'_{\text{w,k}}(t,z) + V'_{\text{g,k}}(t,z)} + \rho_{\text{g,th}} \frac{V'_{\text{g,k}}(t,z)}{V'_{\text{w,k}}(t,z) + V'_{\text{g,k}}(t,z)} \right) g dz \tag{4.13}$$

also:

$$P_{\text{abs}}(t,z) = P_{\text{atm}} + P_{\text{gauge}}(t,z) \tag{4.14}$$

High pressure nucleating gas bubbles grow in the continuous liquid phase, exerting a surface force on the surrounding liquid, and thus displacing it. The amount of displacement that occurs depends primarily on the difference in pressure and dissolved concentration between the gas bubble and surrounding liquid (Lane et al., 1958). At present, the gas bubble size is modelled using the approach outlined by Zeitoun et al. (1994) and bubbles are assumed to nucleate instantaneously. Furthermore, the pressure inside gas bubbles are assumed to be in equilibrium with the surrounding continuous phase. This condition has been previously proposed by Yeoh and Tu (2019). In the case where large volumes of gas are produced rapidly, significant volumes of water and gas are forced upwards. Corresponding inter-phase pressure and force variations are accounted for by the turbulent mixing terms in the wet powder (D_{wp}) and pooled water regions (D_{sus}), respectively.

4.3 Properties of UO_2 Powder Bed Undergoing Volumetric Collapse

The physical system examined in this chapter is identical to the one studied in the previous chapter, with the exception of the data described in the following sections.

4.3.1 Steady-state Scalar Neutron Flux Spatial and Energy Distribution

Group condensed macroscopic neutron cross-sections were evaluated in each cell to consider the heterogeneity introduced into the system by having a spatially varying powder particle number density. This approach ensures that cells that contain no fissile material have zero macroscopic neutron fission cross-section. The functional dependence between the macroscopic neutron cross-sections and the porosity of an axial mesh cell was determined by performing a number of Serpent Monte Carlo neutron transport simulations (Leppänen et al., 2015). These simulations modelled a single spherical UO_2 powder particle contained within a cube of water, with the cube volume corresponding to a specific porosity, with reflective boundary conditions applied at the bounds of the cube. This models an infinite lattice of regularly spaced UO_2 powder particles. Figure 4.2 shows a series of Serpent mesh

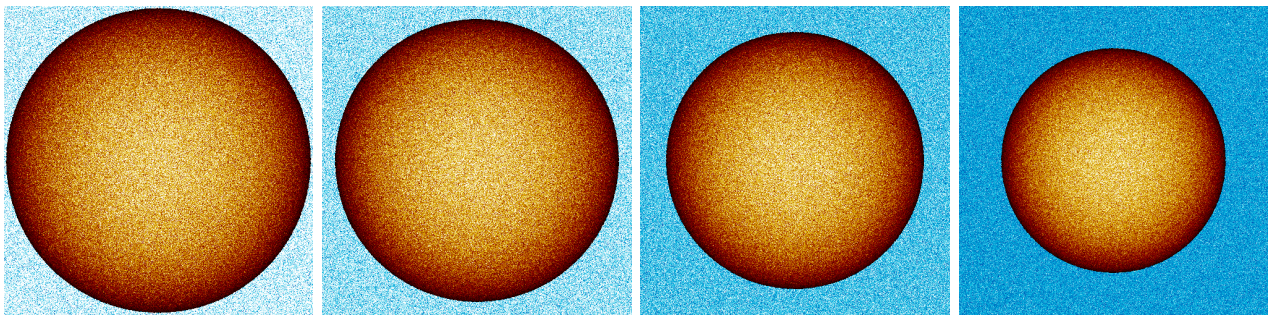

(a) $\epsilon_{\text{wp}} = 0.5$ (b) $\epsilon_{\text{wp}} = 0.6$ (c) $\epsilon_{\text{wp}} = 0.7$ (d) $\epsilon_{\text{wp}} = 0.8$

Figure 4.2: Serpent representation of single UO_2 powder particle surrounded by a volume of water prescribed to ensure a specified domain porosity. Reflective boundary conditions model an infinite number of powder particles at the specified bed porosity.

plots for a powder particle, sized $d_{\text{p}} = 30$ μm, surrounded by a volume of water calculated to ensure a prescribed porosity.

Two-group condensed macroscopic neutron cross-sections were calculated from the point-wise continuous energy Monte Carlo neutron transport code Serpent using the geometries presented in Figure 4.2 (Leppänen et al., 2015). The neutrons with energies below 0.625 eV were classified as thermal, whilst neutrons with energies above this threshold were classified as fast. Furthermore, all prompt neutrons born through fission are assumed to be fast such that $\chi_{\text{p}}(E_{\text{fast}}) = 1$ and $\chi_{\text{p}}(E_{\text{therm}}) = 0$.

The resulting two-group macroscopic neutron cross-sections are shown as a function of bed porosity in Figure 4.3. Small error bars indicate the low variance in the Serpent Monte Carlo neutron transport simulation results. A greater dependence on porosity can be seen for the thermal macroscopic neutron cross-sections than the fast macroscopic neutron cross-sections. Furthermore, within energy group macroscopic neutron scattering cross-sections are a stronger function of porosity than inter-group macroscopic neutron scattering cross-sections. Correlations of the general form described by Equation (4.15), with coefficients listed in Table 4.2, provide an accurate representation of how these macroscopic neutron cross-sections vary as a function of powder bed porosity. The best-fit lines in Figure 4.3 generated using these correlated macroscopic neutron cross-sections supports this.

$$\Sigma_{\text{i,g}} = C_0 + C_1(1 - v_{\text{f,p,wp}}(t)) + C_2(1 - v_{\text{f,p,wp}}(t))^2 \tag{4.15}$$

where i in $\Sigma_{\text{i,g}}$ [cm^{-1}] describes a specific macroscopic neutron reaction cross-section and subscript g refers to the specific, discretised energy group.

The appropriateness of the proposed macroscopic nuclear cross-section correlations was examined by comparing normalised scalar neutron flux distributions calculated using both Serpent and a deterministic steady-state, two-energy group, spatially-dependent, neutron diffusion code. Geometries with high levels of spatially varying powder particle number densities were specified, these can be seen in Figure 4.4. Figure 4.4 shows good agreement between the normalised scalar neutron flux profile calculated using the point-wise continuous energy Monte Carlo neutron transport code, Ser-

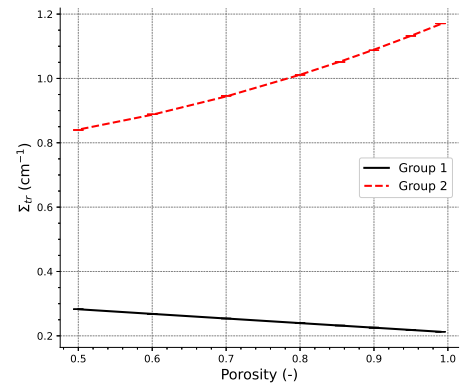

(a) Σ_{tr}.

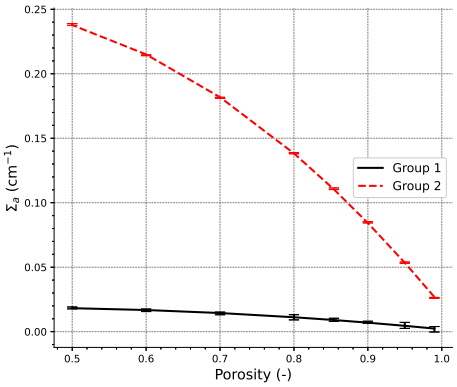

(b) Σ_{a}.

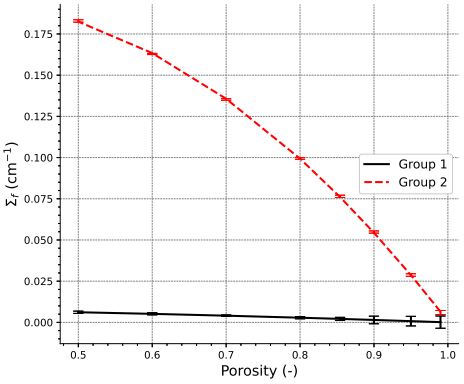

(c) Σ_{f}.

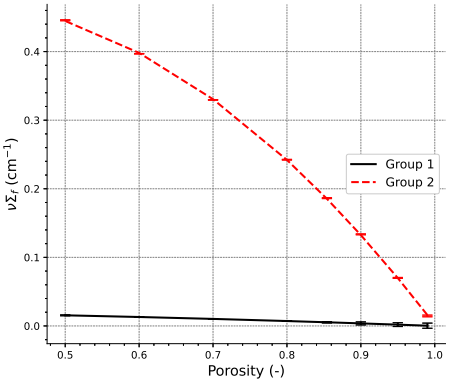

(d) $\bar{\nu}\Sigma_{\mathrm{f}}$.

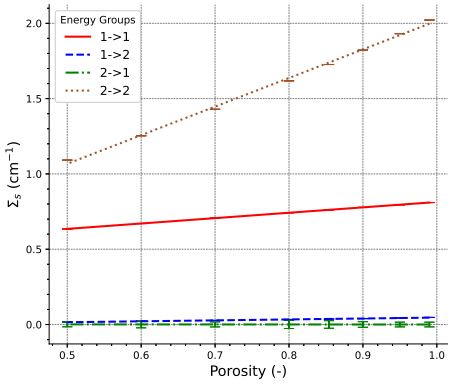

(e) $\Sigma_{\mathrm{s,g}\rightarrow\mathrm{g'}}$

Figure 4.3: The fast and thermal macroscopic nuclear cross-sections of a powder particle surrounded by varying volumes of water, in an infinite medium. The points represent data calculated using Monte Carlo neutron transport code Serpent, the lines represent the correlations used in the proposed model.

Table 4.2: Macroscopic neutron cross-section correlation coefficients.

Cross-Section (cm^{-1})	C_0	C_1	C_2
$\bar{\nu}\Sigma_{f,1}$	0.02297751	−0.00687425	−0.01613239
$\bar{\nu}\Sigma_{f,2}$	0.36194184	0.69095255	−1.05102329
$\Sigma_{a,1}$	0.01139081	0.0368169	−0.04634184
$\Sigma_{a,2}$	0.19590138	0.34348078	−0.51942155
$\Sigma_{f,1}$	0.00915864	−0.00287971	−0.00629015
$\Sigma_{f,2}$	0.14853871	0.2835586	−0.43132937
$\Sigma_{tr,1}$	0.35606652	−0.14885192	0.00405083
$\Sigma_{tr,2}$	0.76885785	−0.12069424	0.52981942
$\Sigma_{s,1\rightarrow1}$	0.45658621	0.35695688	0.0
$\Sigma_{s,1\rightarrow2}$	−0.01566651	0.06185078	0.0
$\Sigma_{s,2\rightarrow1}$	0.00191271	−0.00186743	0.0
$\Sigma_{s,2\rightarrow2}$	0.11795809	1.89864242	0.0

pent, and the steady-state, two-group, spatially dependent, neutron diffusion code developed for this thesis. This supports the use of these macroscopic nuclear cross-section correlations to calculate the normalised scalar neutron flux distribution, ultimately using the results to determine how the fission energy is distributed through the powder bed. The steady-state, spatially dependent, multi-group neutron diffusion equation is solved for every 0.5 $ change in the reactivity of the system.

4.3.2 Mean Powder Particle Size

A nominal mean powder particle size of $d_p = 30$ μm has been chosen for the physical system studied in this chapter. Sensitivity analysis is performed by increasing the particle size to $d_p = 100$ μm and examining the consequence this has on the volumetric slumping of the powder bed. This chapter also examines the effect that particle size and slumping has on the transient nuclear criticality excursion.

4.3.3 Wetting-Induced Slumping Parameter

For the UO_2 powder system under consideration, both the compressibility modulus due to wetting (m_2^s) and the change in matric suction across the wetting front ($\Delta\psi$) are unknown. Therefore, these quantities have been combined in the proposed model into a term that represents the fractional slumping of newly wetted powder, denoted f_{slump}. Physically, the term f_{slump} represents the extent to which the pressure exchange across the wetting front, due to certain change matric potential, will cause a deformation of the powder bed proportional to the rate of water infiltration. The term is defined as:

$$f_{\text{slump}} = m_2^s \Delta\psi \tag{4.16}$$

The fractional slumping of newly wetted powder is varied from 0 to 0.6 for both powder beds considered in this work.

4.3.4 Slumping and Wetting-Induced Reactivity Component

Volumetric slumping of the wetted powder results in varying fissile powder particle and water bulk densities in the wetted powder region. The effect that this reduction in porosity has on the reactivity of the system has been investigated here through a series of Monte Carlo neutron transport simulations

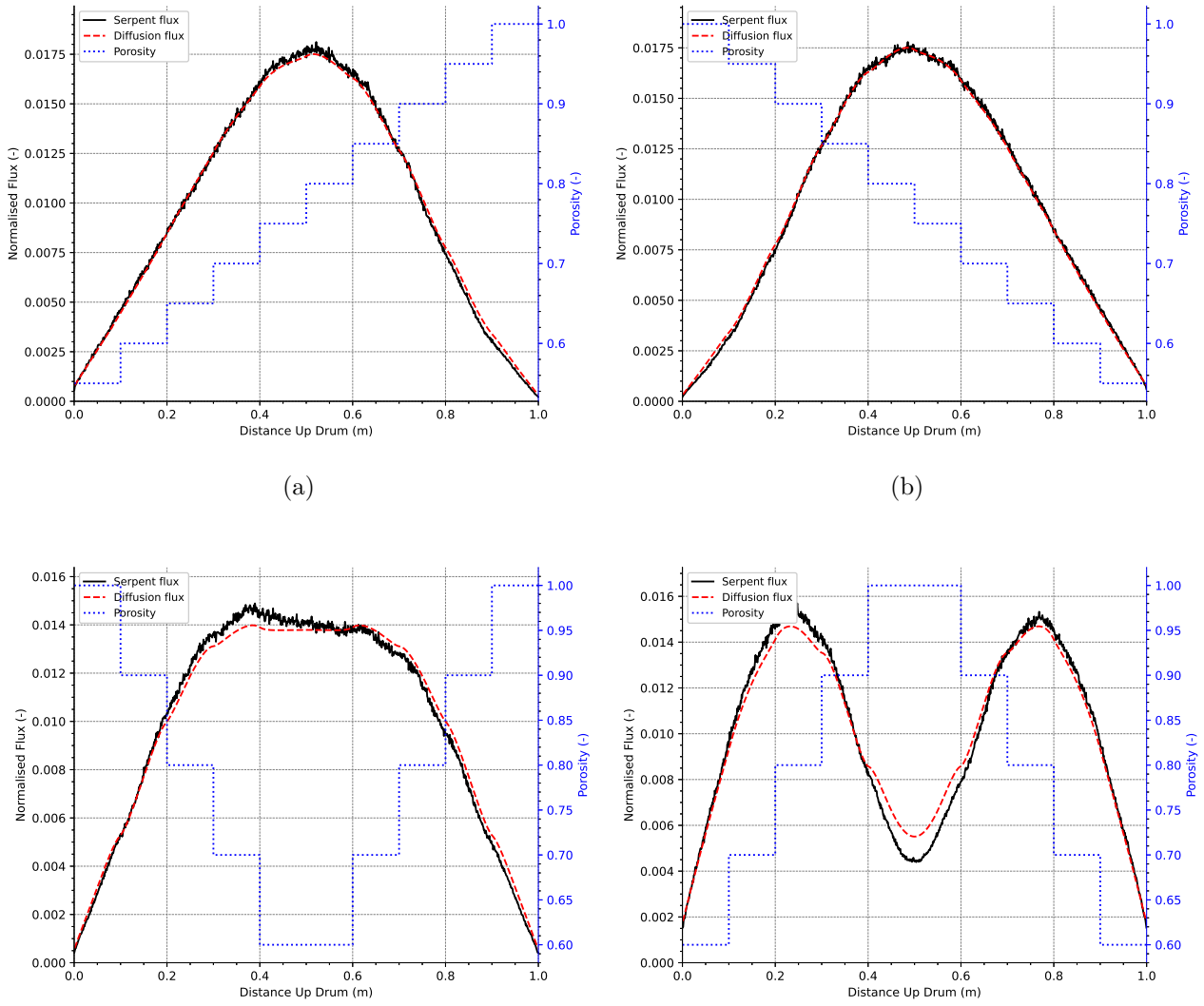

Figure 4.4: Scalar neutron flux distributions obtained through Monte Carlo neutron transport code Serpent alongside the multi-group neutron diffusion code using prescribed macroscopic nuclear cross-section correlations. The variation in the amount of UO_2 powder dispersed in the water is shown by the porosity.

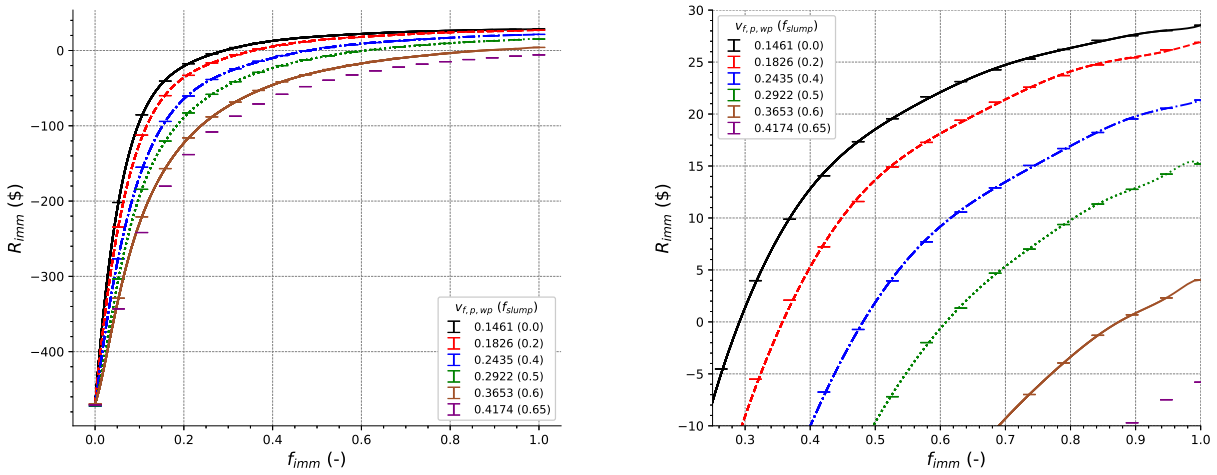

(a) Sub-critical reactivities.

(b) Near- and post-critical reactivities.

Figure 4.5: The sub-critical and post-critical wetting-induced reactivity component is shown for UO_2 powder beds with different volumetric slumping rates.

using MCNP (Werner et al., 2018). The solid volume fraction of the slumped wetted UO_2 powder bed can be found for a given fractional slumping rate, f_{slump}, by re-writing Equation (4.7) as:

$$v_{\text{f,p,wp}} = \frac{v_{\text{f,p,dp}}}{1 - f_{\text{slump}}} \tag{4.17}$$

Therefore, by varying the bed immersion fraction for each prescribed slumped UO_2 powder bed solid volume fraction, it is possible to gain an understanding of the effect that powder bed collapse has on the reactivity throughout the wetting of the powder bed. MCNP simulation data presented in Figure 4.5 suggests that slumping introduces a negative reactivity into the system, which counters the positive reactivity effect of water infiltration. This is shown by the fact that the immersion reactivity component is less for all cases where $f_{\text{slump}} > 0.0$ than for the case where $f_{\text{slump}} = 0.0$. The result is a greater level of powder bed saturation being required before criticality is reached. When the slumping fraction, $f_{\text{slump}} = 0.65$, the MCNP simulation data shown in Figure 4.5 indicates that a nuclear criticality excursion will not occur, regardless of the bed immersion fraction. This is a consequence of the decreased porosity of the wetted UO_2 powder bed, preventing enough water (acting as moderator) from entering the pores to cause a nuclear criticality excursion.

Since each simulation has a constant prescribed slumped UO_2 powder bed solid volume fraction, it is possible to define a unique wetting-induced reactivity component for each powder bed undergoing different levels of volumetric collapse. The wetting-induced reactivity component may take the following form:

$$R_{\text{imm}}(f_{\text{imm}}) = \sum_{i=0}^{n} C_i f_{\text{imm}}^i(t) \tag{4.18}$$

Table 4.3: Coefficients for slumping-adjusted sub-critical wetting-induced reactivity contribution correlation (rounded to 5 s.f.).

	Prescribed Slumping Fraction, f_{slump} (-)				
i	0.0	0.2	0.4	0.5	0.6
0	-471.62	-470.95	-474.21	-472.23	-469.54
1	7520.8	6204.4	4902.2	2627.6	1687.5
2	-5.72e+04	-3.86e+04	-2.4169e+04	3.6926e+04	5.2608e+04
3	2.5869e+05	1.3986e+05	6.8483e+04	-7.6285e+05	-1.0385e+06
4	-7.3841e+05	-3.1042e+05	-1.1515e+05	6.6484e+06	1.0115e+07
5	1.3636e+06	4.2712e+05	1.1327e+05	-3.5854e+07	-6.351e+07
6	-1.625e+06	-3.5498e+05	-6.0129e+04	1.3203e+08	2.7766e+08
7	1.206e+06	1.631e+05	1.3294e+04	-3.4598e+08	-8.7571e+08
8	-5.0692e+05	-3.1794e+04	0.0	6.5686e+08	2.0292e+09
9	9.2149e+04	0.0	0.0	-9.0625e+08	-3.4805e+09
10	0.0	0.0	0.0	8.9918e+08	4.4091e+09
11	0.0	0.0	0.0	-6.246e+08	-4.0719e+09
12	0.0	0.0	0.0	2.8797e+08	2.6654e+09
13	0.0	0.0	0.0	-7.9063e+07	-1.1719e+09
14	0.0	0.0	0.0	9.7696e+06	3.1048e+08
15	0.0	0.0	0.0	0.0	-3.7472e+07
R^2	0.9999	0.9999	0.9999	0.9999	0.9999

where $f_{\text{imm}}(t) = 1 - H_{\text{dp}}(t)/H_{\text{dp+wp,0}}$ is the bed immersion fraction, $H_{\text{dp+wp,0}}$ is the original height of the combined dry and wet powder, before any volumetric collapse of the powder bed has occurred.

Figure 4.5 indicates that the reactivity of the UO_2 powder bed increases by around 500 \$ as the immersion fraction ranges from 0.0 to 1.0. The reactivity feedback correlation coefficients used to model this reactivity component are outlined in Table 4.3. These correlation coefficients correspond to the line of best fit presented in Figure 4.5. Good agreement is predicted when using these correlation coefficients, which is supported by the R^2 values tabulated in Table 4.3.

The void and thermal reactivity feedback components remain unchanged from those stated in Sections 3.4.9 and 3.4.10.

4.3.5 Prescribed Initial Conditions

In a sub-critical fissile powder bed where no gas is being produced, and no significant thermal energy is generated, the model may be reduced to five spatially independent ordinary differential equations (ODEs). Represented by Equations (3.1), (3.2), (3.70), (4.8) and (4.9), these equations may be solved up to a point near delayed critical, where simulation using the full set of equations, including spatially-dependent nuclear thermal hydraulics, radiolytic gas and steam models will begin. These approach-to-critical simulations are performed to save computational expense by calculating initial conditions from where the full set of ODEs will be solved.

Initial region heights for the preliminary approach-to-critical simulation are those that represent a dry UO_2 powder bed where $H_{\text{dp}} = 0.6216$ m, $H_{\text{wp}} = 0.0001$ m (must be non-zero for Equation (3.22)) and $H_{\text{sus}} = 0.3783$ m. The initial neutron density and delayed neutron precursor concentrations for the approach-to-critical simulation may be found using the following expressions:

$$N(0) = -\frac{s_{\mathrm{n}} V_{\mathrm{UO_2}} \Lambda}{R_{\mathrm{t}}(0)\beta_{\mathrm{eff}}} \tag{4.19}$$

and:

$$C_{\mathrm{i}}(0) = -\frac{\beta_{\mathrm{i}} s_{\mathrm{n}} V_{\mathrm{UO_2}}}{\lambda_{\mathrm{i}} R_{\mathrm{t}}(0)\beta_{\mathrm{eff}}} \tag{4.20}$$

where the value for the intrinsic neutron source density, $s_{\mathrm{n}} = 0.135$ neutrons s^{-1} ($\mathrm{cm}^{-3} \cdot \mathrm{UO_2}$). The dry powder bed reactivity has been found through MCNP to be, $R_{\mathrm{t}} = -476$ \$. The mean generation time and delayed neutron data are outlined in Section 3.4.7. Using Equation (4.19), this yields an initial neutron population, $N(0) = 0.094$ neutrons and corresponding group-wise delayed neutron precursor population of $C_1(0) = 33.3$, $C_2(0) = 68.5$, $C_3(0) = 17.8$, $C_4(0) = 16.0$, $C_5(0) = 2.6$ and $C_6(0) = 0.3$.

Simulations up to the point near delayed critical were performed using the dry powder bed initial conditions for each individual volumetric slumping fraction modelled. The approach-to-critical preliminary simulations were stopped once the reactivity became positive. The last negative reactivity evaluated by the ODE solver was used as the final data point of the sub-critical simulation. This value changed between each approach-to-critical simulation (see Table 4.4) because of the temporal resolution of the ODE solver but remained close to zero for all cases modelled. The resulting initial conditions found for the full simulations, beginning near delayed critical, are presented in Table 4.4.

The data presented in Table 4.4 suggests that wetting-induced slumping delays the initiation of the nuclear criticality excursion, leading to a higher bed immersion fraction at the point of criticality. This is expected since wetting-induced slumping of the powder bed displaces water held between powder particles, causing water to build up on top of the powder bed. The movement of water from areas where neutron thermalisation is more likely to areas where fewer neutrons pass through leads to a reduction in the reactivity of the powder bed. Increasing the slumping fraction further results in a decreased wet powder region porosity, which may lead to a scenario where full saturation occurs without initiating a nuclear criticality excursion.

Initial conditions for the case where the mean powder diameter, $d_{\mathrm{p}} = 100$ μm are presented in Table 4.5. Both powder beds modelled exhibit the same slumped wetted bed porosities. As expected, the region heights that correspond to the point close to delayed criticality are very similar, irrespective of mean powder particle size. Figure 4.6 shows how the time to a near delayed critical state increases as both the slumping fraction increases and mean powder particle size decreases.

Other initial conditions prescribed for the full simulation are identical to those listed in Section 4.3.5, excluding the initial neutron population and precursor population which are listed in Tables 4.4 and 4.5.

Table 4.4: Initial system geometry and neutron kinetic data at a point close to criticality for variable slumping fractions with mean powder size, $d_p = 30$ μm.

$d_p = 30$ μm	Prescribed Slumping Fraction, f_{slump} (-)				
Property	0.0	0.2	0.4	0.5	0.6
C_1 (precursors cm^{-3} · UO$_2$)	0.02525	0.02879	0.03570	0.04864	0.08121
C_2 (precursors cm^{-3} · UO$_2$)	0.11383	0.12801	0.15529	0.20685	0.33089
C_3 (precursors cm^{-3} · UO$_2$)	0.07383	0.08073	0.09436	0.12030	0.17931
C_4 (precursors cm^{-3} · UO$_2$)	0.11090	0.11933	0.13626	0.16743	0.23518
C_5 (precursors cm^{-3} · UO$_2$)	0.02665	0.02822	0.03135	0.03689	0.04836
C_6 (precursors cm^{-3} · UO$_2$)	0.00448	0.00466	0.00504	0.00570	0.00703
$f_{imm,0}$ (-)	0.29126	0.35752	0.48108	0.60881	0.87412
H_{dp} (m)	0.44062	0.39943	0.32261	0.24319	0.07826
H_{wp} (m)	0.18108	0.17783	0.17949	0.18930	0.21744
H_{sus} (m)	0.27055	0.28835	0.31507	0.33743	0.38179
n (neutrons cm^{-3} · UO$_2$)	0.00158	0.00162	0.00170	0.00186	0.00219
R_{imm} (\$)	-0.00001	-0.00052	-0.00009	-0.00029	-0.00014
t_{crit} (s)	47.15337	55.74393	72.99537	93.68059	142.34885
$v_{f,p,wp}$ (-)	0.146	0.183	0.244	0.292	0.365

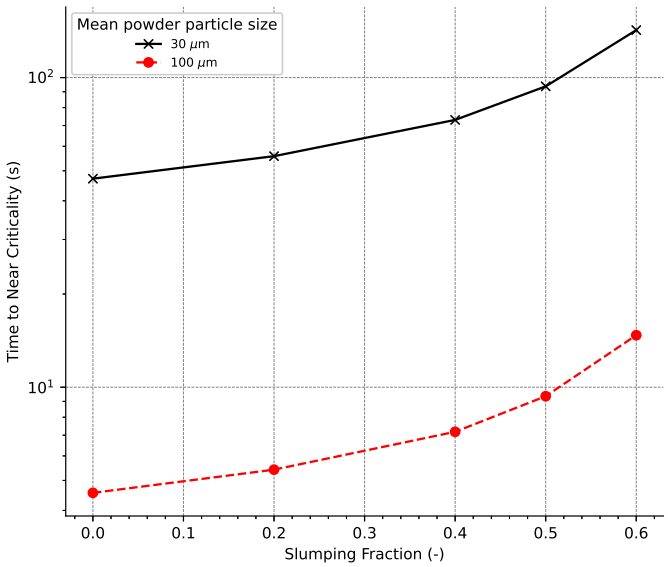

Figure 4.6: The time taken for wetting and slumping to cause the initially unsaturated bed to reach a point near delayed critical.

Table 4.5: Initial system geometry and neutron kinetic data at a point close to criticality for variable slumping fractions with mean powder size, $d_{\mathrm{p}} = 100$ μm.

$d_{\mathrm{p}} = 100$ μm	Prescribed Slumping Fraction, f_{slump} (-)				
Property	0.0	0.2	0.4	0.5	0.6
C_1 (precursors cm^{-3} $\cdot$ UO_2)	0.00299	0.00338	0.00419	0.00567	0.00978
C_2 (precursors cm^{-3} $\cdot$ UO_2)	0.01303	0.01501	0.01901	0.02627	0.04615
C_3 (precursors cm^{-3} $\cdot$ UO_2)	0.01057	0.01217	0.01535	0.02104	0.03558
C_4 (precursors cm^{-3} $\cdot$ UO_2)	0.02094	0.02375	0.02916	0.03878	0.06157
C_5 (precursors cm^{-3} $\cdot$ UO_2)	0.00703	0.00776	0.00916	0.01163	0.01704
C_6 (precursors cm^{-3} $\cdot$ UO_2)	0.00170	0.00183	0.00207	0.00247	0.00328
$f_{\mathrm{imm,0}}$ (-)	0.29126	0.35752	0.48108	0.60881	0.87412
H_{dp} (m)	0.44062	0.39943	0.32261	0.24320	0.07826
H_{wp} (m)	0.18108	0.17783	0.17949	0.18930	0.21744
H_{sus} (m)	0.22818	0.23829	0.24960	0.25355	0.25484
n (neutrons cm^{-3} $\cdot$ UO_2)	0.00108	0.00110	0.00114	0.00120	0.00133
R_{imm} (\$)	-0.00096	-0.00122	-0.00059	-0.00078	-0.00024
t_{crit} (s)	4.55825	5.41630	7.17682	9.35155	14.72212
$v_{\mathrm{f,p,wp}}$ (-)	0.146	0.183	0.244	0.292	0.365

4.4 Results

4.4.1 Wetting-induced Volumetric Slumping of Powder Beds

The initial conditions outlined for the powder beds in Section 5.4.4 yield the slumped wetted region porosities presented in Figure 4.7. Figure 4.7 confirms that the model implemented in this work produces a wetting-induced volumetric slump of the powder bed that is independent of the mean powder particle size. Furthermore, there is a non-linear relationship between the prescribed slumping fraction and the homogeneous wetted powder region porosity.

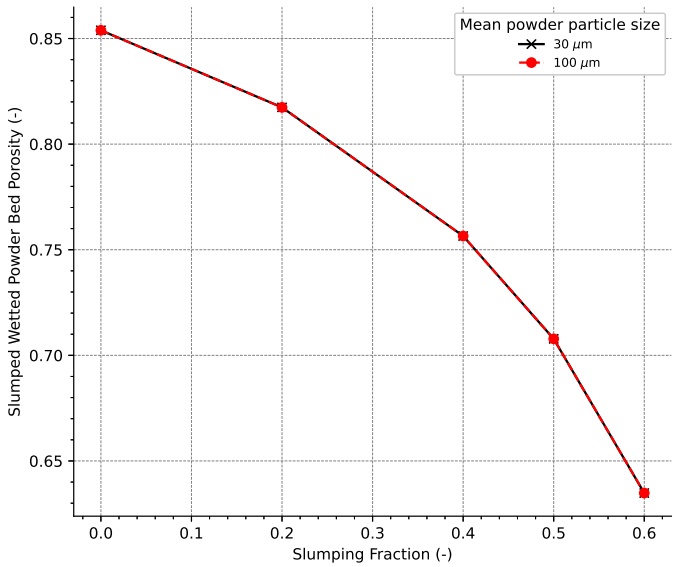

Figure 4.7: The slumped wetted powder bed porosity as a function of the prescribed slumping fraction.

Figure 4.8 shows how the bulk density of the powder varies as a function of time throughout the domain, for each prescribed slumping fraction. The horizontal axes shown in Figure 4.8 represent the position from the base of the domain at 0 m, where the dry powder sits, up to the top of the domain at 1 m, above the pooled water region. Repeated plots of the data moving to the left in Figure 4.8 correspond to an increasing simulation time by increments of 25 seconds, starting from $t - t_{\text{crit}} = 0$ seconds and proceeding until $t - t_{\text{crit}} = 100$ seconds.

The powder bulk density, $\rho_{\text{p,bulk}} = 0$ kg m^{-3} in the pooled water region, which can be seen in either image in Figure 4.8, at the upper portion of the domain. The set of vertical lines shown for each slumping fraction, located furthest right in the image, corresponds to the interface between the wetted powder and pooled water regions. Over time, for cases where $f_{\text{slump}} > 0$ this moves progressively downwards as the wetting-induced slump causes the powder bed to collapse. The solid black vertical line (the case where $f_{\text{slump}} = 0$) at 0.6217 m, reaching 1600 kg m^{-3}, remains the same irrespective of time, since no collapse takes place.

Furthermore, for cases where $f_{\text{slump}} > 0$, a set of secondary vertical lines appear in both images shown in Figure 4.8, located lower down the domain. The vertical lines move further down the domain

(to the left of the image) as time increases. This second vertical line corresponds to the location of the wetting front since the volumetric collapse (slump) occurs across the wetting front. The spatial bulk densities that are greater than the nominal dry powder bulk density of 1600 kg m^{-3} correspond to the slumped UO_2 powder bulk density for the prescribed slumping fraction. The location of the wetting front for the case where $f_{slump} = 0$ cannot be seen in Figure 4.8, since there is no slumping to produce a second vertical line at the wetting front.

The location of the wetting front and wet powder-pooled water interfaces, whose locations have been previously stated, varies as a function of the prescribed mean UO_2 powder particle size. This is due to differences in the advection rate of water through the powder beds as a result of different permeabilities. The slumped powder bed bulk density is shown to not vary as a function of the mean powder particle size, which corresponds with Figure 4.7.

4.4.2 Transient Nuclear Criticality Excursion Behaviour in Slumping UO_2 Powder Beds

30 μm Powder Bed

Each simulation began from the calculated initial condition for the prescribed value of f_{slump} and was executed for $t - t_{crit} = 100$ s. Figure 4.9a shows that there are similar characteristics between the nuclear criticality transient regardless of the amount of wetting-induced slumping. Figure 4.9a also shows that the magnitude of the initial peak power varies as a function of the prescribed slumping fraction. The wetting-induced collapse of the powder bed led to an increase in the peak power, from 29.2 MW when $f_{slump} = 0.0$, to 106 MW when $f_{slump} = 0.5$. The fission energy deposited 100 seconds after the initial nuclear criticality excursion ranged from 48 MJ when $f_{slump} = 0.0$, to 42 MJ $f_{slump} = 0.6$.

Volumetric collapse of the UO_2 powder bed significantly affects the reactivity of the system. This is evidenced in Figure 4.9c by examining the slumping reactivity component, which is derived by subtracting the wetting-induced reactivity component (which accounts for slumping) for the case where $f_{slump} = 0.0$, with the wetting-induced reactivity for cases where $f_{slump} \neq 0.0$. The total reactivity of the system is the sum of the individual components in Figure 4.9c (excluding the slumping component since this is accounted for in the wetting-induced reactivity component), and is shown in Figure 4.9b.

Figure 4.9a shows that the peak power is reached shortly after the initiation of the nuclear criticality excursion. The dissociation of water molecules via radiolysis introduces voids into the system, adding negative reactivity which limits this power peak. This effect is shown by the increase in the H_2 void fraction in Figure 4.10c and also Figure 4.10d at a time that corresponds to the initial power peak. The negative void reactivity component is balanced by the increase in reactivity due to wetting, leading to a gradual increase in power until the onset of boiling. The initiation of boiling causes large voids to be created in the pores around powder particles (see Figure 4.10c), introducing a correspondingly large negative reactivity into the system (see Figure 4.9c), resulting in a reduction in power by greater than an order of magnitude. The reactivity feedback due to thermal effects and voids in the pooled water region are not shown in Figure 4.9c since they are not significant in comparison to the effects of voids in the wet powder region and the combined effects of infiltration.

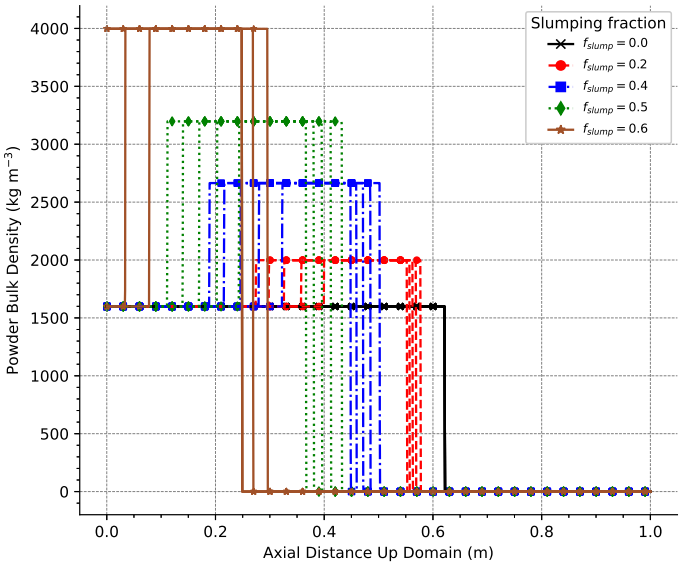

(a) $d_{\mathrm{p}} = 30$ μm.

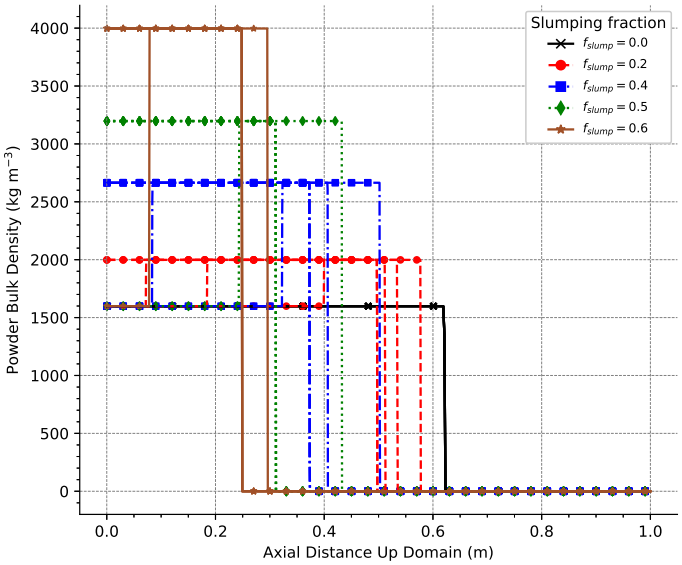

(b) $d_{\mathrm{p}} = 100$ μm.

Figure 4.8: The spatial variation in the UO_2 powder bulk density as a function of the prescribed slumping fraction. Multiple lines per slumping fraction correspond to the variation in powder bed bulk density over time, starting from $t - t_{\mathrm{crit}} = 0$ seconds on the right of the graph, moving leftwards in increments of 25 seconds up to $t - t_{\mathrm{crit}} = 100$ seconds.

Average phase and region temperatures presented in Figure 4.10a highlight the large amounts of thermal energy deposited into the dispersed multiphase media once the power peaks.

The height of each region and the time to criticality, t_{crit}, depicted in Figure 4.10b suggests that for the case where $f_{\text{slump}} = 0.6$, the dry UO_2 powder bed will reach almost full saturation ($f_{\text{imm},0} = 0.878$) before a critical state is reached. The remaining wetting-induced reactivity that may be added to the system, once criticality is reached, in the case where $f_{\text{slump}} = 0.6$, is shown in Figure 4.9c to be less than 5 \$.

Simulated wetting-induced reactivity profiles for the other prescribed slumping fractions, shown in Figure 4.9c, suggest that a greater wetting-induced reactivity will be added to the system over the 100 seconds of simulated time. Furthermore, the wetting-induced reactivity addition rate, shown by the slopes of the dashed lines in Figure 4.9c, is higher as the prescribed slumping fraction tends to zero. These two factors imply that powder beds exhibiting less collapse will have higher reactivities at a given time after the initiation of the transient nuclear criticality excursion. Figure 4.9a shows that the consequence of this is that higher fission energies are deposited in the systems with a lower prescribed slumping fraction. Figures 4.10a and 4.10c shows that the pore voidage and dry UO_2 powder region temperatures are higher for the cases with a higher fission energy deposition. The wet UO_2 powder temperature, shown in Figure 4.10a, is limited to the boiling point of water as a result of efficient interfacial convection between the phases.

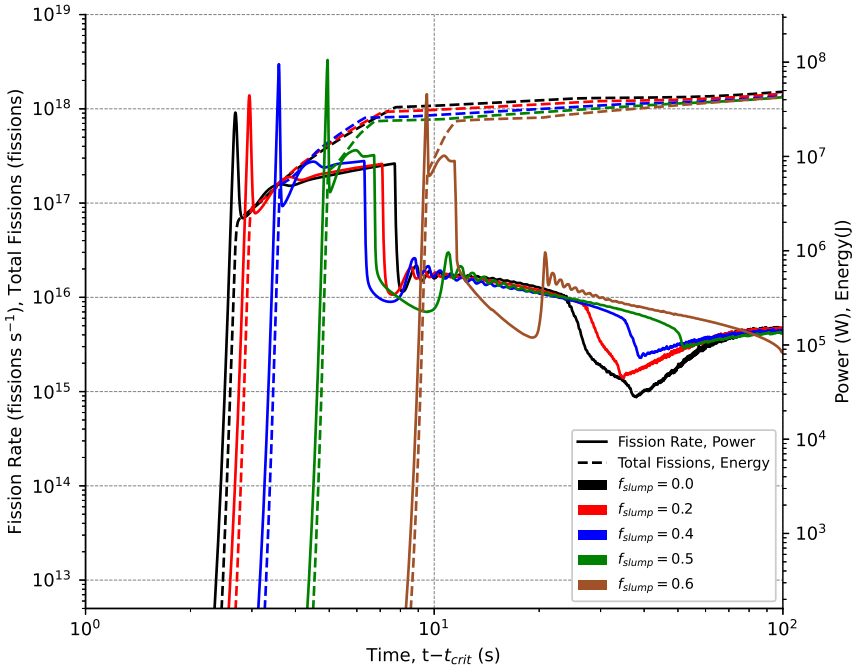

(a) Fission rate, integrated fissions, power and Energy.

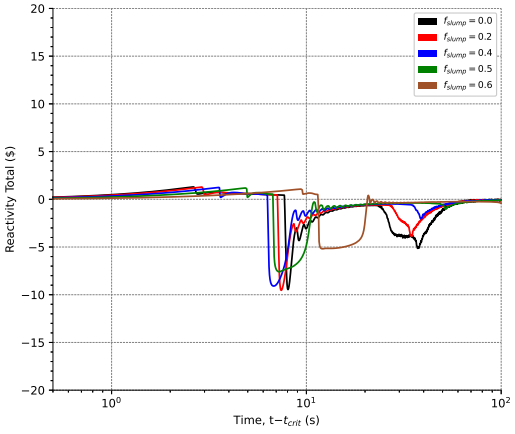

(b) Reactivity total.

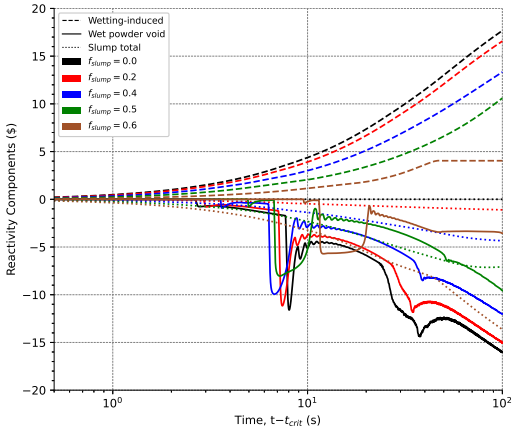

(c) Reactivity components.

Figure 4.9: The fission power, energy and reactivity components 100 seconds post initial criticality for cases with varying slumping fraction, f_{slump}. All results are for the case where $d_{\text{p}} = 30$ μm.

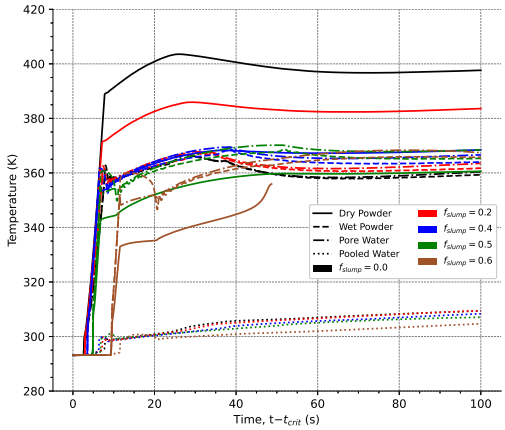

(a) Phase and region average temperatures.

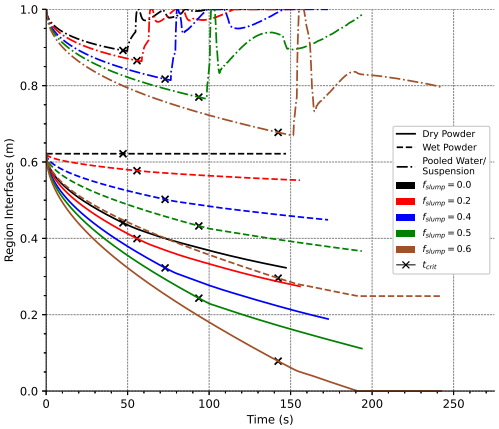

(b) Region heights.

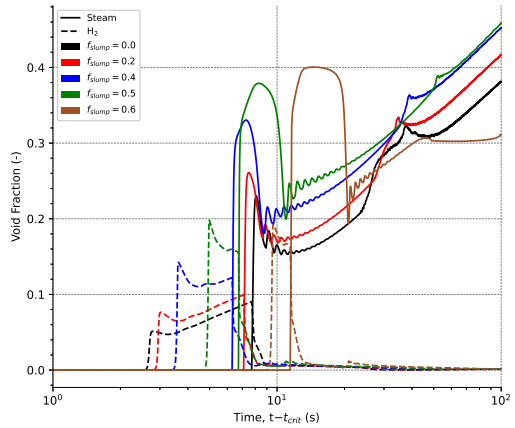

(c) Pore voidage due to H_2 and steam.

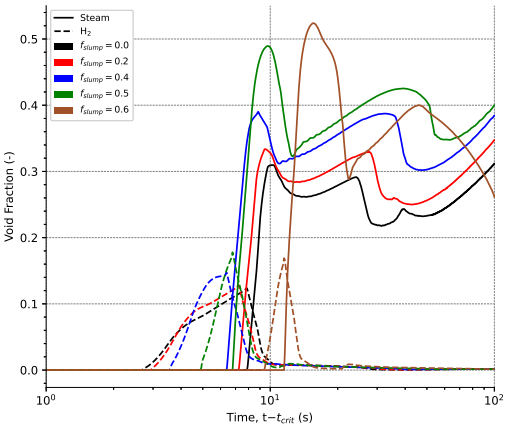

(d) Pooled water voidage due to H_2 and steam.

Figure 4.10: Associated thermophysical system properties (for $d_{\mathrm{p}} = 30$ μm powder bed) 100 seconds post initial criticality for cases with varying slumping fraction, f_{slump}.

100 μm Powder Bed

Data regarding the transient nuclear criticality excursion for the case where $d_p = 100$ μm is presented in Figures 4.11 and 4.12. In this case, the nuclear criticality transient is initiated quicker than for the smaller sized UO_2 powder bed due to the increased rate of infiltration. This is a consequence of the comparatively higher rates of water infiltration, illustrated through a lower dry UO_2 powder region interface location at a given time in Figure 4.12b when compared to Figure 4.10b.

Figure 4.11a shows that there are similar characteristics between the nuclear criticality transient regardless of the amount of wetting-induced slumping. Figure 4.11a also shows that the magnitude of the initial peak power varies as a function of the prescribed slumping fraction. The wetting-induced collapse of the powder bed led to an increase in the peak power, from 255 MW when $f_{\text{slump}} = 0.0$, to 501 MW when $f_{\text{slump}} = 0.5$. The fission energy deposited 100 seconds after the initial nuclear criticality excursion ranged from 57 MJ when $f_{\text{slump}} = 0.0$, to 43 MJ $f_{\text{slump}} = 0.6$.

Figure 4.11c shows that slumping introduces a negative reactivity into the system. The slumping reactivity component is derived from the wetting-induced reactivity component, which already accounts for the effects of slumping (see Section 4.3.4). An oscillatory power response is observed in Figure 4.11a within the interval of $t - t_{\text{crit}} = 4$ seconds to $t - t_{\text{crit}} = 30$ seconds. This oscillatory response is attributed to oscillations in the creation of steam interstitially between UO_2 powder particles (see Figure 4.12c), which introduces an oscillatory wetted powder region void reactivity feedback component, as shown in Figure 4.11c. The gas present in the wetted powder region advects into the pooled water region, shown in Figure 4.12d.

Full saturation of the UO_2 powder bed is shown in Figure 4.12b, for each prescribed slumping fraction, by the solid lines intersecting with the x-axis. At this point in time, the dashed lines, representing the height of the wetted UO_2 powder region, become constant in time. Physically this represents that the wetted powder bed has become static and the wetting-induced volumetric collapse has ceased.

The reactivity feedback due to thermal effects and voids in the pooled water region are not shown in Figure 4.11c since they are not significant in comparison to the effects of voids in the wet powder region, infiltration and slumping.

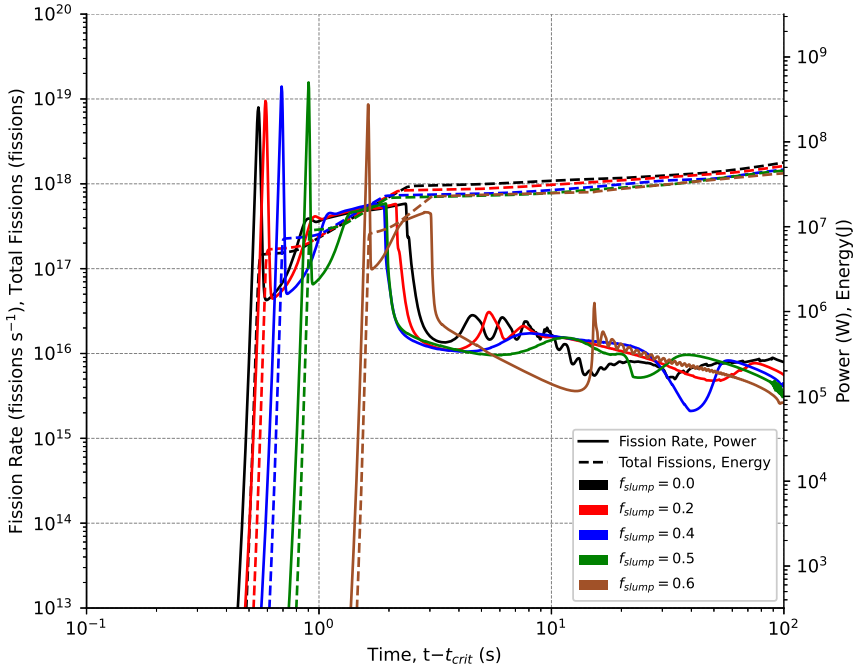

(a) Fission rate, integrated fissions, power and Energy.

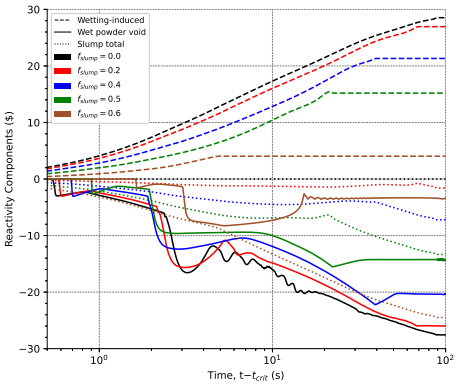

(b) Reactivity components.

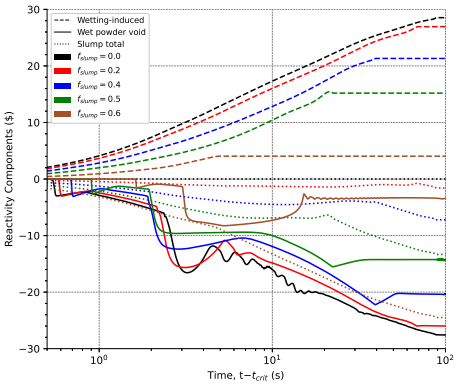

(c) Reactivity total.

Figure 4.11: The fission power, energy and reactivity components 100 seconds post initial criticality for cases with varying slumping fraction, f_{slump}. All results are for the case where $d_{\text{p}} = 100$ μm.

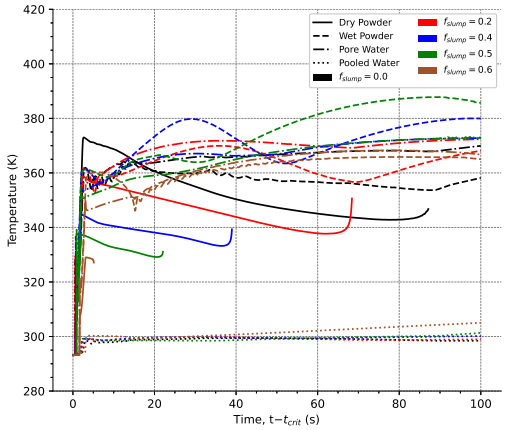

(a) Phase and region average temperatures.

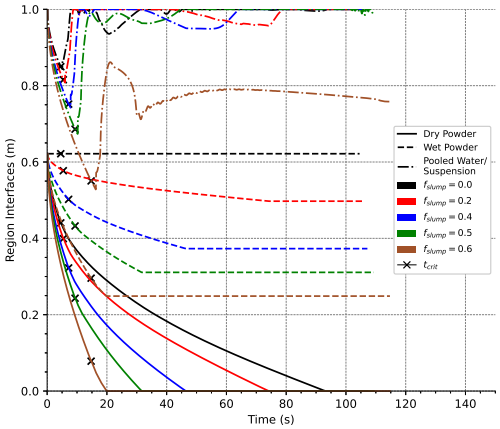

(b) Region heights.

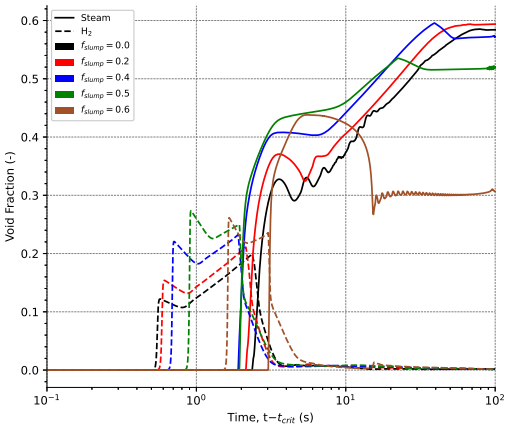

(c) Pore voidage due to H_2 and steam.

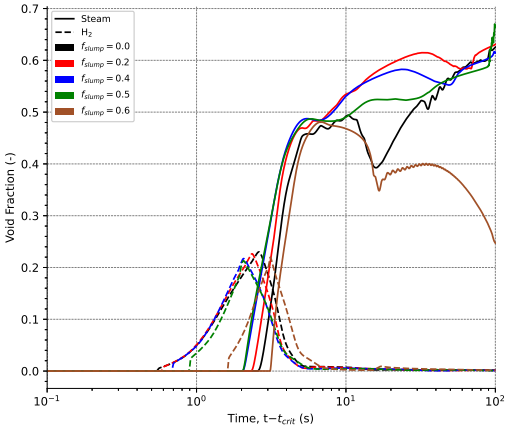

(d) Pooled water voidage due to H_2 and steam.

Figure 4.12: Associated thermophysical system properties (for $d_p = 100$ μm powder bed) 100 seconds post initial criticality for cases with varying slumping fraction, f_{slump}.

4.4.3 Peak Power to Boiling Time

Figures 4.9a and 4.11a show that there is a period of time early during the transient nuclear criticality excursion, just after the first power peak, where the power of the system increases to around 10 MW, before there is a second sharp drop in power. Figures 4.9c and 4.11c suggest that during this time, wetting-induced reactivity is matched by a negative reactivity due to voids present in the wet powder.

Competing reactivity components at this time cause the total reactivity of the system, shown in Figures 4.9b and 4.11b, to indicate that a delayed critical state is reached ($0\$ \leq R_{\mathrm{T}} < 1\$$). The delayed critical state remains until the second sharp drop in power. The time at which this sharp drop in power occurs coincides with the creation of steam in the pores, shown in Figures 4.10c and 4.12c, indicating that boiling occurs at this time. The time taken for boiling to occur and for the second sharp drop in power to occur is for each simulated case is shown in Figure 4.13.

Figure 4.13 indicates the total energy deposited for the 100 seconds after the initial nuclear criticality excursion as a function of the time between peak power and boiling. Generally, as the time from the initial power peak to the onset of boiling decreases, less fission energy is generated. The case where $f_{\mathrm{slump}} = 0.6$ is an exception where a greater peak power to boiling time results in less fission energy generated over the simulated time than for the case where $f_{\mathrm{slump}} = 0.5$. This is due to the low rate of reactivity insertion predicted for the case where $f_{\mathrm{slump}} = 0.6$ when the initial delayed critical point is reached. With a lower rate of reactivity insertion predicted, the amount of time required for boiling to be reached is greater.

Figures 4.9a and 4.11a show that the fission energy deposited into the system over the 100 seconds of simulation time decreases as the prescribed slumping fraction increases. This may be attributed to the fact that the slumping reactivity component, shown in Figures 4.9c and 4.11c, is lower with increased slumping fraction.

4.4.4 Hydrostatic Pressure in Wetted Powder Bed

The gauge hydrostatic pressure of the powder bed is calculated from the surface of the pooled water to the interface between the wet and dry powder regions (the wetting front). Figure 4.14 highlights how the hydrostatic pressure at the final time, $t - t_{\mathrm{crit}} = 100$ seconds, varies as a function of the prescribed slumping fraction. The hydrostatic gauge pressure increases as the evaluation point moves further down the domain. The slope of the curve represents the rate of change in hydrostatic pressure axially down the domain. This is affected by the contents of the domain at the point of interest (see Equation (4.13)). Equation (4.13) also indicates that the hydrostatic pressure gradient in locations with increased gas content is less than in locations with greater water content. The lowest point plotted in Figure 4.14 is the location of the wetting front and therefore represents the hydrostatic pressure at the wetting front. This point also corresponds to the maximum hydrostatic pressure.

Figure 4.14a shows that an increase in the slumping fraction produces a larger hydrostatic pressure at the wetting front for the case where $d_{\mathrm{p}} = 30$ μm. This may be attributed to the fact that the wetting front has progressed further down the domain, producing a greater gravitational potential at the wetting front. The larger gravitational potential at the wetting front for increasing slumping fraction exists despite the increased voidage with an increased slumping fraction (for cases where

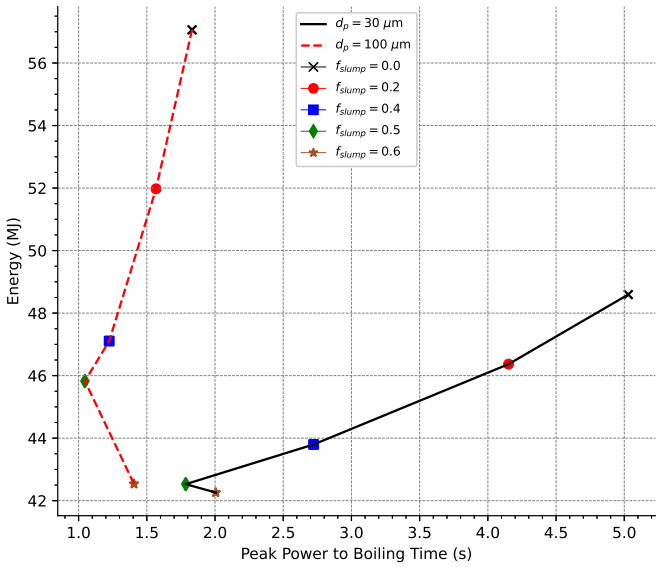

Figure 4.13: The total fission energy generated is plotted as a function of the time taken for the onset of boiling, from the initial power peak.

$f_{\text{slump}} < 0.6$) shown in Figures 4.10c and 4.10d. This suggests that the increased percolation height is more dominant in determining the hydrostatic pressure at the wetting front than voids for these specific cases.

Figure 4.14b suggests that the hydrostatic pressure at the wetting front does not significantly vary with varying slumping fraction when $f_{\text{slump}} < 0.6$. Differences that are present may be attributed to the voidage in the pores and pooled water regions, shown in Figures 4.12c and 4.12d, respectively. The hydrostatic pressure when $f_{\text{slump}} = 0.6$ is far greater than in the other cases because of the lower present at $t - t_{\text{crit}} = 100$ s.

Figure 4.14a shows that an increase in the slumping fraction produces a larger hydrostatic pressure at the wetting front for the case where $d_{\text{p}} = 30\ \mu$m since the wetting front has progressed further down the domain. For the UO_2 powder bed with size, $d_{\text{p}} = 100\ \mu$m, shown in Figure 4.14b, the slumping fraction does not significantly affect the hydrostatic pressure at the wetting front, except for when $f_{\text{slump}} = 0.6$. A larger hydrostatic pressure for the case where $f_{\text{slump}} = 0.6$ due to the lower amount of voidage in the system (see Figures 4.10c and 4.12c).

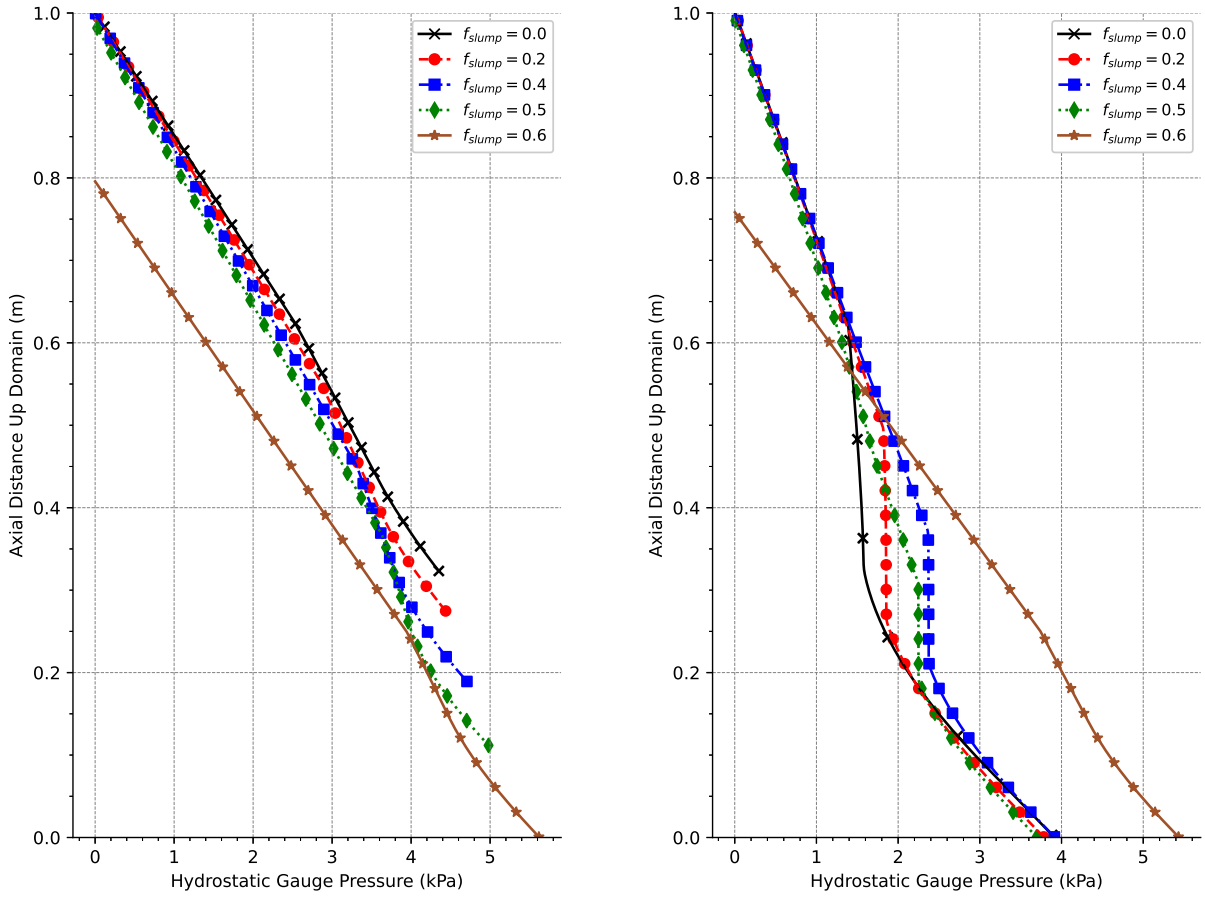

(a) $d_{\mathrm{p}} = 30$ μm.

(b) $d_{\mathrm{p}} = 100$ μm.

Figure 4.14: The hydrostatic gauge pressure is shown at the final time, $t - t_{\mathrm{crit}} = 100$ s. The reference point is taken from the top of the pooled water region.

4.5 Conclusions

This chapter has outlined an extension to the previous chapter's model, capable of examining the effects of wetting-induced volumetric collapse of UO_2 powder beds, and associated wetting-induced transient nuclear criticality excursions. The dynamic characteristics of a transient nuclear criticality excursion initiated by water infiltration into a UO_2 powder bed with varying rates of volumetric collapse was compared to the case with no collapse. Numerical values for the collapsing fraction were prescribed in order to simulate a range of meta-stable UO_2 powder bed structures. The sensitivity of the collapse phenomenon, with respect to particle size, was examined by specifying two powder bed configurations with mean powder particle sizes of $d_{\mathrm{p}} = 30$ μm and $d_{\mathrm{p}} = 100$ μm respectively.

A non-linear relationship was predicted between the prescribed slumping fraction and the homogeneous wet powder region porosity. Simulations also confirmed that the wetted powder continuity equation ensures that the wet powder region porosity remained homogeneous throughout the simulation. Additionally, volumetric collapse of the powder bed ceased in cases where the fissile powder bed became fully saturated within 100 seconds of the initial nuclear criticality excursion, such as for simulations when $d_{\mathrm{p}} = 100$ μm and $0.0 \leq f_{\mathrm{slump}} \leq 0.6$.

Point-wise continuous energy Monte Carlo neutron transport simulations, performed using MCNP, indicated that the volumetric collapse of the powder bed introduced a negative reactivity into the system, which became larger for greater rates of collapse. This was due to the decreased volume of water present in pore interstices, causing a lower probability for neutron thermalisation in areas with large fissile mass densities.

The model predicted that the peak power and fission energy were sensitive to the level of slumping and the mean size of UO_2 powder particles. For the case where $d_{\mathrm{p}} = 30$ μm, the total energy released varied from 42 MJ to 48 MJ and initial peak powers varied widely from 29.2 MW to 106 MW, with the largest power predicted for the case where the slumping fraction, $f_{\mathrm{slump}} = 0.5$. For the 100 μm UO_2 powder bed, the peak power increased from 255 MW for the unslumped case to 501 MW for the case where $f_{\mathrm{slump}} = 0.5$. Integrated fission power, or energy released, over the period of 100 seconds after the initial nuclear criticality excursion, varied from 57 MJ to 42 MJ as the slumping fraction varied from $f_{\mathrm{slump}} = 0.0$ to $f_{\mathrm{slump}} = 0.6$, for the case where $d_{\mathrm{p}} = 100$ μm.

Chapter 5

Nuclear Criticality Excursion Models for Three-Phase Fluidised Fissile UO_2 Suspensions

5.1 Introduction

The majority of work presented in this chapter is reproduced from Jones et al. (2023).

Previous chapters have suggested that an important characteristic of wetting-induced transient nuclear criticality excursions in UO_2 powder beds is the creation of radiolytic gas and steam bubbles as a means of quenching the nuclear criticality excursion. Thus far, gas bubble induced displacement of the UO_2 powder bed has not been directly modelled. Fan (1989) extensively describes a phenomenon, known as fluidisation, whereby powder in static powder beds may begin to become displaced when gas-bubbles impart enough momentum on the powder bed structure to cause movement. The point at which the powder bed transitions from static to moving is known as incipient fluidisation (Larachi et al., 2000). For a counter-current flow, such as for a typical delayed or prompt super-critical UO_2 powder system undergoing wetting from above, with upward gas bubble advection, three hydrodynamic states may be observed (Muroyama and Fan, 1985). These states correspond to a fixed bed, fluidised bed and 'true' flooding bed (Fan, 1989). At low gas velocities, the bed remains in a stationary or fixed bed state. This type of bed has been modelled previously by a number of authors (Jones et al., 2022b; Basoglu, 1992; Basoglu et al., 1994; Yamane et al., 2003a). As the gas flow rate exceeds the minimum fluidisation velocity, the powder particles become fluidised. The rate at which the powder bed transitions from a fixed to fully fluidised state has been studied by Tichy and Douglas (1972). At even higher gas volume fractions and velocities, it is possible for the three-phase suspension to transition to a transportive flow, where the water and powder becomes entrained in the gas (Fan, 1989).

This chapter examines how the transition between the first two of these three hydrodynamic states may affect a transient nuclear criticality excursion in a partially saturated UO_2 powder bed.

The proposed model extends the work of previous chapters, to include a phenomenological model, describing gas-bubble induced fluidisation of the UO_2 powder bed, leading to the re-distribution of fissile mass into a highly dispersed suspension. Additionally, a sedimentation-dispersion model, similar to the approach proposed by Cova (1966) has been implemented to represent the gravity-driven advective flow of agglomerated, suspended UO_2 powder particles, as well as gas-bubble induced turbulent mixing in the suspension. Furthermore, this study also conservatively and approximately investigates the extent to which ejection of UO_2 powder and water from the suspension due to the eruption of gas bubbles on the surface of the suspension may occur. Also modelled is the overflowing of the container caused by the significant volumes of gas products that may be introduced into the system. All of these phenomenological processes are captured in the point neutron kinetics through the use of additional reactivity feedback components, whose significance is estimated using bivariate B-splines that are fitted to reactivity data, derived from continuous energy Monte Carlo code simulations, performed using MCNP.

5.2 Extensions to Model

5.2.1 Extensions to Governing Equations for Component and Region Mass Transfer

Gas-bubble induced fluidisation may cause a dynamic suspension of UO_2 powder to form, above the settled wet UO_2 powder bed. Therefore, the equation governing the continuity of mobile components outlined in Equation (3.13), must be extended in the pooled water/suspension region, to include the motion of agglomerated suspended UO_2 powder particles. Mass transfer of UO_2 powder across the interface between the suspension and settled wet powder regions is governed by fluidisation and sedimentation phenomena. Fluidisation causes UO_2 powder to enter the suspension region from the settled wet powder bed as a result of gas bubble induced interactions with powder particles, creating a highly dispersed, three-phase, solid-liquid-gas suspension where water is the continuous phase. The resulting system may be likened to a three-phase bubble column, where solid particles and gas bubbles are dispersed in a continuous liquid phase. A graphical representation of the system is shown in Figure 5.1. In these types of systems, powder particle behaviour is influenced by the velocity of the solid phase, as well as dynamics of turbulent eddies formed as radiolytic gas and steam advects through the suspension (Jean et al., 1989; Fan, 1989). The continuity equation for the suspended powder takes the form of a sedimentation-dispersion model, which has been previously outlined by Cova (1966) and Smith and Ruether (1985). Since the advection-dispersion model is of the same form of the previously defined governing equation given by Equation (3.13), it is possible to define a governing equation for continuity of all components, j = p, w, rg, v, in the suspension region, k = sus, as:

$$\frac{\partial V'_{\mathrm{j,k}}(t,z)}{\partial t} = \frac{\partial}{\partial z}\left(D_{\mathrm{k}}(t,z)\frac{\partial V'_{\mathrm{j,k}}(t,z)}{\partial z} + U_{\mathrm{net,j,k}}(t,z)V'_{\mathrm{j,k}}(t,z)\right) + S'_{\mathrm{j,k}}(t,z) \tag{5.1}$$

This equation also applies to the pore water and pore gas products in the settled wet powder region, where j = w, rg, v and k = wp.

The powder particle number density, or volume fraction, in the settled wet powder region and dry powder region do not vary spatially and are instead prescribed a constant value. Therefore, as previously stated, Equation (3.13) does not apply to the powder held within the settled wet powder region. The total volume fraction of components in the wet powder region is found using Equation (3.14). When continuity of the UO_2 powder may be expressed by Equation (5.1) (such as in the suspension region), the following condition applies:

$$v_{\mathrm{f,p,sus}}(t,z) + v_{\mathrm{f,w,sus}}(t,z) + v_{\mathrm{f,rg,sus}}(t,z) + v_{\mathrm{f,v,sus}}(t,z) = 1 \tag{5.2}$$

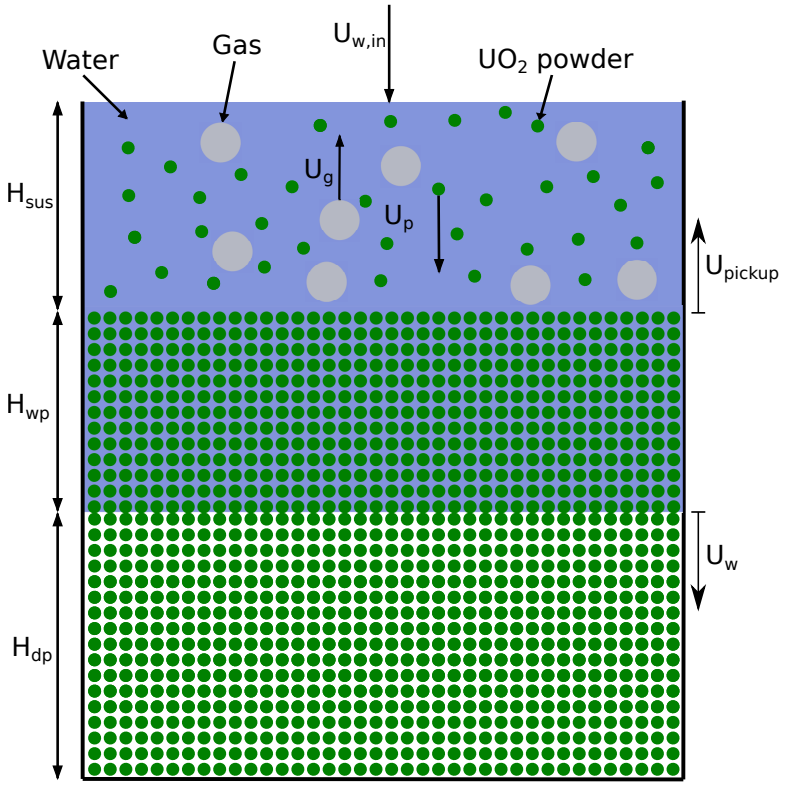

Figure 5.1: Graphical representation of three-phase, three-region powder bed, with suspended powder located above the bed.

Since UO_2 powder particles are now present in the suspension region, an additional advective term is required. The component and region advective terms are summarised in Table 5.1. All of these terms have previously been described with the exception of the hindered settling rate of the UO_2 powder, U_{p} [m s^{-1}], which is described in detail in Section 5.2.6. The description of the volumetric sources/sinks in the domain are defined by Table 5.2.

The method of solution remains unchanged from the methodology described in Section 3.2.3, with a slight variation to the prescription of certain boundary and interface conditions. New conditions at the interface between the settled wet powder and suspension regions will now be prescribed, other interface conditions that remain the same as previous sections will be re-stated. At the wetting front, the filling of the interface cell is expressed by the following condition:

Table 5.1: Net advective mass transfer for each component in each region with advective term in continuity equation.

Region, k	Component, j	$U_{\mathrm{net,j,k}}(t,z)$ [m s^{-1}]
Settled wet powder	Water	$-U_{\mathrm{w}}(t) + U_{\mathrm{adj}}(t,z)$
Settled wet powder	Radiolytic gas	$-U_{\mathrm{w}}(t) + U_{\mathrm{g}}(t,z) + U_{\mathrm{adj}}(t,z)$
Settled wet powder	Steam	$-U_{\mathrm{w}}(t) + U_{\mathrm{g}}(t,z) + U_{\mathrm{adj}}(t,z)$
Suspension	UO_2 powder	$-U_{\mathrm{w}}(t)\,(1 - v_{\mathrm{f,p,wp}})\,\Delta S_{\mathrm{w}} - U_{\mathrm{p}}(t,z) + U_{\mathrm{adj}}(t,z)$
Suspension	Water	$-U_{\mathrm{w}}(t)\,(1 - v_{\mathrm{f,p,wp}})\,\Delta S_{\mathrm{w}} + U_{\mathrm{adj}}(t,z)$
Suspension	Radiolytic gas	$-U_{\mathrm{w}}(t)\,(1 - v_{\mathrm{f,p,wp}})\,\Delta S_{\mathrm{w}} + U_{\mathrm{g}}(t,z) + U_{\mathrm{adj}}(t,z)$
Suspension	Steam	$-U_{\mathrm{w}}(t)\,(1 - v_{\mathrm{f,p,wp}})\,\Delta S_{\mathrm{w}} + U_{\mathrm{g}}(t,z) + U_{\mathrm{adj}}(t,z)$

Table 5.2: Source and sinks for each component in each region in the continuity equation.

Region, k	Component, j	$S'_{\mathrm{j,k}}(t,z)$ [m^2 s^{-1}]
Settled wet powder	Water	$-S'_{\mathrm{boil,w}}(t,z) - S'_{\mathrm{H_2O}}(t,z)$
Settled wet powder	Radiolytic gas	$S'_{\mathrm{H_2}}(t,z)$
Settled wet powder	Steam	$S'_{\mathrm{boil,v}}(t,z)$
Suspension	Water	$-S'_{\mathrm{boil,w}}(t,z) - S'_{\mathrm{H_2O}}(t,z)$
Suspension	Radiolytic gas	$S'_{\mathrm{H_2}}(t,z)$
Suspension	Steam	$S'_{\mathrm{boil,v}}(t,z)$

$$D_{\mathrm{wp}}(t,H_{\mathrm{dp}})\frac{\partial V'_{\mathrm{j,wp}}(t,H_{\mathrm{dp}})}{\partial z} + U_{\mathrm{net,j,wp}}(t,H_{\mathrm{dp}})V'_{\mathrm{j,wp}}(t,H_{\mathrm{dp}}) = 0 \tag{5.3}$$

The corresponding expression for $Q_{\mathrm{i}}(t)$ at the mesh cell containing the wetting front models the pores of the interface cell filling with water and gas products that advect downwards due to the continuous phase flow potential:

$$Q_i(t) = \pi R^2 U_{\mathrm{w}}(t)(1 - v_{\mathrm{f,p,dp}}) \tag{5.4}$$

The interface between the settled wet powder and suspension regions is prescribed a Robin condition, with different expressions for U_{adj} each side of the interface, producing a net flow of components either side of the interface, depending on the dominant phenomenon. The phenomena affecting the net rate of component transfer between each region and the resulting location of the interface are the sedimentation of the suspended UO_2 powder particles (described in Section 5.2.6) and fluidisation of the settled wet powder bed due to gas bubble-particle interactions (described in Section 5.2.3). Sedimentation is dominant when the average gas velocity, $\bar{U}_{\mathrm{g}}(t)$ though the settled wet powder and suspension region is less than the critical gas velocity, $U_{\mathrm{g,crit}}$ [m s^{-1}], otherwise pickup of the UO_2 powder particles (fluidisation) into the suspension is the dominant interface phenomenon. Applying this interface condition numerically would typically require switching the prescribed interface condition depending on whether the critical gas velocity condition is satisfied. However, this would also introduce a discontinuity into the set of ODEs, which is challenging to numerically solve due to spurious numerical artifacts that would be generated near the discontinuity. To avoid this issue, the following sigmoid functions are defined, approximating the step change in interface condition:

$$\mathbf{S}_1 = \frac{1}{1 + e^{\zeta(U_{\mathrm{g,crit}} - \bar{U}_{\mathrm{g}})}} \tag{5.5}$$

and:

$$\mathbf{S}_2 = \frac{1}{1 + e^{\zeta(\bar{U}_{\mathrm{g}} - U_{\mathrm{g,crit}})}} \tag{5.6}$$

where ζ [s m^{-1}] is a factor, set to increase the derivative of the sigmoid around the critical gas velocity, giving a better approximation of the step change.

A graphical representation of these functions as well as the derivative of Equation (5.5) is shown in Figure 5.2, for the case where $\zeta = 10^5$ s m^{-1} and $U_{\mathrm{g,crit}} = 0.22$ m s^{-1}.

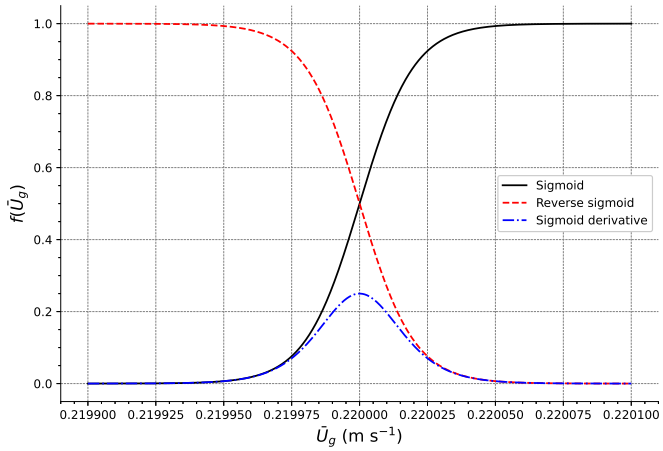

Figure 5.2: Sigmoid function for variable interface condition, representing whether sedimentation or fluidisation is dominant interface phenomenon.

Using this approximation, the interface condition for both the pickup of UO_2 powder particles and sedimentation is given by:

$$\begin{aligned} D_{\mathrm{sus}}(t, H_{\mathrm{dp+wp}}) \frac{\partial V'_{\mathrm{p,sus}}(t, H_{\mathrm{dp+wp}})}{\partial z} + U_{\mathrm{net,p,sus}}(t, H_{\mathrm{dp+wp}}) V'_{\mathrm{p,sus}}(t, H_{\mathrm{dp+wp}}) \\ = U_{\mathrm{pickup}} V'_{\mathrm{p,wp}} \mathbf{S}_1 - (U_{\mathrm{p}}(t, H_{\mathrm{dp+wp}}) + U_{\mathrm{w}}(t)(1 - v_{\mathrm{f,p,wp}}) \Delta S_{\mathrm{w}}) V'_{\mathrm{p,sus}}(t, H_{\mathrm{dp+wp}}) \mathbf{S}_2 \end{aligned} \tag{5.7}$$

The general form of the interface condition for the water, radiolytic gas and steam products is given by:

$$D_{\mathrm{wp}}(t, H_{\mathrm{dp+wp}})\frac{\partial V'_{\mathrm{j,wp}}(t, H_{\mathrm{dp+wp}})}{\partial z} + U_{\mathrm{net,j,wp}}(t, H_{\mathrm{dp+wp}})V'_{\mathrm{j,wp}}(t, H_{\mathrm{dp+wp}}) = D_{\mathrm{sus}}(t, H_{\mathrm{dp+wp}})\frac{\partial V'_{\mathrm{j,sus}}(t, H_{\mathrm{dp+wp}})}{\partial z} + U_{\mathrm{net,j,sus}}(t, H_{\mathrm{dp+wp}})V'_{\mathrm{j,sus}}(t, H_{\mathrm{dp+wp}}) \quad (5.8)$$

The corresponding expressions for $Q_{\mathrm{i}}(t)$, used to calculate $U_{\mathrm{net,j,wp}}(t, H_{\mathrm{dp+wp}})$ in Equation (5.8), on the settled wet powder side and the suspension side of the interface cell, are respectively defined as:

$$Q_{\mathrm{i}}(t) = -\pi R^2(1 - v_{\mathrm{f,p,wp}})U_{\mathrm{pickup}}\mathbf{S}_1 + \left(\frac{1}{v_{\mathrm{f,p,wp}}} - 1\right)(U_{\mathrm{p}}(t, H_{\mathrm{dp+wp}}) + U_{\mathrm{w}}(t)(1 - v_{\mathrm{f,p,wp}})\Delta S_{\mathrm{w}})V'_{\mathrm{p,sus}}(t, H_{\mathrm{dp+wp}})\mathbf{S}_2 \quad (5.9)$$

and:

$$Q_{\mathrm{i}}(t) = \pi R^2 U_{\mathrm{pickup}}\mathbf{S}_1 - \frac{1}{v_{\mathrm{f,p,wp}}}(U_{\mathrm{p}}(t, H_{\mathrm{dp+wp}}) + U_{\mathrm{w}}(t)(1 - v_{\mathrm{f,p,wp}})\Delta S_{\mathrm{w}})V'_{\mathrm{p,sus}}(t, H_{\mathrm{dp+wp}})\mathbf{S}_2 \quad (5.10)$$

When the immersed part of the UO_2 bed becomes fully fluidised, $H_{\mathrm{wp}} = 0$ m, the rate of fluidisation of the dry powder, U_{pickup}, is limited and set equal to the infiltration rate, U_{w}. Phenomenologically, this corresponds to a regime where UO_2 powder wetted through hydrostatic pressure-driven water infiltration becomes instantaneously fluidised and enters the suspension region.

When the average gas velocity through the suspension is below the critical gas velocity, ($\bar{U}_{\mathrm{g}}(t) < U_{\mathrm{g,crit}}$), as described in more detail in Section 5.2.3, sedimentation will be the dominant interface phenomenon. The UO_2 powder is assumed to settle on the surface of the settled wet powder at a constant bulk density, ensuring that the UO_2 powder in the settled wet powder region remains homogeneously distributed.

At the top of the domain the following boundary condition is prescribed to the gaseous components, j = rg, v:

$$D_{\mathrm{sus}}(t, H_{\mathrm{dp+wp+sus}})\frac{\partial V'_{\mathrm{j,sus}}(t, H_{\mathrm{dp+wp+sus}})}{\partial z} + U_{\mathrm{net,j,sus}}(t, H_{\mathrm{dp+wp+sus}})V'_{\mathrm{j,sus}}(t, H_{\mathrm{dp+wp+sus}}) = -U_{\mathrm{g}}(t, H_{\mathrm{dp+wp+sus}})V'_{\mathrm{j,sus}}(t, H_{\mathrm{dp+wp+sus}}) \quad (5.11)$$

For the suspended powder (j = p), the following boundary condition is prescribed:

Table 5.3: Source and sinks for each component in each region in the thermal energy equations.

Region, k	Component, j	$E'_{\text{net,j,k}}(t,z)$ [J m^{-1} s^{-1}]
Dry powder	UO_2 powder	$E'_{\text{gen,p}}(t,z)$
Settled wet powder	UO_2 powder	$E'_{\text{gen,p}}(t,z) - E'_{\text{convec,p}}(t,z) - E'_{\text{boil,p}}(t,z)$
Settled wet powder	Water	$E'_{\text{gen,w}}(t,z) + E'_{\text{convec,p}}(t,z)$
Suspension	UO_2 powder	$E'_{\text{gen,p}}(t,z) - E'_{\text{convec,sus}}(t,z) - E'_{\text{boil,p}}(t,z)$
Suspension	Water	$E'_{\text{gen,w}}(t,z) + E'_{\text{convec,sus}}(t,z)$

$$D_{\text{sus}}(t,H_{\text{dp+wp+sus}})\frac{\partial V'_{\text{p,sus}}(t,H_{\text{dp+wp+sus}})}{\partial z} + U_{\text{net,p,sus}}(t,H_{\text{dp+wp+sus}})V'_{\text{p,sus}}(t,H_{\text{dp+wp+sus}}) = 0 \quad (5.12)$$

and for the water component (j = w), the following boundary condition is prescribed:

$$D_{\text{sus}}(t,H_{\text{dp+wp+sus}})\frac{\partial V'_{\text{w,sus}}(t,H_{\text{dp+wp+sus}})}{\partial z} + U_{\text{net,w,sus}}(t,H_{\text{dp+wp+sus}})V'_{\text{w,sus}}(t,H_{\text{dp+wp+sus}}) = -U_{\text{w,in}}\pi R^2 \quad (5.13)$$

5.2.2 General Form of Governing Equations for Nuclear Thermal Hydraulics

The governing equations for the nuclear thermal hydraulics are similar to those stated in Section 3.2.7, with alterations introduced to account for the fluidisation and sedimentation of UO_2 powder particles in the suspension region, located above the settled wet powder bed. For the dry and settled wet static UO_2 powder (i.e. for j = p, k = dp, wp), Equation (3.46) remains valid.

The following thermal energy equation previously outlined by Equation (3.48), is now applicable not only to pore water and suspended water, but also to the suspended UO_2 powder (i.e. for j = w, k = wp, sus and for when j = p, k = sus):

$$c_{\text{j}}\left[\frac{\partial}{\partial t}\left(M'_{\text{j,k}}(t,z)T_{\text{j,k}}(t,z)\right) - \frac{\partial}{\partial z}\left(D_{\text{k}}(t,z)\frac{\partial}{\partial z}\left(M'_{\text{j,k}}(t,z)T_{\text{j,k}}(t,z)\right) + U_{\text{net,j,k}}(t,z)M'_{\text{j,k}}(t,z)T_{\text{j,k}}(t,z)\right)\right] = E'_{\text{net,j,k}}(t,z) \quad (5.14)$$

where the expression for $U_{\text{net,j,k}}$ is given in Table 5.1. The thermal energy source/sink term, $E'_{\text{net,j,k}}$, now has additional components related to thermal energy generation and exchange in the suspension region and is described in Table 5.3.

The interface and boundary conditions take a similar form to those for the mass continuity equations. At the wetting front, where $z = H_{\text{dp}}$, when $H_{\text{wp}} > 0$ m, the powder interface condition is given

by:

$$\kappa_{\mathrm{p}}(T_{\mathrm{p,dp}})v_{\mathrm{f,p,dp}}\frac{\partial T_{\mathrm{p,dp}}(t,H_{\mathrm{dp}})}{\partial z}=\kappa_{\mathrm{p}}(T_{\mathrm{p,wp}})v_{\mathrm{f,p,wp}}\frac{\partial T_{\mathrm{p,wp}}(t,H_{\mathrm{dp}})}{\partial z} \tag{5.15}$$

No thermal exchange of the pore water is permitted across the wetting front, leading to the following prescribed interface condition at $z=H_{\mathrm{dp}}$:

$$D_{\mathrm{wp}}(t,H_{\mathrm{dp}})\frac{\partial}{\partial z}\left(M'_{\mathrm{w,wp}}(t,H_{\mathrm{dp}})T_{\mathrm{w,wp}}(t,H_{\mathrm{dp}})\right)+U_{\mathrm{net,w,wp}}(t,H_{\mathrm{dp}})M'_{\mathrm{w,wp}}(t,H_{\mathrm{dp}})T_{\mathrm{w,wp}}(t,H_{\mathrm{dp}})=0 \tag{5.16}$$

The Robin boundary condition at the interface between the pore water and water present in the suspended powder region is defined as:

$$\begin{aligned}D_{\mathrm{wp}}(t,H_{\mathrm{dp+wp}})\frac{\partial}{\partial z}&\left(M'_{\mathrm{w,wp}}(t,H_{\mathrm{dp+wp}})T_{\mathrm{w,wp}}(t,H_{\mathrm{dp+wp}})\right)\\&+U_{\mathrm{net,w,wp}}(t,H_{\mathrm{dp+wp}})M'_{\mathrm{w,wp}}(t,H_{\mathrm{dp+wp}})T_{\mathrm{w,wp}}(t,H_{\mathrm{dp+wp}})\\&=D_{\mathrm{sus}}(t,H_{\mathrm{dp+wp}})\frac{\partial}{\partial z}\left(M'_{\mathrm{w,sus}}(t,H_{\mathrm{dp+wp}})T_{\mathrm{w,sus}}(t,H_{\mathrm{dp+wp}})\right)\\&\quad+U_{\mathrm{net,w,sus}}(t,H_{\mathrm{dp+wp}})M'_{\mathrm{w,sus}}(t,H_{\mathrm{dp+wp}})T_{\mathrm{w,sus}}(t,H_{\mathrm{dp+wp}})\end{aligned} \tag{5.17}$$

When the average gas velocity through the settled wet powder exceeds the critical gas velocity and there is a mass transfer and thermal energy transfer of UO_2 powder from the settled wet powder region to the suspension. When sedimentation is the dominant interface phenomenon, there is a thermal advective component applied at the interface that corresponds to the settling of UO_2 powder particles on the surface of the static wet UO_2 powder bed. The following interface condition may be applied:

$$\begin{aligned}c_{\mathrm{p}}\Bigg[D_{\mathrm{sus}}(t,H_{\mathrm{dp+wp}})\frac{\partial}{\partial z}&\left(M'_{\mathrm{p,sus}}(t,H_{\mathrm{dp+wp}})T_{\mathrm{p,sus}}(t,H_{\mathrm{dp+wp}})\right)\\&+U_{\mathrm{net,p,sus}}(t,H_{\mathrm{dp+wp}})M'_{\mathrm{p,sus}}(t,H_{\mathrm{dp+wp}})T_{\mathrm{p,sus}}(t,H_{\mathrm{dp+wp}})\Bigg]\\&=\kappa_{\mathrm{p}}(T_{\mathrm{p,wp}})V'_{\mathrm{p,wp}}\frac{\partial T_{\mathrm{p,wp}}(t,H_{\mathrm{dp+wp}})}{\partial z}+M'_{\mathrm{p,wp}}c_{\mathrm{p}}U_{\mathrm{pickup}}T_{\mathrm{p,wp}}(t,H_{\mathrm{dp+wp}})\mathbf{S}_1\\&\quad-M'_{\mathrm{p,sus}}(t,H_{\mathrm{dp+wp}})c_{\mathrm{p}}\left(U_{\mathrm{p}}(t,H_{\mathrm{dp+wp}})\right.\\&\quad\left.+U_{\mathrm{w}}(t)(1-v_{\mathrm{f,p,wp}})\Delta S_{\mathrm{w}}\right)V'_{\mathrm{p,sus}}(t,H_{\mathrm{dp+wp}})T_{\mathrm{p,sus}}(t,H_{\mathrm{dp+wp}})\mathbf{S}_2\end{aligned} \tag{5.18}$$

At the top of the domain, the infiltration of water from a fire-suppression system, introduces thermal energy into the system. This is represented in the thermal energy equation by the following boundary condition:

$$D_{\text{sus}}(t, H_{\text{dp+wp+sus}})\frac{\partial}{\partial z}\left(M'_{\text{w,sus}}(t, H_{\text{dp+wp+sus}})T_{\text{w,sus}}(t, H_{\text{dp+wp+sus}})\right)$$
$$+ U_{\text{net,w,sus}}(t, H_{\text{dp+wp+sus}})M'_{\text{w,sus}}(t, H_{\text{dp+wp+sus}})T_{\text{w,sus}}(t, H_{\text{dp+wp+sus}}) = -U_{\text{w,in}}\pi R^2\rho_{\text{w,th}}T_{\text{w,in}} \quad (5.19)$$

The following boundary condition is prescribed for the thermal energy exchange of UO_2 powder across the surface of the suspension:

$$D_{\text{sus}}(t, H_{\text{dp+wp}})\frac{\partial}{\partial z}\left(M'_{\text{p,sus}}(t, H_{\text{dp+wp}})T_{\text{p,sus}}(t, H_{\text{dp+wp}})\right)$$
$$+ U_{\text{net,p,sus}}(t, H_{\text{dp+wp}})M'_{\text{p,sus}}(t, H_{\text{dp+wp}})T_{\text{p,sus}}(t, H_{\text{dp+wp}}) = 0 \quad (5.20)$$

5.2.3 UO_2 Settled Powder Bed Fluidisation Under Critical Gas Velocity Conditions

A transient nuclear criticality excursion initiated by the infiltration of water into the low-enriched UO_2 powder bed has been predicted in previous chapters to lead to significant gas production through the radiolysis and boiling of water. The creation and advection of gas bubbles is expected to result in gas bubble-particle interaction forces (Abraham et al., 1992). Gas bubbles, at high enough velocities or with enough force, may displace UO_2 powder particles, causing them to become suspended above the settled wet powder bed, through a process known as fluidisation (Fan and Newcomer, 1981). The re-distribution of fissile mass within the continuous water phase (acting as moderator) is expected to significantly alter the reactivity of the wetted UO_2 powder system.

The critical gas velocity corresponds to the gas bubble velocity required for all particles in a suspension to become and remain suspended due to gas bubble-particle interactions (Fan and Newcomer, 1981). These interactions may either be direct contact or interactions through wakes and turbulent eddies left by advecting gas bubbles (Abraham et al., 1992). Fan (1989) notes that a number of factors affecting this critical point, including the liquid flow rate, liquid viscosity, powder particle diameter and powder particle density. Abraham et al. (1992) provides a comprehensive summary of the range of empirical equations that have been developed for evaluating the critical gas velocity in three-phase bubble columns. However, Badgujar et al. (1986) and Koide et al. (1983) have noted that generally, these empirical critical gas velocity equations are not applicable to systems for which the correlations were not created for. Muroyama and Fan (1985) also lists a variety of correlations for the critical gas velocity in counter-current three-phase fluidised beds where gas is the continuous phase and water enters the system as a spray from the upper surface. However, a similar conclusion as in Abraham et al. (1992) is made where these correlations are purely empirical and estimates of the minimum gas fluidisation velocity varies significantly between each correlation. A more theoretical approach

described in Ergun and Orning (1949) has been successfully used to model two-phase fluidisation phenomenon. A similar approach for three-phase fluidised beds has proposed by Fan (1989) which requires an empirical relation for the apparent friction coefficient for the counter-current three-phase system. However, an empirical relation for the apparent friction coefficient does not exist for the system proposed.

Furthermore, industrial use of three-phase fluidised beds usually uses a perforated plate for gas-bubble entry, located at the bottom of the fluidised bed column, which can significantly affects the hydrodynamic behaviour of the fluidised bed (Gel'perin et al., 1968). This is significantly different from the proposed model where gas bubble nucleation and growth occurs from within the powder bed itself, on the surface of UO_2 powder particles. In the proposed model, these gas bubbles then advect upwards whilst water moves downwards through gravity, similar to a counter-current three-phase fluidised bed (Fan, 1989). This difference between the gas-bubble entry/nucleation phenomenon supports the conclusion that the three-phase fluidised bed critical gas velocity and fluidisation rate empirical correlations cannot be used for the proposed model.

Since the empirical correlations listed by Abraham et al. (1992) and Muroyama and Fan (1985) were developed for systems that do not bear significant similarities to the present UO_2 powder, water, radiolytic gas and steam system, an alternative parametric approach has been used. Using this method a specific critical gas velocity, $U_{\text{g,crit}}$ [m s^{-1}], and a rate of fluidisation, U_{pickup} [m s^{-1}], have been defined. Mass transfer from the settled wet powder region to the suspension region occurs when the average gas velocity through the settled wet powder exceeds the critical gas velocity. In this regime, the dominant mass transfer process within the suspension is predicted to be gas-bubble induced turbulent mixing, this is described further in Section 5.2.8. When the mean gas velocity around settled wet UO_2 powder particles falls below the critical gas velocity, the mass transfer regime in the suspension changes to become one where sedimentation is dominant. When complete fluidisation of the settled wet powder bed occurs, i.e. when $H_{\text{wp}} = 0$ m, the average gas velocity is calculated across the suspension region. The critical gas velocity and rate of fluidisation parameters were varied and the resulting transient nuclear criticality excursion characteristics were simulated. This approach captured the characteristics of transient nuclear criticality excursions for the full range of critical gas velocities and fluidisation rates expected. The mean gas velocity through the settled wet powder and suspension, $\bar{U}_{\text{g}}(t)$ [m s^{-1}], is calculated from Equation (3.45), using region averaged dynamic viscosity and effective bulk densities.

5.2.4 Water Infiltration Into Powder Beds With Fluidisation

The present model assumes that water infiltration may be modelled by the Green-Ampt equation (Green and Ampt, 1911). This approach, previously described in Section 3.2.4, assumes that the flow of water may be characterised as incompressible and creeping, with a low Reynolds number (Green and Ampt, 1911). The distance over which the pressure head acts is usually the height of the settled wet powder bed, H_{wp}. When the wetted UO_2 powder bed does not remain static and fluidisation occurs, a reduction in the settled wet powder bed height due to fluidisation results in an increase in the pressure gradient and a corresponding increase in the water infiltration rate into the dry powder. This leads to the following limit, preventing complete fluidisation of the settled wet powder bed:

$$\lim_{H_{\mathrm{wp}} \to H_{\mathrm{wp,min}}} \left(U_{\mathrm{w}}(t) \right) = U_{\mathrm{pickup}} \tag{5.21}$$

where $H_{\mathrm{wp,min}}$ [m] is the height of the wet powder bed that causes an equal rate of penetration into the dry powder with the rate at which settled wet UO_2 powder particles enter the suspension through fluidisation.

For high fluidisation rates, the increased pressure gradient, resulting in an increased water infiltration rate, may cause large positive reactivities to be inserted into the system, as dry UO_2 powder becomes wetted and well dispersed in moderator at a far higher rate than when there is no fluidisation. Phenomenologically, a significant increase in the water infiltration rate at high fluidisation rates would not be predicted, since the weight of material above the wetting front does not increase. Therefore, to prevent significant increases in the water infiltration rate and to allow for complete fluidisation of the wetted UO_2 powder, the gradient over which the pressure acts is prescribed $H_{\mathrm{dp+wp}}(0) - H_{\mathrm{dp}}(t)$, where the term $H_{\mathrm{dp+wp}}(0) = 0.6217$ m represents the initial fully unsaturated height of the UO_2 powder bed. This results in the following expression for the rate of water infiltration into the dry UO_2 powder:

$$U_{\mathrm{w}}(t) = -\frac{k(1 - \bar{v}_{\mathrm{f,g,wp}}(t))}{2(1 - v_{\mathrm{f,p,wp}})\Delta S_{\mathrm{w}} \mu_{\mathrm{w}} (H_{\mathrm{dp+wp}}(0) - H_{\mathrm{dp}}(t))} \Delta P_{\mathrm{tot}}(t) \tag{5.22}$$

where $\Delta P_{\mathrm{tot}}(t) = \Delta P_{\mathrm{sus}}(t) + \Delta P_{\mathrm{wp}}(t)$ [Pa] is the change in pressure due to gravity from the free surface, located at the top of the suspension, above the settled powder bed, to the wetting front and k is the permeability of the UO_2 powder bed.

The proposed model estimates the pressure drop across the suspended powder region using the equation described by Wozniak (1977) for the pressure drop across a counter-current fluidised bed:

$$\Delta P_{\mathrm{sus}}(t) = \int_{H_{\mathrm{dp+wp}}}^{H_{\mathrm{dp+wp+sus}}} \left(v_{\mathrm{f,p,sus}}(t,z)\rho_{\mathrm{p,th}} + v_{\mathrm{f,w,sus}}(t,z)\rho_{\mathrm{w,th}} + v_{\mathrm{f,g,sus}}(t,z)\rho_{\mathrm{g,th}} \right) g dz \tag{5.23}$$

This expression assumes that the pressure drop can be expressed using only the static pressure component. This has been deduced for the steady-state case by Wallis (1969), when neglecting the frictional drag on the walls of the cylindrical container and by neglecting the acceleration of the gas and liquid flows. This equation has been successfully used to evaluate pressure drops in three-phase fluidised beds under counter-current flow conditions by Ermakova (1970) and Barile and Meyer (1971).

The pressure drop across the settled wet powder bed, ΔP_{wp}, is given by the following expression:

$$\Delta P_{\mathrm{wp}}(t) = \int_{H_{\mathrm{dp}}}^{H_{\mathrm{dp+wp}}} \left(v_{\mathrm{f,w,wp}}(t,z)\rho_{\mathrm{w,th}} + v_{\mathrm{f,g,wp}}(t,z)\rho_{\mathrm{g,th}} \right) g dz \tag{5.24}$$

5.2.5 Gas Bubble Induced Ejection of Powder and Water

The production of large volumes of radiolytic gas bubbles and steam may introduce a phenomenon whereby mixtures of fluid and solid UO_2 particles are ejected from the suspension, into the 'freeboard' region, located axially above the suspension. The following section outlines a numerical approach to simulating single particle trajectories in air, which may be used to estimate the volume of the ejected material that may leave the domain and not return. To evaluate whether this effect may be neglected, certain approximations are made. These approximations include assuming that the ejected material remains as one spherical mass. Realistically, the ejected material may form a number of different UO_2 powder-water agglomerated masses that may be ejected at numerous angles. Additionally, it is assumed that all the momentum imparted onto the ejected material at the initial point of ejection is in the direction of the launch. This ensures that maximum momentum is prescribed parallel to the initial launch angle. In the literature, competing hypotheses exist regarding the source of the energy that causes the material ejection (Levy et al., 1983). Santana et al. (2005) notes that ejection may occur due to energy transfer across the bubble dome or through the bubble wake. Pemberton and Davidson (1986) and Do et al. (1972) suggested that the amount of material ejected from the suspension corresponded to the amount of material located above the bubble bulge once it reached the surface.

Pemberton and Davidson (1986) proposed a three-stage approach to modelling this phenomenon, whereby initially particles are entrained on the upper surface of the gas bubble, forming a dome-like shape. As the gas bubble moves upwards, particles fall off the side of the bubble. Once the bubble reaches the surface of the fluidised bed, momentum exchange from the material in the wake to the material on the dome of the bubble provide an impulse that ejects upwards from the suspension.

The mechanistic model outlined by Pemberton and Davidson (1986) for two-phase gas-solid bubbling fluidised beds relies on a conservation of momentum between the wake of a bubble and the upper dome section of the bubble. This methodology has been applied to the proposed three-phase fluidised bed model. The approach assumes that the momentum of the wake generates an impulsive force on the hemispherical dome of powder and water, located just above the bubble, as it advects upwards. The thickness of this dome decreases due to the 'falling off' of powder particles and water from the top of the sphere past the edges and back into the bulk suspension. The final thickness of the dome at the point of bubble eruption has been shown to be similar to the diameter of a single powder particle (Almendros-Ibáñez et al., 2006). Therefore, for a single bubble in a three-phase fluidised bed, it is assumed that eruption at the surface causes a volume of material of thickness, d_{agg} [m], and diameter, d_{b} [m], to be ejected from the bed. The variable d_{agg} refers to the size of an agglomerated UO_2 powder-water particle, which is described further in Section 5.2.6.

The present model uses the conservation of momentum proposed by Pemberton and Davidson (1986) to evaluate the approximate initial velocity of the ejected layer, U_{eject} [m s^{-1}]:

$$U_{\text{eject}}(t) = U_{\text{g}}(t, H_{\text{dp+wp+sus}}) f_{\text{w}} \frac{d_{\text{b}}(t, H_{\text{dp+wp+sus}})}{3 d_{\text{agg}}} \tag{5.25}$$

where $f_w = 0.1$ is the volume fraction of the bubble occupied by the wake. Although significant research has been carried out examining this parameter (see Fan (1989)), most correlations are empirical in nature and derived for systems not similar to the UO_2 powder-water-radiolytic gas/steam system considered here. Therefore, a constant value is prescribed for this mechanistic approach. Increasing the wake volume fraction is expected to result in greater momentum exchange into the ejected material, enabling higher ejection velocities.

By calculating the material trajectory, it is possible to determine whether the material will escape the cylindrical vessel housing the UO_2 suspension. Using the method described in Do et al. (1972), the equation of motion for a spherical particle trajectory can be derived directly from Newton's second law, by balancing drag with gravitational forces. Buoyancy is neglected in the air above the suspension since the density of the continuous gas/air mixture above the suspension is expected to be of sufficiently low density relative to the ejected material density, which consists of UO_2 powder and water. Furthermore, the ejected material is assumed to act as one agglomerated spherical particle and neglects the influence of turbulence in the 'freeboard' region above the suspension. This is a significant approximation since it is likely that ejected material will form a number of individual agglomerated particles rather than a single particle. A single heavier particle will have a greater momentum than smaller particles travelling at the same velocity, which may cause the particle to travel further, depending on the relative magnitudes of the drag force. The single particle approach would then estimate the furthest distance that the particulate may travel. However, smaller particulates may have larger trajectories than a single large particulate if a large fraction of the total impulse from the bubble wake is imparted on it, since this would produce larger initial ejection velocities. The gas bubble velocity and corresponding dome and wake material velocities are assumed to have only vertical components to flow. Therefore, for the conservation of momentum across the bubble between the material in the wake and the dome, the ejected material must be launched at an angle perpendicular to the top of the suspension. This would suggest that all ejected material would re-enter the suspension after some time, since no horizontal component to the trajectory of the ejected material will exist. Practically, the material may be ejected at some angle from vertical along the surface of the hemispherical gas bubble bulge. Santana et al. (2005) experimentally showed that the ejection velocity of particulates from a gas-bubble varied linearly over the angle of ejection, with the peak ejection velocity occurring for the case of vertical ejection. Other velocity profiles across the gas bubble dome have been proposed, all of which propose that the peak velocity occurs for vertical ejection (Fung and Hamdullahpur, 1993; Peters and Prybylowski, 1983). The proposed model aims to calculate maximum ejection distances by taking a conservative approach, assuming a flat velocity profile is present across the hemispherical dome.

A two-dimensional representation of the forces acting on an ejected mass is shown in Figure 5.3 where $\mathbf{F}_d$ [N] is the drag force vector, $\mathbf{F}_g$ [N] is the force vector of gravity, θ is the ejection angle relative to the surface of the suspension and $\mathbf{v}$ is the velocity vector.

The expression for the equation of motion of the ejected particle is:

$$\frac{d\mathbf{v}(t)}{dt} = -\frac{3C_D(t)\rho_{g,free}\mathbf{v}(t)|\mathbf{v}(t)|}{4\rho_{agg}d_{agg}} + g\hat{\mathbf{z}} \tag{5.26}$$

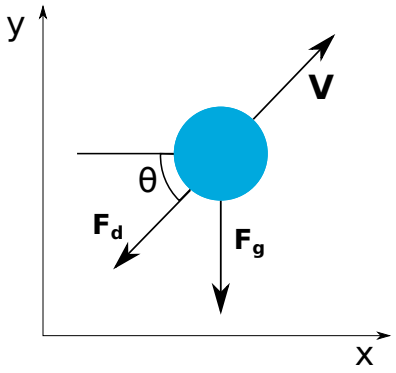

Figure 5.3: An illustrative representation of ejected material force balance.

where $\mathbf{v}(t)$ is the velocity of the ejected material, $\rho_{\text{g,free}}$ is the free air density [kg m^{-3}] and ρ_{agg} is the agglomerate density [kg m^{-3}]. The speed of the air in the 'freeboard' region is assumed to be negligible compared to the ejected material velocity and is therefore neglected. The variable C_{D} [-] represents the drag coefficient.

Using the approximation that the ejected particle is spherical, the drag coefficient, C_{D}, may be is given by (Do et al., 1972):

$$C_{\text{D}}(t) = \frac{24}{Re_{\text{eff}}(t)}(1 + 0.15Re_{\text{eff}}^{0.687}(t)) + \frac{0.42}{1 + 4.25 \times 10^4 Re_{\text{eff}}^{-1.16}(t)} \tag{5.27}$$

where the agglomerated spherical ejected material Reynolds number through air is given by:

$$Re_{\text{eff}}(t) = \frac{\rho_{\text{g,free}}|\mathbf{v}(t)|d_{\text{agg}}}{\mu_{\text{g,free}}} \tag{5.28}$$

where Re_{eff} [-] is the agglomerate Reynolds number in the 'freeboard' region, located above the suspension, and $\mu_{\text{g,free}}$ [Pa s] is the corresponding air viscosity.

The position of the ejected material, $\mathbf{s}(t)$, at a time, t, is given by:

$$\frac{d\mathbf{s}(t)}{dt} = \mathbf{v}(t) \tag{5.29}$$

The material ejection speed, as a function of the gas bubble size is shown in Figure 5.4. Gas bubble velocities were estimated using Equation (3.45).

Using the data given in Table 5.4, Equations (5.26) and (5.29) have been solved numerically using a Python-based BDF ODE solver, for varying material launch angle, initial ejection speed and material composition (amount of UO_2 powder relative to water). The predicted trajectories of the material are shown in Figure 5.5. The maximum trajectory height is found for a vertical launch angle, with high solid volume fraction and high initial ejection speed. This is expected since the denser material (higher solid volume fraction), travelling at higher initial ejection rates, has a greater initial momentum and

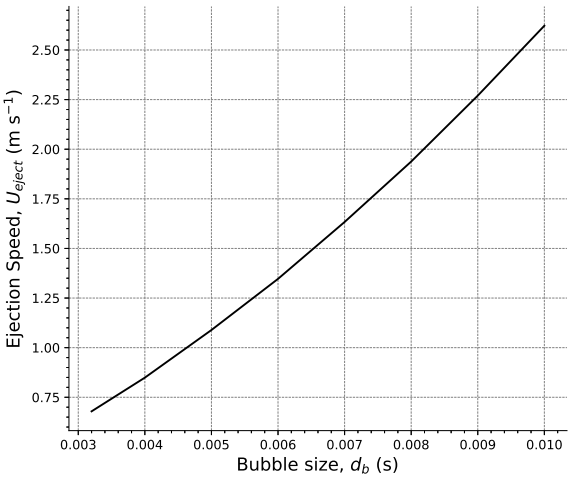

Figure 5.4: The ejection speed of agglomerated material as a function of the erupting gas bubble size.

therefore travels further. The maximum ejection height is shown to be 0.019 m and the corresponding maximum radial distance travelled is approximately 0.0215 m. These values are significantly less than the proposed cylindrical vessel geometry that houses the UO_2 suspension, where $R_{\text{cyl}} = 0.4$ m and $H_{\text{cyl}} = 1.0$ m, and therefore, a significant volume of ejected material is expected to land back onto the surface of the suspension. Consequently, the proposed phenomenological model neglects the ejection of material from the domain. However, the proposed phenomenological model in this Chapter still considers the overflowing of the domain due to significant void creation pushing material upwards, which may cause large volumes of material to leave the domain.

Table 5.4: Parameters used to estimate trajectory of UO_2-water agglomerated mixture.

$\rho_{\text{p,th}}$	$\rho_{\text{w,th}}$	$\rho_{\text{g,free}}$	$\mu_{\text{g,free}}$	d_{agg}	$t(0)$	$\mathbf{s}(0)$
10950.0 kg m^{-3}	998.1 kg m^{-3}	1.204 kg m^{-3}	18.13×10^{-6} Pa s	30 μm	0 s	0.0 m

5.2.6 Characterisation of Agglomerated UO_2 Powder Hindered Settling Velocity

A nuclear criticality excursion may occur in a fissile suspension when geometric changes, caused by sedimentation, leads UO_2 powder particles to form a more dense configuration at the bottom of the vessel. This process is in part governed by the concentration and agglomeration characteristics of the particles in the suspension (Janov et al., 1972). At low concentrations, the sedimentation rate of spherical particles can be characterised using Stokes law. Such an approach was used by Cova (1966) when modelling three-phase bubbling suspensions. At moderate concentrations, hindered settling occurs, where hydrodynamic interactions between particles reduce the settling speed of individual particles (Tadros, 2012).

The process whereby particles and fluid aggregate into effectively larger particles is known as agglomeration. Fissile particles, bound loosely by inter-molecular forces, form larger agglomerated particles that have larger effective sizes and different densities (Hartley et al., 1985; Balakrishna et al., 2009). These larger effective particles have been shown to sediment at a rate far greater than their constituent particles (Janov et al., 1972).

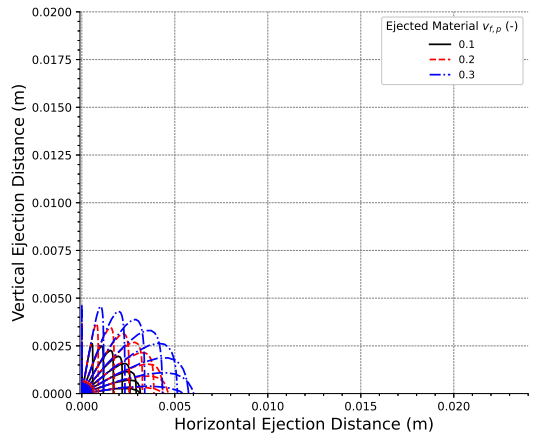

(a) $U_{\text{eject}} = 0.75$ m s^{-1}

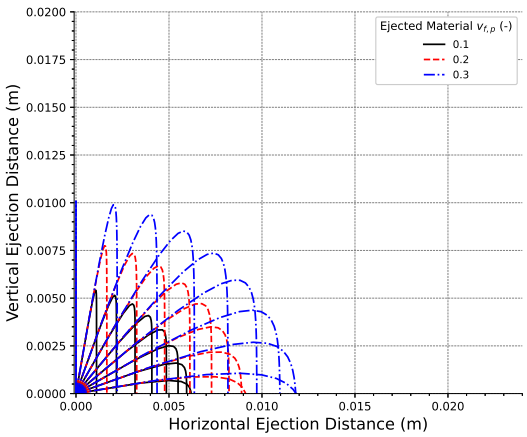

(b) $U_{\text{eject}} = 1.5$ m s^{-1}

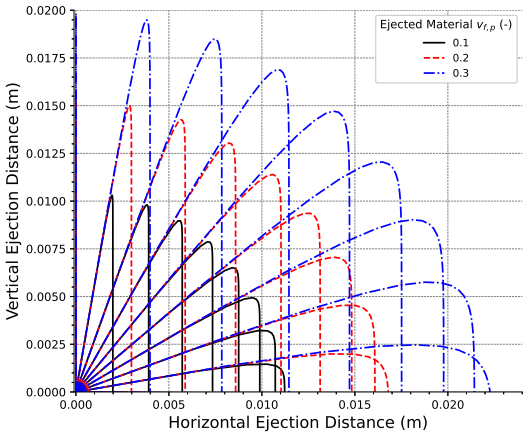

(c) $U_{\text{eject}} = 2.5$ m s^{-1}

Figure 5.5: Trajectory of ejected material with varying solid volume fraction ($v_{\text{f,p}}$), intial ejection speed (U_{eject}), and launch angle (θ).

Steinour (1944c) describes an adjustment to Stokes law that describes the free settling speed of agglomerated particles as (Steinour, 1944a,b):

$$U_{\text{st}} = \frac{d_{\text{agg}}^2}{18} \frac{\rho_{\text{agg}} - \rho_{\text{w,th}}}{\mu_{\text{w}}(1+\alpha)} g \tag{5.30}$$

where α is the ratio of immobilised liquid volume to the particle volume in the agglomerate. The effective density of the agglomerated particle, ρ_{agg}, is calculated as:

$$\rho_{\text{agg}} = \frac{\alpha \rho_{\text{w,th}} + \rho_{\text{p,th}}}{1+\alpha} \tag{5.31}$$

Steinour (1944c) outlines an empirical methodology for correcting the agglomerated particle Stokes equation to take the hydrodynamic forces between particles in the hindered settling regime into con-

sideration. The correction is defined as:

$$U_{\mathrm{p}}(t,z) = U_{\mathrm{st}}(1 - v_{\mathrm{f,agg}}(t,z))^2 10^{-1.82 v_{\mathrm{f,agg}}(t,z)} \tag{5.32}$$

where the agglomerated suspension volume fraction, $v_{\mathrm{f,agg}}$ is defined as:

$$v_{\mathrm{f,agg}}(t,z) = v_{\mathrm{f,p,sus}}(t,z)(1+\alpha) \tag{5.33}$$

By extrapolating experimental data relating to a number of particulates found throughout the nuclear fuel cycle shown in Figure 5.6a, to where the solid volume fraction, $v_{\mathrm{f,p,sus}} = 0$ and by using Equation (5.32), the parameter, α may be evaluated. Once the ratio of immobilized liquid volume to the particle volume in the agglomerate, α, is known, Equation (5.30) may be used to determine the effective agglomerate size, d_{agg}. Figure 5.6a shows that the empirical correlation can be well-fitted to experimental hindered settling data for uranium trioxide hydrate ($UO_3{\cdot}H_2O$) particles suspended in water (Boyd and Whitton, 1958), ammonium uranate ($(NH_4)_2U_2O_7$) particles in uranyl nitrate ($UO_2(NO_3)_2$) (Janov et al., 1972), uranium dioxide (UO_2) in acetone and benzene (Sesonske, 1961) and thorium dioxide (ThO_2) particles suspended in water (Reed and Crowley, 1956). Figure 5.6b shows that the size of agglomerated particles for the UO_2 suspension and ThO_2 suspension are similar, with similar values for α also being indicated. Furthermore, the density of these fissile powders and the size of individual powder particles are similar, indicating that the agglomeration and hindered settling properties of these suspensions may also be similar. The agglomerate size and α value for ADU slurry varied widely depending on the pH of the precipitant. This may be due to the complex network of agglomerates that were observed when precipitating ADU at different pH values (Janov et al., 1972).

The approach outlined by Steinour (1944c) is used in this study to characterise hindered settling rates for the agglomerated UO_2 suspension. The present study assumes that the mean agglomerate size is $d_{\mathrm{agg}} = 30$ μm. The corresponding predicted hindered settling rates of the UO_2 agglomerated particles in water are shown in Figure 5.7.

To determine the convective heat transfer coefficient and rate of convective heat transfer, the present model assumes that each UO_2 powder particle is fully surrounded by mobile liquid, neglecting the effect that the immobilised liquid has on interfacial heat transfer. This is not expected to introduce large errors into the model, since a large specific surface area between the powder and water has already been shown to lead to efficient interphase thermal convection and subsequent local thermal equilibrium between the UO_2 powder particles and water.

5.2.7 Gas Bubble Induced Turbulent Mixing

Turbulent mixing occurs in the fissile suspension due to the advection of radiolytic gas and steam bubbles through the system. The wakes and turbulent eddies left behind from the motion of the gas bubbles introduce significant mixing into the suspension (Fan, 1989). Since full turbulence models are complex, computationally expensive and beyond the scope of the proposed model, a simpler method using a Fickian approach as described by Nielsen and Teakle (2004) is used. This is characterised by

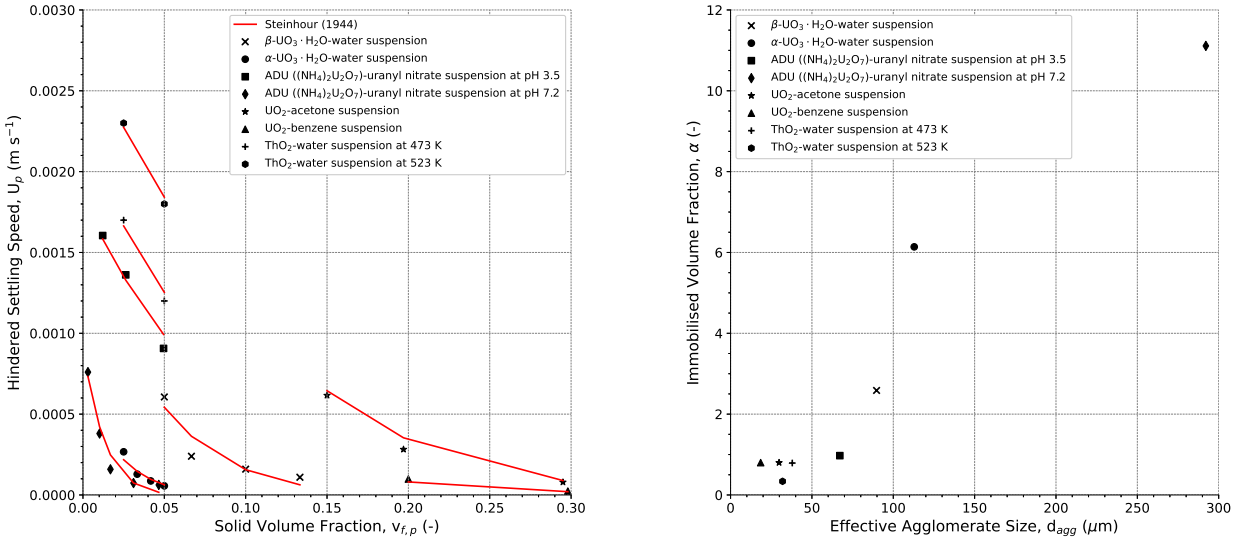

(a) (b)

Figure 5.6: (a) The hindered settling rate of an agglomerated suspension is shown as a function of the solid volume fraction of the suspension. Markers indicate the hindered settling speed of various agglomerated fissile particles from experimental investigations. The line corresponds to the Steinour hindered settling speeds calculated at the prescribed agglomerate solid volume fractions as outlined in Equation (5.33). (b) Parameters used to describe the agglomerate properties in the Steinour empirical equation.

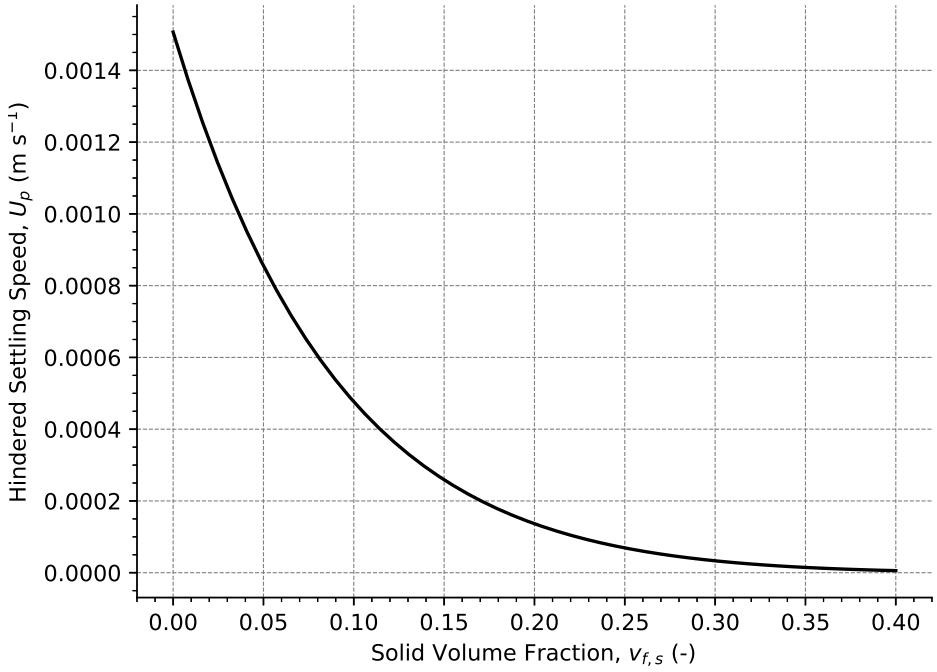

Figure 5.7: Predicted hindered settling rates for UO_2 powder dispersed in water with $\alpha = 0.8$ and $d_{\text{agg}} = 30$ μm.

the dispersion term in Equation (5.1). Quantification of this term in the proposed model relies on the use of empirical correlations from relevant literature.

Argo and Cova (1965) and Levenspiel and Bischoff (1959) showed that gas flow in two-phase water-gas systems introduced considerable mixing of the liquid. Kato et al. (1972) and Imafuku et al. (1968) found that for certain systems, a model of two-phase mixing is capable of successfully predicting particle mixing due to gas bubble advection in three-phase suspensions. Furthermore, in three-phase systems, the amount of mixing experienced by the particles and surrounding water due to the gas bubbles have been shown to be similar (Kalinske and Pien, 1943).

An empirical correlation described by Kato et al. (1972) relates the dimensionless Péclet and Froude numbers to determine the mixing coefficient of powder due to the interaction between radiolytic gas and steam bubbles and the surrounding liquid and powder in a three-phase slurry bubble column:

$$D_{\text{sus}}(t,z) = \frac{2U_{\text{g}}(t,z)R_{\text{cyl}}\left(1+8Fr(t,z)^{0.85}\right)}{13Fr(t,z)} \tag{5.34}$$

where the Froude number, $Fr(t,z) = U_{\text{g}}(t,z)/\sqrt{2gR_{\text{cyl}}}$.

Equation (5.34) corresponded well with experimental data produced by Imafuku et al. (1968) who looked at glass spheres, $FeSiO_2$ powder and copper (Cu) powder in water. This correlation also corresponds well with data produced by Smith and Ruether (1985), modelling glass beads in water and ethanol.

This empirical equation has been shown to model mixing in systems with particle sizes in the range of tens to hundreds of microns, which is comparable to the particle and agglomerate size of UO_2 powder particles (Kato et al., 1972; Imafuku et al., 1968; Clayton and Aronson, 1958). The vessel radii used to develop these correlations were much less (up to $R_{\text{cyl}} = 0.224$ m (Badgujar et al., 1986)) than for the present system, where $R_{\text{cyl}} = 0.4$ m. This is an important parameter since Badgujar et al. (1986) has shown that for mono-dispersed systems, larger diameter vessels have correspondingly larger turbulent mixing coefficients, leading to flatter powder particle distributions in the suspension. Figure 5.8 supports this, showing that the turbulent mixing coefficient, calculated using Equation (5.34), varies by over an order of magnitude for the present system when compared to the system described by Kato et al. (1972) with a lower vessel diameter.

5.2.8 Ratio of Powder Particle Advection to Dispersion in Suspension Region

The ratio of the advective motion of the UO_2 powder particles held within the suspension region, to the dispersive motion may be otherwise characterised as the Péclet number (Pe). For mass transfer problems in suspension systems, such as considered here, the Péclet number may be defined as:

$$Pe(t,z) = \frac{LU_{\text{p}}(t,z)}{D_{\text{sus}}(t,z)} \tag{5.35}$$

where L [m] is the characteristic length scale, which is the length over which the dispersive flux acts, the column diameter (D [m]). Figure 5.9 shows how the Péclet number varies as a function of

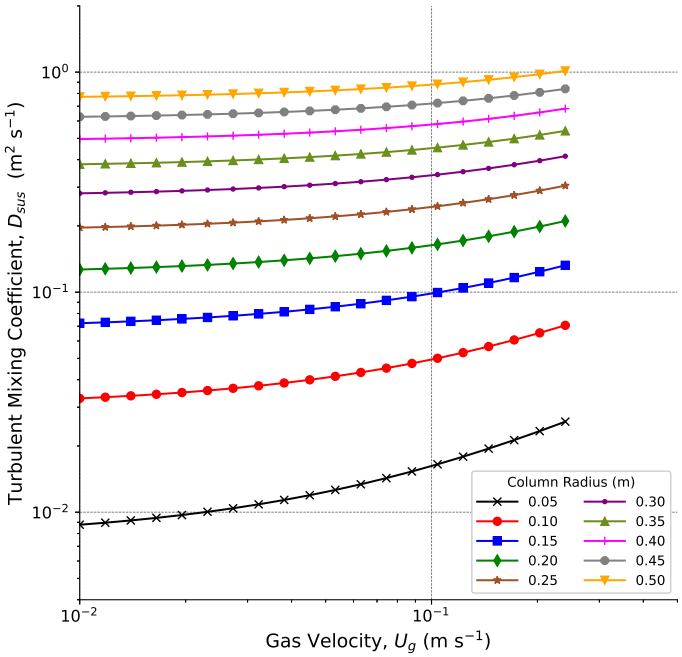

Figure 5.8: The turbulent mixing coefficient is plotted against the gas bubble velocity for a range of column diameters.

the dispersion coefficient and settling rate of the UO_2 suspension. The data has been produced by examining the expected range of dispersion coefficients and settling rates for the empirical correlations described in Equation (5.34) and Equation (5.32), respectively. The ratio of the advective to dispersive contributions to UO_2 agglomerate flow indicate that $Pe << 1$ for all particle and gas velocities predicted by these correlations, for this suspension system. This suggests that gas induced turbulent mixing of the suspension is a far more dominant process than sedimentation. This may be attributed to the large column to agglomerate diameter ratio that is present in this system ($D/d_{\text{agg}} = 26667$).

5.2.9 Region Height Change

New expressions are required for the change in height of each region that take into account sedimentation and fluidisation phenomena. The height of the settled wetted powder is a function of the infiltration rate, settling rate, settling density and the gas-induced re-suspension properties of the system. The corresponding equation may be defined as:

$$\frac{dH_{\text{wp}}(t)}{dt} = U_{\text{w}}(t) - U_{\text{pickup}}\mathbf{S}_1 + \frac{(U_{\text{p}}(t, H_{\text{dp+wp}}) + U_{\text{w}}(t)(1 - v_{\text{f,p,wp}})\Delta S_{\text{w}})V'_{\text{p,sus}}(t, H_{\text{dp+wp}})}{\pi R^2 v_{\text{f,p,wp}}}\mathbf{S}_2 \quad (5.36)$$

The change in height of the suspension is a function of the settling rate, infiltration rate, water incursion rate, gas bubble advection out of the system and the net change in volume of the discretised cell containing the free surface due to the generation of voids in the system (see Section 5.2.1). Using an intermediate variable to refer to the nominal change in height of the suspension, which does not

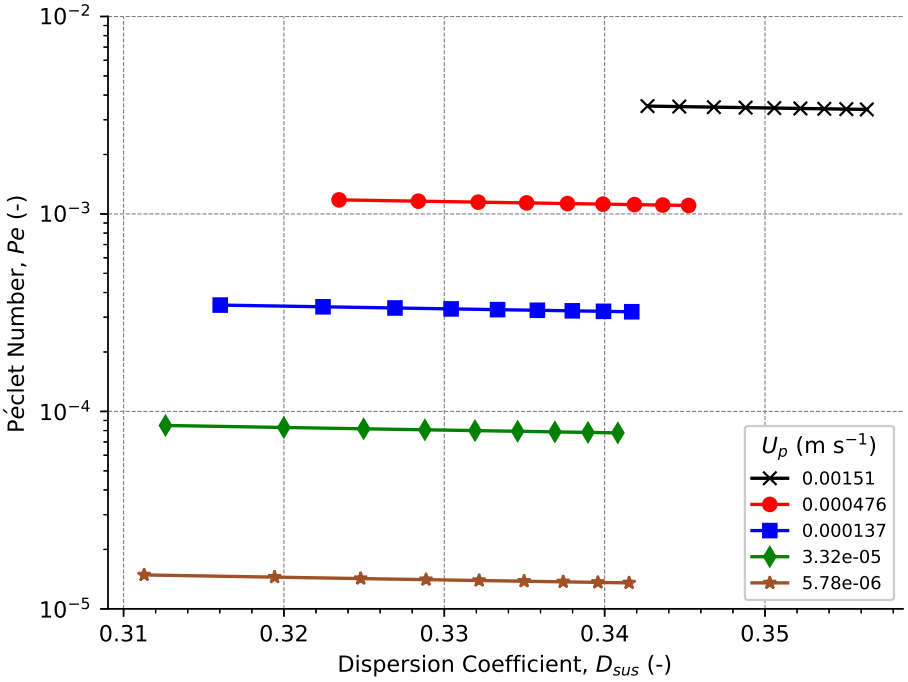

Figure 5.9: Péclet number for a range of dispersion coefficients and hindered settling rates.

depend on conditional phenomenon:

$$\frac{dH_{\text{nom}}(t)}{dt} = -U_{\text{w}}(t)\,(1 - v_{\text{f,p,wp}})\,\Delta S_{\text{w}} + U_{\text{w,in}} + U_{\text{adj,N}}(t) - \frac{U_{\text{g}}(t, H_{\text{dp+wp+sus}})}{\pi R^2}(V'_{\text{rg,sus}}(t, H_{\text{dp+wp+sus}}) + V'_{\text{v,sus}}(t, H_{\text{dp+wp+sus}})) \quad (5.37)$$

where $dH_{\text{nom}}(t)/dt$ [m s^{-1}] is an intermediate variable for Equation (5.38).

The change in height of the suspension may then be expressed as:

$$\frac{dH_{\text{sus}}(t)}{dt} = \frac{dH_{\text{nom}}(t)}{dt} + U_{\text{pickup}}\mathbf{S}_1 - \frac{(U_{\text{p}}(t, H_{\text{dp+wp}}) + U_{\text{w}}(t)(1 - v_{\text{f,p,wp}})\Delta S_{\text{w}})V'_{\text{p,sus}}(t, H_{\text{dp+wp}})}{\pi R^2 v_{\text{f,p,wp}}}\mathbf{S}_2 \quad (5.38)$$

where subscript N here refers to the discretised mesh cell that contains the top of the suspension (free surface).

The change in height of the dry powder region is a function of the infiltration rate of water into the powder bed as well as the pickup rate of dry powder, if there is no settled wet powder region:

$$\frac{dH_{\mathrm{dp}}(t)}{dt} = -U_{\mathrm{w}}(t) \tag{5.39}$$

5.3 Reactivity Feedback

5.3.1 Total Reactivity

The total reactivity, denoted R_{T}, consists of a number of individual reactivity components. In previous chapters, these components aimed to capture how the dynamics of temperature, voidage and moderation affect the neutron kinetic response of a sub- or prompt super-critical UO_2 powder-water-gas system. This chapter introduces two additional reactivity components, used to capture the effects that the re-distribution and loss fissile mass in the system has on the total reactivity. The total reactivity may now be expressed as:

$$\begin{aligned} R_{\mathrm{T}} = R_{\mathrm{imm}}(f_{\mathrm{imm,0}}) + \Delta R_{\mathrm{th,p,dry}}(\bar{T}_{\mathrm{p,dp}}, f_{\mathrm{imm,0}}) + \Delta R_{\mathrm{th,p,wp}}(\bar{T}_{\mathrm{p,wp}}, f_{\mathrm{imm,0}}) \\ + \Delta R_{\mathrm{th,w}}(\bar{T}_{\mathrm{w}}, f_{\mathrm{imm,0}}) + \Delta R_{\mathrm{void,wp}}(v_{\mathrm{f,g,wp}}, M_{\mathrm{p,wp}}) + \Delta R_{\mathrm{void,sus}}(v_{\mathrm{f,g,sus}}, M_{\mathrm{p,sus}}) \\ + \Delta R_{\mathrm{suspension}}(M_{\mathrm{p,sus}}, f_{\mathrm{imm,0}}) + \Delta R_{\mathrm{loss}}(M_{\mathrm{p,lost}}, f_{\mathrm{imm,0}}) \end{aligned} \tag{5.40}$$

The effect that fissile mass re-distribution has on the reactivity of the three-phase system is captured through the term $\Delta R_{\mathrm{suspension}}$. The term ΔR_{loss} represents the reactivity feedback component due to the reduction of UO_2 powder in the system as a result of overflowing of the domain from radiolytic gas and steam production. With the exception of the water infiltration reactivity feedback term, all components of reactivity are bi-variate. All reactivity components are stated in units of dollars ($).

The intrinsic neutron source used in Equation (3.1), calculated as the product of the intrinsic neutron source density and the volume of fissile material must now account for the variable volume of fissile material that may be present in the domain. In order to achieve this, it is necessary to define the following relation for the volume of UO_2 powder as a function of time in the domain:

$$V_{\mathrm{UO_2}}(t) = A_{\mathrm{cyl}} \left(v_{\mathrm{f,p,dp}} H_{\mathrm{dp}}(t) + v_{\mathrm{f,p,wp}} H_{\mathrm{wp}}(t) + \int_{H_{\mathrm{dp+wp}}}^{H_{\mathrm{dp+wp+sus}}} v_{\mathrm{f,p,sus}}(t, z) dz \right) \tag{5.41}$$

5.3.2 Wetting-Induced UO_2 Powder Bed Reactivity

Water infiltration into the UO_2 powder bed due to activation of a fire sprinkler system governs the rate of reactivity insertion into the sub-critical UO_2 powder bed. The reactivity component is modelled using the correlation described in Section 4.3.4 for the case of no slumping. The reactivity component equation and feedback coefficients are summarised in Equation (5.42) and Table 5.5, respectively.

$$R_{\text{imm}}(f_{\text{imm},0}) = \sum_{i=0}^{n} C_{\text{i}} f_{\text{imm},0}^{\text{i}} \tag{5.42}$$

Table 5.5: Wetting-induced reactivity feedback coefficients.

C_i	Sub-critical	Near/post delayed critical
0	-471.52	-120.44
1	7343.8	819.09
2	-5.1246e+04	-2016.5
3	1.8800e+05	2621.3
4	-3.4548e+05	-1735.8
5	2.4906e+05	460.90
R^2	0.9999	0.9999

5.3.3 Parameterisation of Reactivity Feedback Components Using Bivariate B-Spline Interpolation

Bivariate reactivity feedbacks capture the coupled effects that the primary independent variable and secondary parameter have on the reactivity of the system. Previously, bivariate polynomial representations of reactivity feedback surfaces have been used to estimate the effect of temperature, voidage and powder bed compaction on system reactivity, at values between those directly modelled using MCNP. Here, a bivariate B-spline interpolation technique is used for evaluating each reactivity feedback component outlined in Equation (5.40), with the exception of the wetting-induced reactivity component, denoted R_{imm}, which is evaluated using Equation (5.42). Using this approach, the tensor product of two sets of one-dimensional basis splines may be used to construct a bivariate spline that fits the recorded reactivity data found using MCNP. The bivariate B-spline is represented as (Hayes and Halliday, 1974):

$$S(x,y) = \sum_{i=1}^{N_x} \sum_{j=1}^{N_y} a_{\text{spline}}(i,j) B_{\text{x}}(i) B_{\text{y}}(j) \tag{5.43}$$

where $B_{\text{x}}(i)$ and $B_{\text{y}}(j)$ are one-dimensional B-spline basis functions and coefficients $a_{\text{spline}}(i,j)$ are the calculated B-spline coefficients, found using a least-squares regression algorithm (Dierckx, 1981). The number of basis splines in each dimension are given by N_{x} and N_{y}.

The suite of Fortran '77 subroutines developed by Dierckx (1981) may be used to generate the bivariate B-spline represented by Equation (5.43) for each reactivity feedback component. This approach uses a single smoothing parameter, ξ, to govern the compromise between fitting the recorded data perfectly and ensuring that the spline has minimal discontinuities in its derivatives. The use of this smoothing parameter and the methods developed in Dierckx (1981) eliminate the requirement for the user to determine the number and location of knots. The smoothing parameter, ξ, may be estimated using the number of recorded data points, N_{d}, as:

$$\xi = N_{\text{d}} - \sqrt{2N_{\text{d}}} \tag{5.44}$$

The polynomial order of each set of one-dimensional B-splines is varied for each reactivity component. Values of any given reactivity component may then be found at intermediate data points by interpolating the bivariate B-spline described by Equation (5.43).

5.3.4 Powder Suspension Reactivity Feedback

Gas-induced motion of the settled wet powder under critical gas velocity conditions will cause significant variations to the reactivity of the system by pushing powder into a less compact suspension. The proposed reactivity feedback component is modelled as a function of the bed immersion fraction, $f_{\text{imm},0}$, which gives information about the height of the dry powder bed, and the mass of UO_2 powder present in the suspension, denoted $M_{\text{p,sus}}(t)$. The suspension-based reactivity component may therefore be described as:

$$\Delta R_{\text{suspension}} = f(M_{\text{p,sus}}, f_{\text{imm},0}) - f(M_{\text{p,sus},0}, f_{\text{imm},0}) \tag{5.45}$$

where $f(M_{\text{p,sus}}, f_{\text{imm},0})$ is constructed using the method described in Section 5.3.3 and $M_{\text{p,sus},0} = 0$ kg.

A series of MCNP simulations were performed at regular bed immersion fractions, $f_{\text{imm},0}$ with varying powder suspension mass, $M_{\text{p,sus}}$. The MCNP simulations assume that the UO_2 powder entering the suspension is homogeneously dispersed throughout the region at a constant solid volume fraction. This is assumed to be an appropriate assumption due to the high turbulent mixing coefficients predicted by Equation (5.34), suggesting that the powder concentration profile will be homogeneous. The reactivities evaluated using MCNP were used to create the bivariate B-spline reactivity component shown in Figure 5.10. The polynomial order of the two one-dimensional B-spline sets were 5 and 4, corresponding to the bed immersion fraction and UO_2 suspension mass dimensions, respectively. Good agreement is predicted between the MCNP data and the bivariate B-spline ($R^2 = 0.98548$).

Under critical gas velocity conditions, results of these MCNP simulations indicate that fluidisation of the settled wet powder bed, generally introduces negative reactivity into the system. The initial negative reactivity feedback may be attributed to the re-distribution of powder from an under-moderated region to a region where the H/U ratio is very high. Figure 5.10 indicates that there is a maximum negative reactivity feedback effect as the powder becomes suspended. Past this point, any further re-distribution of powder from the settled region, where, $v_{\text{f,p,wp}} = 0.1461$, into the suspension begins to cause the reactivity feedback to become less negative. This may be attributed to the system becoming under-moderated, meaning that when the H/U ratio in the suspension decreases, there is a corresponding increase in the reactivity feedback component relative to the higher H/U ratio. For low bed immersion fractions where $f_{\text{imm},0} < 0.35$, complete fluidisation results in a positive reactivity feedback effect.

5.3.5 Void Reactivity Feedback

Previous chapters have shown that voids present in pore interstices introduce a negative reactivity feedback into the system by reducing the probability that a neutron will interact with target nuclei before leaking from the system. Previously this has been shown through a reactivity feedback compo-

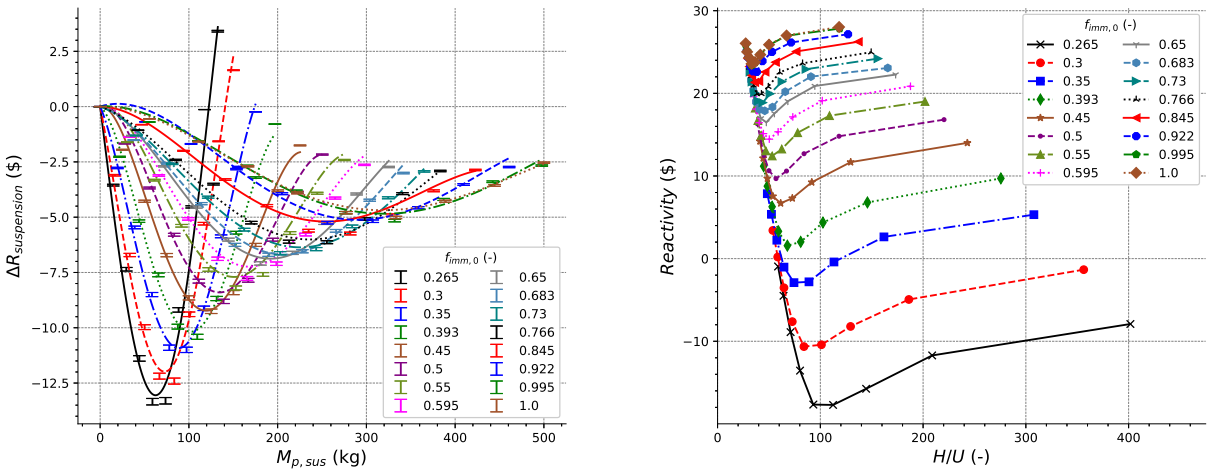

(a) (b)

Figure 5.10: (a) The reactivity component corresponding to the pickup of the powder from the bed, entering the suspension region. The error-bars correspond to MCNP simulated data points and the lines correspond to evaluated values of the reactivity feedback component, calculated using a bivariate B-spline interpolation technique. (b) The magnitude of the powder pickup reactivity feedback component as a function of the H/U ratio for the MCNP simulated cases.

nent that depends both on the void fraction, $v_{\mathrm{f,g}}$, and the bed immersion fraction, $f_{\mathrm{imm,0}}$. However, when fluidisation of the settled wet powder bed is taken into consideration, the mass of settled wet powder surrounding voids varies not only as a function of the bed immersion fraction, f_{imm}, but also as a function of the rate of fluidisation, U_{pickup}. Therefore, the reactivity feedback due to voids present in pore interstices must be described as a function of voidage and the mass of fissile material surrounding the void rather than the bed immersion fraction such that:

$$\Delta R_{\mathrm{void,wp}} = f(V_{\mathrm{g,wp}}, M_{\mathrm{p,wp}}) - f(V_{\mathrm{g,wp,0}}, M_{\mathrm{p,wp}}) \tag{5.46}$$

Similarly, in the suspended powder region, the void reactivity feedback component may be described by:

$$\Delta R_{\mathrm{void,sus}} = f(V_{\mathrm{g,sus}}, M_{\mathrm{p,sus}}) - f(V_{\mathrm{g,sus,0}}, M_{\mathrm{p,sus}}) \tag{5.47}$$

MCNP simulations were performed, examining the change in reactivity of the UO_2 powder bed as the void fraction in the settled wet powder and suspended powder regions varied from 0.0 to 0.5. For these MCNP simulations, the mass of powder present in the settled wet powder and suspended powder regions were also varied. In each case, the remaining mass not present in the phase under consideration was allocated to the dry powder region such that the total mass of UO_2 powder remained at 500 kg. Two-dimensional reactivity plots are shown in Figure 5.11.

Figure 5.11a indicates that the magnitude of the negative reactivity feedback due to the presence

of voids in the settled wet powder is greater when the mass of powder in the region is also greater. Voids introduced into the suspension region introduce negative reactivity into the system when the suspended powder mass is above approximately 220 kg, as shown in Figure 5.11b. Figure 5.11b also indicates that when the suspended UO_2 powder mass is below 220 kg, there are cases where voids introduce a positive reactivity feedback. This is a consequence of over-moderation in the suspension region, as shown in Figure 5.12b by the high H/U ratio, which means that the introduction of voids reduces moderation content and increases the reactivity of the system. Once a certain void fraction is exceeded, the system becomes under-moderated, leading to a less positive and eventually negative void reactivity feedback component. Figure 5.12a shows that the settled wet powder bed remains under-moderated regardless of the mass of UO_2 powder present in the settled region. This is expected since the solid volume fraction of UO_2 powder is far greater than in the suspension region ($v_{\mathrm{f,p,wp}} = 0.1461$).

Bivariate B-splines used to approximate the effect of these reactivity components are shown by the lines plotted in Figure 5.11. The B-spline sets used to construct the best-fit line in Figure 5.11a are of polynomial order 3 and 4 in the gas volume and wet powder mass dimensions, respectively. The bivariate B-spline fits the data well, this is supported by a value of $R^2 = 0.99693$. The polynomial order of the B-spline sets used to create the lines shown in Figure 5.11b are of orders 3 and 5 in the gas volume and suspended UO_2 powder mass dimensions, respectively. A good fit is also shown against the simulated MCNP data for the void reactivity feedback in the suspension ($R^2 = 0.99792$).

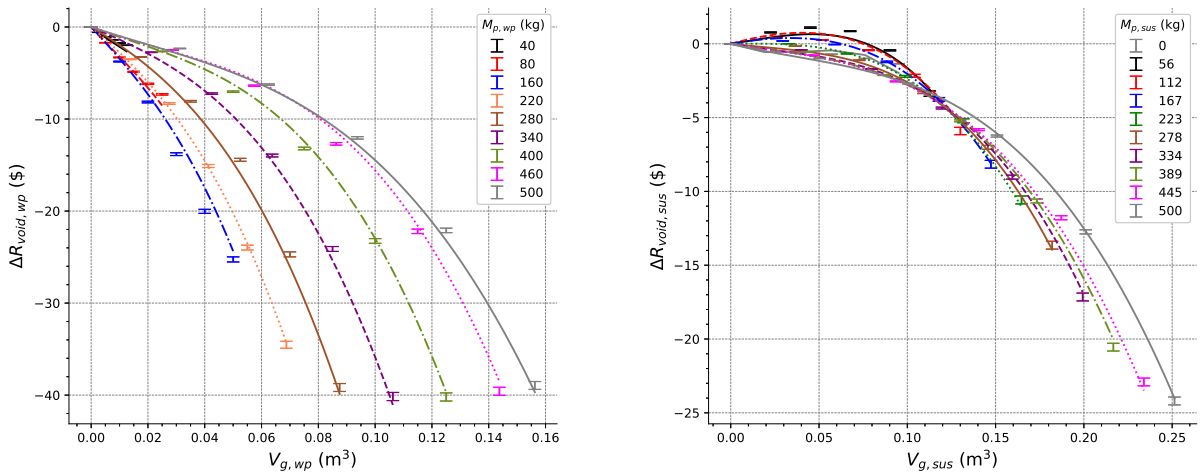

(a) Settled wet powder region.

(b) Suspended powder region.

Figure 5.11: Void reactivity feedbacks are shown, where the error-bars correspond to MCNP simulated data points and the lines correspond to evaluated values of the reactivity feedback component, calculated using a bivariate B-spline interpolation technique.

5.3.6 Thermal Reactivity Feedback

Thermal reactivity feedbacks for the dry UO_2 powder, wet UO_2 powder and water held within pores for the present system have been documented in Section 3.4.9. These components exist due to a combination of thermal expansion and Doppler broadening, and take the following form:

$$\Delta R_{\mathrm{th,p,dp}} = f(\bar{T}_{\mathrm{p,dp}}, f_{\mathrm{imm},0}) - f(\bar{T}_{\mathrm{p,dp},0}, f_{\mathrm{imm},0}) \tag{5.48}$$

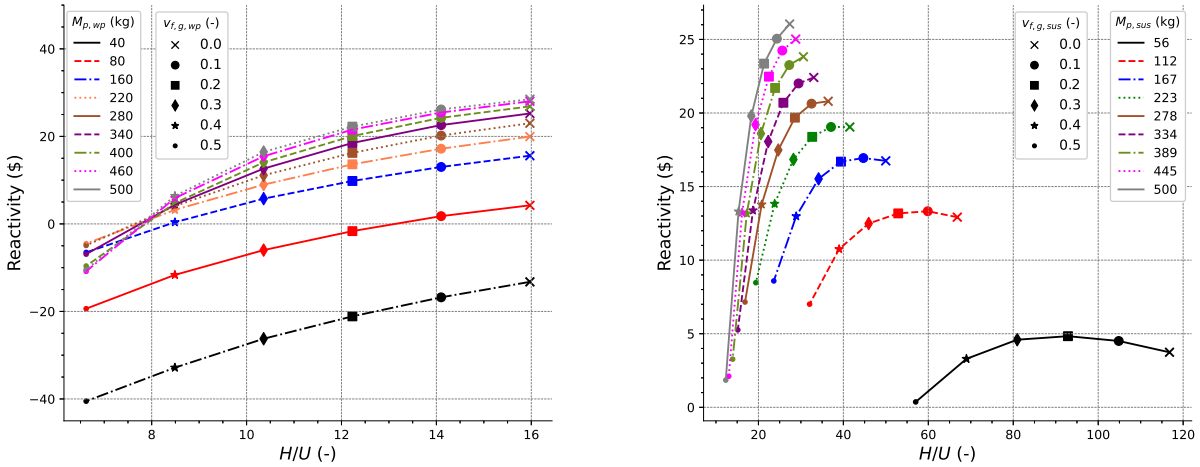

(a) Settled wet powder region.

(b) Suspended powder region.

Figure 5.12: System reactivity as a function of the H/U ratio, varied by altering the void fraction present in the respective region and the solid volume fraction for the case suspended UO_2 powder.

$$\Delta R_{\text{th,p,wp}} = f(\bar{T}_{\text{p,wp}}, f_{\text{imm},0}) - f(\bar{T}_{\text{p,wp},0}, f_{\text{imm},0}) \tag{5.49}$$

$$\Delta R_{\text{th,w}} = f(\bar{T}_{\text{w}}, f_{\text{imm},0}) - f(\bar{T}_{\text{w},0}, f_{\text{imm},0}) \tag{5.50}$$

When performing the MCNP simulations examining the thermal reactivity feedback of the dry powder region, the temperature of wetted UO_2 powder and the water was held constant at 293 K. Similarly, when simulating the effects of wetted UO_2 powder temperature on the reactivity of the system, the interstitial pore water, pooled water, and dry powder remained at 293 K. The same method was carried out when simulating the water thermal reactivity feedback component, by keeping the UO_2 powder temperature at 293 K. This ensured that the independent contribution of each thermal reactivity component could be known.

The bivariate B-spline constructed in Figure 5.13a was generated using polynomial orders for dry powder temperature and bed immersion fraction of 1 and 3, respectively ($R^2 = 0.94122$). One-dimensional B-spline sets used to create Figure 5.13b are of order 2 and 4 in the wet powder temperature and bed immersion fraction dimensions, respectively ($R^2 = 0.99591$). Furthermore, the B-spline sets that form the correlation shown in Figure 5.13c are of polynomial order 2 and 4 in the water temperature and bed immersion fraction dimensions, respectively ($R^2 = 0.96259$). Reasonable agreement is predicted by using the bivariate B-spline interpolation for these reactivity components.

5.3.7 Reactivity Feedback Due to UO_2 Powder Leaving System

The initial model of transient nuclear criticality excursions in static UO_2 powder beds under wetting conditions, described in Chapter 3, predicted that radiolytic gas and steam bubble generation may cause significant volumes of water, held in the pooled water/suspension region, to leave the system

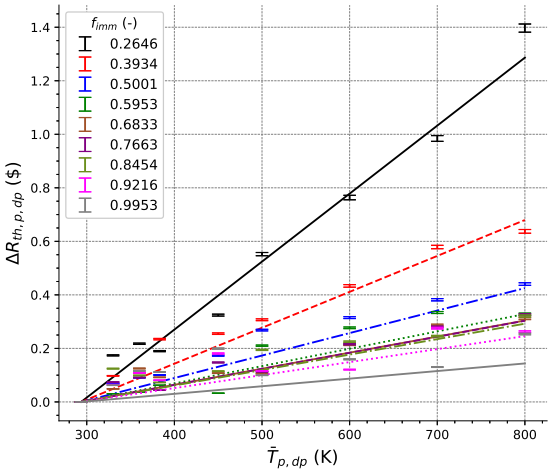

(a) Dry powder.

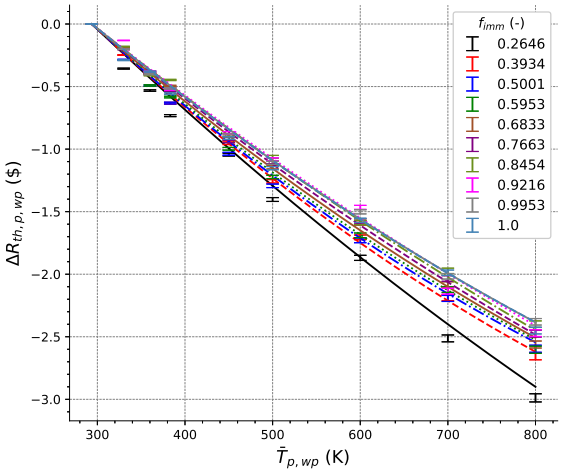

(b) Wet powder.

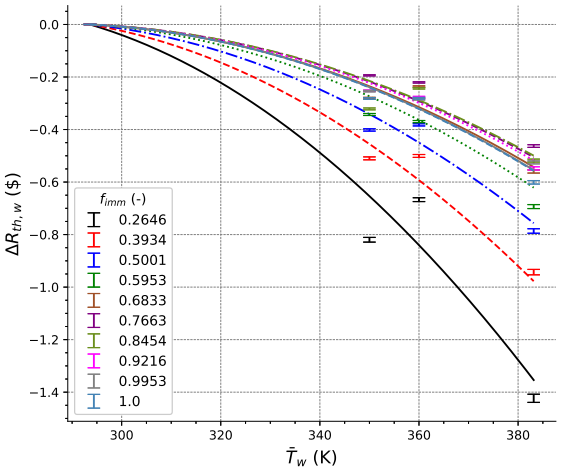

(c) Water.

Figure 5.13: Thermal reactivity feedbacks are shown, where the error-bars correspond to MCNP simulated data points and the lines correspond to evaluated values of the reactivity feedback component, calculated using a bivariate B-spline interpolation technique.

due to a 'boil over'. The same phenomenon is expected to occur here, however, this chapter takes the potential fluidisation of the UO_2 powder into account, which may result in significant volumes of UO_2 powder present in the suspension also leaving the system due to 'boil over'. To account for this phenomenon in the neutronics, an additional reactivity feedback component is prescribed. This component, denoted $\Delta R_{\text{loss}}(M_{\text{p,lost}}, f_{\text{imm,0}})$, corresponds to the reactivity feedback due to the reduction in fissile mass present within the system. A series of MCNP simulations were performed where the effective multiplication factor of the three-phase system was found when the mass of UO_2 powder leaving the system was varied from zero, to half of the available wetted mass of UO_2, for a given bed immersion fraction. The change in reactivity derived from the effective multiplication data, calculated using MCNP, is plotted using error-bars in Figure 5.14. The bivariate B-spline that has been fitted to the MCNP derived reactivity feedback data is also shown in Figure 5.14. The change

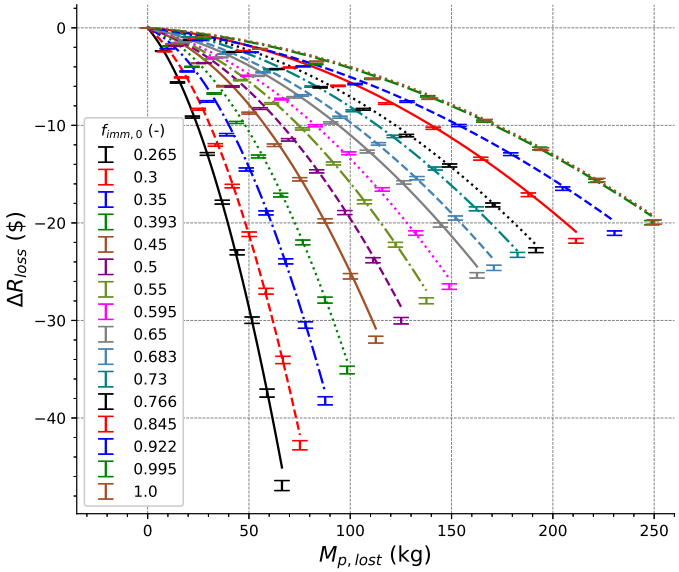

Figure 5.14: The change in reactivity due to the reduction of fissile mass in the system from boil over.

in reactivity due to the loss of powder from the domain is given by:

$$\Delta R_{\text{loss}}(M_{\text{p,lost}}, f_{\text{imm,0}}) = R_{\text{loss}}(M_{\text{p,lost}}, f_{\text{imm,0}}) - R_{\text{loss}}(0.0, f_{\text{imm,0}}) \tag{5.51}$$

Good agreement is predicted when the one-dimensional B-spline set corresponding to the mass of UO_2 powder lost is of order 2 and the B-spline set corresponding to the bed immersion fraction is of order 5. This is supported by an $R^2 = 0.99661$.

5.4 Properties of Settled UO_2 Powder Bed and Suspension

5.4.1 System Thermophysical, Geometric and Neutronic Properties

Many thermophysical and other properties of the UO_2 powder bed have been state in previous chapters and are summarised in Tables 5.6 and 5.7, along with additional parameters specific to this thesis chapter.

Table 5.6: Summary of properties of the UO_2 powder bed, water, radiolytic gas (H_2) and steam.

Property	Symbol	Value	Discussed
Specific heat capacity of UO_2	c_{p}	274 J kg^{-1} K^{-1}	Section 3.4.3
Specific heat capacity of steam	c_{v}	2.060×10^3 J kg^{-1} K^{-1}	Section 3.4.3
Specific heat capacity of water	c_{w}	4.2×10^3 J kg^{-1} K^{-1}	Section 3.4.3
Mean suspended agglomerate diameter	d_{agg}	30 μm	Section 5.2.6
Minimum mean gas bubble size for fluidisation	$d_{\text{b,min}}$	0.0035 m	Section 5.4.3

Mean powder particle diameter	d_p	10 μm	Section 3.4.2
Pore water turbulent mixing coefficient	D_{wp}	10^{-4} m^2 s^{-1}	Section 3.4.4
Energy released per fission event	E_f	3.2×10^{-11} J fission^{-1}	James (1969)
Volumetric H_2 generation coefficient at STP	$G(H_2)$	5.36777×10^{-9} m^3 J^{-1}	Section 3.4.5
Volumetric H_2O loss coefficient at STP	$G(H_2O)$	3.36×10^{-12} m^3 J^{-1}	Section 3.4.5
Container height	H_{cyl}	1.0 m	-
Latent heat of vaporisation	$h_{l,v}$	2.2512×10^6 J kg^{-1}	Section 3.4.3
Container radius	R_{cyl}	0.4 m	-
Mean fission fragment range	R_{fiss}	7 μm	Section 3.4.6
Intrinsic UO_2 neutron source density	s_n	0.135 neutrons s^{-1} (cm^{-3} · UO_2)	Section 3.2.2
Boiling point of water	T_{sat}	373.15 K	-
Water incursion rate onto powder bed	$U_{w,in}$	9.947×10^{-4} m s^{-1} (0.5 L s^{-1})	Section 3.4.1
Dry UO_2 powder bed packing fraction	$v_{f,p,dp}$	0.1461	Section 3.4.3
Settled wet UO_2 powder bed packing fraction	$v_{f,p,wp}$	0.1461	Section 3.4.3
Fast neutron speed	$V_{n,1}$	1.4×10^9 cm s^{-1}	-
Thermal neutron speed	$V_{n,2}$	2.2×10^5 cm s^{-1}	-
Ratio of immobilised liquid volume to UO_2 volume in agglomerate	α	0.8	Section 5.2.6
Total effective delayed neutron fraction	β_{eff}	733×10^{-5}	Section 3.4.7
Thermal expansion coefficient of water	η	2.14×10^{-4} K^{-1}	Section 3.4.3
Mean neutron generation time	Λ	5.32959×10^{-5} s	Section 3.4.7
Thermal conductivity of UO_2	κ_p	see Equation (3.81)	Section 3.4.3
Thermal conductivity of gas	κ_v	0.0246 W m^{-1} K^{-1}	Section 3.4.3
Thermal conductivity of water	κ_w	0.608 W m^{-1} K^{-1}	Section 3.4.3
Dynamic viscosity of gas	μ_v	1.271×10^{-5} Pa s	Section 3.4.3
Dynamic viscosity of water	μ_w	see Equation (3.82)	Section 3.4.3
Density of UO_2	$\rho_{p,th}$	10950 kg m^{-3}	Section 3.4.3
Density of gas	$\rho_{v,th}$	0.5863 kg m^{-3}	Section 3.4.3
Density of water	$\rho_{w,th}$	998.1 kg m^{-3}	Section 3.4.3

5.4.2 Macroscopic Nuclear Cross-section Correlations

Group condensed macroscopic nuclear cross-sections were found for UO_2 powder at varying porosities in Section 4.3.1. This data is also used in the present chapter to solve the multi-group neutron diffusion equation, obtaining an axial power shape function, every 0.5 $ of reactivity change.

Table 5.7: Delayed neutron precursor group data.

Group, i	β_i ($\times 10^{-5}$)	λ (s)
1	25 ± 1	0.01335 ± 0.00000
2	129 ± 4	0.03264 ± 0.00000
3	122 ± 3	0.12099 ± 0.00000
4	279 ± 5	0.30482 ± 0.00001
5	125 ± 4	0.85704 ± 0.00003
6	53 ± 2	2.87888 ± 0.00015

5.4.3 Critical Gas Velocity and Powder Bed Suspension Rates

This study uses a simple approach, outlined in Section 5.2.3, to model the incipient fluidisation point of the UO_2 powder bed and the rate at which fluidisation, or pickup, occurs. Phenomenologically, the critical gas velocity corresponds to the average gas velocity through the settled wet powder region where enough gas bubble-particle interactions occur with sufficient force to cause the UO_2 powder particles to become suspended. The prescribed range of critical gas velocities is subject to the magnitude of gas bubble velocities predicted by Equations (3.40) and (3.45). Figure 5.15 suggests that the gas bubble size does not vary greatly as a function of the solid volume fraction, for the dilute suspensions considered here. This is a result of small variations to the effective viscosity for the predicted range of UO_2 powder concentrations.

However, large differences are predicted for the gas bubble advection speed as a function of the UO_2 solid volume fraction and bubble size. Figure 5.15b indicates that at low gas bubble sizes, the rate of change of the gas advection speed is large and positive with increasing bubble size. This may be attributed to the small bubbles being able to travel through pore interstices without losing large amounts of momentum through gas bubble - particle interactions (Tsuchiya et al., 1997). As the gas bubbles get larger, the gas advection speed reaches a peak and subsequently decreases. This may be attributed to the introduction of significant gas bubble - particle interactions that retard the gas bubble, slowing the rate at which it rises. This occurs at increasingly lower gas bubble speeds and bubble sizes as the dispersed UO_2 powder becomes more concentrated. The model, proposed by Tsuchiya et al. (1997) suggests that increasing the gas bubble size further, leads to increased gas bubble advection speed.

Taking these different regimes into consideration, the condition for incipient fluidisation, described in Section 5.2.3, should not be satisfied at low void fractions and gas bubble sizes where a correspondingly low number of gas bubble - particle interactions are predicted. The present model therefore prescribes a minimum bubble size that must also be satisfied, as well as the critical gas velocity condition. This minimum bubble size for gas bubble - particle interactions to cause fluidisation are is assumed to be at the point where increasing bubble size begins to also increase gas advection speed. For the settled wet powder bed with solid volume fraction, $v_{f,p,wp} = 0.1461$, the minimum bubble size is prescribed to be $d_{b,min} = 0.0035$ m. The average bubble size in the settled wet powder region may be calculated using Equation (3.40) with an average settled wet powder bed void fraction and average effective density and viscosity.

The range of critical gas velocities can be directly obtained by investigating the range of radiolytic

gas and steam bubble sizes and advection rates, defined in Equations (3.40) and (3.45), respectively. The minimum critical gas velocity corresponds to the gas bubble advection rate at the minimum bubble diameter, $d_{\mathrm{b,min}} = 0.0035$ m, giving a lower critical gas velocity limit of $U_{\mathrm{g,crit}} = 0.192$ m s^{-1}. The maximum critical gas velocity corresponds to a case where no fluidisation occurs, which is satisfied when $U_{\mathrm{g,crit}} > 0.24$ m s^{-1}. Therefore, the prescribed critical gas velocities in the present study are within the following range:

$$0.192 \text{ m s}^{-1} \leq U_{\mathrm{g,crit}} \leq 0.24 \text{ m s}^{-1} \tag{5.52}$$

For the present study, two critical gas velocities have been selected, $U_{\mathrm{g,crit}} = 0.2$ m s^{-1} and $U_{\mathrm{g,crit}} = 0.22$ m s^{-1}. The corresponding rate of pickup, U_{pickup} is varied to capture a range of different fluidisation rates.

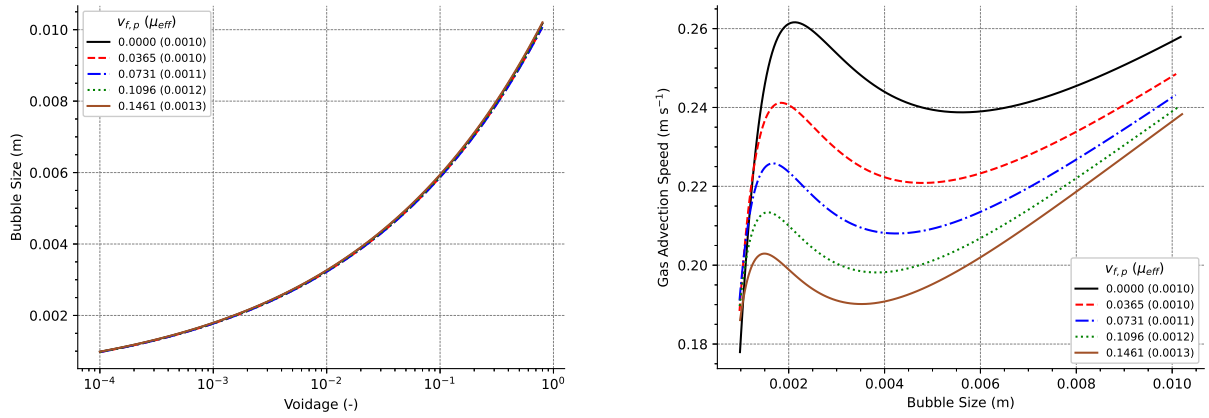

(a) (b)

Figure 5.15: Correlations between the voidage, gas bubble size and gas bubble advection rates through the three-phase fissile powder bed.

5.4.4 Prescribed Initial Conditions

The deeply sub-critical and near-delayed critical initial conditions have already been evaluated for the UO_2 powder bed under consideration in Section 4.3.5 and are summarised in Table 5.8. The term, T_{all}, in Table 5.8 corresponds to the prescribed temperature of all regions and components, since initially, they are in thermal equilibrium at room temperature.

5.5 Results

5.5.1 Sensitivity of Critical Gas Velocity and Pickup Rate on Transient Nuclear Criticality Excursion

The simulations were initiated from the near delayed critical state since the period of time when the system is deeply sub-critical was not of interest in this study. Therefore, the time from the start of the simulation, T, to the time from the beginning of the infiltration of water into the dry UO_2 powder bed, t may be given as $T = t - t_{\mathrm{crit}}$.

Table 5.8: Initial system geometry and neutron kinetic data for the near fully unsaturated case and at a point close to criticality for mean powder size, $d_{\mathrm{p}} = 10$ μm.

Property	Deeply Sub-Critical State	Near-Critical State
C_1 (precursors)	33.12	6284
C_2 (precursors)	69.92	23640
C_3 (precursors)	17.84	111500
C_4 (precursors)	16.19	14050
C_5 (precursors)	2.580	2718
C_6 (precursors)	0.3257	379.6
$f_{\mathrm{imm,0}}$ (-)	0.0002	0.2868
H_{dp} (m)	0.6216	0.4444
H_{sus} (m)	0.3783	0.3783
H_{wp} (m)	0.0001	0.1773
N (neutrons)	0.09428	115.6
R_{T} (\$)	-476.0	-0.01353
T_{all} (K)	293.15	293.15
t_{crit} (s)	N/A	346.5
$v_{\mathrm{f,p,dp}}$ (-)	0.1461	0.1461
$v_{\mathrm{f,g}}$ (-)	0.0	0.0
$v_{\mathrm{f,p,sus}}$ (-)	0.0	0.0
$v_{\mathrm{f,p,wp}}$ (-)	0.1461	0.1461

The effect that the critical gas velocity, $U_{\mathrm{g,crit}}$, and the rate of fluidisation, U_{pickup}, have on the dynamics of a wetting-induced transient nuclear criticality excursion was examined. The prescribed rate of UO_2 powder pickup and critical gas velocity may significantly alter the reactivity of the fissile system, through fissile mass redistribution.

Figures 5.16a and 5.20a show the variation in power and integrated fissions, or fission energy, over 4000 s, starting from a near delayed critical state, for the cases where $U_{\mathrm{g,crit}} = 0.22$ m s^{-1} and $U_{\mathrm{g,crit}} = 0.20$ m s^{-1}, respectively. Varying rates of fluidisation, denoted U_{pickup}, are examined for each of the two prescribed critical gas velocities. The neutron kinetic response of the fissile system prior to boiling does not depend on the critical gas velocity or rate of fluidisation used in this study. This is shown in Figures 5.16a and 5.20a by the similar neutron kinetic response of the fissile system up to the onset of boiling at $T = 32.3$ s.

Figures 5.16b to 5.16d and 5.20b to 5.20d, indicate that the reactivity components also remain very similar up to the point of boiling at $T = 32.3$ s. These figures show that the reactivity added to the system by the infiltration of water (acting as a moderator), is matched by a corresponding negative reactivity feedback due to the creation of voids through radiolysis.

Figures 5.17a and 5.21a indicate that the voidage prior to boiling, in the settled wet powder region (pore interstices), due to the presence of gas bubbles from radiolysis reaches 0.04 before boiling. By relating the voidage to the gas advection speed in Figure 5.15, one can immediately see that the radiolytic gas advection speed is below either of the prescribed critical gas velocities up to boiling at $T = 32.3$ s.

The time taken for incipient fluidisation and the corresponding void fraction that initiates flu-

idisation is described in Table 5.9 for the two critical gas velocities studied. The time for incipient fluidisation is determined by calculating the difference in time between the start of the simulation and the time at which the settled wet powder region interface location, shown in Figures 5.17d and 5.21d, begins to decrease from the initial value of $H_{\mathrm{dp}} + H_{\mathrm{wp}} = 0.6217$ m. The data presented suggests that fluidisation first occurred later in time and with a higher pore void fraction for the case where the critical gas velocity was higher. The time required for boiling to first occur in the pores was calculated by determining the time at which the wetted powder steam void fraction, shown in Figures 5.17a and 5.21a, became non-zero. This information is shown in Table 5.9. For the case where the critical gas velocity, $U_{\mathrm{g,crit}} = 0.20$ m s^{-1}, boiling occurred very soon after incipient fluidisation. A far greater period of time elapsed between incipient fluidisation and boiling for the case where $U_{\mathrm{g,crit}} = 0.22$ m s^{-1}.

Table 5.9: Simulating time and pore void fraction at incipient fluidisation as a function of the prescribed critical gas velocity.

Critical gas velocity, $U_{\mathrm{g,crit}}$ (m s^{-1})	Pore void fraction at fluidisation, $v_{\mathrm{f,g,wp}}$ (-)	Incipient fluidisation time (s)	Boiling time (s)
0.20	0.09	32.51	32.3
0.22	0.32	356.09	32.3

The average temperature of the dry UO_2 powder, shown in Figure 5.17b, is much greater when fluidisation occurs than for the case where the UO_2 powder bed remains stationary. Higher rates of fluidisation, also produced a higher average dry UO_2 powder temperature. These temperatures remain below the melting point of UO_2. The settled wet UO_2 powder and pore water are in thermal equilibrium at the boiling point of water at standard pressure, due to the high interfacial area as a result of the small size of UO_2 powder particles ($d_{\mathrm{p}} = 10$ μm).

The axial temperature distribution of UO_2 powder in each region is shown in Figure 5.18 at different snapshots in time. The temperatures shown at 0 K correspond to spatial locations where there is no powder present, i.e. before fluidisation in the pooled water region. The sharp change in temperature towards the base of the cylindrical domain corresponds to the location of the wetting front distinguishing the dry and wet UO_2 powder regions. The dry UO_2 powder retains significant thermal energy since it is not in contact with the high heat capacity water (no interfacial convection), and also does not lose energy through water vapourisation. This fact, combined with the low thermal conductivity of UO_2 powder, causes the sharp thermal gradient at the wetting front shown in Figure 5.18. The sharp decrease in the dry UO_2 powder temperature present in Figure 5.17b can also be seen in Figure 5.18, which shows that at $T = 4000$ s, the dry UO_2 powder bed's temperature has significantly reduced when compared to earlier times in the transient. This is attributable to the discretisation scheme which introduces progressively larger interface thermal energy gradients as the interface mesh cell gets smaller, due to water infiltration. The advantage of implementing this scheme is that the spatial powder temperature acts continuously when solved numerically whilst still being able to represent sharp thermal gradients.

Figures 5.16b to 5.16d and 5.17a show that after the onset of boiling at $T = 32.3$ s, reactivity added to the system through water infiltration is matched by an equal amount of negative reactivity

introduced by the process of water boiling on the surface of UO_2 powder particles, maintaining the fissile system's delayed critical state. Once the void fraction in the pores reaches 0.32, which occurs at $T = 356$ s, the settled wet powder bed reaches incipient fluidisation. The reduction in the height of the settled wet powder bed due to fluidisation is shown in Figure 5.17d. A fluidisation dominant regime is shown in Figure 5.17d by the decrease in the settled wet powder region interface height. Conversely, an increasing settled wet powder region interface height in Figure 5.17d corresponds to a sedimentation dominant regime in the suspension, as UO_2 powder in the suspension settles on the surface of the settled wet powder bed.

Figures 5.16a, 5.16c and 5.16d suggest that the negative reactivity added to the system by the re-distribution of fissile mass, reduces the power of the system, ultimately causing less steam to be produced. Figure 5.17a supports this by showing that for all cases where fluidisation may occur, the void fraction is limited by the fraction of gas required to satisfy the critical gas velocity condition, at $v_{\mathrm{f,p,wp}} \approx 0.32$.

A slightly oscillatory response is predicted in the wet powder void and fluidisation (or pickup) reactivity components, shown in Figures 5.16c and 5.16d when $T > 356$ s. Figures 5.16c and 5.16d also highlight the coupled nature of the settled wet powder voidage and fluidisation reactivity components after incipient fluidisation at $T = 356$ s, suggesting that an increase in the reactivity of one component leads to a decrease in the other. The coupled nature between fluidisation and voidage in the settled wet powder region is evidenced by comparing the time at which fluidisation occurs, represented in Figure 5.17d as a decrease in the settled wet powder region interface location, and the time at which the void fraction oscillates, peaking at the critical 0.32 value (shown in Figure 5.17a). The oscillations indicate that negative reactivity added to the system by fluidisation reduces the volume of steam present in the settled wet powder region (pore interstices). The reduction in the steam volume leads to sedimentation, shown in Figure 5.17d by the gradual increase in the settled wet powder region interface location. The subsequent sedimentation adds reactivity to the system, shown in Figures 5.16c and 5.16d, by concentrating the fissile mass. The less negative fluidisation reactivity component is then compensated for by further steam production, as shown by the increasing steam void fraction in Figure 5.17a at the time corresponding to an increase in the settled wet powder bed interface height.

Additionally, Figure 5.17c suggests that fluidisation of the settled wet UO_2 powder bed, may cause large masses of UO_2 powder to overflow from the system. The overflowing of the suspension occurs due to the volumetric sources causing the available space in the domain to be exceeded. These sources include the production of radiolytic gas and steam, as well as the incursion of water from the fire sprinkler system. The short time between incipient fluidisation and UO_2 powder leaving the domain suggests that the UO_2 powder rapidly reaches the top of the suspension region. This may be expected since the very low Péclet number, $Pe < 10^{-2}$ (see Figure 5.9), causes the UO_2 powder to become homogeneously dispersed in the suspension rapidly after incipient fluidisation. Figure 5.19 supports this for the case where $U_{\mathrm{g,crit}} = 0.22$ m s^{-1} and $U_{\mathrm{pickup}} = 0.01$ m s^{-1}, by showing that the UO_2 powder particles present in the suspension are homogeneously distributed at $T = 382$ s, shortly after incipient fluidisation at $T = 356$ s.

A significantly different system response is shown in Figure 5.20a which represents the case where

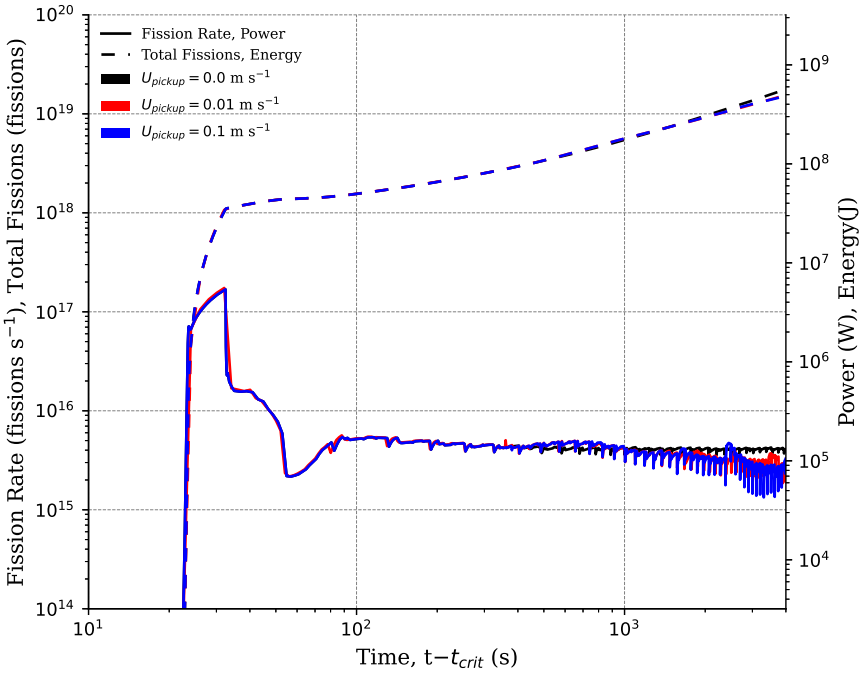

(a) Power and fission energy, $U_{\mathrm{g,crit}} = 0.22$ m s^{-1}.

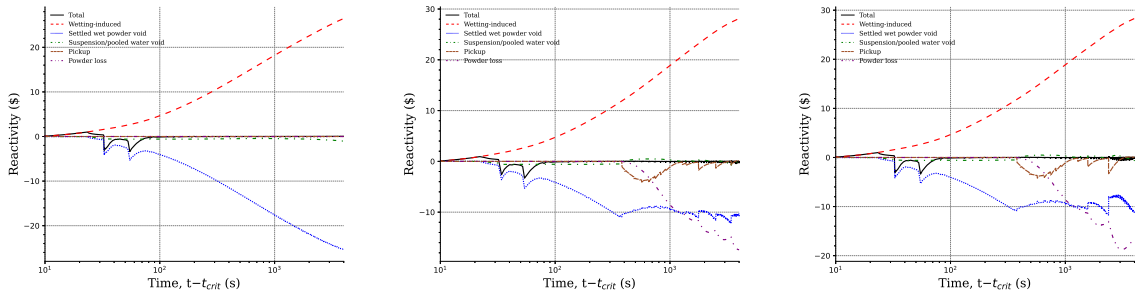

(b) Reactivity, $U_{\mathrm{pickup}} = 0.0$ m s^{-1}.

(c) Reactivity, $U_{\mathrm{pickup}} = 0.01$ m s^{-1}.

(d) Reactivity, $U_{\mathrm{pickup}} = 0.1$ m s^{-1}.

Figure 5.16: Fission power and reactivity response of wetted UO_2 powder system over 4000 s of a transient nuclear criticality excursion for the case where $U_{\mathrm{g,crit}} = 0.22$ m s^{-1} with different rates of fluidisation.

$U_{\mathrm{g,crit}} = 0.20$ m s^{-1}, after the onset of boiling. Prior to boiling at $T = 32.3$ s, similar neutron kinetics are shown compared to the case where $U_{\mathrm{g,crit}} = 0.22$ m s^{-1}, for all rates of fluidisation. Figures 5.20c and 5.20d suggest that this occurs because the condition for incipient fluidisation, shown by the sharp reduction in the settled wet powder interface location at $T = 32.51$ s in Figure 5.21d, is not satisfied until enough voids have been created, which requires boiling. The fission energy deposited in the system, shown in Figure 5.20a, varies depending on the prescribed rate of fluidisation.

Figure 5.20a suggests that the fission power response is oscillatory after boiling at $T = 32.3$ s, with large variations in fission power expected when the rate of fluidisation is low, such as when $U_{\mathrm{pickup}} = 0.01$ m s^{-1}. These oscillations are approximately two orders of magnitude in amplitude and

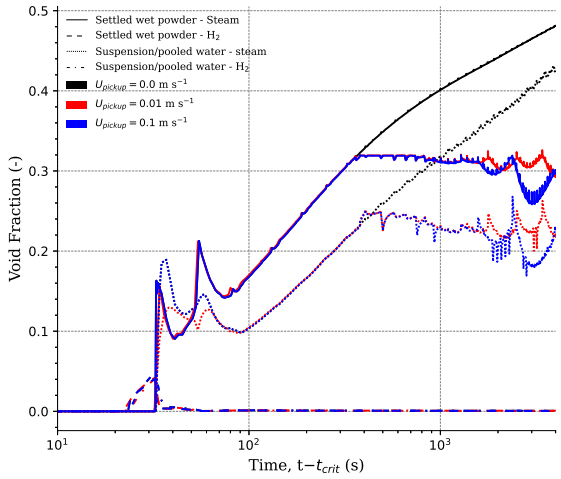

(a) Region and component specific void fractions.

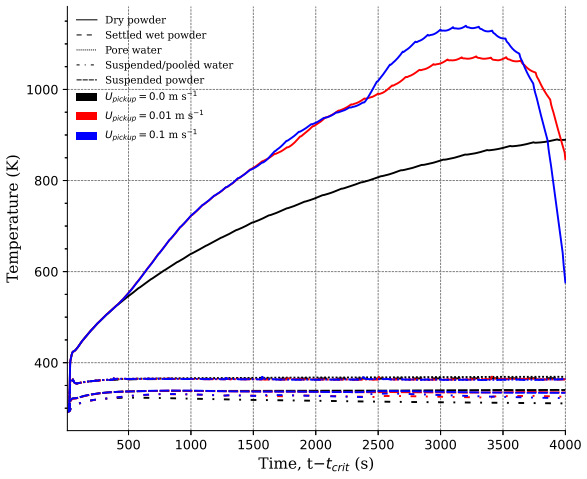

(b) Region and component average temperatures.

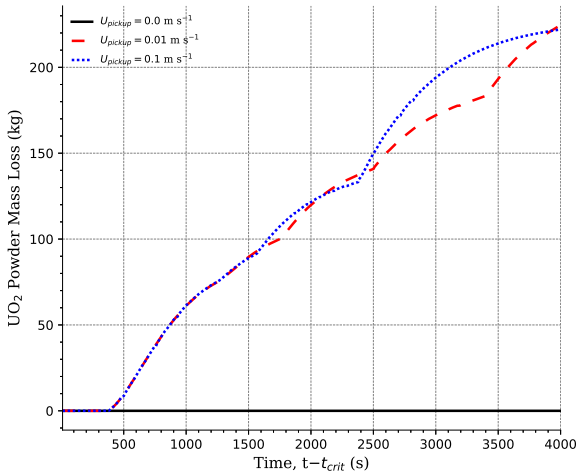

(c) UO_2 powder mass lost leaving system.

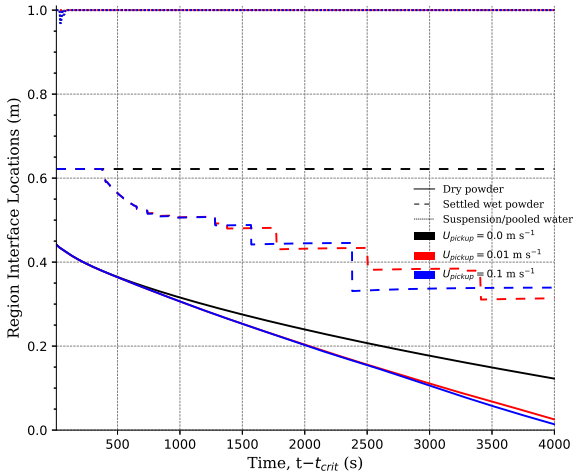

(d) Axial location of region interfaces.

Figure 5.17: Voidage, temperature, UO_2 powder mass lost and three-region interface location variations over 4000 s of the transient nuclear criticality excursion for the case where $U_{\text{g,crit}} = 0.22$ m s^{-1} with different rates of fluidisation.

are similar to the initial peak power that occurs before the onset of boiling at $T = 32.3$ s. The frequency of the oscillations for the case where $U_{\text{pickup}} = 0.01$ m s^{-1} corresponds to the time taken for enough UO_2 powder to sediment to re-introduce a delayed critical state into the system. This feature can be seen graphically by comparing sedimentation times, shown through the increasing region height of the settled wet powder region in Figure 5.21d, to the oscillations in the fluidisation reactivity component shown in Figure 5.20c. Figure 5.21c indicates that a large mass of UO_2 powder overflows from the system over the 4000 s of the simulated transient nuclear criticality excursion, with $M_{\text{p,lost}} = 310$ kg. These oscillations are also exhibited in Figure 5.21a, which show that sharp pulses in voidage occur. The reduction in fission power due to fluidisation, shown through the negative reactivity component of fluidisation in Figure 5.20c, prevents sustained steam production. When the UO_2 powder bed becomes fully immersed at $T = 3030$ s, no further wetting-induced reactivity is added to the system and the

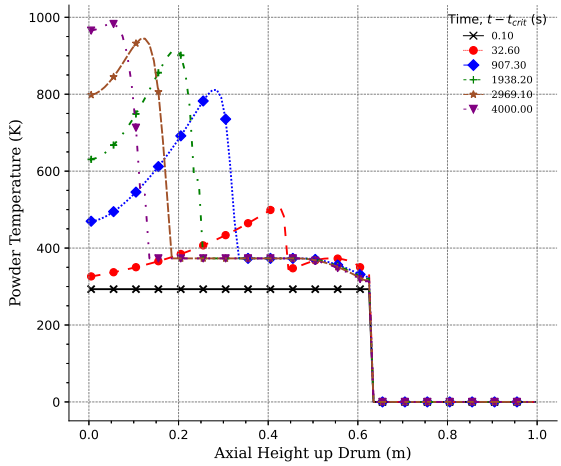

(a) $U_{\text{pickup}} = 0.0$ m s^{-1}.

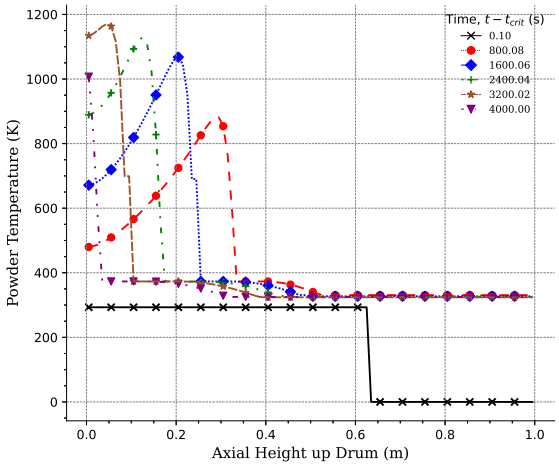

(b) $U_{\text{pickup}} = 0.01$ m s^{-1}.

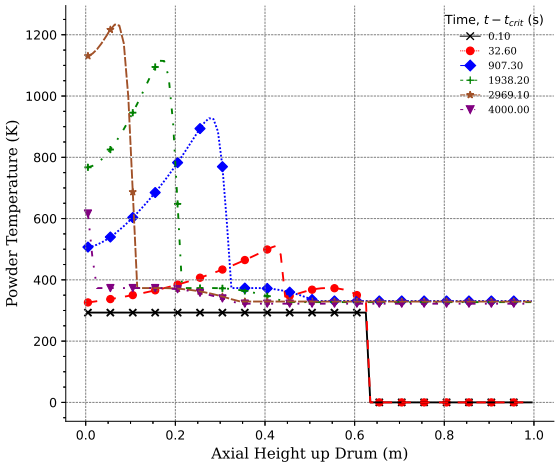

(c) $U_{\text{pickup}} = 0.1$ m s^{-1}.

Figure 5.18: Spatial distribution of UO_2 powder temperature over 4000 s of a transient nuclear criticality excursion for the case where $U_{\text{g,crit}} = 0.22$ m s^{-1} with different rates of fluidisation.

fission power decreases to below 0.01 W.

The temperature of UO_2 powder that is in contact with the water, shown in Figure 5.21b, is limited to 373.15 K due to boiling. However, repeated delayed criticalities for the case where $U_{\text{pickup}} = 0.01$ m s^{-1} cause the pore water and settled wet UO_2 powder temperature to oscillate, peaking at the boiling point. The dry UO_2 powder temperature rises with each subsequent nuclear criticality excursion, as a high fission power causes more thermal energy deposition in the region. Average temperatures reach up to 1750 K as the UO_2 bed nears full saturation. Since the powder bed is near full saturation, it is only a small mass of UO_2 powder that reaches these high temperatures.

The simulations suggest a different response for the case where $U_{\text{g,crit}} = 0.20$ m s^{-1} and $U_{\text{pickup}} = 0.1$ m s^{-1}, as complete fluidisation of the settled wet UO_2 powder bed is predicted much earlier, at $T = 70.7$ s, when compared to the case where $U_{\text{g,crit}} = 0.20$ m s^{-1} and $U_{\text{pickup}} = 0.01$ m s^{-1}. Complete

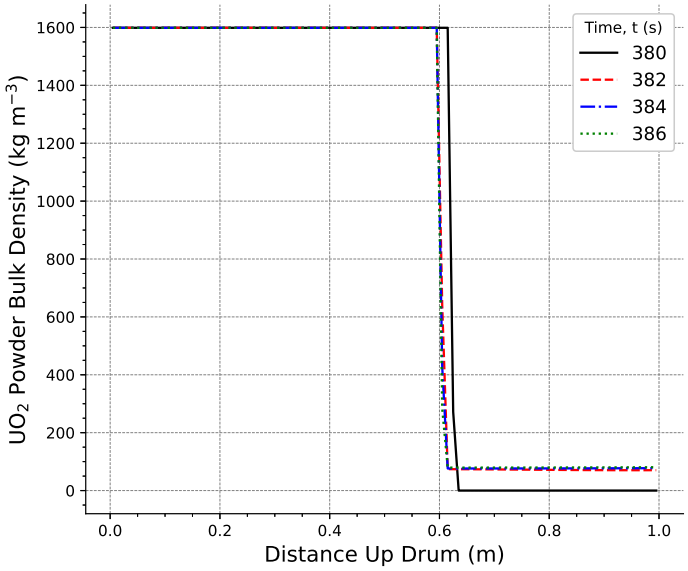

Figure 5.19: Spatial UO_2 powder bulk density at different times after incipient fluidisation, throughout the transient nuclear criticality excursion for the case where $U_{\text{g,crit}} = 0.22$ m s^{-1} and $U_{\text{pickup}} = 0.01$ m s^{-1}.

fluidisation is shown in Figure 5.21d as the point where the settled wet powder region interface location is equal to the dry powder region interface location. This point in time coincides with a secondary fission power spike in Figure 5.20a and a spike in the steam void fraction in the settled wet powder, shown in Figure 5.21a. This suggests that enough steam was produced to satisfy the critical gas velocity condition, causing rapid suspension of the settled wet UO_2 powder. Complete fluidisation of the wetted UO_2 powder bed causes the system to go deeply sub-critical, reducing the power over time and causing approximately 20 kg of UO_2 powder to overflow from the system (see Figure 5.21c). As water infiltration of the UO_2 powder bed continues, fluidisation of the newly infiltrated UO_2 powder reduces the H/U ratio in the suspension, which causes the pickup reactivity component to become less negative. A delayed critical state is once again reached at $T = 140$ s once the addition of water adds sufficient reactivity to the system. Removal of UO_2 powder from the domain, shown in Figure 5.21c, causes the system reactivity, shown in Figure 5.20d, to go sub-critical. Further reactivity added to the system through water infiltration and subsequent fluidisation of the remaining dry UO_2 powder causes a delayed critical state to be reached at $T = 485$ s, resulting in a corresponding fission power peak of 10 kW. Given the high specific heat capacity of water in the suspension and the latent heat of vaporisation, this power does not result in vigorous boiling. The three-phase suspension remains in a critical state as wetting-induced reactivity is added through the production of radiolytic gas voids. An equilibrium power of 100 W is reached.

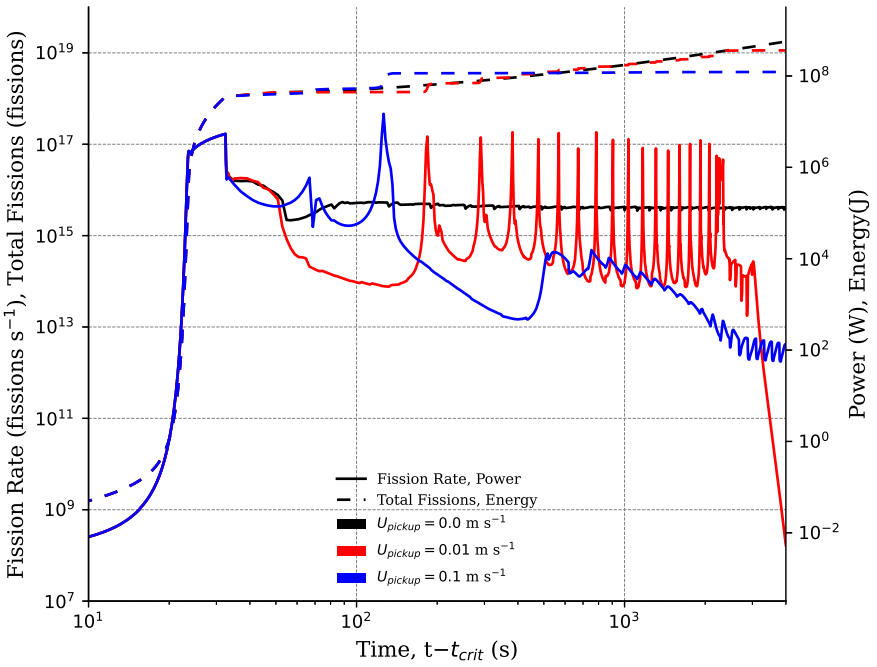

(a) Power and fission energy, $U_{\mathrm{g,crit}} = 0.20$ m s^{-1}.

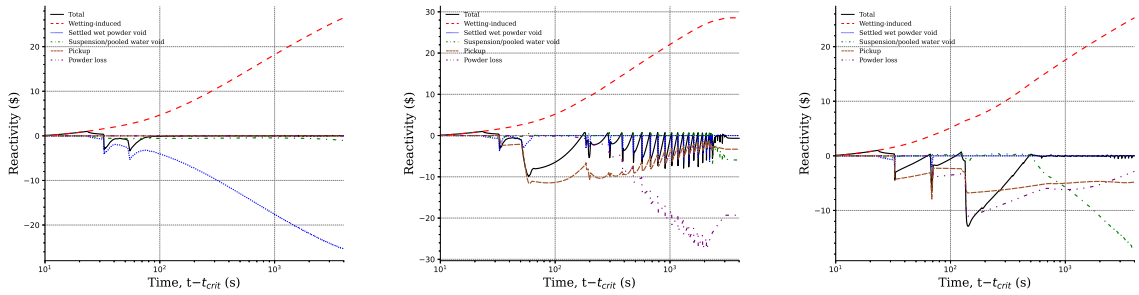

(b) Reactivity, $U_{\mathrm{pickup}} = 0.0$ m s^{-1}.

(c) Reactivity, $U_{\mathrm{pickup}} = 0.01$ m s^{-1}.

(d) Reactivity, $U_{\mathrm{pickup}} = 0.1$ m s^{-1}.

Figure 5.20: Fission power and reactivity response of wetted UO_2 powder system over 4000 s of a transient nuclear criticality excursion for the case where $U_{\mathrm{g,crit}} = 0.20$ m s^{-1} with different rates of fluidisation.

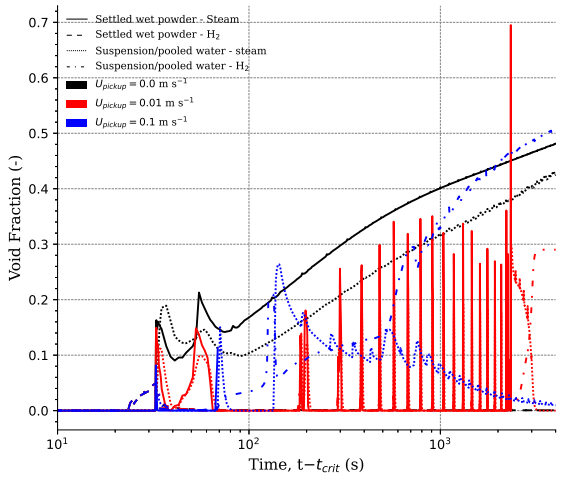

(a) Region and component specific void fractions.

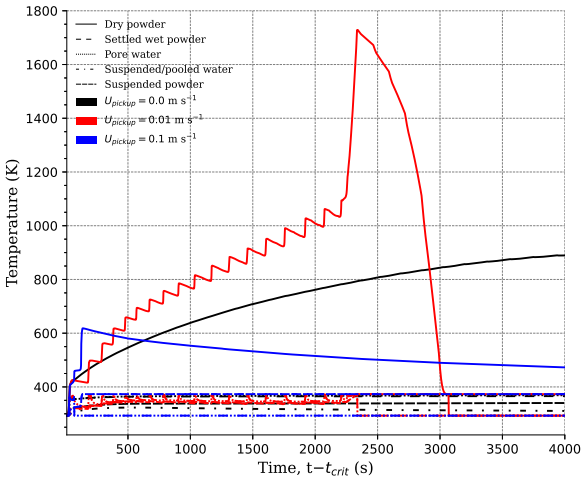

(b) Region and component average temperatures.

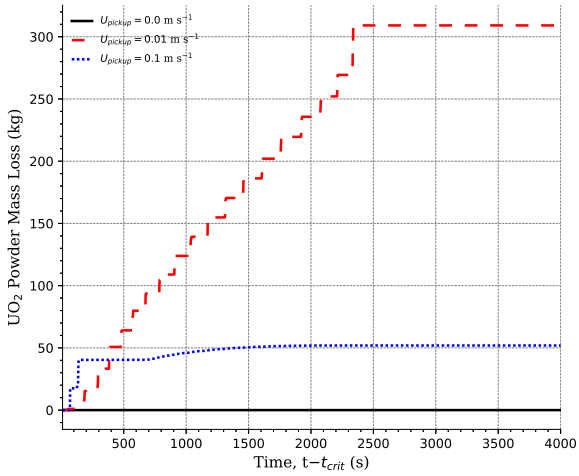

(c) UO_2 powder mass lost leaving system.

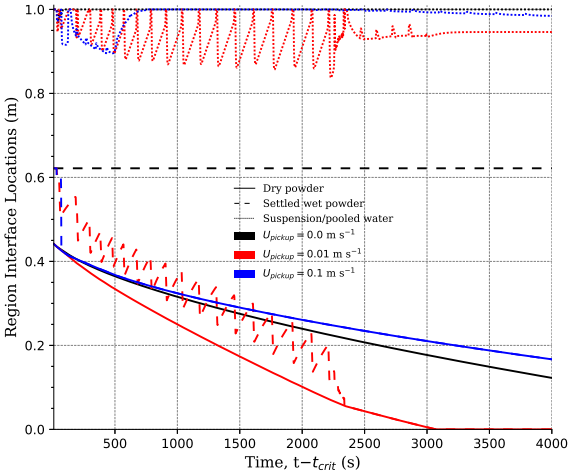

(d) Axial location of region interfaces.

Figure 5.21: Voidage, temperature, UO_2 powder mass lost and three-region interface location variations over 4000 s of a transient nuclear criticality excursion for the case where $U_{\mathrm{g,crit}} = 0.20$ m s^{-1} with different rates of fluidisation.

5.5.2 Transient Neutron Kinetic Response of System With Increasing UO_2 Powder Hindered Settling Speed

The impact of the UO_2 powder hindered settling speed on the neutron kinetic response of the three-phase fluidised bed system has been examined by prescribing increased rates of settling for two separate critical gas velocity conditions. The hindered settling velocity, $U_p = 0.0015$ m s^{-1} was chosen as this represents the approximate free settling speed of a single UO_2 powder-water agglomerate, based on the data shown in Figure 5.7. An additional hindered settling velocity, $U_p = 0.015$ m s^{-1}, has also been prescribed to examine the effect that significantly increasing the settling rate has on the dynamics of the system.

The fission power, energy and reactivity of the system for the case where $U_{g,crit} = 0.20$ m s^{-1} is shown in Figure 5.22. Figure 5.22a suggests that prior to incipient fluidisation at $T = 32.54$ s, no effect on the fission power or energy was seen as a function of the prescribed hindered settling rate. This is a result of no UO_2 powder having entered the suspension region before fluidisation had first occurred. Once gas bubble induced fluidisation of the settled wet powder bed had been initiated, the oscillatory power response, shown in Figure 5.22a, had a higher frequency for the correspondingly higher rate of sedimentation. This is a result of the more frequent oscillations in the reactivity shown in Figure 5.22b compared to Figure 5.22c. The total energy deposited in the system for the case where $U_{g,crit} = 0.20$ m s^{-1}, showin in Figure 5.22a, varied with the prescribed hindered settling rate with values of 340.46 MJ and 414.41 MJ, when $U_p = 0.0015$ and 0.015 m s^{-1}, respectively. The larger fission energy released corresponded to the simulated case with a higher prescribed UO_2 agglomerate hindered settling because of the higher frequency of fission power oscillations that are shown in Figure 5.22a.

Figure 5.23a indicates that no variations in power or fission energy occur when varying the hindered settling rate for the case where $U_{g,crit} = 0.22$ m s^{-1}. This suggests that for higher critical gas velocities, the neutron kinetic response of the system is not governed by the settling rate of UO_2 powder particles from the suspension. Figures 5.23b and 5.23c indicates that the reactivity of the system is governed by the competing reactivity effects of water infiltration and void production.

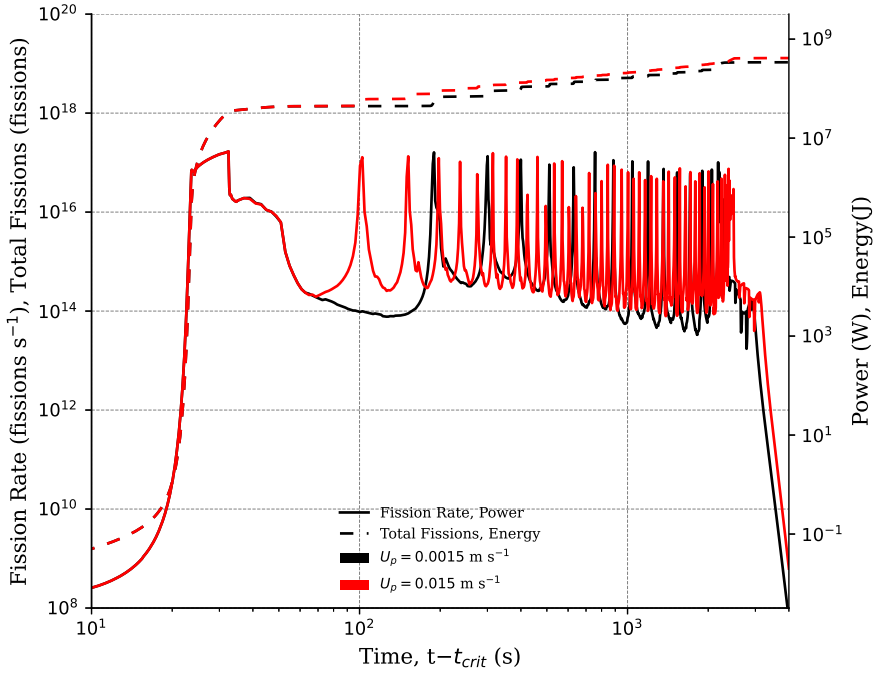

(a) Power and energy.

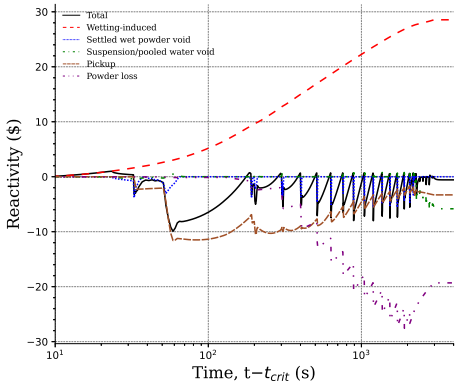

(b) Reactivity, $U_\mathrm{p} = 0.0015$ m s^{-1}.

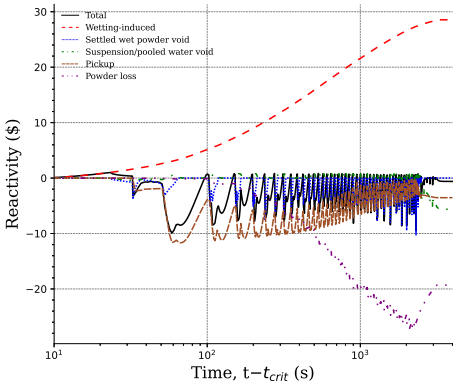

(c) Reactivity, $U_\mathrm{p} = 0.015$ m s^{-1}.

Figure 5.22: Response of wetted UO_2 powder system over 4000 s of a transient nuclear criticality excursion with varying rates hindered settling rate, U_p and $U_{\mathrm{g,crit}} = 0.20$ m s^{-1}.

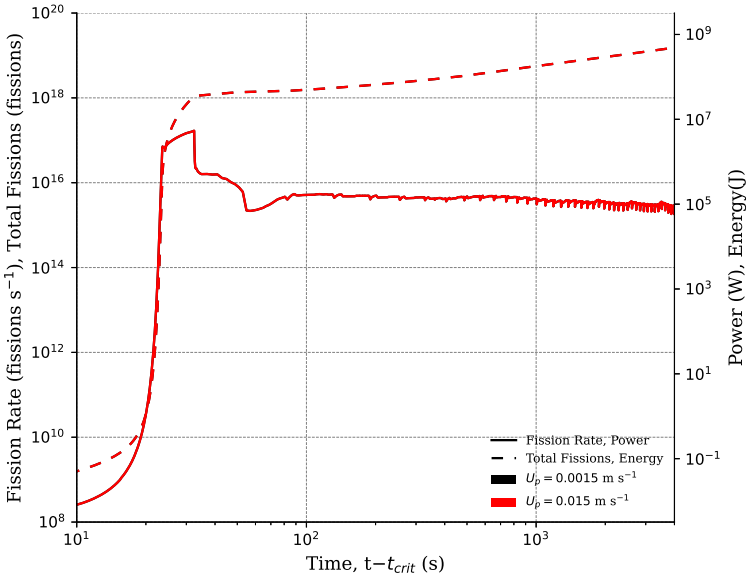

(a) Power and energy.

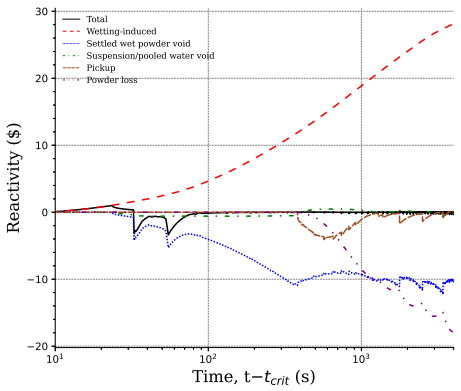

(b) Reactivity, $U_\mathrm{p} = 0.0015$ m s^{-1}.

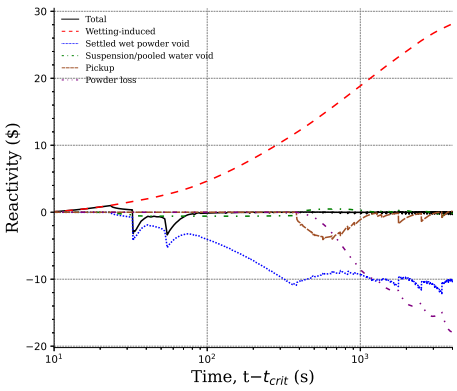

(c) Reactivity, $U_\mathrm{p} = 0.015$ m s^{-1}.

Figure 5.23: Response of wetted UO_2 powder system over 4000 s of a transient nuclear criticality excursion with varying rates hindered settling rate, U_p, and $U_{\mathrm{g,crit}} = 0.22$ m s^{-1}.

5.5.3 Sensitivity of Effective Medium Viscosity on Gas Speeds

Large variations in gas bubble velocity as a function of the void fraction, through the three-phase medium, may be expected when there are significant variations to the effective medium viscosity of the highly dispersed UO_2 powder-water mixture. This relationship is shown in Figure 5.24, indicating that a reduction in gas bubble advection speed increases the effective dynamic viscosity. The effect that this has on the transient nuclear criticality excursion for the case where $U_{\mathrm{g,crit}} = 0.20$ m s^{-1} and the rate of fluidisation, $U_{\mathrm{pickup}} = 0.01$ m s^{-1} has been examined. Simulations were performed with an effective medium viscosity, $\mu_{\mathrm{eff}} = 1$, 10 and 100 mPa s.

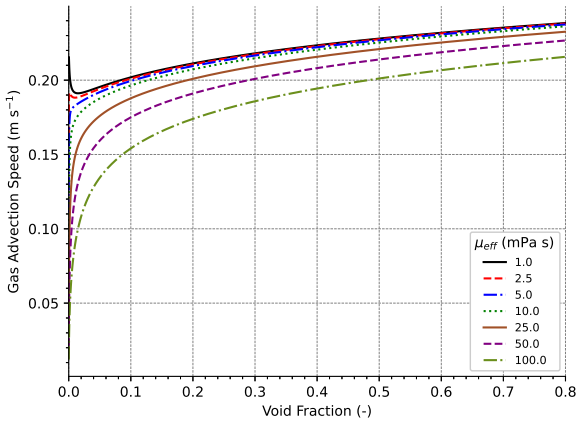

Figure 5.24: The variation in the advective gas bubble speed as a function of void fraction, for varying effective dynamic viscosities, when the solid volume fraction of UO_2 powder, $v_{\mathrm{f,p}} = 0.1461$.

Figure 5.25a shows that the total fission energy release does not depend strongly on the prescribed effective dynamic viscosities. The fission power before enough energy has been deposited in the system to cause boiling at $T = 32.3$ s, is similar for each of the cases shown in Figure 5.25a. Fluidisation first occurring at $T = 32.51$ s, causes the fission power of the fissile system, shown in Figure 5.25a, to decrease. The subsequent oscillatory behaviour of the fissile system depends on the effective medium viscosity, as this will govern the flowability of UO_2 and gas bubbles through the three-phase suspension.

As previously mentioned, an increasing settled wet powder region interface height corresponds to a sedimentation dominant regime whereas a fluidisation dominant regime is shown by a decrease in the settled wet powder region interface height. Figure 5.25c indicates that the transition from fluidisation to sedimentation occurs earlier for the simulated cases with higher effective medium viscosities. The reason for this can be deduced by inspecting Figure 5.24, which indicates that a higher void fraction is required to produce a given gas advection rate, as the suspension becomes more viscous. Therefore, as gas bubbles advect out of the system and the void fraction decreases, lower gas velocities exist for more viscous suspensions. This means that the transition from a fluidised bed state to a sedimenting bed will first occur in more viscous suspensions.

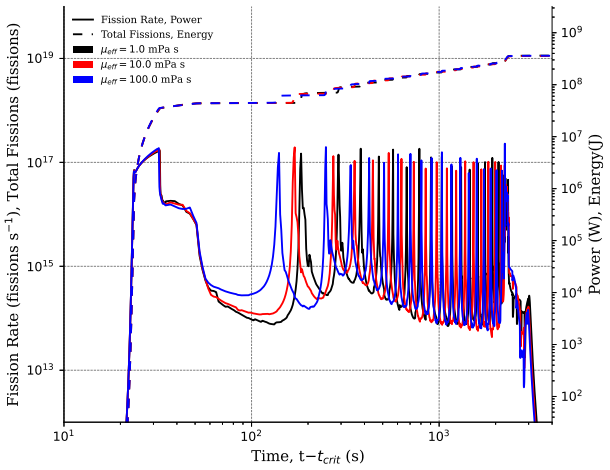

(a) Fission power and energy.

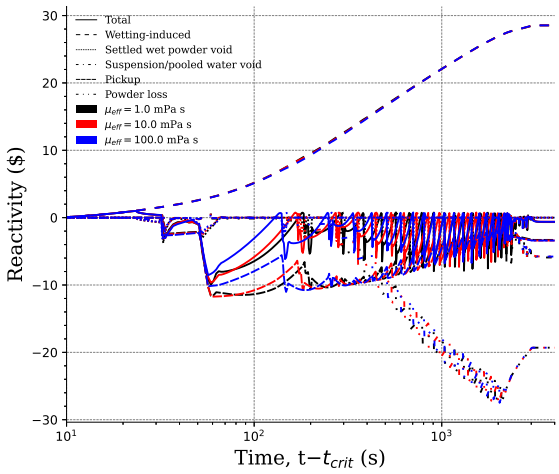

(b) Reactivity.

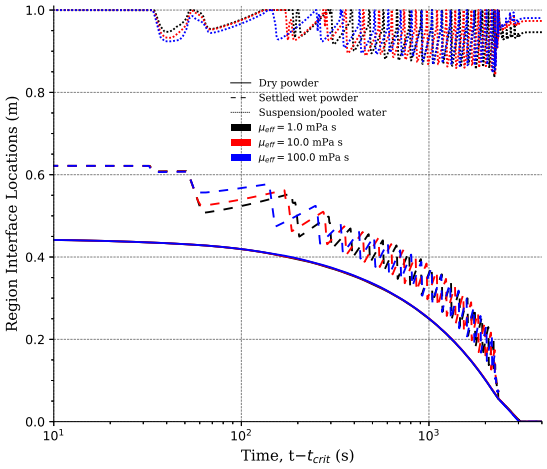

(c) Region interface locations.

Figure 5.25: The dynamics of the transient nuclear criticality excursion as a function of the suspension effective viscosity for the case where $U_{\mathrm{g,crit}} = 0.20$ m s^{-1} and $U_{\mathrm{pickup}} = 0.01$ m s^{-1}.

5.6 Conclusions

The previous three-region, three-phase phenomenological-based model of transient nuclear criticality excursions in highly dispersed, low-enriched, partially saturated UO_2 powder beds, with mean powder size, $d_p = 10$ μm, has been extended to include gas bubble-UO_2 powder particle interactions and sedimentation. The fundamental aim of this chapter was to perform sensitivity analysis, investigating how different fluidisation and sedimentation characteristics of three-phase, wetted UO_2 powder beds, may affect a transient nuclear criticality excursion initiated through the addition of water into a fissile powder bed.

Extensions to models described in previous chapters were introduced for the gas-bubble induced fluidisation of UO_2 powder particles, which resulted in the formation of a highly dispersed suspension above a static powder bed. Furthermore, agglomeration characteristics of UO_2 powder were found from the literature and used to construct a model of sedimentation. An important aspect of this chapter was to examine how the re-distribution of fissile mass in the moderator (water) affected the characteristics of a transient nuclear criticality excursion in three-phase wetted UO_2 powder systems.

Multivariate reactivity feedback components that couple the continuity and thermal phenomenological models to the point neutron kinetics model, have been found by fitting bivariate B-splines to MCNP derived reactivity data.

The mean size of a variety of agglomerated fissile powders, in various continuous phase fluids, were empirically determined using the method proposed by Steinour (1944b). This method utilised hindered settling data from various experimental studies found in the relevant literature. The mean size of agglomerated particles of UO_2 powder-benzene, UO_2 powder-acetone and ThO_2 powder-water suspensions were empirically determined to be between 18 μm and 40 μm.

The empirical correlations for the hindered settling speed of agglomerated UO_2 powder particles and the dispersivity of the suspended powder were used to evaluate the Péclet number of the UO_2 powder in the suspension. The range of Péclet numbers calculated from these empirical correlations suggested that gas-bubble induced turbulent mixing was a more dominant flow characteristic than sedimentation.

The neutronic behaviour of the system remained the same for all cases until incipient fluidisation. However, once fluidisation began, the neutronics of the system varied significantly with the prescribed critical gas velocity and rate of fluidisation.

The simulations indicated that incipient fluidisation occurred at higher interstitial pore void fractions when the critical gas velocity, $U_{g,crit} = 0.22$ m s^{-1} than for the case where $U_{g,crit} = 0.20$ m s^{-1}. Additionally, the simulations suggested that fluidisation occurred later in time for the higher of the two critical gas velocities studied. The settled wet powder void reactivity component dominated the negative reactivity feedback in the system when $U_{g,crit} = 0.22$ m s^{-1}. Fluidisation of the UO_2 powder introduced negative reactivity into the system. For the case where $U_{g,crit} = 0.22$ m s^{-1}, shortly after boiling, the system reached constant power.

A key finding of this study was that an oscillatory power response was seen for the case where $U_{\mathrm{g,crit}} = 0.20$ m s^{-1} and $U_{\mathrm{pickup}} = 0.01$ m s^{-1}. This response is due to the cyclical nature fluidisation and sedimentation that occurs in the suspension as a result of variations to the void fraction and reactivity components in the system. The oscillatory response was of a higher frequency when the hindered settling rate was increased by an order of magnitude. The oscillations began earlier in the transient as the effective medium viscosity in the suspension was increased. The total fission energy released over the duration of the simulated transient was found to be independent of the effective dynamic viscosity for the case where $U_{\mathrm{g,crit}} = 0.20$ m s^{-1} and $U_{\mathrm{pickup}} = 0.01$ m s^{-1}.

At a fluidisation rate of, $U_{\mathrm{pickup}} = 0.1$ m s^{-1} (with $U_{\mathrm{g,crit}} = 0.20$ m s^{-1}), fewer oscillations in the fission power occurred. This was the result of a large negative reactivity introduced due to the re-distribution of UO_2 powder from the static powder bed into a suspension. At this rate of fluidisation, the static UO_2 powder bed became fully suspended.

Chapter 6

Stochastic Nuclear Criticality Excursion Models for Wetted UO_2 Powder Beds

6.1 Introduction

In the presence of weak neutron sources and low neutron population, the neutron level may fluctuate as a result of the probabilistic nature of the competing processes of neutron production and loss (Radkowsky, 1964). In this neutronic regime, an accidental nuclear criticality excursion may have different dynamics depending on these random fluctuations. If a fissile system is prompt super-critical, a single neutron may be enough to initiate and sustain a persistent fission chain, whereas in a delayed super-critical system, all neutron chains are dying (Authier et al., 2014). From an NCS perspective, the delay that may occur from a delayed or prompt super-critical state first being reached, to the generation of a persistent, divergent neutron chain, is fundamentally important. For multiple realisations of the same system, the variance around this delay may lead to a greater reactivity being inserted into the fissile system by the time that the neutron population multiplies enough to be modelled deterministically (Williams, 2016; Winter et al., 2018). Therefore, as a given neutron population may occur at higher reactivities, the subsequent initial power spike that initiates negative reactivity feedback effects may be greater.

At present, no studies of low neutron source wetting-induced transient nuclear criticality excursions in highly enriched UO_2 powder systems have been performed. Therefore, the effect that a delay from the initial wetting to the onset of a deterministic transient nuclear criticality excursion has on the initial peak power has not yet been examined. This is of importance in the field of NCS since deterministic models of transient nuclear criticality excursions in these systems may under-predict the peak power by multiple factors. Alternatively, the peak power may be over-predicted if the reactivity of the system is less than one may expect from a deterministic study, at a prescribed neutron population.

This chapter examines the levels of UO_2 powder bed enrichment that may result in the low

neutron source condition outlined by Hansen et al. (1959) being satisfied. The applicability of the Hansen et al. (1959) criterion to a wetted UO_2 powder system is also examined. The enrichment of the UO_2 powder is classified in this thesis using the weight fraction of ^{235}U relative to ^{238}U. This ratio governs the suitability of the nuclear fuel for different applications. The concept of low-enriched uranium (LEU) was first outlined by the U.S. Atomic Energy Commission in 1955 (Glaser, 2006) as uranium enriched up to 20 %. This criterion was later adopted by the IAEA (IAEA, 2003). The specification of this limit ensured that enriched uranium used in research reactors could not be also used in the proliferation of nuclear weapons (Brown and Glaser, 2016). HEU as defined in IAEA (2003) is any uranium compound with an enrichment of > 20 %. The U.S. Nuclear Regulatory Commission (NRC) classify HEU, specifically the ^{235}U contained within it, as a special nuclear material (SNM). The SNM classification also applies to ^{239}Pu and ^{233}U, meaning that they are considered a risk and have the potential to be used directly in nuclear weapons.

For the study in this chapter, a specific case of an enriched UO_2 powder bed that satisfies the low neutron source criterion is modelled using the forward stochastic balance equation, as described by Williams (2016), to obtain the mean and variance in the neutron population and delayed neutron precursor populations as a function of time. A mean wait-time distribution is calculated, using the Gamma distribution method, which yields the distribution of times and conditions in the wetted UO_2 powder bed that produce a prescribed neutron population. The Gamma distribution method has been successfully applied in modelling the wait-time distribution of the CALIBAN (Authier et al., 2014; Williams, 2016) experimental test reactor. A threshold neutron population is prescribed that demarcates the stochastic from the deterministic regime. Deterministic simulations are then performed with initial conditions that are sampled from these Gamma wait-time probability distribution functions (PDFs), using the coupled point neutron kinetics, water infiltration, radiolysis, nuclear thermal hydraulics and boiling models that have been described in the previous chapters. Ultimately, the sensitivity of the initial peak power to the stochastically derived initial conditions are examined.

6.2 Sub-critical Intrinsic Neutron Source Multiplication

6.2.1 Intrinsic Neutron Sources

There are a number of processes that lead to the presence of distributed intrinsic neutron sources in fissile systems. These include neutron sources due to SF (Flerov and Petrjak, 1940; Scharff-Goldhaber and Klaiber, 1946), (α, n) reactions (Kudryavtsev et al., 2020), cosmic ray induced spallation neutron sources (Rossi, 1933) and (γ, n) reactions (Bernstein et al., 1947). The most important of these neutron sources in NCS excursion problems (in the absence of a localised extraneous source), are usually attributable to SF and (α, n) interactions. The (α, n) neutron source occurs through the interaction of α particles, released through radioactive decay, with isotopes of lighter nuclei such as oxygen (^{17}O and ^{18}O) in the UO_2 powder. Radioactive α decay, which consists of the releasing of a ^{4}He nuclei from the nucleus, typically occurs in heavier nuclides (Shultis and Faw, 2016). Isotopes of uranium present in enriched UO_2 powder such as ^{238}U and ^{235}U both exhibit α decay into ^{234}Th and ^{231}Th, respectively (Kojima et al., 2018). SF neutron sources are far more frequent in the ^{238}U isotope of UO_2 than the ^{235}U (Shultis and Faw, 2016).

Neutron sources that arise due to cosmic ray induced spallation of atomic nuclei on Earth as well as in the Earth's atmosphere constitute approximately 100 to 300 neutrons per unit area per second (Phillips et al., 2005). Although this may seem large, the UO_2 powder vessel will largely be shielded from this source of neutrons, due to the concrete wall and ceiling of the nuclear fuel fabrication facility. This neutron source is neglected from further consideration in this analysis. Similarly, (γ, n) reactions that occur in UO_2 powder particles may not significantly contribute to the total intrinsic neutron source. This is suggested through using the JANIS nuclear cross-section visualisation tool for incident γ data from the ENDF/B-VIII.0 library (Nouri et al., 2002). It can be seen that (γ, n) nuclear reactions for ^{238}U and (γ, 2n) nuclear reactions for both ^{238}U and ^{235}U, have microscopic nuclear cross-sections that peak on the order of 100's of millibarns in the 10 MeV γ energy range. This is considerably lower than other microscopic nuclear cross-sections, and therefore, the probability of (γ, n) and (γ, 2n) may be considered low relative to other interactions. It should be noted that the present model has no extraneous (external/installed or prescribed) neutron sources.

The concept of an equivalent fundamental-mode neutron source corresponds to a neutron source with an identical phase-space distribution to that of the fission source, that produces the same multiplication as the original fixed source (Spriggs et al., 1999). Since the proposed UO_2 powder bed is mono-dispersed, uniformly packed and of identical enrichment throughout, the intrinsic neutron source is assumed to be uniformly distributed throughout the powder bed. However, the spatial locality of the neutrons produced through SF and (α, n) interactions in a homogeneously distributed intrinsic neutron source field, may be applied an adjoint weighting to understand the importance of the neutron sources (Spriggs et al., 1997). Intrinsic distributed source neutron weighting is out of the scope of this study.

6.2.2 Intrinsic Neutron Source of UO_2

The intrinsic neutron source density of uranium dioxide (UO_2) has been determined as a function of enrichment using the deterministic SOURCES-4C code (Wilson et al., 2002). This code is capable of calculating the production of neutrons through both SF and (α-n) interactions. Figure 6.1 shows how the total intrinsic neutron source strength, calculated using Equation (6.1) varies for the UO_2 system studied in this thesis, where the initial mass of UO_2 powder is $M_{UO_2} = 500$ kg. The SOURCES-4C data suggests that at low levels of enrichment, the total intrinsic neutron source is dominated by SF. This is in-line with the analysis of Griesheimer et al. (2015), who also suggested that for low-enriched UO_2, the SF contribution was orders of magnitude greater than the (α, n) contribution. As the fraction of ^{235}U increases relative to ^{238}U (higher enrichment), the contribution of SF to the total intrinsic neutron source decreases, whilst the neutrons produced through (α, n) interactions increases slightly. Radkowsky (1964) also notes the dependency of SF and (α, n) neutron source strength as a function of enrichment. When the enrichment, $\gamma = 95$ wt-%, the total intrinsic neutron source is approximately equally due to SF and (α, n) interactions. This is in accordance with the data reported in Goddard and Croft (2013) which also states that the neutron production ratio, defined as the ratio of SF to (α, n) fission, decreases as the enrichment level rises.

$$S_{\mathrm{n}}(\gamma) = s_{\mathrm{n}}(\gamma)\frac{M_{\mathrm{UO_2}}}{\rho_{\mathrm{p,th}}} \tag{6.1}$$

where γ is the enrichment of UO_2 powder.

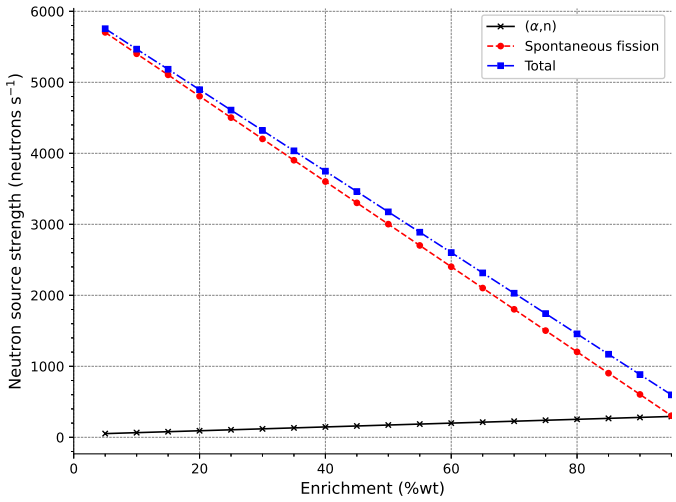

Figure 6.1: Intrinsic neutron source of UO_2 powder as a function of enrichment.

The intrinsic neutron source energy spectrum due to SF and (α, n) interactions are shown in Figure 6.2. Figure 6.2a suggests that the level of enrichment of the UO_2 powder does not change the energy spectrum of neutrons produced through SF, but the magnitude changes significantly. The peak of the SF neutron energy spectrum is located at 1 MeV, decreasing with increasing UO_2 powder enrichment. Conversely, Figure 6.2b shows that the (α, n) source in UO_2 increases as the enrichment increases. The peak of the energy spectrum is found at 2 MeV, with a secondary peak located below 0.5 MeV, in the thermal energy region.

6.2.3 Physics of Sub-critical Systems

Research surrounding the physics of sub-critical systems, specifically the sub-critical multiplication and power, has been performed to aid the development of accelerator-driven systems (ADS) (Shahbunder et al., 2010). ADS' have been proposed to produce spallation neutrons which may then be directed at radioactive waste consisting of long-lived radionuclides, transmuting the long-lived fission products into radionuclides with shorter half-lives. ADS' may also be used to provide a spallation neutron source to a sub-critical nuclear reactor, operating at a steady-state sub-critical power.

The neutron balance equation in a steady-state fissile system, neglecting delayed neutron precursors and assuming that there is no neutron source present, can be derived from Equation (2.16), in the fundamental mode as (Gandini and Salvatores, 2002):

$$L_{\mathrm{t}}\Phi(\mathbf{r}, E, \mathbf{\Omega}) + \frac{1}{k_{\mathrm{eff}}} M_{\mathrm{t}}^{\mathrm{p}}\Phi(\mathbf{r}, E, \mathbf{\Omega}) = 0 \tag{6.2}$$

where L_{t} has previously been defined in Section 2.4 as the streaming operator and $M_{\mathrm{t}}^{\mathrm{p}}$ is the neutron production operator.

The conventional fundamental mode eigenvalue, k_{eff}, is then defined as the ratio of production to

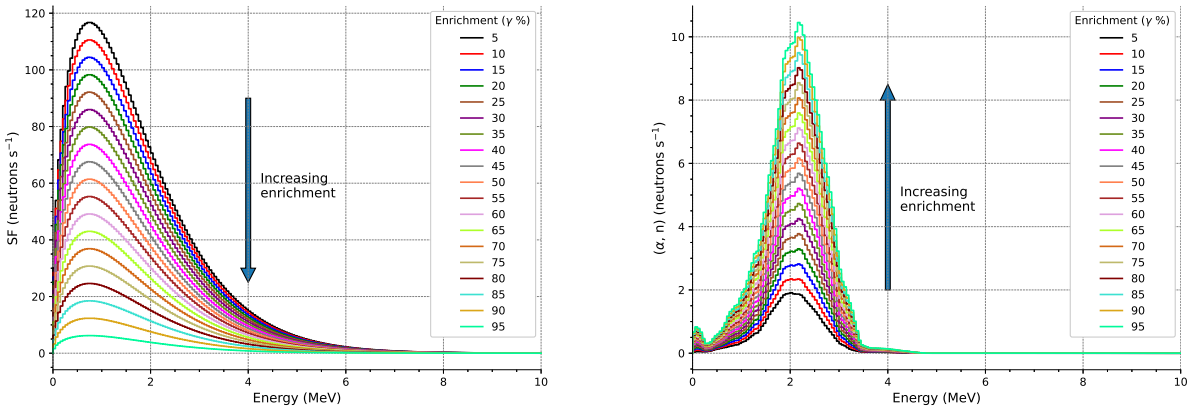

(a) (b)

Figure 6.2: Intrinsic neutron source energy spectrum calculated for spontaneous fission and (α, n) interactions using SOURCES-4C with 200 equally spaced neutron energy groups.

loss, with some weighting function, denoted $\mathbf{u}$ (Gandini, 2002):

$$k_{\text{eff}} = -\frac{\langle \mathbf{u}, M_{\text{t}}^{\text{p}} \Phi(\mathbf{r}, E, \mathbf{\Omega}) \rangle}{\langle \mathbf{u}, L_{\text{t}} \Phi(\mathbf{r}, E, \mathbf{\Omega}) \rangle} \tag{6.3}$$

where $\mathbf{u}$ is a weighting factor. Appropriate weighting factors have been described by Gandini (2002).

However, the fundamental mode eigenvalue (k_{eff}) is only valid at or near criticality, since near criticality the physical behaviour of the system is dominated by the fundamental mode of the system (Kobayashi and Nishihara, 2000). In practice, a sub-critical fissile system in the presence of some intrinsic distributed or extraneous neutron source, will have a neutron multiplication that may differ significantly from this value. In fact, Saracco and Ricco (2009) notes that the neutron multiplication of a sub-critical fissile system may be classified into three states. The first of these is known as the deeply sub-critical state ($k_{\text{eff}} < 0.8$ to 0.9), where the sub-critical power responds almost immediately to a variation of the source, leaving a fraction β_{eff} to evolve over the timescale of the delayed neutrons. In this regime, significant deviations between the fundamental mode neutron flux and the sub-critical neutron flux are expected (Shahbunder et al., 2010). The close to critical regime (0.95 to 0.97 $< k_{\text{eff}}$) is one where the sub-critical multiplication of the system approaches the fundamental mode eigenvalue, k_{eff}, recovering the usual system evolution predicted by the steady-state eigenvalue calculations (Saracco and Ricco, 2009). There is also an intermediate regime (0.8 to 0.9 $< k_{\text{eff}} <$ 0.95 to 0.97) where the behaviour of the system is different from the two previously described cases and is more complex. It should also be noted that in the absence of any neutron source, the power of the system would go to zero and the sub-critical multiplication factor of the system would be undefined.

The sub-critical multiplication of the system has been defined in numerous ways, by a variety of authors. Greenspan (1975) first describes the sub-critical multiplication as the ratio of the intrinsic or extraneous neutron source to the loss of neutrons, weighted by the adjoint neutron flux of a critical

reference reactor. This approach has also been specified by Kobayashi and Nishihara (2000) who defined two separate sub-critical multiplication relations. The first of which is derived from Greenspan (1975) and refers to the multiplication of source neutrons within the system. The alternative measure is associated with the multiplication of fission neutrons within the system. This second measure has been formalised by Gandini (2002) into a generalised definition of neutron multiplication, defined as the ratio of fission neutron production to neutron loss. This definition of sub-critical multiplication, which can also be found within Shahbunder et al. (2010); Gandini and Salvatores (2002), has been used in the present study and may be given as the weighted ratio of fission neutron production to neutron loss integrated over the whole phase-space:

$$k_{\mathrm{s}} = \frac{\langle \mathbf{u}, M_{\mathrm{t}}^{\mathrm{p}} \Phi(\mathbf{r}, E, \mathbf{\Omega}) \rangle}{\langle \mathbf{u}, M_{\mathrm{t}}^{\mathrm{p}} \Phi(\mathbf{r}, E, \mathbf{\Omega}) \rangle + \langle \mathbf{u}, s_{\mathrm{n}}(\mathbf{r}, E) \rangle} \tag{6.4}$$

where the weighting function $\mathbf{u}$ may be a variety of different parameters of interest. Gandini (2002) describes that one may use the sub-critical power level of the fissile system. Alternatively, a unity weighting may be applied (unweighted approach) or an adjoint-neutron flux weighting may also be used to account for the importance of neutrons in the reactor when estimating the sub-critical multiplication factor, k_{s}.

6.2.4 Sub-critical Multiplication and Power UO_2 Powder Bed

The reactivity of a fissile UO_2 powder bed that is undergoing wetting has already been shown in Section 3.4.8 to span all three sub-critical states elucidated by Saracco and Ricco (2009). Therefore, the neutron multiplication of the UO_2 powder bed as it approaches a critical state, due to water infiltration, will be better represented by the sub-critical multiplication factor (k_{s}) rather than the fundamental mode eigenvalue (k_{eff}). The variation between these measures of criticality has been examined here using the continuous energy Monte Carlo neutron transport code Serpent (Leppänen et al., 2015).

Serpent was used to create a three-region model of a 5-wt% and 95-wt% enriched UO_2 powder bed, where each distinct region was homogenised. The appropriateness of the homogenisation procedure, removing the double heterogeneity associated with modelling fissile powder-based systems, has already been discussed in Section 3.4.11. An illustration of the system is shown in Figure 6.3. The geometric properties of the system are given in Table 6.1. When sub-critical, the UO_2 powder bed has no radiolytic gas or steam present and remains at room temperature. The height of the powder bed ($H_{\mathrm{dp}} + H_{\mathrm{wp}}$) can be determined from the prescribed porosity of the UO_2 powder bed and the mass of powder in the system. For these Serpent simulations, the height of the pooled water region, denoted H_{sus}, is specified such that the full height of the bed is occupied. The system approaches criticality as the bed immersion fraction, f_{imm}, calculated using Equation (3.5), increases.

The Serpent simulations have been performed both in fixed-source mode, using the 'set nps' card, as well as in fundamental eigenvalue mode, using the 'set pop' card, to estimate k_{s} and k_{eff} as a function of f_{imm}, respectively. Serpent provides a variety of estimates of these parameters. One method calculates the ratio of the total number of fission neutrons produced during the simulation by the sum of the number of initial source particles and the number of neutrons produced through fission.

An alternative measure, which is the preferred method used in this section, is calculated by tallying the total fission neutron production and dividing by the tallied neutron loss, with a unity weighting, $\mathbf{u} = 1$. This is similar to using Equations (6.3) and (6.4). Vacuum boundary conditions are prescribed at the axial ends of the cylindrical domain as well as in the radial direction.

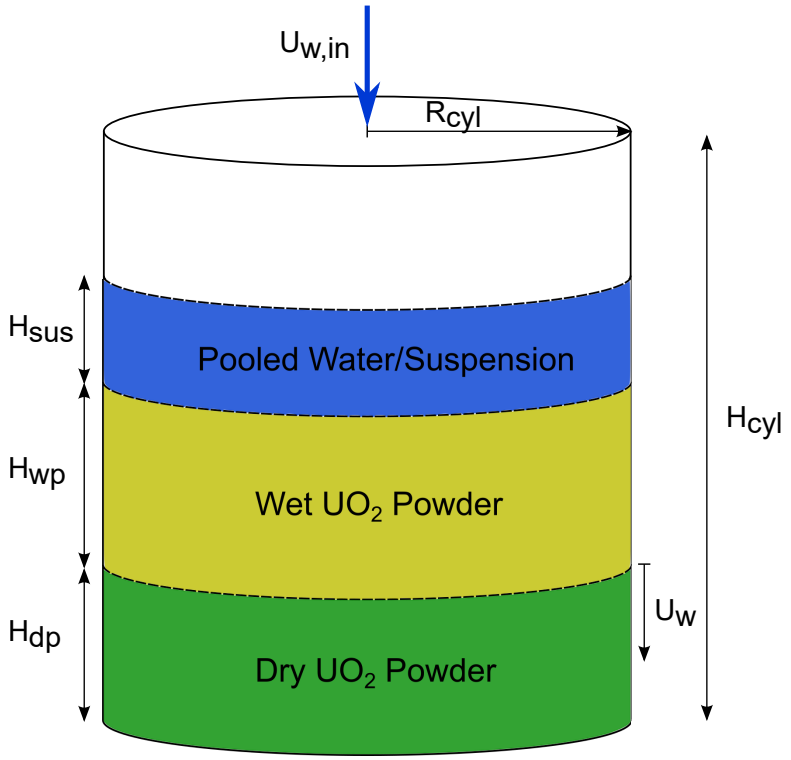

Figure 6.3: Representation of three-region UO_2 powder bed with region interfaces separating dry powder region, wet powder region and pooled water region.

Table 6.1: Serpent sub-critical and fundamental mode simulation system physical properties.

Property	Value
R_{cyl}	0.4 m
H_{cyl}	1.0 m
$v_{\text{f,p,dp}}$	0.1461
$v_{\text{f,p,wp}}$	0.1461
$v_{\text{f,p,sus}}$	0.0
$\rho_{\text{p,th}}$	10950 kg m^{-3}
$\rho_{\text{w,th}}$	998.1 kg m^{-3}
M_{p}	500 kg

The results, shown in Figure 6.4a, indicate that the true sub-critical neutron multiplication of the UO_2 powder bed as it is wetted deviates significantly from what is predicted when performing fundamental mode eigenvalue calculations. Figure 6.4b shows that the neutron multiplication of the system increases as the UO_2 powder bed becomes more immersed with water. The fractional deviation between the two measures of neutron multiplication, shown in Figure 6.5, becomes less as the system approaches criticality. This is because the contribution of the source term on the numerator in Equation (6.4) becomes less important as the system approaches criticality; the system recovers the behaviour predicted by the fundamental mode eigenvalue calculation.

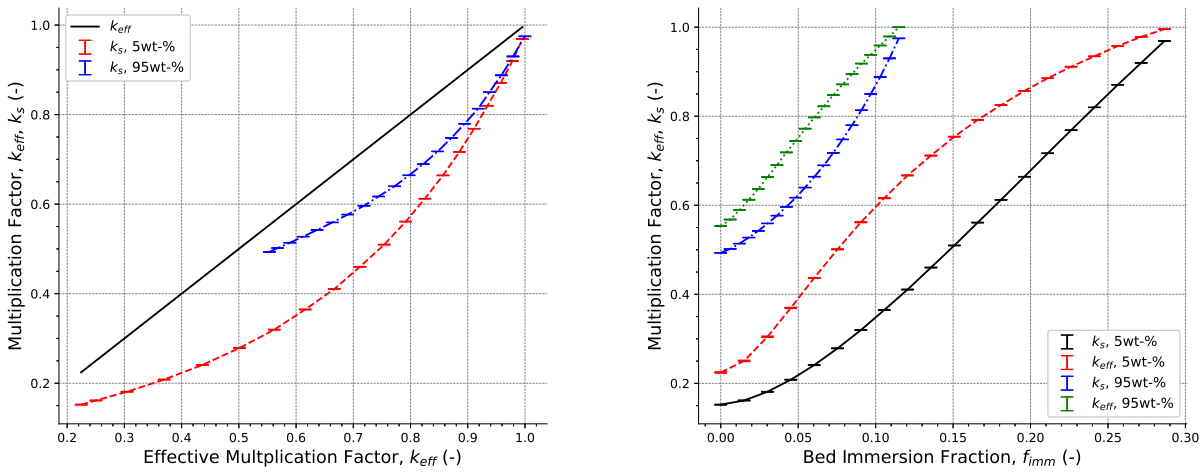

(a) (b)

Figure 6.4: Variation of the sub-critical multiplication factor (k_s) and the fundamental mode, effective multiplication factor (k_{eff}), both calculated using the continuous energy Monte Carlo neutron transport code Serpent.

Figure 6.5 also suggests that the difference between the two neutron multiplication measures is greater for the powder bed with an enrichment of 5-wt% as opposed to the 95-wt% enrichment case. This increased error between the fundamental mode eigenvalue (k_{eff}) and the sub-critical multiplication factor (k_s) may be attributed to the fact that there is an increased likelihood of fission in the UO_2 powder bed with a higher enrichment, meaning that the source term is less dominant in Equation (6.4).

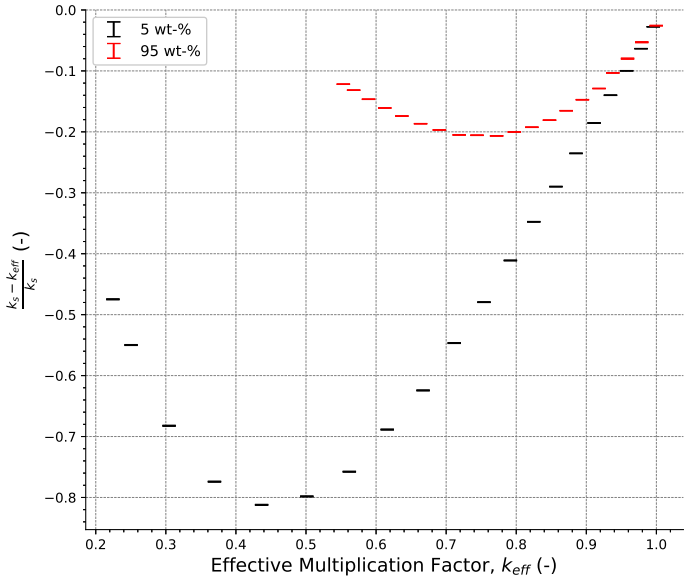

Figure 6.5: Fractional deviation between the effective multiplication factor (k_{eff}) and the sub-critical multiplication (k_s).

Serpent normalises the total power and neutron density to some other property of the system.

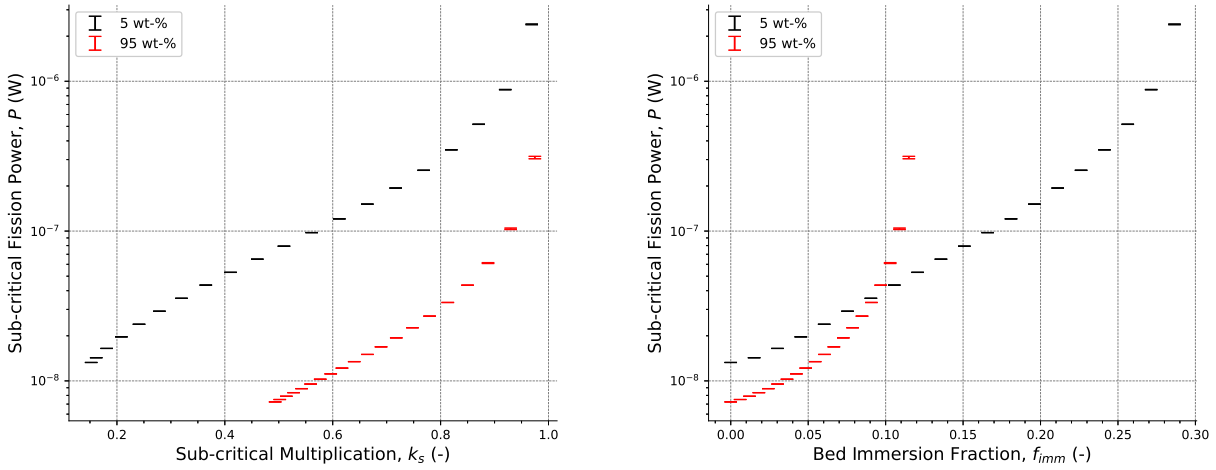

(a) (b)

Figure 6.6: Variation of the steady-state sub-critical power as a function of the sub-critical multiplication (k_s) and the bed immersion fraction (f_{imm}), calculated using Serpent.

For sub-critical multiplication calculations the fission power and neutron density can be normalised to the value of the intrinsic distributed neutron source present in the UO_2 powder bed due to SF and (α, n) interactions. This procedure yields the true steady-state sub-critical power and neutron density of the fissile system. The values of the intrinsic distributed neutron source strength can be read from Figure 6.1 as 5754.57 neutrons s^{-1} and 586.07 neutrons s^{-1}, for the case where the enrichment of the UO_2 powder bed is 5 wt-% and 95 wt-%, respectively. The energy spectrum of the neutron source is modelled in Serpent using the data supplied in Figure 6.2. Leppänen (2015) notes that the source normalisation cannot be used in the same way for criticality eigenvalue (k_{eff}) calculations to obtain the true power and neutron density of the system.

The steady-state sub-critical power of the system at different bed immersion fractions for each enrichment case is shown in Figure 6.6. Figure 6.6a shows that an increase in sub-critical multiplication leads to a corresponding rise in the steady-state sub-critical power of the wetted UO_2 powder bed. Figure 6.6a also indicates that the steady-state sub-critical power is higher for the case where the enrichment is lower, due to the increase intrinsic neutron source strength, for a given sub-critical multiplication. However, as a function of the immersion of the UO_2 powder bed, which is shown in Figure 6.6b, the same relationship is not seen.

In previous chapters of this thesis, the initial neutron density of an unsaturated UO_2 powder bed, prior to water infiltration is determined using the volume-averaged point kinetics equation described by Equation (3.7). This equation uses the fundamental mode eigenvalue (k_{eff}) to obtain the steady-state neutron density and may be re-formulated to as:

$$n = -\frac{s_n \Lambda k_{eff}}{k_{eff} - 1} \tag{6.5}$$

However, as described earlier, a more appropriate measure of neutron multiplication in a sub-

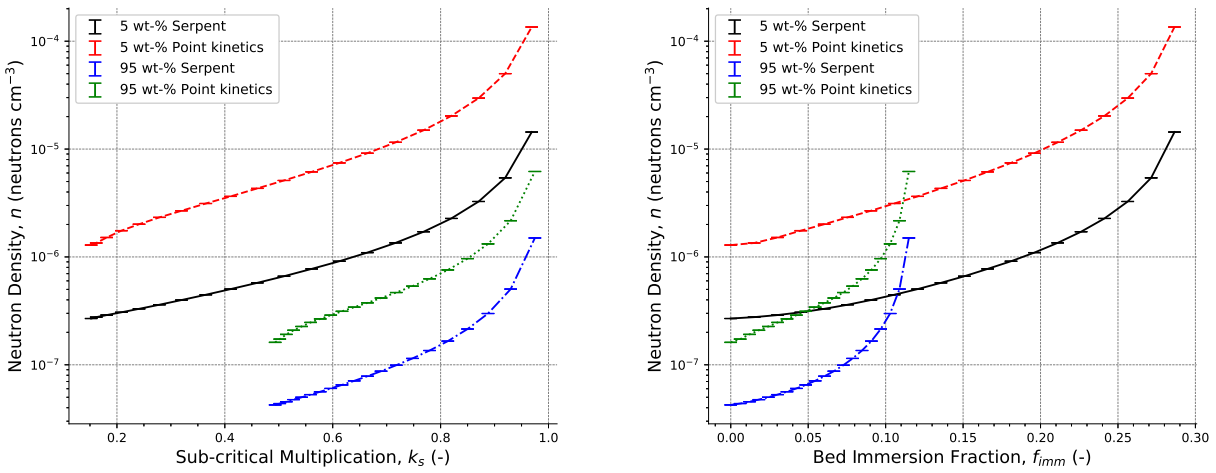

(a) (b)

Figure 6.7: Variation of the steady-state neutron density as a function of the sub-critical multiplication (k_s) and the bed immersion fraction (f_imm), calculated using Serpent and the volume-averaged point kinetics equation.

critical system is the sub-critical multiplication factor (k_s). Therefore, Equation (6.5) may be redefined to obtain the steady-state neutron density using the sub-critical multiplication factor as:

$$n = -\frac{s_\mathrm{n}\Lambda k_\mathrm{s}}{k_\mathrm{s} - 1} \tag{6.6}$$

This volume-averaged point kinetics equation outlined in Equation (6.6) homogenises any spatial variation in the neutron source and does not take specific boundary conditions into account. To examine the applicability of this measure in determining the true steady-state neutron density, it may be compared to the neutron density calculated through Serpent. A set of different bed immersion fractions, corresponding to different sub-critical multiplication factors are investigated. Figure 6.7 shows that Equation (6.6) over-predicts the steady-state neutron density by approximately an order of magnitude. This may be attributed to the fact that spatial effects such as radial and axial leakage are not taken into account in the point kinetics equation. Although there is a large relative deviation between the two measures, the absolute deviation is very small, ranging between 1.19×10^{-7} neutrons cm^{-3} and 1.21×10^{-4} neutrons cm^{-3}. For the UO_2 powder beds modelled in this thesis with mass of 500 kg and UO_2 density of $10,950$ kg m^{-3}, the difference between Serpent and the point kinetics equation ranges from 0.005 neutrons to 5.53 neutrons. Given that difference in neutron population between the two methods is small, the point kinetics equation is considered an appropriate approach in determining the initial conditions of the initially dry UO_2 powder bed, prior to water infiltration.

6.3 Low-Source Stochastic Study Methodology

6.3.1 Forward Probability Balance Equation for Stochastic Neutron Kinetics

The conventional point neutron kinetics equations are deterministic and may be used to estimate the mean (expected or expectation value) of the neutron population and delayed neutron precursor populations. However, the actual dynamics of low neutron source, low neutron population fissile systems is inherently stochastic in nature, with potentially significant stochastic fluctuations from the mean (or expected) value of the angular and scalar neutron fluxes (Pázsit and Pál, 2007). There are four approaches to modelling stochastic neutron transport and kinetic problems. The first is the forward probability balance equation (Govorkov, 1963, 1964, 1965; Williams, 2009), the second is the backward probability balance (or Pál-Bell) equation (Pál, 1962; Bell, 1965), the third is analogue Monte Carlo methods (Cooling et al., 2016) and the fourth is Itô-calculus methods (Hayes and Allen, 2005). Each method has its own advantages and disadvantages in terms of numerical accuracy and computationally efficiency when numerically discretised. A detailed comparison of the different approaches to modelling and simulating stochastic neutron transport and kinetics problems is presented elsewhere (Gordon et al., 2021).

In this Chapter the forward probability balance equation is used to determine the stochastic neutron kinetics behaviour of a wetted UO_2 powder bed, modelled using zero-dimensional and a one neutron energy group (or one-speed) approximation. An alternative approach would be to utilise the backwards probability balance (or Pál-Bell) equation for the stochastic representation of point neutron kinetics (Pázsit and Pál, 2007). It is important to note that the major difference between the forward and backward probability balance equations is when they are applied to multidimensional and multiple neutron energy groups. For multidimensional problems the forward probability balance equation forms a spatially correlated system of PIDEs unlike the more tractable backward probability balance (or Pál-Bell) equation which takes a much simpler mathematical form (Govorkov, 1963, 1964, 1965; Williams, 2009). In addition, in multiple neutron energy groups the backward probability balance (or Pál-Bell) equation is much more tractable than the equivalent forward probability balance equation. Also note that the mean solution from the forward and backward probability balance equations are the standard forward (primal) and adjoint point neutron kinetics equations respectively (Pál, 1962; Bell, 1965).

A multivariate probability generating function defining the probability that there are a given number of neutrons and delayed neutron precursors present in a system at a time, t, given some initial neutron population and delayed neutron precursor population at an earlier time has been used by numerous authors to model the stochastic behaviour of neutrons and delayed neutron precursors in low neutron source nuclear criticalities (Pál, 1958; Bell, 1963; Williams, 2016). The generating function is given in Williams (2016) as:

$$F(x,\vec{y},t) = \sum_{N=0}^{\infty}\sum_{C_1=0}^{\infty}\ldots\sum_{C_6=0}^{\infty} x^N y_1^{C_1}\ldots y_I^{C_6} \times P(N,C_1,\ldots,C_6,t|N(0)=0,C_1(0)=0,\ldots,C_6(0)=0) \quad (6.7)$$

where N and $C_1, .., C_6$ are now the stochastic neutron population and delayed neutron precursor populations. The variable x is associated with the neutron population and y_i is associated with the i-th delayed neutron precursor group.

The differential of the generating function of these continuous stochastic variables with respect to time yields the forward form of the stochastic balance equation (Williams, 1974):

$$\frac{\partial F(x,\vec{y},t)}{\partial t} = S_\mathrm{n}(t)(x-1)F(x,\vec{y},t) + \sum_{i=1}^{6}\lambda_i(x-y_i)\frac{\partial F(x,\vec{y},t)}{\partial y_i} + g(x,\vec{y},t)\frac{\partial F(x,\vec{y},t)}{\partial x} \tag{6.8}$$

The total distributed intrinsic source, denoted S_n, is due to (α, n) and spontaneous fission (SF), assumed Poisson in its emission rate, and $g(x,\vec{y},t)$ is given as:

$$g(x,\vec{y},t) = \lambda_\mathrm{c}(t)(1-x) + \lambda_\mathrm{f}(f(x,\vec{y}) - x) \tag{6.9}$$

where $\lambda_\mathrm{c}(t) = \lambda_\mathrm{a}(t) - \lambda_\mathrm{f}(t)$ and $\lambda_\mathrm{f}(t) = k_\mathrm{eff}(t)\lambda_\mathrm{a}(t)/\bar{\nu}$ are the time-dependent transition rates that allow for a time varying reactivity and correspond to capture and fission, respectively. The absorption transition rate is given by $\lambda_\mathrm{a}(t) = 1/\tau(t)$. The term, $f(x,\vec{y})$, is a probability generating function corresponding to the neutron emission probability from prompt and delayed neutrons. This may be given as:

$$f(x,\vec{y}) = f(x)f_1(y_1)...f_I(y_I) \tag{6.10}$$

where $f(x)$ for prompt neutrons and given by:

$$f(x) = \sum_{n=0}^{N}\frac{(-1)^n}{n!}\chi_n(1-x)^n \tag{6.11}$$

The present model truncates Equation (6.11) at the second order and assumes that only one neutron is emitted from a delayed neutron precursor. The parameters χ_1 [-] and χ_2 [-] are obtained in Section 6.4.1 using experimentally derived neutron emission probabilities. The following expression may be given for the neutron emission probability generating function for the delayed neutrons:

$$f_i(y_i) = 1 - \bar{\nu}\beta_i(1-y_i) \tag{6.12}$$

By differentiating Equation (6.7) with respect to the stochastic variables and setting $x = \vec{y} = 1$, the k-th factorial moments of the probability generating function may be obtained. These derivatives are given in Williams (2016) as:

$$\frac{\partial F(1,\vec{1},t)}{\partial x} = \sum_{N=0}^{\infty}\sum_{\vec{C}=0}^{\infty} NP(N,...,t) = E(N) = \bar{N} \tag{6.13}$$

$$\frac{\partial^2 F(1,\vec{1},t)}{\partial x^2} = E(N(N-1)) = \mu_{\mathrm{NN}} \tag{6.14}$$

$$\frac{\partial F(1,\vec{1},t)}{\partial y_{\mathrm{i}}} = E(C_{\mathrm{i}}) = \bar{C}_{\mathrm{i}} \tag{6.15}$$

$$\frac{\partial^2 F(1,\vec{1},t)}{\partial y_{\mathrm{i}}^2} = E(C_{\mathrm{i}}(C_{\mathrm{i}}-1)) = \mu_{\mathrm{ii}} \tag{6.16}$$

$$\frac{\partial^2 F(1,\vec{1},t)}{\partial y_{\mathrm{i}} y_{\mathrm{j}}} = E(C_{\mathrm{i}}C_{\mathrm{j}}) = \mu_{\mathrm{ij}} \tag{6.17}$$

$$\frac{\partial^2 F(1,\vec{1},t)}{\partial x y_{\mathrm{i}}} = E(NC_{\mathrm{i}}) = \mu_{\mathrm{Ni}} \tag{6.18}$$

The variance of the neutron population and delayed neutron precursor group, i, may then be determined respectively from the following:

$$\sigma^2_{\mathrm{std,N}}(t) = \langle N^2\rangle - \langle N\rangle^2 = \mu_{NN}(t) + \bar{N}(t) - \bar{N}(t)^2 \tag{6.19}$$

and:

$$\sigma^2_{\mathrm{std,i}}(t) = \langle C_{\mathrm{i}}^2\rangle - \langle C_{\mathrm{i}}\rangle^2 = \mu_{\mathrm{ii}}(t) + \bar{C}_{\mathrm{i}}(t) - \bar{C}_{\mathrm{i}}(t)^2 \tag{6.20}$$

Differentiating Equations (6.13) to (6.18) with respect to time, the k-th factorial moments of the neutron population and delayed neutron precursor populations may be obtained. The resulting set of ODEs may then be solved numerically for the mean and variance in the neutron population and delayed neutron precursor populations as a function of time. These ODEs are given as follows:

$$\frac{d\bar{N}(t)}{dt} = \frac{\beta_{\mathrm{eff}}}{\Lambda(t)}(R_{\mathrm{T}}(t)-1)\bar{N}(t) + \sum_{\mathrm{i}=1}^{I}\lambda_{\mathrm{i}}(t)\bar{C}_{\mathrm{i}}(t) + S_{\mathrm{n}}(t) \tag{6.21}$$

$$\frac{d\bar{C}_{\mathrm{i}}(t)}{dt} = -\lambda_{\mathrm{i}}(t)\bar{C}_{\mathrm{i}}(t) + \frac{\beta_{\mathrm{i}}}{\Lambda(t)}\bar{N}(t) \tag{6.22}$$

$$\frac{d\mu_{\mathrm{NN}}(t)}{dt} = 2S_{\mathrm{n}}(t)\bar{N}(t) + 2\sum_{\mathrm{i}=1}^{\mathrm{I}} \lambda_{\mathrm{i}}(t)\mu_{\mathrm{Ni}}(t) + \frac{2\beta_{\mathrm{eff}}}{\Lambda(t)}(R_{\mathrm{T}}(t)-1)\mu_{\mathrm{NN}}(t) + \frac{\chi_2}{\bar{\nu}\Lambda(t)}\bar{N}(t) \tag{6.23}$$

$$\frac{d\mu_{\mathrm{Nj}}(t)}{dt} = S_{\mathrm{n}}(t)\bar{C}_{\mathrm{j}}(t) + \sum_{i=1}^{I} \lambda_{\mathrm{i}}(t)\mu_{\mathrm{ij}}(t) - \lambda_{\mathrm{j}}(t)\mu_{\mathrm{Nj}}(t) + \frac{\beta_{\mathrm{j}}}{\Lambda(t)}\mu_{\mathrm{NN}}(t) + \frac{\beta_{\mathrm{eff}}}{\Lambda(t)}(R_{\mathrm{T}}(t)-1)\mu_{\mathrm{Nj}}(t) + \frac{\bar{\nu}(1-\beta_{\mathrm{eff}})\beta_{\mathrm{j}}}{\Lambda(t)}\bar{N}(t) \tag{6.24}$$

$$\frac{d\mu_{\mathrm{ij}}(t)}{dt} = -(\lambda_{\mathrm{i}} + \lambda_{\mathrm{j}})\mu_{\mathrm{ij}}(t) + \frac{(\beta_{\mathrm{j}}\mu_{\mathrm{ni}}(t) + \beta_{\mathrm{i}}\mu_{\mathrm{nj}}(t))}{\Lambda(t)} + \frac{\bar{\nu}\beta_{\mathrm{i}}\beta_{\mathrm{j}}(1-\delta_{\mathrm{ij}})}{\Lambda(t)}\bar{N}(t) \tag{6.25}$$

6.3.2 Gamma Distribution and Threshold Neutron Population

The mean and variance of the neutron population have been suggested by Harris (1964) to approach a Gamma distribution when the system is highly multiplicative and stationary.

This Gamma PDF for the neutron population ($P_{\gamma,\mathrm{N}}$ [-]) has been given in Williams (2016) as:

$$P_{\gamma,\mathrm{N}}(N,t) = \frac{\eta_{\mathrm{N}}(t)}{\bar{N}(t)\Gamma(\eta_{\mathrm{N}}(t))}\left(\frac{\eta_{\mathrm{N}}(t)N}{\bar{N}(t)}\right)^{\eta_{\mathrm{N}}(t)-1}\exp\left(-\frac{\eta_{\mathrm{N}}(t)N}{\bar{N}(t)}\right) \tag{6.26}$$

and for delayed neutron precursors ($P_{\gamma,\mathrm{i}}$):

$$P_{\gamma,\mathrm{i}}(C_{\mathrm{i}},t) = \frac{\eta_{\mathrm{i}}(t)}{\bar{C}_{\mathrm{i}}(t)\Gamma(\eta_{\mathrm{i}}(t))}\left(\frac{\eta_{\mathrm{i}}(t)C_{\mathrm{i}}}{\bar{C}_{\mathrm{i}}(t)}\right)^{\eta_{\mathrm{i}}(t)-1}\exp\left(-\frac{\eta_{\mathrm{i}}(t)C_{\mathrm{i}}}{\bar{C}_{\mathrm{i}}(t)}\right) \tag{6.27}$$

The mean and variance found by solving the forward stochastic balance equation presented in Section 6.3.1 may be used to fully define the Gamma distribution by noting the following:

$$\eta_{\mathrm{N}}(t) = \frac{\bar{N}^2(t)}{\sigma^2_{\mathrm{std,N}}(t)} \tag{6.28}$$

and:

$$\eta_{\mathrm{i}}(t) = \frac{\bar{C}^2_{\mathrm{i}}(t)}{\sigma^2_{\mathrm{std,i}}(t)} \tag{6.29}$$

The relative standard deviation of the neutron population distribution and delayed neutron precursor population may readily be determined from Equations (6.28) and (6.29) respectively as:

$$R_{\mathrm{std,N}}(t) = \frac{1}{\sqrt{\eta_{\mathrm{N}}(t)}} \tag{6.30}$$

and:

$$R_{\mathrm{std,i}}(t) = \frac{1}{\sqrt{\eta_{\mathrm{i}}(t)}} \tag{6.31}$$

A transient nuclear criticality excursion in a highly enriched UO_2 powder bed undergoing wetting, will ultimately lead to a persistent chain of neutrons that causes the neutron population to increase. As the neutron population and delayed neutron precursor population increases, the standard deviation of these properties also increases. However, as Cooling et al. (2018) notes, the relative standard deviation of these stochastic variables converge to a single value, indicating self-similarity between the stochastic variables. This can readily be seen by considering that if $R_{\mathrm{std,N}}$ and $R_{\mathrm{std,i}}$ are constant, Equations (6.26) and (6.27) become dependent only on $N/\bar{N}(t)$ and $C_{\mathrm{i}}/\bar{C}_{\mathrm{i}}$, respectively. Williams (2016) states that the time taken to reach this point corresponds to the maturity time. Both Stacey (2018) and Williams (2016) indicate that this may correspond to the transition from the stochastic to the deterministic regime. The threshold neutron population, which denotes the transition between the two regimes, may then be calculated by solving the ODEs presented in Equations (6.21) to (6.25) for the mean and variance of the neutron population and delayed neutron precursor population, and looking for convergence of the relative standard deviation of the stochastic variables. Although Stacey (2018) has stated that this convergence usually occurs at around 10^5 neutrons cm^{-3}, this study prescribes a range of threshold neutron populations for a highly enriched wetted UO_2 powder system.

6.3.3 Mean Wait-Time Distribution

The mean wait-time distribution corresponds to the probability distribution of time taken for some stochastic variable to reach a prescribed level. The importance of the mean wait-time distribution is that a given neutron population or fission rate may be observed at different times, due to the stochasticity of the system. When the prescribed level is defined as the transition between the stochastic and deterministic regime, such as in this case with the threshold neutron population, there exists a distribution of conditions that may be present in the system at this transition. Therefore, there is a probability that a greater bed immersion fraction and total reactivity may be observed for a given neutron population and delayed neutron precursor population. The consequence of this from a nuclear criticality safety perspective is that the system will be at a higher reactivity before the neutron population and fission rate increase enough for negative reactivity feedbacks become dominant. Therefore, variations are predicted in the peak power observed during a postulated transient nuclear criticality accident. These differences may be quantified by performing a series of deterministic studies using initial conditions that are at the mean and extremes of the wait-time distribution.

The present model approximates the wait-time distribution as a Gamma distribution. This approximation is accurate when the system is highly multiplicative and stationary (Harris, 1964). Cooling et al. (2016) compared the neutron population PDFs generated using both the Gamma distribution method and the solution of the exact backward generating function equations. It was shown that in

certain cases, usually those where the neutron source strength is high and the reactivity ramp is low, the Gamma distribution method approximated the exact shape of the PDF well. However, in cases with a low neutron source strength and high ramp rate, deviations between the Gamma distribution method and the exact solution of the backwards generating function equations exist. The Gamma distribution is assumed to be a reasonable approximation of the true wait-time distribution and is therefore used in the proposed model. A comparison between the Gamma distribution method and the exact backwards generating function equations would require the solution of the backwards generating function equations which is much more complex than solving the forward stochastic balance equation and is out of the scope of the present study.

The wait-time distribution is obtained by first recognising that the Gamma distribution cumulative distribution function (CDF) may be given as the ratio of an incomplete to a complete gamma function at a prescribed threshold neutron population, N_{thresh}:

$$Q(N_{\text{thresh}}, t) = \frac{\gamma(\eta_{\text{N}}(t), \eta_{\text{N}}(t) N_{\text{thresh}} / \bar{N}(t))}{\Gamma(\eta_{\text{N}}(t))} \tag{6.32}$$

Numerical differentiation of the CDF then yields the following expression for the wait-time distribution:

$$P_{\text{wait}}(t) = \frac{dQ(N_{\text{thresh}}, t)}{dt} \tag{6.33}$$

The first moment (k = 1) of this distribution may be determined through numerical integration, yielding the mean. The k-th moment is given by:

$$\langle t^{\text{k}} \rangle = \int_0^\infty t^{\text{k}} P_{\text{wait}}(t) dt \tag{6.34}$$

The variance of the wait-time distribution, denoted $\sigma^2_{\text{std,t}}$, is determined using the first and second moment of the wait-time distribution:

$$\sigma^2_{\text{std,t}} = \langle t^2 \rangle - \langle t \rangle^2 \tag{6.35}$$

Initial conditions for the deterministic simulation are obtained at the mean and one standard deviation either side of the mean. Additional deterministic simulations are performed using initial conditions that are found when the threshold neutron population is reached at times corresponding to two standard deviations either side of the mean wait-time. The necessary initial conditions that must be found are the neutron population, delayed neutron precursor populations and the heights of the dry powder bed, wetted powder bed and pooled water. With the height of each region, the initial reactivity of the system may readily be determined using Equation (6.40).

6.4 Low Intrinsic Neutron Source Stochastic Neutron Kinetics Simulation Parameters

6.4.1 Neutron Kinetic Parameters

In this chapter, the consequence of stochastic effects due to a low intrinsic neutron source on the peak power of a wetting-induced transient nuclear criticality excursion in a 95-wt% enriched UO_2 powder bed is examined. To establish whether the HEU powder bed is in the stochastic regime, an evaluation of the Hansen et al. (1959) criterion is required. For this, the prompt neutron lifetime must be determined. Since the effective multiplication factor and neutron mean generation time are expected to vary as a function of the bed immersion fraction (f_{imm}), the prompt neutron lifetime, calculated using Equation (6.36), may also vary as a function of the bed immersion fraction. To understand this dependency on the bed immersion fraction, MCNP simulations were performed to establish the effective multiplication factor and kinetic parameters for the three-region problem described in the previous chapters of this thesis but for a UO_2 powder system of varying enrichment, undergoing wetting. MCNP simulation results for the prompt neutron mean generation time, Λ, is shown in Figure 6.8 as a function of enrichment and powder bed immersion fraction.

$$\tau(f_{\text{imm}}) = \Lambda(f_{\text{imm}})k_{\text{eff}}(f_{\text{imm}}) \tag{6.36}$$

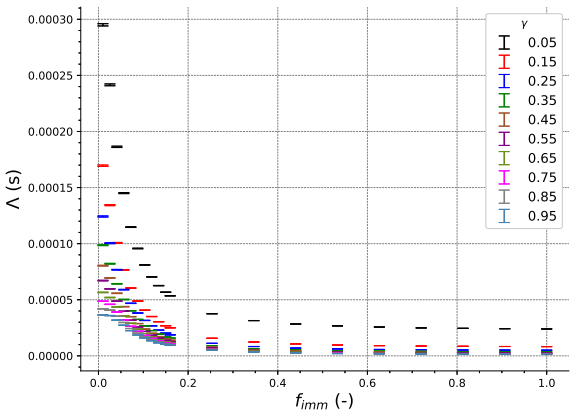

Figure 6.8: Mean prompt neutron generation time of UO_2 powder as a function of enrichment and bed immersion fraction.

The associated effective multiplication factor (k_{eff}) is shown in Figure 6.9b. The results of these simulations indicate that the effective multiplication factor is greater as the enrichment increases. This may be attributed to the increased probability of thermal fission that arises as the ratio of ^{235}U increases in the nuclear fuel powder. The associated low neutron source criterion specified by Hansen et al. (1959) has been calculated and is shown in Figure 6.9a, indicating that the low neutron source condition becomes more satisfied as the UO_2 powder bed approaches criticality. Near criticality, $S_n\tau < 0.1$ for cases where $\gamma > 0.25$. This suggests that wetting induced transient nuclear criticality excursions may initially behave stochastically at enrichments at or above this level. For the remainder

of this study, the case where $\gamma = 0.95$ is chosen as the level of enrichment.

To solve the forward stochastic balance equation, outlined in Section 6.3.1, the precursor group decay constants (λ_i), the effective fraction of neutrons from delayed neutron precursor groups (β_i) and the first and second neutron multiplicities ($\chi_{1,2}$) are required. All of these neutron kinetic parameters, apart from the multiplicity, have been established from the previously mentioned MCNP simulations. The neutron kinetic data is shown in Figure 6.10. No discernable pattern to the variable, β_i, is apparent as a function of the bed immersion fraction, therefore constant average values for this parameter are prescribed. The same approach is taken for the delayed neutron precursor decay constants, λ_i. However, large variations in the mean generation time, Λ, shown in Figure 6.8, occur at low bed immersion fractions, before reaching a more constant value. To model this, a polynomial representation of the generation time as a function of the bed immersion fraction is presumed. The following expression may be used to determine the mean generation time of neutrons for the UO_2 powder bed with $\gamma = 0.95$, when the bed immersion fraction, f_{imm}, lies between MCNP data points:

$$\Lambda(f_{\text{imm}}) = \sum_{i=0}^{6} C_i f_{\text{imm}}(t) \tag{6.37}$$

where the correlation coefficients are listed in Table 6.2.

Table 6.2: Mean neutron generation time correlation coefficients.

i	C_i
0	0.00004624
1	−0.00040536
2	0.00145324
3	−0.00245737
4	0.00189002
5	−0.00044202
6	−0.00008353

Other neutron kinetic data is summarised in Table 6.3.

Table 6.3: Delayed neutron precursor group data.

Group, i	β_i ($\times 10^{-5}$)	λ_i (s^{-1})
1	24.7895 ± 2.15789	0.01249 ± 0.00000
2	127.632 ± 4.78947	0.0318184 ± 0.00000
3	125.105 ± 4.73684	0.109402 ± 0.00000
4	349.947 ± 8.05263	0.317108 ± 0.00000
5	103.421 ± 4.31579	1.35369 ± 0.0000105263
6	36.2632 ± 2.57895	8.64506 ± 0.000523158
Total	767.158 ± 26.6316	-

The neutron multiplicities of prompt neutrons may be determined using the following relation as noted in (Cooling et al., 2018):

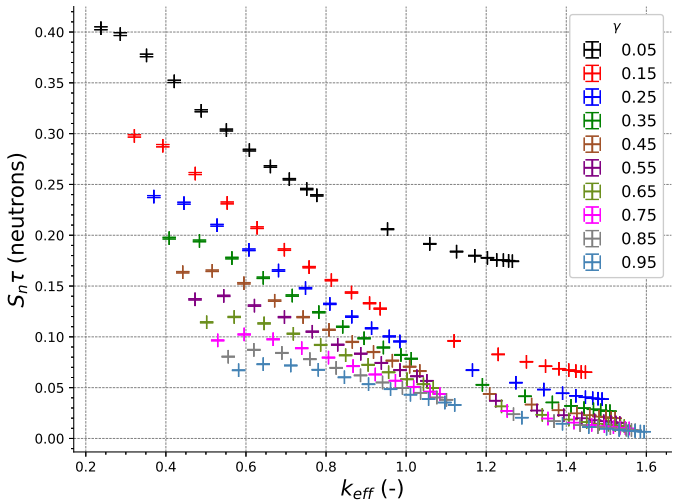

(a)

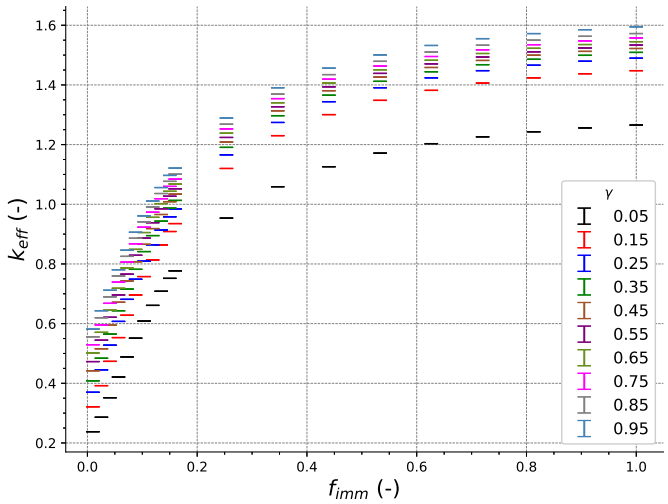

(b)

Figure 6.9: Low neutron source criterion evaluation and effective multiplication factor of a UO_2 powder bed at various enrichment levels and bed immersion fractions, determined using MCNP.

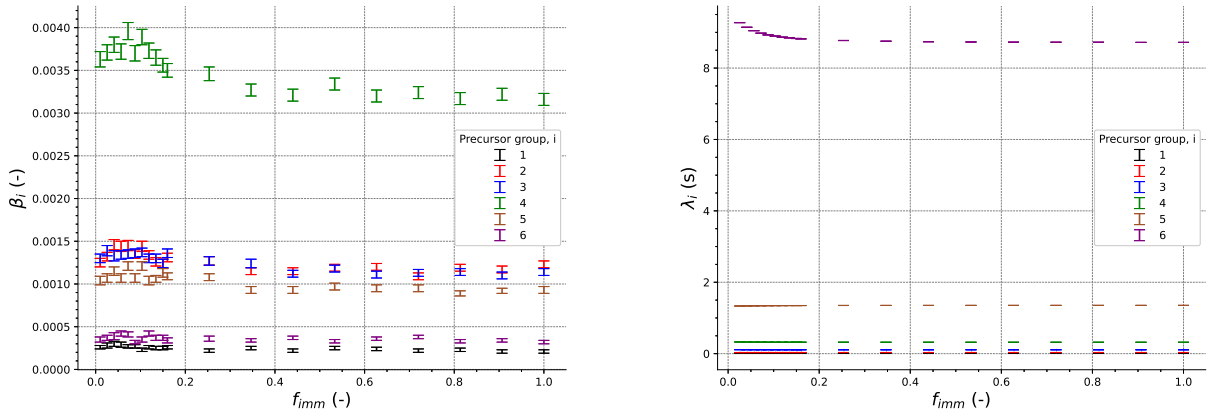

(a) (b)

Figure 6.10: Delayed neutron precursor group neutron kinetic data and the delayed neutron precursor decay constants, determined using MCNP.

$$\chi_{\mathrm{i}} = \sum_{\nu=i}^{\nu_{\max}} \frac{\nu!}{(\nu-i)!} P_{\mathrm{f}}(\nu) \tag{6.38}$$

where ν is the number of neutrons born through a fission, $\nu_{\max}$ is the maximum number of neutrons born through a fission and $P_{\mathrm{f}}(\nu)$ is the neutron emission probability distribution corresponding to the probability that ν neutrons are produced through fission.

It may be deduced from Equation (6.38) that for the case where i = 1, the first multiplicity is given by:

$$\chi_1 = \sum_{\nu=1}^{\nu_{\max}} \nu P_{\mathrm{f}}(\nu) = \bar{\nu} \tag{6.39}$$

Hansen et al. (1959) notes that the probability distribution, $P_{\mathrm{f}}(\nu)$ is known for some common fissionable materials. Terrell (1957) has been able to fit a Gaussian distribution with $(\nu - \bar{\nu}) = 0$ and standard deviation, $\sigma_{\mathrm{std}} = 0.108$, to experimental data corresponding to the neutron emission probability. Figure 6.11 shows the neutron emission probability distribution for ^{235}U, as a continuous Gaussian. Experimental discrete neutron emission data found by Diven et al. (1956) for ^{235}U is given in Table 6.4 and also shown in Figure 6.11 for $\nu_{\max} = 8$. The negative probability shown in Table 6.4 exists due to two corrections applied to the experimental data. The first accounted for neutron capture coincidence by altering the fission data, the second was an adjustment due to the presence of background neutron radiation. These corrections are described in greater detail within Diven et al. (1956).

The mean number of neutrons produced through fission is given in Diven et al. (1956) as $\bar{\nu} = 2.47 \pm 0.003$. This data may now be used in Equation (6.38) to determine the first and second neutron multiplicities, which are $\chi_1 = 2.47$ and $\chi_2 = 4.88$. Alternative neutron emission probability

information may be found in Boldeman and Hines (1985); Santi and Miller (2008).

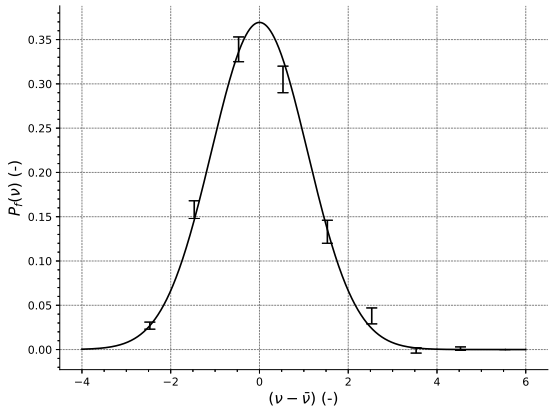

Figure 6.11: Continuous (Gaussian) representation of the neutron emission probability, produced using data from Terrell (1957). The error-bars represent the experimental neutron emission probabilities for ^{235}U, stated in Diven et al. (1956).

Table 6.4: Experimental neutron emission probability data from Diven et al. (1956) for ^{235}U.

ν	0	1	2	3	4	5	6	7	8
$P_{\mathrm{f},\nu}$	0.027	0.158	0.339	0.305	0.133	0.038	-0.001	0.001	0.000

The driving reactivity component that brings the wetted, highly enriched UO_2 powder bed to criticality is the infiltration of water, that permeates the pores of the powder bed. A polynomial line of best-fit has been prescribed that fits to the MCNP derived reactivity data shown in Figure 6.12, with good agreement shown through an R-squared value of $R^2 = 0.9999$. The polynomial line of best-fit is given by the following:

$$R_{\mathrm{imm}}(f_{\mathrm{imm}}) = \sum_{\mathrm{i}=0}^{X} C_{\mathrm{i}} f_{\mathrm{imm}}(t) \tag{6.40}$$

where the coefficients of the polynomial are stated in Table 6.5.

Table 6.5: Wetting-induced reactivity component correlation coefficients.

i	C_{i}
0	-1.11882118×10^2
1	1.85531717×10^3
2	-1.15353680×10^4
3	4.33889356×10^4
4	-1.01608118×10^5
5	1.48520288×10^5
6	-1.31492585×10^5
7	6.44273945×10^4
8	-1.33953689×10^4

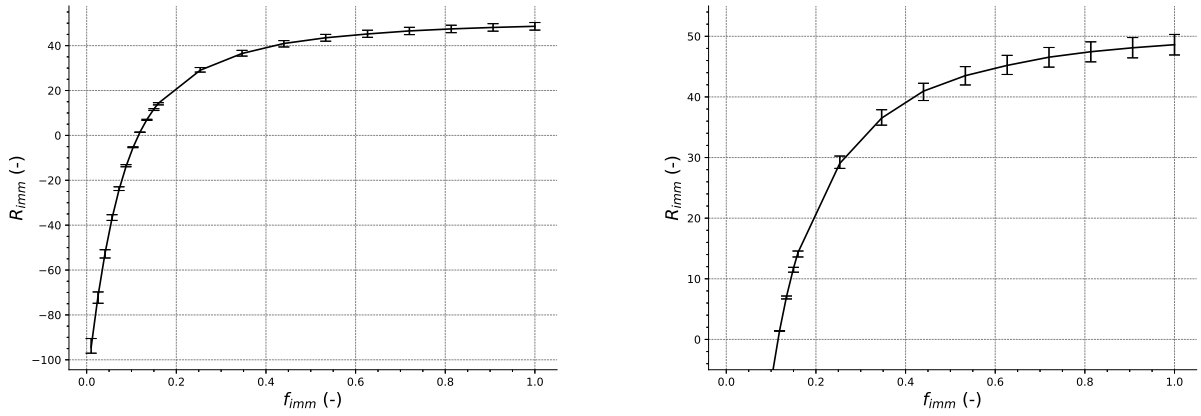

(a) (b)

Figure 6.12: Wetting-induced reactivity profile, showing the change in reactivity as the wetting front permeates the highly enriched UO_2 powder bed. Error-bars correspond to MCNP simulation data.

6.4.2 Stochastic Simulation Initial Conditions and Wetting Parameters

The initial UO_2 powder bed and water region heights are outlined in Table 6.6. A fully unsaturated case is not prescribed due to the limitations previously described regarding the solution of the Green-Ampt infiltration equation. Initial conditions for the mean neutron population, mean delayed neutron precursor population and corresponding second derivatives of the forward stochastic balance equation may be determined for the unsaturated UO_2 powder bed. However, the region height data in Table 6.6 corresponds to an initial bed immersion fraction, $f_{\text{imm}}(0) = 1.61 \times 10^{-4}$, which when substituted into Equation (6.40), suggests that the UO_2 powder bed is deeply sub-critical. Williams (2016) notes, for a deeply sub-critical system, it makes little difference if the initial conditions for the stochastic variables are prescribed zero. Therefore, the present study assumes that the initial conditions for the dependent stochastic variables are zero.

Table 6.6: Initial condition for the height of each of the three regions of the UO_2 powder bed domain.

Region	Value
H_{dp}	0.6216 m
H_{sus}	0.3873 m
H_{wp}	0.0001 m

The associated parameters that govern the rate of wetting through the highly enriched UO_2 powder bed are similar to those prescribed in Table 5.6 and are summarised in Table 6.7.

6.5 Wait-Time Distribution for $\gamma = 0.95$

A Python-based BDF ODE solver has been used to solve the forward stochastic balance equation. The neutron population and corresponding relative standard deviation is shown as a function of time in Figure 6.13a. The corresponding mean delayed neutron precursor population and the associated standard deviation is given in Figure 6.13b. The system reactivity as a function of time, shown in Figure 6.14, indicates that shortly after $t = 235.0$ s the system reaches a prompt super-critical

Table 6.7: Initial condition for the height of each of the three regions of the UO_2 powder bed domain.

Property	Symbol	Value
Mean powder particle diameter	d_p	10 μm
Container height	H_{cyl}	1.0 m
Container radius	R_{cyl}	0.4 m
Water incursion rate onto powder bed	$U_{w,in}$	9.947×10^{-4} m s^{-1} (0.5 L s^{-1})
Dry UO_2 powder bed packing fraction	$v_{f,p,dp}$	0.1461
Settled wet UO_2 powder bed packing fraction	$v_{f,p,wp}$	0.1461
Dynamic viscosity of water	μ_w	0.001 Pa s
Density of UO_2	$\rho_{p,th}$	10950 kg m^{-3}
Density of water	$\rho_{w,th}$	998.1 kg m^{-3}

state. This causes the mean neutron population and delayed neutron precursor population to increase exponentially. The reactivity is calculated by also solving for the propagation of the wetting front through the UO_2 powder bed and the rate of pooling. The height of each region as a function of time is shown in Figure 6.15.

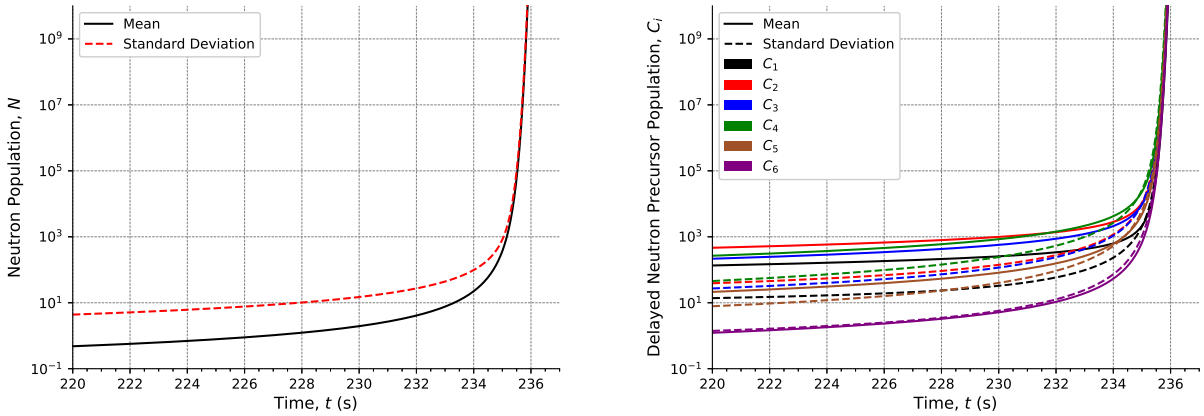

(a) (b)

Figure 6.13: Mean neutron population, mean delayed neutron precursor populations and associated standard deviations for both variables.

The relative standard deviation for the neutron population and delayed neutron precursor populations are shown in Figure 6.16. As the wetted UO_2 powder bed becomes delayed super-critical, the relative standard deviation of the neutron population begins to sharply decrease. Self-similarity between the relative standard deviation of the neutron population and delayed neutron precursor populations is then predicted very close to the time at which the system becomes prompt super-critical. This self-similarity has been noted by Cooling et al. (2018) to correspond to the maturity time, which may be defined as the time at which the relative standard deviation in the neutron population and delayed neutron precursor population reach an asymptotic value.

The wait-time probability distributions have been approximated as a Gamma distribution for a range of different threshold neutron populations. The resulting PDFs are shown in Figure 6.17, with associated CDFs shown in Figure 6.18. The results indicate that as the threshold neutron population increases, the peak of the probability distribution function becomes centred closer to the mean. At low

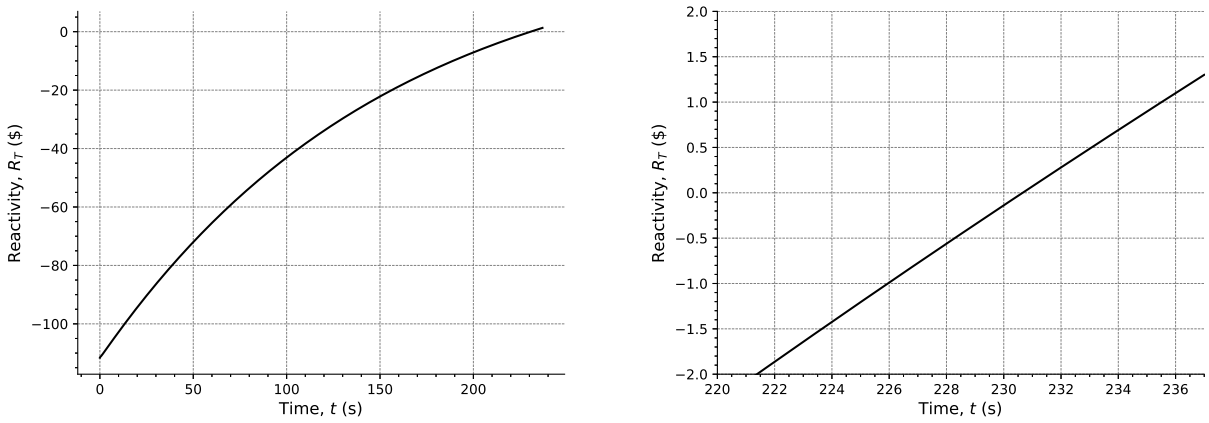

(a) (b)

Figure 6.14: Reactivity of UO_2 powder bed due to wetting from the start of the transient and close to criticality.

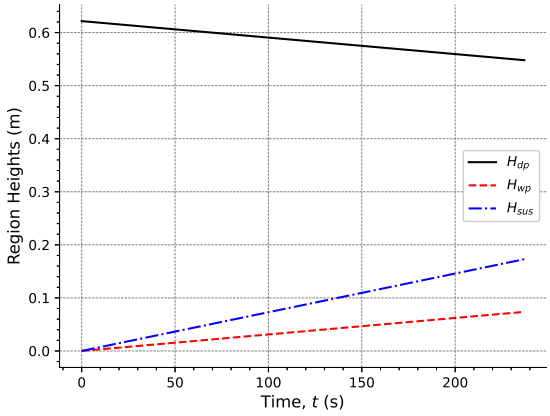

Figure 6.15: Height of dry UO_2 powder, wet UO_2 powder and pooled water regions as a function of time.

threshold neutron populations, the probability distribution is more spread, corresponding to a greater variance in the time taken to reach the prescribed threshold neutron population. The mean wait-time as a function of the threshold neutron population is shown in Figure 6.19. This indicates that as the threshold neutron population exponentially increases, the mean wait-time increases non-linearly. This may be attributed to the fact that a prompt super-critical state is reached, which exponentially increases the power linearly in time, meaning that the variance in the mean wait-time as a function of the threshold neutron population is small.

The CDFs shown in Figure 6.18 are sampled in quarterly increments to obtain the time and system geometry at which the deterministic simulation will begin, for a prescribed threshold neutron population. The deterministic simulation has been chosen to end once the boiling point of the water held interstitially between UO_2 powder particles is reached. Since a particular amount of fission energy must be deposited into the system for boiling to occur, this simulation stopping criterion is similar to stopping the simulation once a prescribed fission energy deposition level has been reached. The

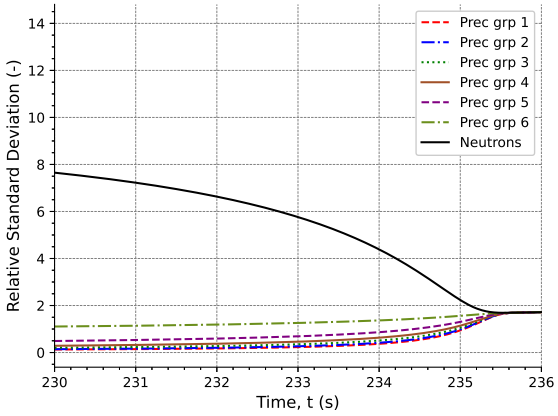

Figure 6.16: Relative standard deviation for the neutron population and delayed neutron precursor populations.

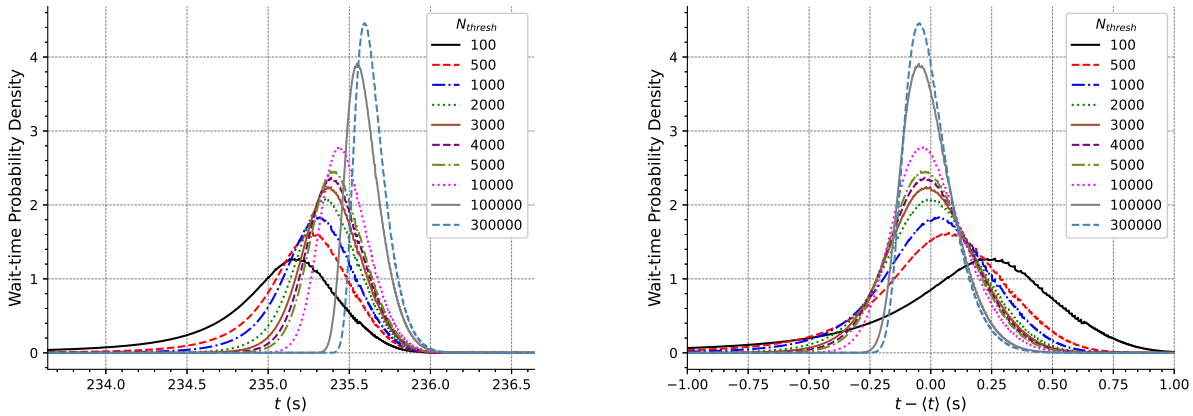

(a) (b)

Figure 6.17: Wait time probability distributions, modelled using the Gamma distribution.

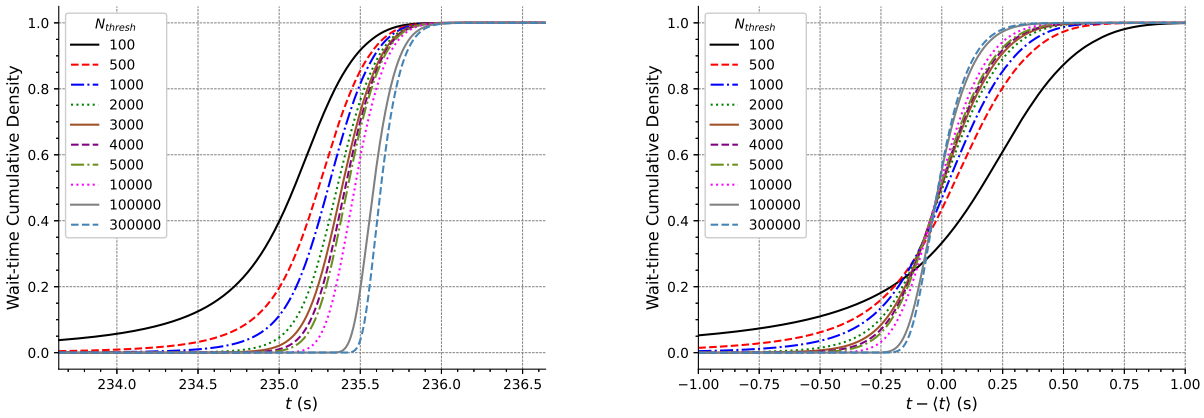

(a) (b)

Figure 6.18: Wait time cumulative distributions, modelled using the Gamma distribution.

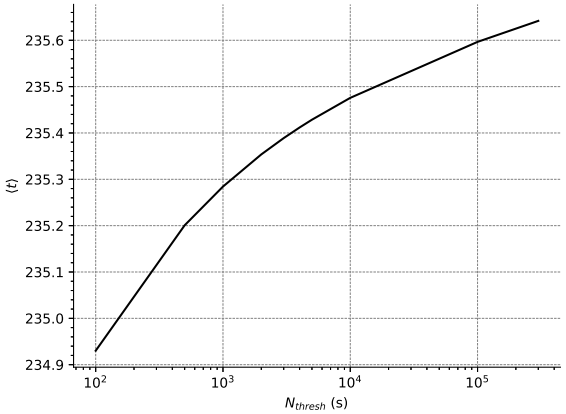

Figure 6.19: Mean wait-time calculated using the Gamma distribution method as a function of the prescribed threhold neutron population.

effect that the low neutron source stochasticity has on the first peak power and time to boiling may be examined. A distribution of the peak power and time to boiling may be obtained by running the deterministic simulations from the sampled initial conditions along the CDFs shown in Figure 6.18. The variation of the peak power and time to boiling as a function of the threshold neutron population is also examined. The group-wise delayed neutron precursor populations at the threshold neutron population are calculated by examining what the mean delayed neutron precursor populations are that produce the prescribed threshold neutron population. Table 6.8 shows how the mean delayed neutron precursor populations vary as a function of the threshold neutron population.

Table 6.8: Mean delayed neutron precursor population for prescribed threshold neutron population.

Group, i		1	2	3	4	5	6
N_{thresh}	100	1156.418	5484.461	4579.819	10337.386	1861.015	209.205
	499	2537.970	12542.350	11307.211	27994.241	5999.094	868.145
	999	3747.326	18739.064	17272.991	43975.146	9978.809	1589.952
	2000	5710.767	28811.203	27008.941	70287.358	16726.030	2907.485
	2999	7412.326	37545.506	35471.194	93277.156	22729.357	4139.107
	4000	8974.065	45564.701	43249.899	114468.567	28318.606	5319.298
	4999	10444.469	53116.475	50580.837	134476.235	33630.862	6463.548
	9999	17035.442	86977.850	83492.543	224563.789	57817.962	11859.062
	99999	101836.503	522972.913	508477.844	1396105.514	381407.278	91599.689
	300000	255484.068	1313200.422	1279764.463	3529388.828	979051.953	247291.802

The corresponding height of the dry powder, wet powder and pooled water regions are specified in Tables 6.9 to 6.11 at different points along the CDF as a function of the threshold neutron population. The associated reactivity at the start of the deterministic simulations are presented in Figure 6.20. The wetting-induced reactivity at the start of the deterministic simulation depends strongly on the sampled time on the wait-time CDF. Larger variations in reactivity are predicted for lower threshold neutron populations due to the larger variance in the wait-time PDF at lower threshold neutron populations. As the threhold neutron population increases, the reactivities calculated at various points along the wait-time CDF begin to converge.

Table 6.9: Dry powder UO_2 bed heights (H_{dp}) for varying threshold neutron population and position along wait-time distribution CDF.

N_{thresh}	0.01	0.25	0.5	0.75	1.0
100	0.54964	0.54868	0.54859	0.54853	0.54839
500	0.54892	0.54860	0.54855	0.54849	0.54838
1000	0.54878	0.54857	0.54853	0.54848	0.54837
2000	0.54868	0.54855	0.54851	0.54847	0.54837
3000	0.54864	0.54854	0.54850	0.54846	0.54836
4000	0.54862	0.54853	0.54849	0.54846	0.54836
5000	0.54861	0.54852	0.54849	0.54845	0.54836
10000	0.54857	0.54850	0.54848	0.54844	0.54835
100000	0.54850	0.54846	0.54844	0.54841	0.54834
300000	0.54847	0.54844	0.54843	0.54840	0.54833

Table 6.10: Static wet UO_2 powder bed heights (H_{wp}) for varying threshold neutron population and position along wait-time distribution CDF.

N_{thresh}	0.01	0.25	0.5	0.75	1.0
100	0.07206	0.07302	0.07311	0.07317	0.07331
500	0.07278	0.07310	0.07315	0.07321	0.07332
1000	0.07292	0.07313	0.07317	0.07322	0.07333
2000	0.07302	0.07315	0.07319	0.07323	0.07333
3000	0.07306	0.07316	0.07320	0.07324	0.07334
4000	0.07308	0.07317	0.07321	0.07324	0.07334
5000	0.07309	0.07318	0.07321	0.07325	0.07334
10000	0.07313	0.07320	0.07322	0.07326	0.07335
100000	0.07320	0.07324	0.07326	0.07329	0.07336
300000	0.07323	0.07326	0.07327	0.07330	0.07337

Table 6.11: Pooled water region heights (H_{sus}) for varying threshold neutron population and position along wait-time distribution CDF.

N_{thresh}	0.01	0.25	0.5	0.75	1.0
100	0.16906	0.17130	0.17150	0.17165	0.17198
500	0.17073	0.17148	0.17161	0.17173	0.17201
1000	0.17107	0.17154	0.17166	0.17177	0.17202
2000	0.17129	0.17160	0.17170	0.17179	0.17204
3000	0.17138	0.17163	0.17172	0.17181	0.17204
4000	0.17143	0.17165	0.17173	0.17182	0.17205
5000	0.17147	0.17167	0.17174	0.17183	0.17205
10000	0.17156	0.17171	0.17178	0.17185	0.17206
100000	0.17173	0.17181	0.17186	0.17192	0.17210
300000	0.17178	0.17185	0.17189	0.17195	0.17212

6.6 Wait-Time Distribution Sensitivity to Enrichment

Figure 6.9b indicates that the effective multiplication factor, k_{eff}, and therefore the reactivity, varies significantly as a function of the enrichment of the UO_2 powder. The intrinsic distributed neutron source strength and neutron kinetic parameters also depend strongly on the level of enrichment

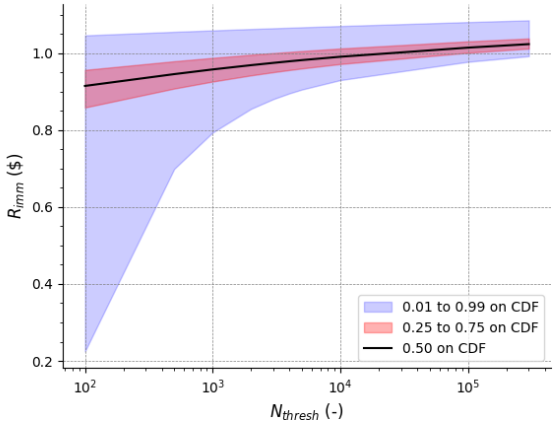

Figure 6.20: Reactivity at the start of the deterministic simulation due to the location of the wetting front in the UO_2 powder bed.

of the fissile system. As a consequence, the stochastic properties of the system at different prescribed threshold neutron populations may be affected by the enrichment level. The forward stochastic balance equation and Gamma distribution method has been used to examine the dependency of the wait-time PDF on the enrichment of the UO_2 powder bed.

Figure 6.21 shows how the wait-time PDFs, calculated using the Gamma distribution method at various prescribed threshold neutron populations, vary as a function of the enrichment of the powder bed. The location of the peak wait-time and it's distribution depends strongly on the enrichment of the UO_2 powder bed. This is a result of the greater rate of reactivity addition due to the wetting of UO_2 powder beds with higher fractions of ^{235}U. The effect is quite considerable, with Figure 6.21 indicating that the mean wait-time may vary by over 100 seconds for a HEU system at either end of the enrichment spectrum.

A better representation of the wait-time PDF around the mean wait-time is given in Figure 6.22. For all enrichment levels represented, the distribution around the mean wait-time becomes less dispersed as the threshold neutron population increases. This corresponds to a decreased distribution of times at which a prescribed threshold population is predicted to be observed. Generally, similar distributions are predicted as a function of the level of UO_2 powder bed enrichment, however, the skewness and flatness of the distribution does depend slightly on the level of enrichment. The distribution around the mean wait-time is represented in Figure 6.23 through the relative standard deviation of the wait-time. Data presented in Figure 6.23 suggests that typically, as the enrichment increases, the standard deviation of the wait-time relative to the mean increases. This means that there is a greater distribution of times at which that threshold neutron population would be observed in the stochastic system. This may be attributable to increased stochasticity of the fissile system as the level of enrichment increases. However, the opposite is predicted for the case where $N_{\text{thresh}} = 500$ neutrons, where the time taken to reach this neutron population becomes less distributed around the mean as the intrinsic neutron source strength enters deeper into the stochastic regime.

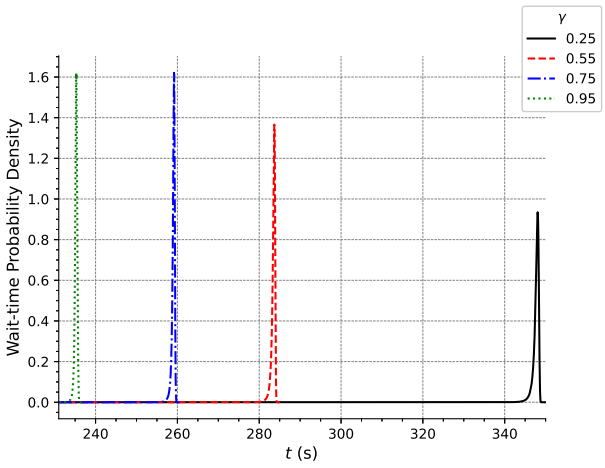

(a) $N_{\text{thresh}} = 500$ neutrons

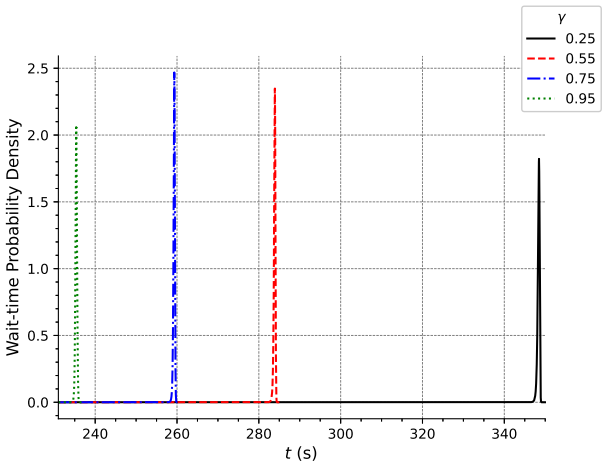

(b) $N_{\text{thresh}} = 2000$ neutrons

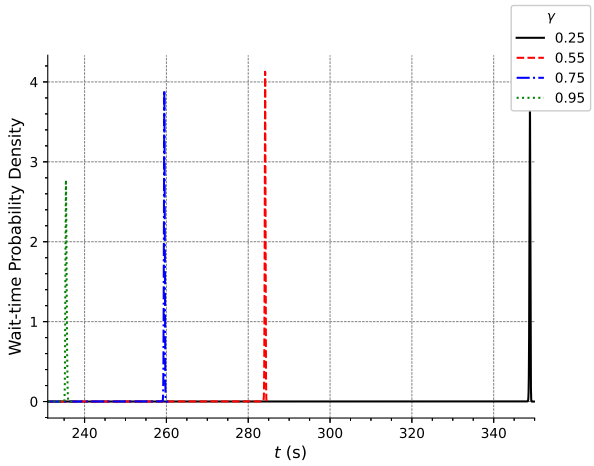

(c) $N_{\text{thresh}} = 10000$ neutrons

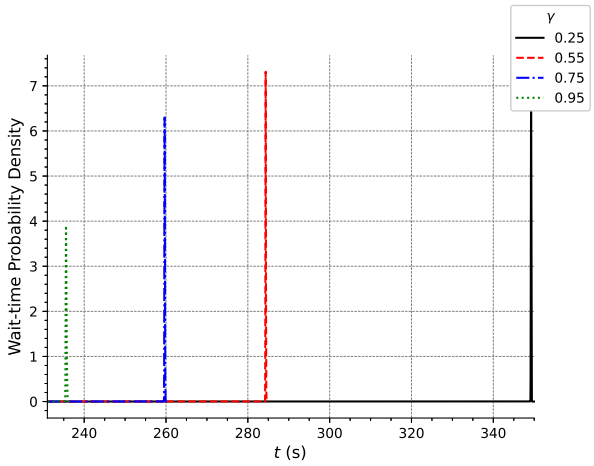

(d) $N_{\text{thresh}} = 100000$ neutrons

Figure 6.21: Wait-time PDFs as a function of the UO_2 powder bed enrichment level, at varying threshold neutron populations.

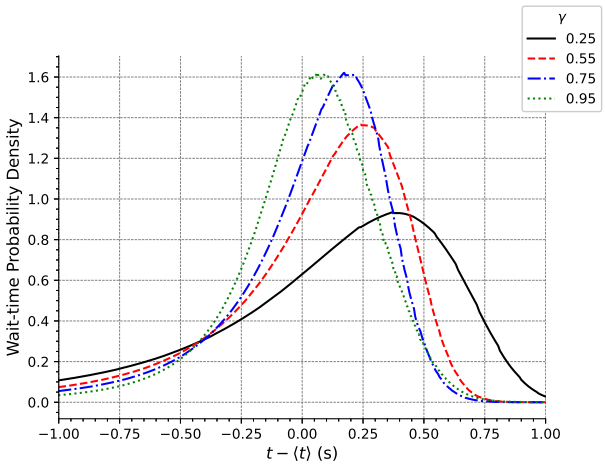

(a) $N_{\text{thresh}} = 500$ neutrons

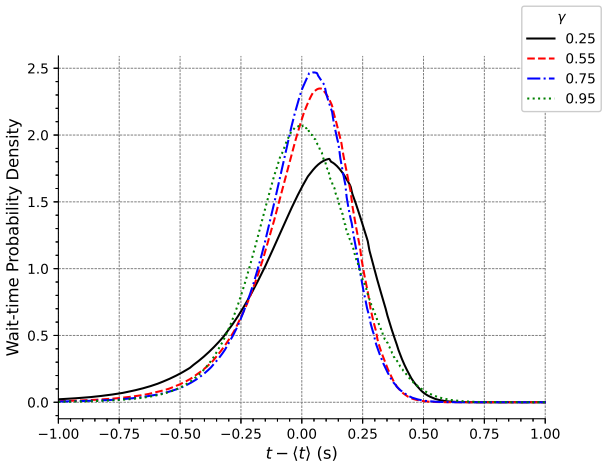

(b) $N_{\text{thresh}} = 2000$ neutrons

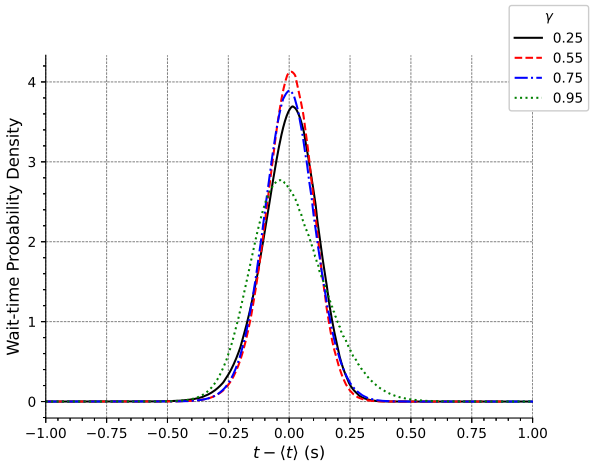

(c) $N_{\text{thresh}} = 10000$ neutrons

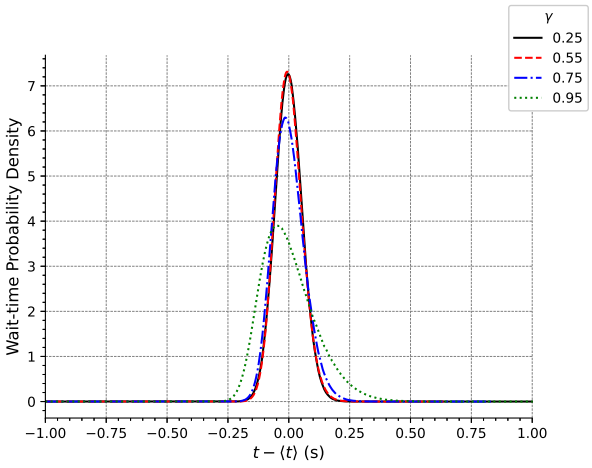

(d) $N_{\text{thresh}} = 100000$ neutrons

Figure 6.22: Wait-time PDFs, shown as $t - \langle t \rangle$, as a function of the UO_2 powder bed enrichment level, at varying threshold neutron populations.

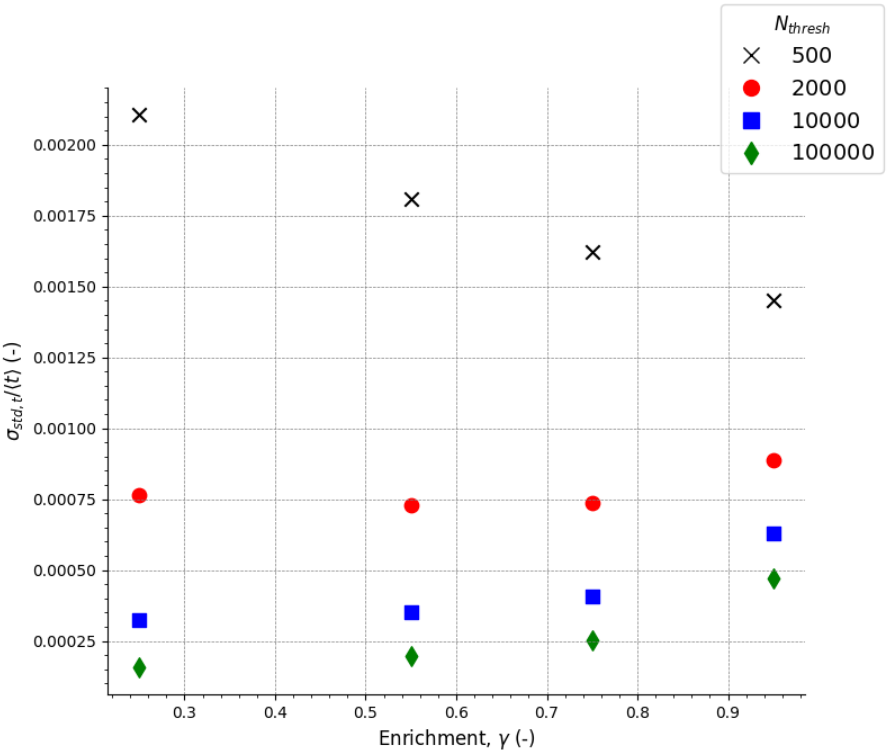

Figure 6.23: The variation in the relative standard deviation of the wait-time PDF as a function of enrichment and threshold neutron population.

6.7 Deterministic Simulations of Transient Nuclear Criticality Excursions

6.7.1 HEU Reactivity Components

Since the simulations stop once boiling is reached, the only reactivity feedbacks that are included are those that relate to thermal expansion, Doppler broadening and radiolytic gas-induced void creation. Reactivity contributions due to the re-distribution of UO_2 powder as a result of fluidisation are neglected since this effect has previously been modelled to occur at the onset of boiling, which is not simulated here. Consequently, the reactivity component associated with the loss of UO_2 powder from the system is also neglected. The total reactivity may then be expressed as:

$$R_{\mathrm{T}} = R_{\mathrm{imm}}(f_{\mathrm{imm},0}) + \Delta R_{\mathrm{th,p,dry}}(\bar{T}_{\mathrm{p,dp}}, f_{\mathrm{imm},0}) + \Delta R_{\mathrm{th,p,wp}}(\bar{T}_{\mathrm{p,wp}}, f_{\mathrm{imm},0}) + \Delta R_{\mathrm{th,w}}(\bar{T}_{\mathrm{w}}, f_{\mathrm{imm},0}) + \Delta R_{\mathrm{void,wp}}(v_{\mathrm{f,g,wp}}, f_{\mathrm{imm},0}) + \Delta R_{\mathrm{void,sus}}(v_{\mathrm{f,g,sus}}, f_{\mathrm{imm},0}) \quad (6.41)$$

The water infiltration-based reactivity feedback component has already been outlined in Section 6.4.1. The void reactivity components in the settled wet powder region and pooled water / suspension region have been determined by performing a series of MCNP simulations. The results of these simulations are shown in Figure 6.24. Good agreement is predicted ($R^2 = 0.9978$) for the settled wet powder void reactivity feedback component when the B-spline is of orders 3 and 2 in the void fraction and bed immersion dimensions, respectively. Good agreement is also predicted ($R^2 = 0.9990$) for the suspension/pooled water void reactivity feedback component when the B-spline is of orders 3 and 5 in the void fraction and bed immersion dimensions, respectively.

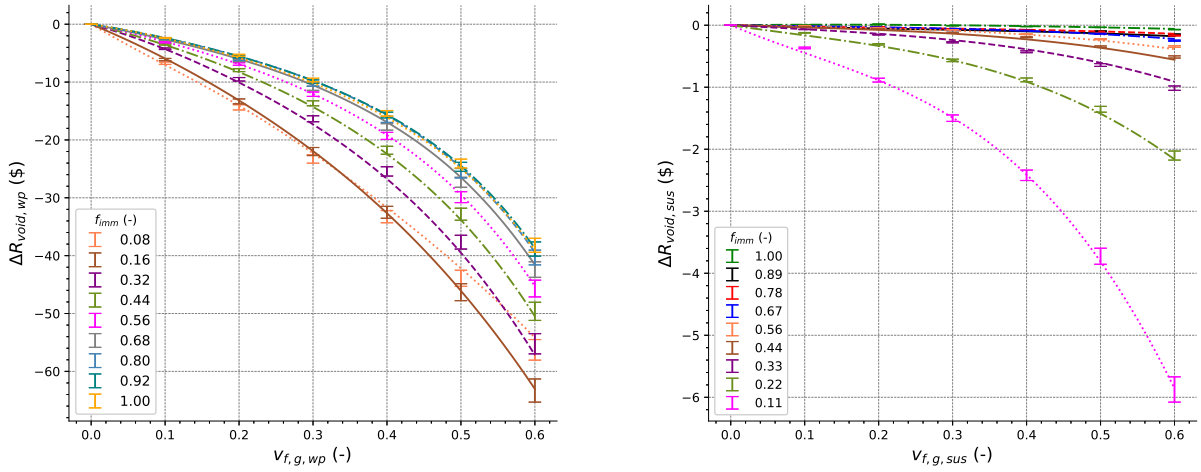

(a) (b)

Figure 6.24: Settled wet powder and pooled water/suspension region void reactivity feedback profiles. Error-bars correspond to MCNP simulation data, lines correspond to the bi-variate B-spline.

Table 6.12: Thermal reactivity feedback component B-spline polynomial orders and associated R^2 between B-splines and MCNP data.

Component, i	Region, j	f_{imm} poly order	$T_{\text{i,j}}$ poly order	R^2
Pore water	Wet powder region	2	3	0.9997
UO_2 powder	Dry powder region	2	4	0.9994
UO_2 powder	Wet powder region	2	4	0.9935

Thermal reactivity feedback components that account for the effect of thermal expansion and Doppler broadening on system reactivity are shown in Figure 6.25 for the dry UO_2 powder, wet UO_2 powder and pore water. The methodology used to evaluate the thermal reactivity feedback components is identical to the method proposed in Section 3.4.9. Good agreement is predicted between the MCNP derived thermal reactivity feedback data and the bi-variate B-spline that has been fitted to each of the thermal reactivity components. The orders of the B-splines in each dimension and the associated R-squared data for the thermal reactivity feedback components are shown in Table 6.12.

Previously stated reactivity feedback correlations are not applicable to highly enriched UO_2 powder systems involving 5-wt% enriched UO_2 powder. Therefore, New reactivity feedback components are required for the highly enriched UO_2 powder bed. Thermal reactivity feedbacks, void reactivity feedbacks. We only consider to point up to boiling and therefore do not consider resuspension, pickup etc.

6.7.2 Nuclear Cross-Sections for Neutron Diffusion Equation

An estimate for the axial distribution of fissions in the system is required to calculate the linear power density which contributes to thermal energy deposition in the UO_2 powder and water, as well as radiolysis. For this, a series of Serpent Monte Carlo simulations were performed using a similar methodology to the one used in Section 3.4.11, but for a UO_2 powder bed with enrichment, $\gamma = 0.95$ wt-%. Correlation coefficients for the nuclear cross-sections used to evaluate the scalar neutron flux distribution shape function as a function of the region of interest are shown in Tables 6.13 to 6.15. The macroscopic nuclear cross-section data and the associated correlations are shown in Figures 6.26 and 6.27, indicating that a good-fit is found when using these correlations.

Table 6.13: Macroscopic neutron cross-section correlation coefficients for the dry UO_2 powder bed.

Cross-section (cm^{-1})	C_0	C_1	C_2	C_3
$\bar{\nu}\Sigma_{\text{f,1}}$	0.01301	0.01726	−0.03691	0.03266
$\bar{\nu}\Sigma_{\text{f,2}}$	1.18684	−0.11186	0.25391	−0.16356
$\Sigma_{\text{a,1}}$	0.00604	0.01072	−0.02279	0.02007
$\Sigma_{\text{a,2}}$	0.57120	−0.05158	0.11694	−0.07489
$\Sigma_{\text{f,1}}$	0.00507	0.00712	−0.01522	0.01343
$\Sigma_{\text{f,2}}$	0.48707	−0.04589	0.10414	−0.06708
$\Sigma_{\text{tr,1}}$	0.03726	0.00519	−0.00870	0.00559
$\Sigma_{\text{tr,2}}$	0.51142	0.10715	−0.29614	0.26255
$\Sigma_{\text{s,1}\to\text{1}}$	0.04858	0.00150	0.00000	0.00000
$\Sigma_{\text{s,1}\to\text{2}}$	−0.00000	0.00001	0.00000	0.00000
$\Sigma_{\text{s,2}\to\text{1}}$	0.00071	0.00016	0.00000	0.00000
$\Sigma_{\text{s,2}\to\text{2}}$	0.07836	−0.00376	0.00000	0.00000

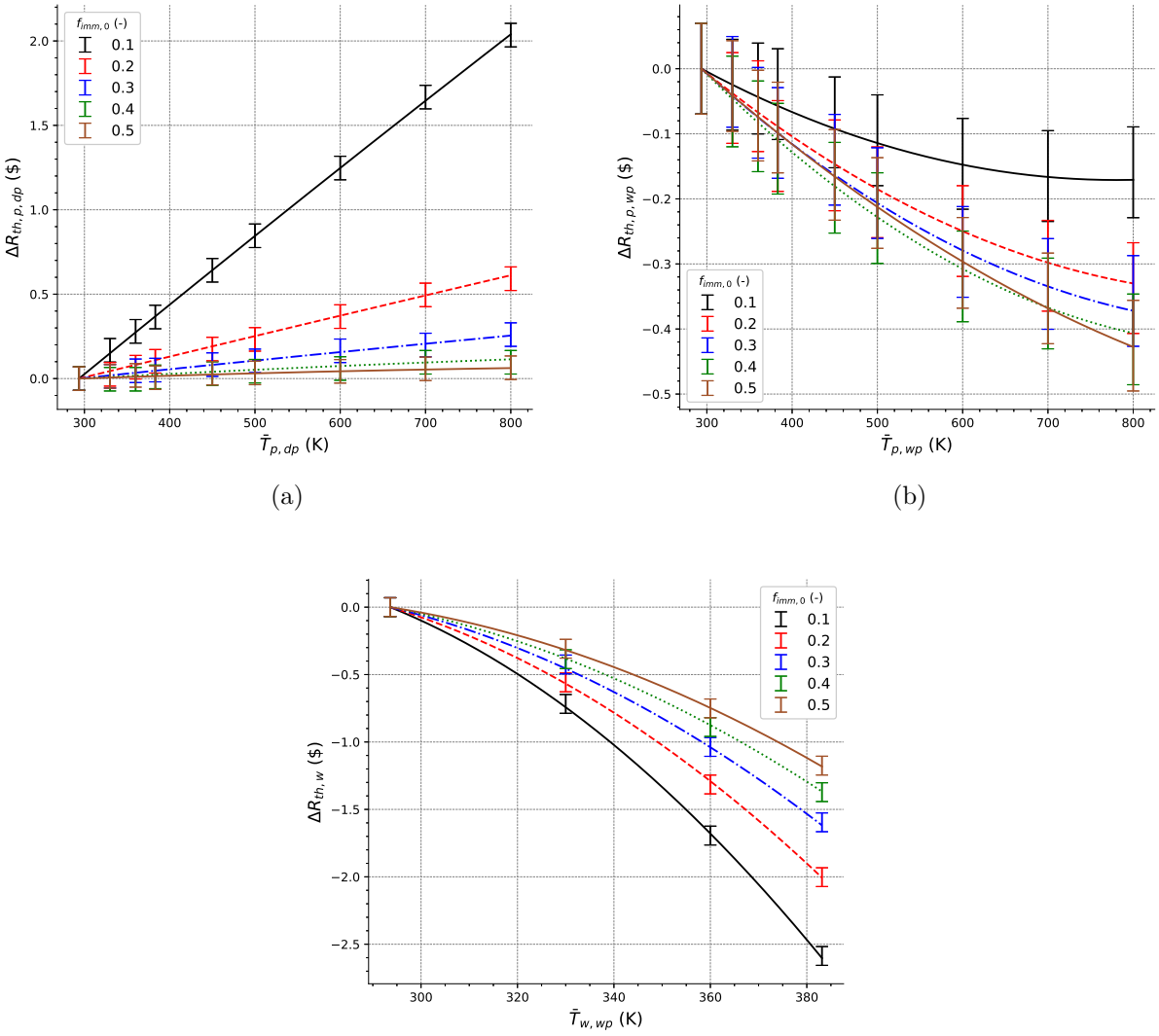

Figure 6.25: Settled wet powder and pooled water/suspension region void reactivity feedback profiles. Error-bars correspond to MCNP simulation data, lines correspond to the bi-variate B-spline.

The appropriateness of the proposed macroscopic nuclear cross-section correlations was examined by comparing normalised scalar neutron flux distributions calculated using both Serpent and a deterministic steady-state, two-energy group, spatially-dependent, neutron diffusion code, for a range of UO_2 powder bed immersion fractions. The resulting axially normalised neutron flux shapes are shown in Figure 6.28. Good agreement between the two methods are predicted when the bed immersion fraction is high. At lower bed immersion fractions, some considerable differences are predicted between the normalised neutron flux shape calculated using the neutron diffusion approach, and the flux shape evaluated using the Monte Carlo code, Serpent. This could be attributed to the two energy group approximation for the macroscopic nuclear cross-sections used in the neutron diffusion code. A better agreement may be obtained using a more refined energy group structure, however, for the purpose of this study, the axial flux distribution is deemed appropriate. The steady-state, spatially dependent, multi-group neutron diffusion equation is solved for every 0.5 $ change in the reactivity of the system.

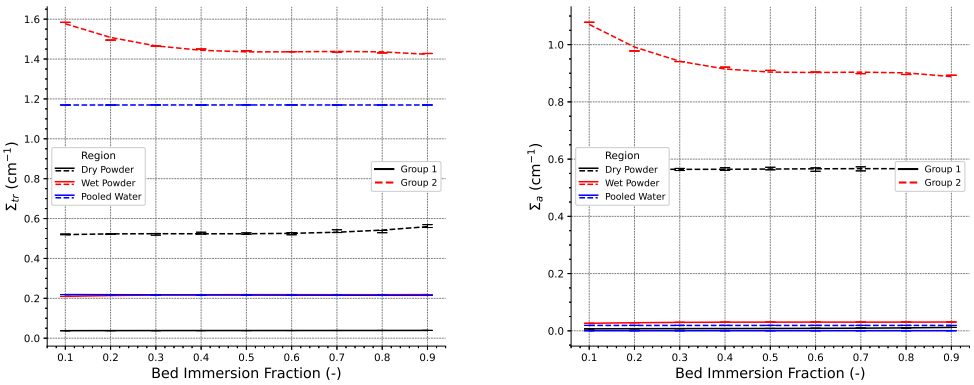

(a) Σ_{tr}.

(b) Σ_{a}.

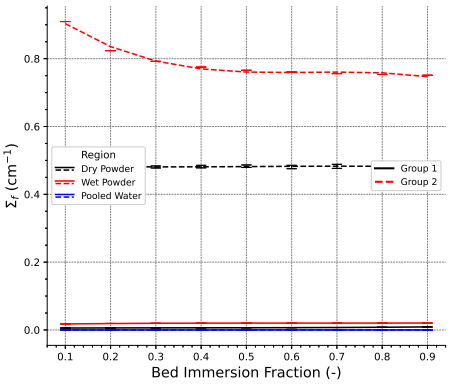

(c) Σ_{f}.

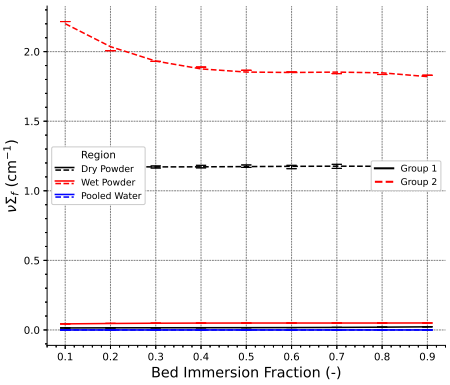

(d) $\bar{\nu}\Sigma_{\mathrm{f}}$.

Figure 6.26: The fast and thermal macroscopic nuclear cross-sections for each region of the highly enriched UO_2 powder bed.

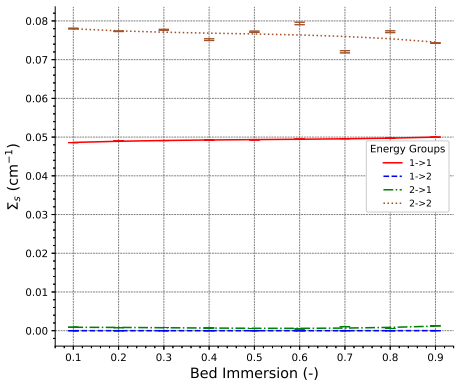

(a) Dry UO_2 powder region.

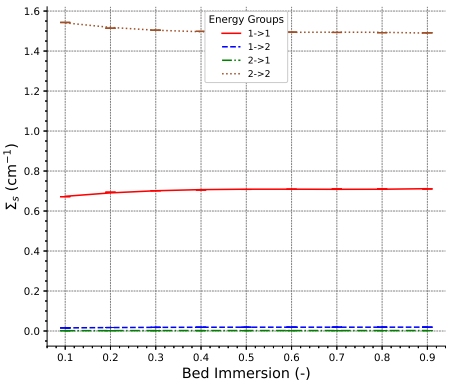

(b) Wet UO_2 powder region.

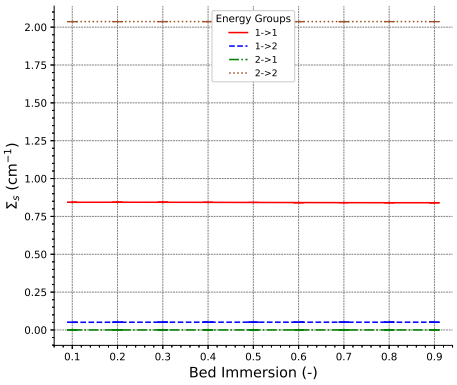

(c) Pooled water region.

Figure 6.27: The fast and thermal macroscopic scattering nuclear cross-sections for each region of the highly enriched UO_2 powder bed.

Table 6.14: Macroscopic neutron cross-section correlation coefficients for the wet UO_2 powder bed.

Cross-section (cm^{-1})	C_0	C_1	C_2	C_3
$\bar{\nu}\Sigma_{f,1}$	0.03932	0.05044	−0.08001	0.04168
$\bar{\nu}\Sigma_{f,2}$	2.44082	−2.82280	4.45054	−2.31100
$\Sigma_{a,1}$	0.02352	0.03318	−0.05265	0.02743
$\Sigma_{a,2}$	1.18587	−1.35409	2.13502	−1.10866
$\Sigma_{f,1}$	0.01592	0.02082	−0.03303	0.01720
$\Sigma_{f,2}$	1.00169	−1.15846	1.82648	−0.94843
$\Sigma_{tr,1}$	0.20383	0.07107	−0.11350	0.05876
$\Sigma_{tr,2}$	1.67788	−1.19271	1.92572	−1.01597
$\Sigma_{s,1\to1}$	0.68361	0.03728	0.00000	0.00000
$\Sigma_{s,1\to2}$	0.01650	0.00377	0.00000	0.00000
$\Sigma_{s,2\to1}$	0.00175	0.00050	0.00000	0.00000
$\Sigma_{s,2\to2}$	1.52786	−0.05003	0.00000	0.00000

Table 6.15: Macroscopic neutron cross-section correlation coefficients for the pooled water region.

Cross-section (cm^{-1})	C_0	C_1	C_2	C_3
$\bar{\nu}\Sigma_{f,1}$	0.00000	0.00000	0.00000	0.00000
$\bar{\nu}\Sigma_{f,2}$	0.00000	0.00000	0.00000	0.00000
$\Sigma_{a,1}$	0.00046	0.00009	−0.00011	0.00005
$\Sigma_{a,2}$	0.01884	0.00003	−0.00005	0.00003
$\Sigma_{f,1}$	0.00000	0.00000	0.00000	0.00000
$\Sigma_{f,2}$	0.00000	0.00000	0.00000	0.00000
$\Sigma_{tr,1}$	0.21941	−0.00651	−0.00108	0.00336
$\Sigma_{tr,2}$	1.16906	0.00298	−0.00434	0.00175
$\Sigma_{s,1\to1}$	0.84431	−0.00456	0.00000	0.00000
$\Sigma_{s,1\to2}$	0.05096	0.00056	0.00000	0.00000
$\Sigma_{s,2\to1}$	0.00008	−0.00000	0.00000	0.00000
$\Sigma_{s,2\to2}$	2.03669	0.00008	0.00000	0.00000

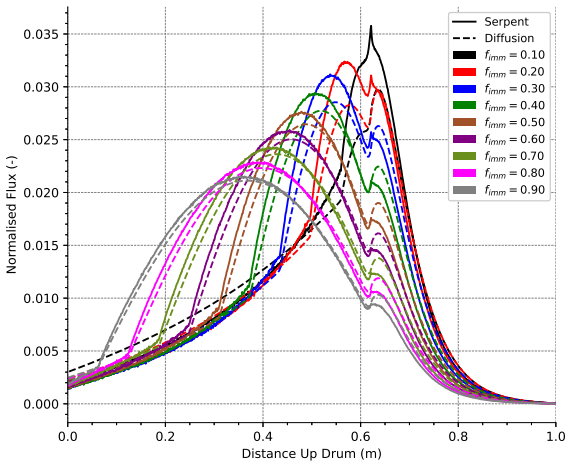

Figure 6.28: Scalar neutron flux distributions obtained through Monte Carlo neutron transport code Serpent alongside a multi-group neutron diffusion code using prescribed macroscopic nuclear cross-section correlations.

Table 6.16: Thermophysical properties of the UO_2 powder bed, water, radiolytic gas (H_2) and steam.

Property	Symbol	Value
Specific heat capacity of UO_2	c_p	274 J kg^{-1} K^{-1}
Specific heat capacity of steam	c_v	2.060×10^3 J kg^{-1} K^{-1}
Specific heat capacity of water	c_w	4.2×10^3 J kg^{-1} K^{-1}
Mean powder particle diameter	d_p	10 μm
Pore water turbulent mixing coefficient	D_{wp}	10^{-4} m^2 s^{-1}
Energy released per fission event	E_f	3.2×10^{-11} J fission^{-1}
Slumping fraction	f_{slump}	0.0
Volumetric H_2 generation coefficient at STP	$G(H_2)$	5.36777×10^{-9} m^3 J^{-1}
Volumetric H_2O loss coefficient at STP	$G(H_2O)$	3.36×10^{-12} m^3 J^{-1}
Container height	H_{cyl}	1.0 m
Latent heat of vaporisation	$h_{l,v}$	2.2512×10^6 J kg^{-1}
Container radius	R_{cyl}	0.4 m
Mean fission fragment range	R_{fiss}	7 μm
Intrinsic UO_2 neutron source density	S_n	586 neutrons s^{-1}
Boiling point of water	T_{sat}	373.15 K
Critical gas velocity	$U_{g,crit}$	∞ m s^{-1}
Water incursion rate onto powder bed	$U_{w,in}$	9.947×10^{-4} m s^{-1} (0.5 L s^{-1})
Dry UO_2 powder bed packing fraction	$v_{f,p,dp}$	0.1461
Settled wet UO_2 powder bed packing fraction	$v_{f,p,wp}$	0.1461
Fast neutron speed	$V_{n,1}$	1.4×10^9 cm s^{-1}
Thermal neutron speed	$V_{n,2}$	2.2×10^5 cm s^{-1}
Thermal expansion coefficient of water	η	2.14×10^{-4} K^{-1}
Thermal conductivity of UO_2	κ_p	see Equation (3.81)
Thermal conductivity of gas	κ_v	0.0246 W m^{-1} K^{-1}
Thermal conductivity of water	κ_w	0.608 W m^{-1} K^{-1}
Dynamic viscosity of gas	μ_v	1.271×10^{-5} Pa s
Dynamic viscosity of water	μ_w	see Equation (3.82)
Density of UO_2	$\rho_{p,th}$	10950 kg m^{-3}
Density of gas	$\rho_{v,th}$	0.5863 kg m^{-3}
Density of water	$\rho_{w,th}$	998.1 kg m^{-3}

6.7.3 Summary of Parameters for Deterministic Simulations

The neutron kinetic parameters for the 95-wt% enriched, partially saturated UO_2 powder bed have been described in Section 6.4.1. The thermophysical properties are similar to those used previously throughout this thesis and are summarised in Table 6.16.

6.7.4 Summary of Initial Conditions for Deterministic Simulations

The initial region heights of the highly enriched UO_2 powder bed for the deterministic simulations are listed in Tables 6.9 to 6.11. The initial neutron populations and delayed neutron precursor populations as a function of the prescribed threshold neutron population have been previously stated in Table 6.8. Additional initial conditions are summarised in Table 6.17.

Table 6.17: Initial conditions for sub-critical partially wetted UO_2 powder bed.

Property	Symbol	Value
Initial dry powder region saturation	$S_{w,0}$	0
Reference temperature	T_0	293.15 K
All-region and component water temperature	T_w	293.15 K
All-region and component void fraction	$v_{f,g}$	0

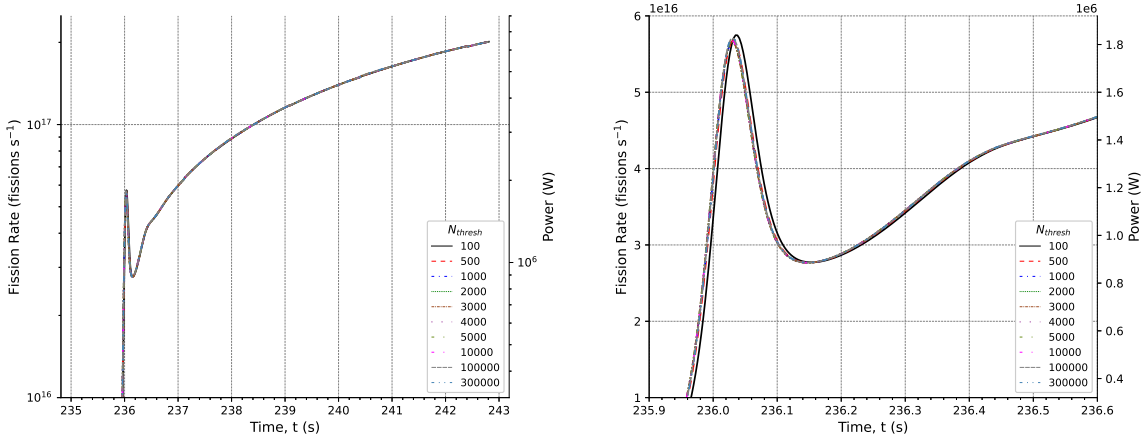

(a) (b)

Figure 6.29: The variation in fission power as a function of the threshold neutron population up to the point of boiling. Also shown, a closer view of the initial peak power before the steady fission power rise.

6.8 Results of Deterministic Simulations

Figure 6.29 shows how the fission power of the highly enriched, wetted UO_2 powder system varies from just before the first power peak, up to the boiling point of the pore water for the cases where the initial conditions are on the mid-point of the wait-time Gamma CDF, for each prescribed threshold neutron population. Also shown in Figure 6.30 is a representative reactivity component profile for the case where $N_{thresh} = 3000$ neutrons. A similar reactivity profile was found for all simulated cases, therefore, for clarity, one is shown. The results indicate that the characteristics of the transient nuclear criticality excursion are similar, regardless of the prescribed threshold neutron population. The initial peak powers, shown in Figure 6.29b are of similar magnitude, but appear to converge to a particular time as the threshold neutron population increases. The initial peak power is limited by the production of radiolytic gas, which causes the system to enter a delayed super-critical state. The subsequent reduction in power is followed by a steady rise as further wetting adds reactivity to the system. This is counter-balanced by greater radiolytic gas void production until boiling occurs. A consequence of the continued increase in wetting-induced reactivity is that the first power peak is significantly less than the true maximum power that is predicted at the point at which interstitial water boils.

Comparisons were also made between transient nuclear criticality excursions with initial conditions that lie at other points of the wait-time Gamma CDFs that have previously been found for each

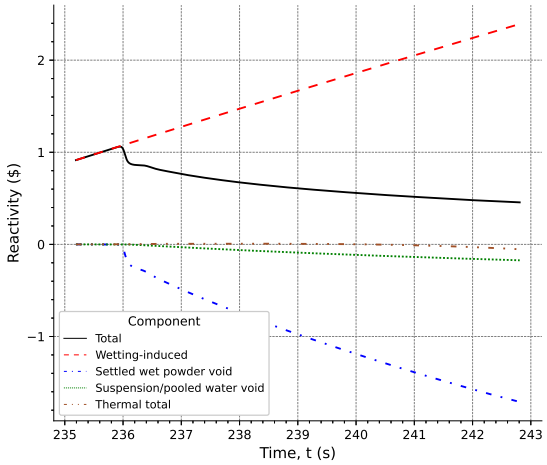

Figure 6.30: Representative reactivity component profile for transient nuclear criticality excursion with initial conditions derived from the mid-point of the Gamma wait-time CDF, for $N_{\text{thresh}} = 3000$ neutrons.

prescribed threshold neutron population. Ten different threshold neutron populations at five different points on the Gamma wait-time CDF were selected as initial conditions for the deterministic simulations. A selection of results from these threshold neutron populations are shown in Figure 6.31. For all prescribed threshold neutron populations, higher initial peak powers were predicted when sampling initial conditions from later in time on the Gamma wait-time CDF. Figure 6.32 indicates that the large variations in power may be predicted by sampling different initial conditions on the wait-time CDFs. A non-uniform distribution of the peak power is predicted around the centre of the wait-time CDF. This may be attributed to the fact that the initial conditions at the point which corresponds to 0.99 on the wait-time CDF resemble a fissile system that is in a prompt super-critical configuration. This differs from other points on the wait-time CDF which are either delayed super-critical or less prompt super-critical. The results suggest that the difference in the reactivity of the system at the start of the deterministic simulation may significantly affect the initial peak power, before any reactivity feedback components begin to play a role in governing the transient nuclear criticality excursion characteristics.

The true peak power that occurs at the onset of boiling, as shown by Figures 6.31a, 6.31c and 6.31e, appears to be weakly dependent on the point along the CDF from where the initial conditions for the deterministic simulation are taken from. This may be attributed to the fact that a significant proportion of the fission energy deposited in the system occurs in the deterministic regime, once reactivity feedback components have become significant. The initial effects of stochasticity on the power only reflect a small amount of energy deposited into the system compared to the subsquent deterministic portion of the transient nuclear criticality excursion. Since the power continues to rise until sufficient energy is deposited in the system for boiling to occur, and this energy deposition is largely deterministic, the actual peak powers do not vary widely as a function of the initial conditions. This feature is illustrated in Figure 6.33, which highlights that the near full span of the wait-time CDF for which initial conditions are found from for the deterministic simulation, corresponds to a variation in peak power of around 0.5 %. Furthermore, 50 % of initial conditions around the centre of

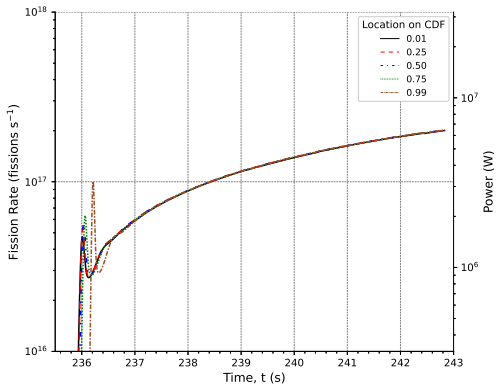

(a) $N_{\text{thresh}} = 100$.

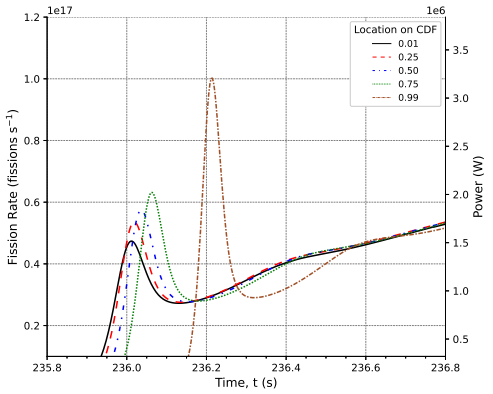

(b) $N_{\text{thresh}} = 100$.

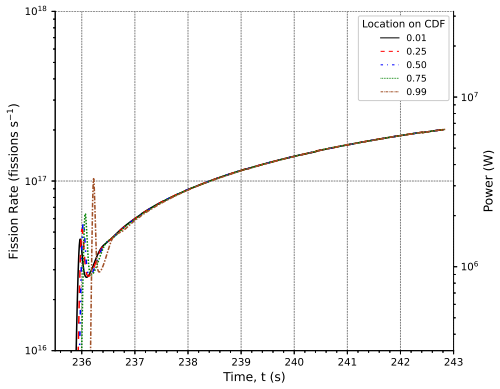

(c) $N_{\text{thresh}} = 3000$.

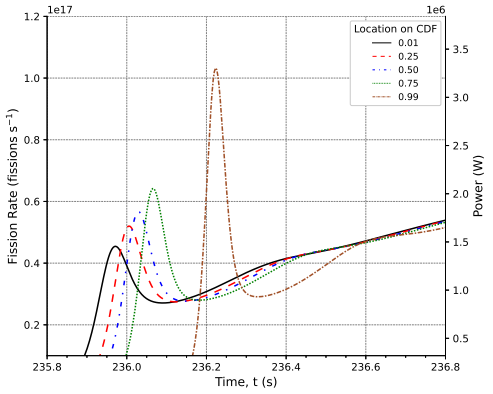

(d) $N_{\text{thresh}} = 3000$.

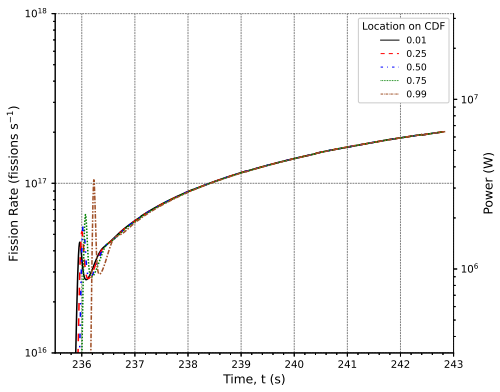

(e) $N_{\text{thresh}} = 300000$.

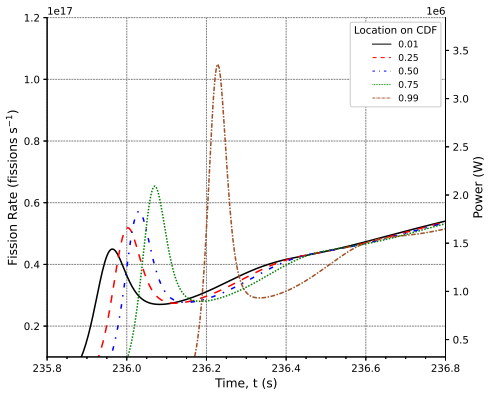

(f) $N_{\text{thresh}} = 300000$.

Figure 6.31: The variation in fission power as a function of the threshold neutron population up to the point of boiling. Also shown, a closer view of the initial peak power before the steady fission power rise.

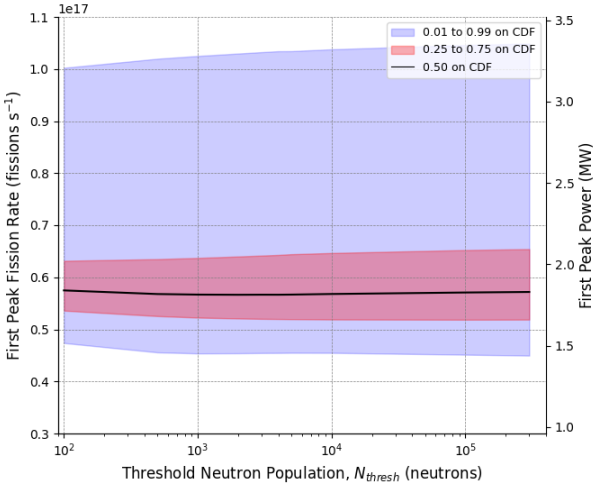

Figure 6.32: Variation in the initial peak power for different initial conditions based on different wait-time CDFs, found using prescribed threshold neutron populations.

the wait-time CDF yield a total peak power that does not vary by more than 0.25 %. The peak power at the onset of boiling is also predicted to be weakly dependent on the prescribed threshold neutron population.

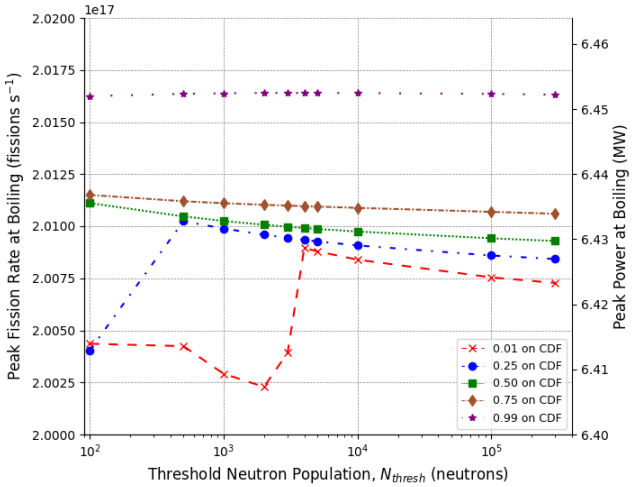

Figure 6.33: Variation in the peak power at the onset of boiling for different initial conditions based on different wait-time CDFs, found using prescribed threshold neutron populations.

The time taken for boiling to occur from the start of the infiltration of water into the HEU powder bed is shown in Figure 6.34. Generally, as the threshold neutron population increases, the time taken for boiling to occur decreases. This effect is more pronounced when the initial conditions are chosen at points corresponding to lower down on the Gamma wait-time CDF. This may be attributable to the wide-ranging initial reactivities of the system at low-threshold neutron populations and points earlier in time on the Gamma wait-time CDF. The span in the time taken to boil between the simulations with different deterministic simulations does not exceed approximately 0.05 s, for any prescribed threshold neutron population, which corresponds to a maximum variation of 0.02 % in the

time taken for interstitial water to boil. This is attributable to the fact that a majority of the fission energy deposited into the system up to boiling occurs after the initial power peak, when the neutron population is high and the system is behaving deterministically.

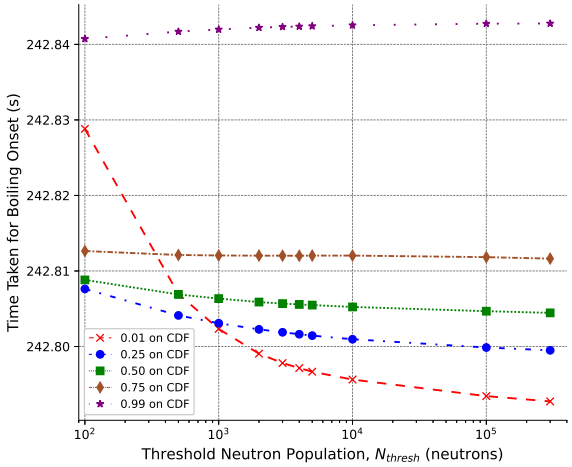

Figure 6.34: Variation in the time taken for boiling from the start of water infiltration as a function of initial conditions found from different threshold neutron populations and points along Gamma wait-time CDF.

6.9 Conclusions

In this thesis chapter the forward stochastic balance equation and the Gamma distribution method were used to examine the effects of a weak intrinsic neutron source, on transient nuclear criticality excursions in a cylindrical container of highly enriched UO_2 powder, undergoing wetting from above. A series of threshold neutron populations, delineating the stochastic from deterministic regime, were perscribed. Gamma wait-time distributions were then obtained at each of these threshold values by numerically differentiating the Gamma CDF. Moments of the distribution were found to obtain the mean wait-time for the prescribed threshold neutron population to be reached, as well as the associated variance. A set of deterministic simulations, using the same coupled wetting, nuclear thermal hydraulic, radiolysis and point neutron kinetics model as described in previous chapters, were performed. The initial conditions for these deterministic simulations were sampled from various points along the Gamma wait-time CDF at the threshold neutron population. The dependency of the stochastically derived initial conditions on the initial peak power and true peak power up to the point at which the interstitial pore water boiled was examined.

SOURCES-4C was used to estimate intrinsic neutron source strength due to a combination of (α,n) interactions and SF in UO_2 powder with varying levels of enrichment. The SF source decreased linearly at a higher rate than the (α,n) increased, with increasing levels of enrichment. At $\gamma = 0.95$ wt-%, the contribution of SF and (α,n) to the total intrinsic neutron source were predicted to be near identical. Combining this data with MCNP derived neutron kinetic parameters for the UO_2 powder bed under various amounts of wetting and with different enrichment levels indicated that the low neutron source criterion, as defined by Hansen et al. (1959), may be satisfied for medium to highly enriched UO_2 powder beds. Therefore, wetting-induced transient nuclear criticality excursions in these systems may exhibit stochastic behaviour early in the transient.

The specific case with $\gamma = 0.95$ wt-% was chosen for the Gamma distribution method wait-time study. The infiltration of water into a UO_2 powder bed with a weak intrinsic neutron source led to a transient nuclear criticality excursion approximately 235.0 seconds after the start of the water infiltration. The mean wait-time taken to reach a prescribed threshold neutron population increased with increasing threshold neutron population. Self-similarity is also predicted between the relative standard deviations determined by solving the forward stochastic balance equation for the neutrons and delayed neutron precursors. Furthermore, the Gamma wait-time probability distribution suggests that the times at which a prescribed threshold neutron population is observed becomes less spread out as the threshold neutron population increases and the criticality excursion behaves more deterministically.

Initial conditions derived from the stochastic study indicated that large variations in reactivity could be predicted, especially if the onset of the deterministic regime occurs at low threshold neutron populations. At these low threshold neutron populations, there is a significant probability that a given realisation may be delayed super-critical, whilst the next realisation is prompt super-critical. The consequence of this variation has been shown through deterministic simulations that predict large variations in the initial peak power that occurs as reactivity feedback components begin to play

a significant role in controlling the transient nuclear criticality excursion. However, the true peak power, which occurs later in the transient, at the onset of the interstitial pore water boiling, is much greater than this initial peak and does not depend strongly on the stochastic initial conditions.

Chapter 7

Conclusions and Future Work

7.1 Conclusions

NCS plays an important role in reducing the risk of nuclear criticality accidents and keeping personnel working in nuclear facilities, as well as the public, safe. Chapter 1 provides an outline of the nuclear fuel cycle, with a specific focus on the widespread handling of fissile powders in the production of UO_2 and MOX fuel pellets. The associated risks of accidental transient nuclear criticality excursions in nuclear fuel processing facilities that handle powdered nuclear fuel has been extensively discussed. Specific interest has been taken in this thesis to model the effects of wetting-induced transient nuclear criticality excursions in enriched, mono-dispersed UO_2 powder beds, contained within cylindrical barrels.

A coupled point neutron kinetics and phenomenological model for simulating a wetting-induced transient nuclear criticality excursion in a UO_2 powder bed has been proposed in Chapter 3. The UO_2 powder bed was modelled as a three-region problem, separated by sharp interfaces. The sharp wetting front separated the dry and wet UO_2 powder regions. The surface of the UO_2 powder bed separated the wetted UO_2 powder region from the pooled water region. Pooled water may accumulate if the water flow rate is greater than the rate at which water can fill interstitial pores around the UO_2 powder particles. The model includes water infiltration, nuclear thermal hydraulics, radiolysis and boiling equations that are coupled to the point neutron kinetics equations through the use of multivariate reactivity feedback correlations. Spatial discretisation is performed using a radially and azimuthally independent FV scheme in cylindrical co-ordinates. A neutron flux shape function was obtained by solving the multi-group steady-state partial integro-differential neutron diffusion equation, which was in turn used to obtain the linear power density axially throughout the domain. Correlations for radiolytic gas and steam bubble sizes, as well as convective and latent heat transfer coefficients, were obtained from the literature. The proposed water infiltration model matched water infiltration derived from sub-critical experiments performed at the SILENE facility, for UO_2 powder particle sizes that were similar to those found in the literature. Furthermore, MCNP simulations suggested that the infiltration of water added large amounts of reactivity into the system, causing the wetted UO_2 powder bed to go prompt super-critical. The subsequent rise in power of the prompt super-critical system led

to the production of radiolytic gas and temperature rise of the UO_2 powder and water. Local thermal equilibrium was shown to occur between the wet UO_2 powder and interstitial water, which may be expected since the specific surface area of the UO_2 powder was large. This limited the rise of the UO_2 powder temperature due to the high specific heat capacity of the interstitial water. This fact, combined with the low effective thermal conductivity of UO_2 powder, meant that a sharp thermal interface developed between the dry and wet UO_2 powder regions. Doppler broadening and thermal expansion are not expected to be sufficient to quench the wetting-induced transient nuclear criticality excursion. The production of radiolytic gas and subsequently, steam, was the primary mechanism for removing reactivity from the system, by promoting neutron leakage. The characteristics of the transient nuclear criticality excursion depend largely on the mean size of UO_2 powder particles.

The model was developed further in Chapter 4 to include a phenomenological approach for simulating wetting-induced volumetric collapse of meta-stable UO_2 powder bed structures into more concentrated formations. A stress-strain relation was formulated for the compression hysteresis of a UO_2 powder bed as the wetting front advected downwards. A parametric study of how slumping may affect the characteristics of a wetting-induced transient nuclear criticality excursion in a UO_2 powder bed was performed. The magnitude of slumping was captured through a single empirical parameter that related the amount that the wetted UO_2 powder bed slumped relative to the progression of the wetting front. MCNP simulations of the partially saturated UO_2 powder bed, indicated that the slumping phenomenon introduced negative reactivity into the system by transporting water (acting as moderator) previously held interstitially in pores, to the pooled water region. Similar characteristics of the transient nuclear criticality excursion were predicted regardless of the slumping fraction, although large variations in the initial peak power were predicted.

Fluidisation and sedimentation, which introduced significant fissile mass re-distribution within the UO_2 powder bed, was modelled in Chapter 5. Through the use of empirical correlations and experimental data found in the literature, an approximation of the agglomerate size of UO_2 and the hindered settling rate of UO_2 agglomerates were established. Similar agglomerate and hindered settling rate properties were predicted for both UO_2 powder particles and ThO_2 powder. Gas-bubble induced fluidisation of the static wetted UO_2 powder bed was modelled through the prescription of a critical gas velocity for incipient fluidisation and a corresponding rate of fluidisation. Gas-bubble induced fluidisation of the UO_2 powder bed led to the formation of a dilute suspension above the static UO_2 powder bed. An empirical correlation was used to determine the gas-bubble induced turbulent mixing of the dilute suspension region. Due to the ratio of the height of the suspension to the radius of the vessel, the correlation estimated that the dilute suspension mass flow would largely be governed by turbulent mixing. This led to a homogeneous distribution of suspended UO_2 powder particles shortly after incipient fluidisation. An important aspect of mass re-distribution caused by fluidisation is the effect that it may have on the characteristics of a wetting-induced transient nuclear criticality excursion in UO_2 powder beds. MCNP simulations indicated that the creation of a dilute suspension region, through fluidisation, generally introduced a negative reactivity feedback into the system. However, there were cases where the H/U ratio was such that further fluidisation of the UO_2 powder bed began to introduce less negative reactivity into the system, which in some cases led to a positive reactivity feedback effect. A parametric study was performed, examining how various critical gas velocities and

rates of re-suspension affected the characteristics of the nuclear criticality transient. At high critical gas velocities, the dominant negative reactivity component was due to radiolytic gas and steam voids present in the system. The re-distribution of fissile mass at varying rates did not significantly alter the characteristics of the transient nuclear criticality excursion. However, prescribing the critical gas velocity such that incipient fluidisation occurred at the onset of boiling, led to a significantly different system power response. At comparatively low rates of fluidisation, an oscillatory power response was predicted, with the frequency governed by the rate of sedimentation. At higher rates of fluidisation, the static powder bed quickly became fully fluidised after boiling began, leading to a less oscillatory system response.

In Chapter 6 the weak intrinsic neutron source criterion was examined for a UO_2 powder bed undergoing wetting as a function of the level of enrichment. The prompt neutron lifetime was shown, through MCNP simulations, to vary as a function of the bed immersion fraction. The low source criterion was satisfied for a range of UO_2 powder bed enrichments. The probability associated with the initiation and continuation of persistent neutron chains in delayed super-critical and prompt super-critical systems in the presence of a weak intrinsic neutron source, at low neutron populations, leads to significant variations in neutron kinetic response of criticality transients. This is specifically important for NCS, since the deterministically calculated response of the system in the event of a nuclear criticality may under-predict what is actually observed. To examine the stochastic behaviour of wetting-induced transient nuclear criticality excursions in highly enriched UO_2 powder beds, the forward stochastic balance equation was solved along with a Gamma distribution method, to obtain mean-wait time distributions at various threshold neutron populations, that corresponded to the transition from stochastic to deterministic neutron kinetic behaviour. Large variations in the reactivity of the system were predicted at the transition to the deterministic regime as a function of the stochastic behaviour of the system. Subsequent deterministic simulations were performed, using the models of the previous chapters, that began from initial conditions sampled from various points along the wait-time distribution. The results indicated that the initial peak power varied significantly as a function of the initial conditions. However, the true peak power, occurring at the onset of boiling, did not vary as a function of the stochastically derived initial conditions since significant portions of the transient were in the deterministic regime leading up to boiling. The chapter highlighted the importance of the stochastic behaviour on the first power peak in a system undergoing a delayed or prompt super-critical nuclear criticality excursion.

7.2 Future Work

7.2.1 Poly-dispersivity

Throughout this thesis, an assumption has been made that the UO_2 powder particles are mono-dispersed. This approximation has also previously been made in other developed codes that investigated nuclear criticality excursions in fissile powders Basoglu et al. (1994); Yamane et al. (2003a); Rozain et al. (1991). However, it is well known that the production of UO_2 powder produces a log-normally distributed particle size distribution (Clayton and Aronson, 1958). The heterogeneity of the UO_2 powder particle size is even accounted for in the manufacture of the nuclear fuel pellets by

having a process step whereby the UO_2 powder particles are mixed in a dry blender, to homogenise them. Introducing a poly-disperse representation of the UO_2 powder particle size would add another dimension to the discretisation scheme, adding complexity. However, it would allow the modeller to examine how the size of the particles packed in a porous structure together affects the permeability of the system. Introducing poly-dispersion into the model would also provide a more accurate representation of fluidisation and sedimentation, by permitting the modelling of layered sediment formation occurring. The deposition of fission energy as heat would also become a function of the UO_2 powder particle size. Furthermore, a more detailed analysis of likely gas bubble nucleation sites may be required, taking poly-dispersed particle sizes into consideration. By including this dimension to the problem, a more accurate representation of the problem may be obtained.

7.2.2 Higher Fidelity Mass Transfer Models and Time-Dependent Neutron Transport/Diffusion

This thesis presented models of water infiltration that were based on the GA method, which used a sharp-wetting front approximation. The GA method required no empirical correlations and therefore was advantageous over some other more complex methods. Furthermore, the sharp wetting front approximation was appropriate for the small particle sizes generally modelled in this thesis. However, as the mean powder particle size in the porous bed increases, the wetting front becomes more dispersed, necessitating an alternative modelling approach. More complex infiltration models that account for dispersion around the wetting front include Richard's equation (Richards, 1931) and the Broadbridge-White model (Broadbridge and White, 1988). Not only can these models account for dispersion around the wetting front, but they also have the ability of modelling transpiration, or the uptake of water through capillary action. A Broadbridge-White model of a UO_2 powder bed in infiltration and transpiration regimes has successfully been employed by Williams (2022), modelling dispersed wetting fronts. It is important to note that these more complex models would require empirical correlations that do not currently exist for UO_2 powder systems.

High-fidelity mass transfer models that fully solve the multiphase Navier-Stokes momentum equation with associated turbulence models may be applied to gain a better understanding of the mass transfer dynamics of the three-phase dispersed UO_2 powder-water-gas system. Although much more computationally expensive than the present approach, it would reduce the use of empirical relations. Alternative approaches that have been successfully applied to modelling flows in porous media include Lattice Boltzmann methods (LBM) (Guo and Zhao, 2002) and cellular automata (Rothman, 1988). The LBM may be coupled with the Discrete Element Method (DEM) for modelling the motion of a dilute suspension and the surrounding continuous fluid phase (Galindo-Torres, 2013).

The advantage of using point neutron kinetics is its relative simplicity and it's ability to parameterise out each component of reactivity so that the effects of voids, Doppler broadening and thermal expansion may be observed in isolation. However, a higher fidelity time-dependent neutron transport method could be used to more accurately model the neutron kinetics of the system. Using this approach, coupling of the neutronics and multi-physics would be achieved through the use of macroscopic nuclear cross-section correlations. A similar approach could also be applied when using the time-dependent NDE.

7.2.3 MOX and Plutonium Powder Systems

The proposed coupled phenomenological model may be extended to include functionality to simulate transient nuclear criticality excursions in wetted fissile powders consisting of Pu, PuO_2 and MOX. Plutonium is typically produced as a by-product of nuclear reactor operation. The re-processing of nuclear fuels using the PUREX process leads to the separation of plutonium from the uranium fuel and fuel poisons (Baumgärtner and Ertel, 1980). As part of this process, Pu and PuO_2 powders may be formed. The subsequent mixing of PuO_2 powder with UO_2 powder in MOX fuel fabrication facilities occurs in the presence of hydrogenous moderation and may pose a significant NCS risk. Of specific interest is the Bowman-Venneri-Kastenburg autocatalytic properties of dilute plutonium-based fissile systems when a transient nuclear criticality excursion occurs. The autocatalysis of spent MOX fuel is a primary safety concern for deep GDFs (Bowman and Venneri, 1996; Kastenberg et al., 1996). The autocatalytic properties of plutonium are unique in that a positive temperature feedback coefficient may exist when there is enough ^{239}Pu present in the plutonium or MOX fuel (Kastenberg et al., 1996). This occurs as the spectrum averaged fission cross-section for ^{239}Pu doubles as the temperature approaches the 0.3 eV resonance energy (Bowman and Venneri, 1996). As a consequence, a far greater portion of neutrons will be absorbed by ^{239}Pu, causing further fission, rather than leak out of the system.

7.2.4 Emulsion Systems

A similar phenomenological approach may be applied in the simulation of layered, multi-fluid systems such as mixtures of fissile aqueous-organic and emulsion solutions. These types of layered multi-fluid systems are widespread within nuclear fuel processing facilities. Indeed, many nuclear criticality excursions, including one at Windscale works on the 24^{th} August 1970 (now Sellafield), have occurred in such systems (McLaughlin et al., 2000). From an NCS perspective, this may be considered an important type of transient nuclear criticality excursion to model. An advantage of applying phenomenological models to emulsion systems is the possibility for some form of V&V due to the fact that there have been real transient nuclear criticality excursions in such systems.

7.2.5 Interacting Fissile Arrays

An important application for the models proposed in this thesis is to study wetting-induced transient nuclear criticality excursions in interacting arrays of uranium, plutonium or MOX fissile powders, emulsions and solutions. The cylindrical drums that house the fissile material may typically be in an array configuration within a nuclear fuel fabrication facility. These systems may be loosely coupled where some array components are sub-critical and some are super-critical (Thomas and Abbey, 1973; Bowen and Busch, 2006; Knief, 1985). The array formation can either be well-defined or ill-defined, corresponding to arrays whose composition, density, size, shape and position are either well-known or unknown (Ackroyd et al., 1961). These types of systems are of particular importance to NCS experts since they are found throughout the front and back-end of the nuclear fuel cycle and have the potential to cause criticality excursions in large combined systems that may be highly non-linear and behave in ways that cannot be predicted by modelling individual elements of the array. Of particular interest may be using linear and non-linear stability methods to investigate the stability of the system when subjected to various perturbations (Murray et al., 1966). The present model could be applied, using multi-point neutron kinetics, to simulate each element of the array independently on separate

CPU cores. Neutronic coupling of the individual elements may be achieved by applying Avery's method, which involves the development of 'coupling coefficients' that link together the elements of the loosely coupled system (Avery, 1958). A variety of approaches could be used to determine the coupling coefficients, one such method being the geometry conforming approach. Using this method, the importance of neutrons leaving one element of the interacting array and entering another may be adjoint weighted. This kind of study could support a criticality safety case in a nuclear fuel fabrication facility by providing key information about the characteristics of loosely coupled nuclear criticality excursions in fissile array systems.

7.2.6 Super-Critical Experiments

As far as the author is aware, at the time of writing, there have been no super-critical experiments performed on fissile powders when wetted. Performing such experiments would allow facilities that handle nuclear fuel to better monitor nuclear criticality safety risks associated with the processes that they carry out. This would be possible by gaining an understanding of the phenomena that would affect a transient nuclear criticality excursion in the damp fissile powder system. Such experiments would also enable the validation of calculational codes which may then be used to model a wide-range of scenarios and postulated nuclear criticality safety cases (Rouyer et al., 2003). The validation of computational codes against critical experiments provides NCS engineers with the ability to perform steady-state calculations using these codes, to increase safety relating to process and equipment design, ensuring that a nuclear criticality excursion cannot occur, even under abnormal conditions.

7.2.7 Slurry and Suspension Reactors

Section 1.3 outlines the extensive experimental research into suspension test reactors, through the development of the KSTR at KEMA (Kersten, 1962). Other suspension reactors have been recommended with varied criticality control mechanisms by Ferguson (1957); Davidson et al. (1959); Laramore et al. (2018). Extensions to the models proposed in this thesis may allow for the coupled phenomenological modelling of the criticality and multi-physics characteristics of suspension based nuclear reactors for breeder or power purposes.

7.2.8 Debris Bed and Core Re-distribution Modelling

Similarities with the phenomenological models developed within this thesis can be made with the phenomena of criticality in nuclear debris beds, formed as a consequence of structural damage to nuclear reactor cores. A reactor core-accident such as the Fukushima Daiichi disaster can cause the nuclear reactor core structure to fragment (Coindreau et al., 2013). The structural facture of the nuclear reactor may lead to the formation of an unstable debris bed that is partially or fully immersed in water (Tuya and Obara, 2017). The resulting fissile system consists of a poly-dispersed fragmented bed of fissile material surrounded by moderator. For the clean-up operation, it is of fundamental importance that NCS analysis be performed to examine whether the continued pumping of water through the core may lead to a re-criticality. The re-distribution of the debris bed due to the removal of elements of the reactor core may also lead to a re-criticality and must be considered. The phenomenological models proposed in this thesis could be applied to wetted debris beds by approximating the system as an array of spherical fissile particulates immersed in water (Fukuda et al., 2021).

Core re-distribution and compaction is the subject of interest for space nuclear safety applications, where atmospheric re-entry accidents may lead to plastic deformation of the core vessel (Marshall, 2008). The plastic deformation and re-arrangement of fissile material in the core may cause a nuclear criticality excursion. The approach used in this thesis regarding the volumetric collapse of a UO_2 powder bed may be adapted and developed further to model such scenarios.

7.2.9 Pyrophoricity in Uranium and Plutonium Hydrides

The pyrophoric behaviour of plutonium and uranium hydride when in a powdered form in the presence of oxygen has been discussed in Section 1.2. The coupled point neutron kinetics and nuclear thermal hydraulic models proposed in this thesis may be extended to reflect a scenario where a sub-critical or super-critical uranium or plutonium hydride powder burns, leading to the aerosolisation of particulates. The subsequent settling of the fissile material may initiate a transient nuclear criticality excursion. Specific interest could be applied to the autocatalytic properties of plutonium whilst exhibiting pyrophoric behaviour.

Bibliography

Abraham, M., Khare, A.S., Sawant, S.B., Joshi, J.B., 1992. Critical gas velocity for suspension of solid particles in three-phase bubble columns. Industrial & Engineering Chemistry Research 31, 1136–1147.

Ackroyd, R.T., Charlesworth, F.R., Thomas, A.F., 1961. Methods of calculation for interacting arrays with special reference to storage problems, in: Criticality Control in Chemical and Metallurgical Plant, Karlsruhe Symposium.

AERB, 2009. AERB Safety Guidelines: Uranium Oxide Fuel Fabrication Facilities. Report AERB/FE-FCF/SG-3. Atomic Energy Regulatory Board (AERB).

Ahn, J.H., 2006. Criticality safety of geologic disposal for high-level radioactive wastes. Nuclear Engineering and Technology 38.

Akcasu, Z., Lellouche, G.S., Shotkin, L.M., 1971. Chapter 2 - point kinetic equations, in: Akcasu, Z., Lellouche, G.S., Shotkin, L.M. (Eds.), Mathematical Methods in Nuclear Reactor Dynamics. Academic Press, pp. 48–87.

Al-Rawas, A.A., 2000. State-of-the-art-review of collapsible soils. Sultan Qaboos University Journal for Science (SQUJS) 5, 115–135.

Alazmi, B., Vafai, K., 1999. Analysis of variants within the porous media transport models. Journal of Heat Transfer 122, 303–326.

Albrecht, K.A., Cartwright, K., 1989. Infiltration and hydraulic conductivity of a compacted earthen liner. Groundwater 27, 14–19.

Almendros-Ibáñez, J.A., Sobrino, C., de Vega, M., Santana, D., 2006. A new model for ejected particle velocity from erupting bubbles in 2-D fluidized beds. Chemical Engineering Science 61, 5981–5990.

Amaldi, E., 1984. From the discovery of the neutron to the discovery of nuclear fission. Physics Reports 111, 1–331.

Amaldi, E., Fermi, E., 1936. On the absorption and the diffusion of slow neutrons. Phys. Rev. 50, 899–928.

Andreev, E.I., Glavin, K.V., Ivanov, A.V., Malovik, V.V., Martynov, V.V., Panov, V.S., 2009. Some

results uranium dioxide powder structure investigation. Russian Journal of Non-Ferrous Metals 50, 281–285.

Andreotti, B., Forterre, Y., Pouliquen, O., 2013. Granular Media: Between Fluid and Solid. 1st ed., Cambridge University Press.

Argo, W.B., Cova, D.R., 1965. Longitudinal mixing in gas-sparged tubular vessels. Industrial & Engineering Chemistry Process Design and Development 4, 352–359.

Authier, N., Richard, B., Humbert, P., 2014. Initiation of persistent fission chains in the fast burst reactor caliban. Nuclear Science and Engineering 177, 169–183.

Avery, R., 1958. Theory of coupled reactors, in: Second United Nations International Conference on the Peaceful Uses of Atomic Energy.

Badgujar, M.N., Deimling, A., Morsi, B.I., Shah, Y.T., Carr, N.L., 1986. Solids distribution in a batch bubble column. Chemical Engineering Communications 48, 127–153.

Balakrishna, P., Murty, B.N., Anuradha, M., 2009. A new process based agglomeration parameter to characterize ceramic powders. Journal of Nuclear Materials 384, 190 – 193.

Bannister, M., 1968. The storage behaviour of uranium dioxide powders review article. Journal of Nuclear Materials 26, 174 – 184.

Barbry, F.Y., 1993. A Review of the SILENE Criticality Excursion Experiments. Report CEA-IPSN-SRSC–93-220. Institut de Protection et Sûreté Nucléaire (IPSN).

Barile, R.G., Meyer, D.W., 1971. Turbulent bed cooling tower. Chemical Engineering Progress, Symposium Series 67, 134–143.

Basoglu, B., 1992. Analysis of a Hypothetical Criticality Accident Involving Damp Low-enriched UO_2 Powder. Master's Thesis. University of Tennessee.

Basoglu, B., Brewer, R.W., Haught, C.F., Hollenbach, D.F., Wilkinson, A.D., Dodds, H.L., Pasqua, P.F., 1994. Simulation of hypothetical criticality accidents involving homogeneous damp low-enriched UO_2 powder systems. Nuclear Technology 105, 14–30.

Baumgärtner, F., Ertel, D., 1980. The modern PUREX process and its analytical requirements. Journal of Radioanalytical Chemistry 58, 28–58.

Bear, J., 1972. Dynamics of Fluids in Porous Media. Dover Publications.

Beenackers, A.A.C.M., Van Swaaij, W.P.M., 1993. Mass transfer in gasliquid slurry reactors. Chemical Engineering Science 48, 3109 – 3139.

Begue, L., Caplin, G., Evo, S., Milin, M., 2013. Criticality safety of enriched UF_6 cylinders, in: 17th International Symposium on the Packaging and Transportation of Radioactive Materials (PATRAM).

Bell, G.I., 1963. Probability distribution of neutrons and precursors in a multiplying assembly. Annals of Physics 21, 243–283.

Bell, G.I., 1965. On the stochastic theory of neutron transport. Nuclear Science and Engineering 21, 390–401.

Bell, G.I., Glasstone, S., 1970. Nuclear Reactor Theory. 1st ed., Van Nostrand Reinhold Company, Litton Educational Publishing Inc.

Belle, J., 1961. Uranium dioxide: properties and nuclear applications. volume 4. Naval Reactors, Division of Reactor Development, US Atomic Energy Commission.

Bentridi, S.E., Gauthier-Lafaye, F., Gall, B., Seghour, A., 2011. Monte-Carlo based numerical modeling and simulation of criticality conditions occurrence in natural reactor zone 9 in Oklo deposit (Gabon). Progress in Nuclear Science and Technology 2, 395–400.

Bernstein, S., Preston, W.M., Wolfe, G., Slattery, R.E., 1947. Yield of photo-neutrons from U^{235} fission products in heavy water. Physical Review 71, 573–581.

Bickley, A., Mather, D., 1991. POWDER - A Computer Code to Model the Transient Behaviour of a Bed of Wetted Uranium Dioxide Powder. Atomic Energy Agency Technology, Report AEA/SRD R549.

Boldeman, J.W., Hines, M.G., 1985. Prompt neutron emission probabilities following spontaneous and thermal neutron fission. Nuclear Science and Engineering 91, 114–116.

Boldt, A.L., Oberg, G.C., 1970. Nuclear and chemical safety analysis: PUREX plant 1970 thorium campaign. Report ARH-1394. Atlantic Richfield Hanford Co.

Boltzmann, L., 1970. Weitere Studien über das Wärmegleichgewicht unter Gasmolekülen. Vieweg+Teubner Verlag, Wiesbaden. pp. 115–225.

Borges Silverio, L., de Queiroz Lamas, W., 2011. An analysis of development and research on spent nuclear fuel reprocessing. Energy Policy 39, 281–289.

Bostick, W.D., McCulla, W.H., Pickrell, P.W., 1985. Sampling, characterization, and remote sensing of aerosols formed in the atmospheric hydrolysis of uranium hexafluoride. Journal of Environmental Science and Health. Part A: Environmental Science and Engineering 20, 369–393.

Bouwer, H., 1966. Rapid field measurement of air entry value and hydraulic conductivity of soil as significant parameters in flow system analysis. Water Resources Research 2, 729–738.

Bowen, D.G., Busch, R.D., 2006. Hand Calculation Methods for Criticality Safety - A Primer. Los Alamos National Laboratory (LANL), Report LA-14244-M. United States.

Bowman, C., Venneri, F., 1996. Underground supercriticality from plutonium and other fissile material. Science and Global Security 5.

Boyd, A.W., Whitton, J.L., 1958. The settling behavior of uranium trioxide-water slurries. The Canadian Journal of Chemical Engineering 36, 277–281.

Brandberg, S.G., 1973. The conversion of uranium hexafluoride to uranium dioxide. Nuclear Technology 18, 177–184.

Brayton, R.K., Gustavson, F.G., Hachtel, G.D., 1972. A new efficient algorithm for solving differential-algebraic systems using implicit backward differentiation formulas. Proceedings of the IEEE 60, 98–108.

Bresson, L.M., Moran, C.J., 2004. Micromorphological study of slumping in a hardsetting seedbed under various wetting conditions. Geoderma 118, 277–288.

Briggs, J.B., Scott, L., Nouri, A., 2003. The international criticality safety benchmark evaluation project. Nuclear Science and Engineering 145, 1–10.

British Petroleum, 2021. Statistical Review of World Energy. Technical Report. British Petroleum (BP).

British Standards Institute, 2015. BS EN 12845: 2015: Fixed firefighting systems. Automatic sprinkler systems. Design, installation and maintenance.

British Standards Institute, 2020. BS EN 14972-1: 2020: Fixed firefighting systems. Water mist systems. Design, installation, inspection and maintenance.

Broadbridge, P., White, I., 1988. Constant rate rainfall infiltration: A versatile nonlinear model: 1. analytic solution. Water Resources Research 24, 145–154.

Brooks, R., Corey, T., 1964. Hydraulic properties of porous media. Hydrology Papers 3. Colorado State University, Fort Collins.

Brown, A., Glaser, A., 2016. On the origins and significance of the limit demarcating low-enriched uranium from highly enriched uranium. Science & Global Security 24, 131–137.

Brown, C.L., 1981. Impact of nuclear criticality on fuel cycles. Transactions of the American Nuclear Society 38, 20–21.

Brown, F.B., Martin, W.R., 2004. Stochastic geometry capability in MCNP5 for the analysis of particle fuel. Annals of Nuclear Energy 31, 2039–2047.

Brown, S.H., Chambers, D.B., 2017. Uranium mining and norm in north america - some perspectives on occupational radiation exposure. Health Physics 113, 13–22.

Burke, J.E., Smith, C.S., 1947. The formation of uranium hydride1. Journal of the American Chemical Society 69, 2500–2502.

Byrne, G.D., Hindmarsh, A.C., 1975. A polyalgorithm for the numerical solution of ordinary differential equations. ACM Trans. Math. Softw. 1, 7196.

Calma, D., IAEA, 2009. Yellowcake [photograph]. [Accessed 2022-04-04] Available from: https://www.flickr.com/photos/iaea_imagebank/4724010712/.

Carman, P.C., 1956. Flow of Gases Through Porous Media. Butterworths Publications.

Carter, R.D., Kiel, G.R., Ridgway, K.R., 1968. Criticality Handbook - Volume I. Atlantic Richfield Hanford Co. Report ARH-600. United States.

Cheng, S., Hirahara, D., Tanaka, Y., Gondai, Y., Zhang, B., Matsumoto, T., Morita, K., Fukuda, K., Yamano, H., Suzuki, T., Tobita, Y., 2011. Experimental investigation of bubbling in particle beds with high solid holdup. Experimental Thermal and Fluid Science 35, 405 – 415.

Cho, S.E., Lee, S.R., 2001. Instability of unsaturated soil slopes due to infiltration. Computers and Geotechnics 28, 185–208.

Choppin, G., Liljenzin, J.O., Rydberg, J., Ekberg, C., 2013. Radiochemistry and Nuclear Chemistry. 4th ed., Academic Press.

Clark, H.K., 1981. The American national standard for nuclear criticality safety in operations with fissionable materials outside reactors. Transactions of the American Nuclear Society , 544–545.

Clayton, E., 1974. Anomalies of criticality. Nuclear Technology 23, 14–27.

Clayton, E.D., 2010. Anomalies of nuclear criticality. Technical Report. Pacific Northwest National Laboratory, Report PNL-SA-4868-Rev.6.

Clayton, J.C., Aronson, S., 1958. Some preparation methods and physical characteristics of UO_2 powders. Technical Report. Westinghouse Electric Corp. Bettis Plant, Pittsburgh, Report WAPD-178.

Cohn, C.E., 1959. Errors in reactivity measurements due to photoneutron effects. Nuclear Science and Engineering 6, 284–287.

Coindreau, O., Fichot, F., Fleurot, J., 2013. Nuclear fuel rod fragmentation under accidental conditions. Nuclear Engineering and Design 255, 68–76.

Colomb, A.L., 1960. Photoneutrons and the control of a pool type reactor. Nuclear Science and Engineering 8, 289–293.

Combs, J., 2016. 8-Nuclear fuel from secondary supplies of uranium and plutonium, in: Hore-Lacy, I. (Ed.), Uranium for Nuclear Power. Woodhead Publishing, pp. 215–238.

Cooling, C., Williams, M., Eaton, M., 2018. CALLISTO-SPK: A stochastic point kinetics code for performing low source nuclear power plant start-up and power ascension calculations. Annals of Nuclear Energy 113, 319–331.

Cooling, C.M., Williams, M.M.R., Eaton, M.D., 2016. Coupled probabilistic and point kinetics modelling of fast pulses in nuclear systems. Annals of Nuclear Energy 94, 655–671.

Cooling, C.M., Williams, M.M.R., Nygaard, E.T., Eaton, M.D., 2014. A point kinetics model of the medical isotope production reactor including the effects of boiling. Nuclear Science and Engineering 177, 233–259.

Coussot, P., 1997. Mudflow Rheology and Dynamics. 1st ed., CRC Press.

Cova, D.R., 1966. Catalyst suspension in gas-agitated tubular reactors. Industrial & Engineering Chemistry Process Design and Development 5, 20–25.

Crossland, I., 2012. Nuclear Fuel Cycle Science and Engineering. Woodhead Publishing Series in Energy, Woodhead Publishing Ltd.

Csanady, G.T., 1973. Turbulent Diffusion in the Environment. volume 3 of *Geophysics and Astrophysics Monographs*. 1st ed., Springer Netherlands.

Dana, J.D., 1864. Manual of Mineralogy. 1st ed., Wiley.

Datta, A., 1991. A review of fire hazards and fire protection concerns of commercial fuel cycle facilities in the United States. Nuclear Engineering and Design 125, 315–323.

Davidson, J., Robb, W., Salmon, O., Sampson, J., 1959. A UO_2-liquid metal slurry reactor for economic power. Nuclear Science and Engineering 5, 227–236.

Delgado, J.M.P.Q., de Lima, A.G.B., 2018. Transport Phenomena in Multiphase Systems. 1st ed., Springer.

Department for Business, Energy and Industrial Strategy, 2020. Energy white paper: Powering our net zero future. CP. 337. HMSO.

Dierckx, P., 1981. An algorithm for surface-fitting with spline functions. IMA Journal of Numerical Analysis 1, 267–283.

DiPeso, G., Peterson, P., 1998. EOS for critical slurry and solution systems. Lawrence Livermore National Laboratory (LLNL), University of California, Berkeley, Report, UCRL-JC-132331.

Diven, B.C., Martin, H.C., Taschek, R.F., Terrell, J., 1956. Multiplicities of fission neutrons. Phys. Rev. 101, 1012–1015.

Do, H.T., Grace, J.R., Clift, R., 1972. Particle ejection and entrainment from fluidised beds. Powder Technology 6, 195–200.

Donnelly, J.V., 2011. Interpolation of temperature-dependent nuclide data in MCNP. Nuclear Science and Engineering 168, 180–184.

Dorning, J., 2010. Nuclear Reactor Kinetics: 1934-1999 and Beyond. Springer Netherlands, Dordrecht. pp. 375–457.

Doucet, M., Zheng, S., Mouton, J., Porte, R., 2003. Framatome-ANP France UO_2 fuel fabrication - criticality safety analysis in the light of the JCO accident. Japan Atomic Energy Research

Agency (JAERI), Kashiwa, Chiba (Japan), in: International Conference on Nuclear Criticality Safety (ICNC2003). Challenges in the pursuit of global nuclear criticality safety, Tokai, Ibaraki (Japan). pp. 755–757.

Duderstadt, J.J., Hamilton, L., 1976. Nuclear Reactor Analysis. John Wiley & Sons.

Duhamel, I., Girault, E., Venard, C., 2005. Proposal of integral critical experiments for low-moderated MOX fissile media, in: Integrating Criticality Safety into the Resurgence of Nuclear Power, American Nuclear Society, LaGrange Park IL.

Dulla, S., Ravetto, P., 2008. Numerical aspects in the study of neutron propagation. Annals of Nuclear Energy 35, 656–664.

Dunn, E., Brown, S., Dodds, M., Thomas, A., 2013. Credible moderation content of uranium oxide powder and pellet systems, in: Topical Meeting held by the ANS Nuclear Criticality Safety Division (NCSD 2013), Criticality Safety in the Modern Era: Raising the Bar, American Nuclear Society, Wilmington, North Carolina, USA. pp. 380–393.

Edwards, C.R., Oliver, A.J., 2000. Uranium processing: A review of current methods and technology. JOM 52, 12–20.

Eichenberg, J.D., Vogel, K.H., Lustman, B., Kisiel, T.J., Frank, P.W., 1957. Effects of irradiation on bulk UO_2. WAPD-183, Bettis Atomic Power Laboratory, Pittsburgh, Pennsylvania.

El-Samrah, M.G., Tawfic, A.F., Chidiac, S.E., 2021. Spent nuclear fuel interim dry storage; design requirements, most common methods, and evolution: A review. Annals of Nuclear Energy 160, 108408.

Ergun, S., Orning, A.A., 1949. Fluid flow through randomly packed columns and fluidized beds. Industrial & Engineering Chemistry 41, 1179–1184.

Ermakova, A., 1970. Hydrodynamics of a gas-liquid reactor with a fluidized bed of solid matter. Theoretical Foundations of Chemical Engineering 4, 84–89.

European Commission Communication, 2018. A Clean Planet for all: A European strategic long-term vision for a prosperous, modern, competitive and climate neutral economy. Report COM/2018/773. European Union.

Faghri, A., Zhang, Y., 2006. Transport Phenomena in Multiphase Systems. 1st ed., Academic Press.

Fan, L.S., 1989. Gas-Liquid-Solid Fluidization Engineering. 1st ed., Butterworth-Heinemann.

Fan, L.T., Newcomer, M.P., 1981. Oxygen transfer in three phase fluidised beds, in: Scientific and Engineering Principles. Pergamon, pp. 643 – 650.

Farthing, M.W., Ogden, F.L., 2017. Numerical solution of Richards' equation: A review of advances and challenges. Soil Science Society of America Journal 81, 1257–1269.

Federovich, E.D., 2007. Technical issues of wet and dry storage facilities for spent nuclear fuel. Springer, Dordrecht. chapter Safety related issues of spent nuclear fuel storage. pp. 189–208.

Ferguson, D., 1957. The chemical processing of two-region aqueous homogeneous reactors. Nuclear Science and Engineering 2, 664–675.

Fernandez, M.H., 2020. Fissionable Materials Handlers Operators-Initial Training. Los Alamos National Laboratory (LANL), Report LA-UR-20-22807.

Fink, J.K., Chasanov, M.G., Leibowitz, L., 1981. Thermophysical properties of uranium dioxide. Journal of Nuclear Materials 102, 17 – 25.

Flerov, G.N., Petrjak, K.A., 1940. Spontaneous fission of uranium. Physical Review 58, 89.

Flugge, S., 1959. Neutrons and related gamma ray problems, in: Encyclopaedia of Physics. Springer Verlag. volume 38.

Fredlund, D.G., Morgenstern, N.R., 1976. Constitutive relations for volume change in unsaturated soils. Canadian Geotechnical Journal 13, 261–276.

Fredlund, D.G., Rahardjo, H., Fredlund, M.D., 2012. Unsaturated Soil Mechanics in Engineering Practice. 1st ed., John Wiley & Sons, Ltd.

Friedlander, S.K., 1957. Behavior of suspended particles in a turbulent fluid. American Institute of Chemical Engineers Journal 3, 381–385.

Fukuda, K., Nishiyama, J., Obara, T., 2021. Supercritical transient analysis for ramp reactivity insertion using multiregion integral kinetics code. Nuclear Science and Engineering 195, 453–463.

Fung, A.S., Hamdullahpur, F., 1993. A gas and particle flow model in the freeboard of a fluidized bed based on bubble coalescence. Powder Technology 74, 121–133.

Galindo-Torres, S., 2013. A coupled discrete element Lattice Boltzmann method for the simulation of fluid-solid interaction with particles of general shapes. Computer Methods in Applied Mechanics and Engineering 265, 107–119.

Gandini, A., 2002. On the multiplication factor and reactivity definitions for subcritical reactor systems. Annals of Nuclear Energy 29, 645–657.

Gandini, A., Salvatores, M., 2002. The physics of subcritical multiplying systems. Journal of Nuclear Science and Technology 39, 673–686.

Gardner, D., 1959. Fission fragment impact trapping by ThO_2 slurry particles. Nuclear Science and Engineering 6, 487–492.

Gear, C.W., 1971. The automatic integration of ordinary differential equations. Commun. ACM 14, 176179.

Gel'perin, N.I., Savchenko, V.I., Grishko, V.Z., 1968. Some hydrodynamic laws of absorption apparatus

packed with fluidized spheres. Theoretical Foundations of Chemical Engineering 2, 65–71.

Gibilaro, L., Gallucci, K., Felice, R.D., Pagliai, P., 2007. On the apparent viscosity of a fluidized bed. Chemical Engineering Science 62, 294 – 300.

Gil, L., 2018. Meet Oklo, the Earth's two-billion-year-old only known natural nuclear reactor. IAEA Bulletin 27.

Glaser, A., 2006. On the proliferation potential of uranium fuel for research reactors at various enrichment levels. Science & Global Security 14, 1–24.

Goddard, B., Croft, S., 2013. High-fidelity passive neutron multiplicity measurements and simulations of uranium oxide. Nuclear Instruments and Methods in Physics Research Section A: Accelerators, Spectrometers, Detectors and Associated Equipment 712, 147–156.

Gomes, J.L.M.A., Pain, C.C., Eaton, M.D., Goddard, A.J.H., Piggott, M.D., Ziver, A.K., de Oliveira, C.R.E., Yamane, Y., 2008. Investigation of nuclear criticality within a powder using coupled neutronics and thermofluids. Annals of Nuclear Energy 35, 2073–2092.

Gomes, J.L.M.A., Pain, C.C., Eaton, M.D., Tollit, B., Goddard, A.J.H., Piggott, M.D., Ziver, K., Yamane, Y., 2011. Coupled neutronics-fluids modelling of criticality within a MOX powder system. Progress in Nuclear Energy 53, 523 – 552.

Gordon, T.L., Cooling, C.M., Williams, M.M.R., Eaton, M.D., 2021. Numerical comparison of mathematical and computational models for the simulation of stochastic neutron kinetics problems. Annals of Nuclear Energy 157, 108161.

Govindaraju, R.S., Or, D., Kavvas, M.L., Rolston, D.E., Biggar, J., 1992. Error analyses of simplified unsaturated flow models under large uncertainty in hydraulic properties. Water Resources Research 28, 2913–2924.

Govorkov, A.B., 1963. Statistical scattering of pulse amplitudes in fast neutron pulse reactors. Soviet Atomic Energy 13, 750–753.

Govorkov, A.B., 1964. Statistical reactor kinetics equations. Soviet Atomic Energy 17, 1236–1241.

Govorkov, A.B., 1965. Statistical equations in reactor kinetics. Journal of Nuclear Energy. Parts A/B. Reactor Science and Technology 19, 804–809.

Green, W.H., Ampt, G.A., 1911. Studies on soil physics. Part I. The flow of air and water through soils. Journal of Agricultural Science 4, 1–24.

Greenspan, E., 1975. A source-multiplication reactivity. Nuclear Science and Engineering 56, 103–106.

Griesheimer, D.P., Gill, D.F., Nease, B.R., Sutton, T.M., Stedry, M.H., Dobreff, P.S., Carpenter, D.C., Trumbull, T.H., Caro, E., Joo, H., Millman, D.L., 2015. MC21 v.6.0 a continuous-energy Monte Carlo particle transport code with integrated reactor feedback capabilities. Annals of Nuclear Energy 82, 29–40.

Griesheimer, D.P., Pavlou, A.T., Thompson, J.T., Holmes, J.C., Zerkle, M.L., Caro, E., Joo, H., 2017. In-line (α,n) source sampling methodology for Monte Carlo radiation transport simulations. Nuclear Engineering and Technology 49, 1199–1210.

Griffith, E.J., 1991. Cake formation in particulate systems. Wiley-VCH.

Guo, Z., Zhao, T.S., 2002. Lattice Boltzmann model for incompressible flows through porous media. Phys. Rev. E 66, 036304.

Guyadec, F.L., Génin, X., Bayle, J., Dugne, O., Duhart-Barone, A., Ablitzer, C., 2010. Pyrophoric behaviour of uranium hydride and uranium powders. Journal of Nuclear Materials 396, 294 – 302.

Haas, D., 1997. MOX fuel fabrication experience at Belgonucleaire. Report IAEA-TECDOC-941. Societe Belge pour l'Industrie Nucleaire. Brussels, Belgium.

Haase, V., Keller-Rudek, H., Manes, L., Schulz, B., Schumacher, G., Vollath, D., Zimmermann, H., 1986. Gmelin Handbook of Inorganic Chemistry. Supplement Volume C5. Uranium Dioxide. 8th ed., Springer-Verlag.

Hankins, D.E., 1966. Effect of reactivity addition rate and of weak neutron source on the fission yield of uranium solutions. Nuclear Science and Engineering 26, 110–116.

Hansen, G.E., 1960. Assembly of fissionable material in the presence of a weak neutron source. Nuclear Science and Engineering 8, 709–719.

Hansen, R., Minturn, R., Clampitt, B., 1959. Some studies of aqueous uranium oxide slurries. Nuclear Science and Engineering 6, 458–460.

Harris, D.R., 1964. Naval Reactors Physics Handbook. Volume I. Selected Basic Techniques. U.S. Atomic Energy Commission, Naval Reactors Branch. chapter 5. pp. 853–1142.

Hartley, P.A., Parfitt, G.D., Pollack, L.B., 1985. The role of the Van der Waals force in the agglomeration of powders containing submicron particles. Powder Technology 42, 35 – 46.

Haschke, J.M., Stakebake, J.L., 2011. The Chemistry of the Actinide and Transactinide Elements. Springer Netherlands. chapter Handling, Storage and Disposition of Plutonium and Uranium. pp. 3199–3272.

Hayes, J.G., Allen, E.J., 2005. Stochastic point-kinetics equations in nuclear reactor dynamics. Annals of Nuclear Energy 32, 572–587.

Hayes, J.G., Halliday, J., 1974. The least-squares fitting of cubic spline surfaces to general data sets. IMA Journal of Applied Mathematics 14, 89–103.

Health and Safety at Work etc. Act, 1974. [Accessed 2022-03-29] Available from: https://www.legislation.gov.uk/ukpga/1974/37.

Hebert, A., 2020. Applied Reactor Physics. 3rd ed., Presses internationales Polytechnique.

Henry, A.F., 1955. Computation of Parameters Appearing in the Reactor Kinetics Equations. Report WAPD-142. Westinghouse Electric Corp.. Pittsburgh, PA.

Herbst, R., Baron, P., Nilsson, M., 2011. 6 - Standard and advanced separation: PUREX processes for nuclear fuel reprocessing, in: Nash, K.L., Lumetta, G.J. (Eds.), Advanced Separation Techniques for Nuclear Fuel Reprocessing and Radioactive Waste Treatment. Woodhead Publishing. Woodhead Publishing Series in Energy, pp. 141–175.

Hermans, M.E.A., 1959. The Preparation of Uranium Dioxide Fuel for a Suspension Reactor. Report A/CONF.15/P/552. Reactor Centrum Nederland. Arnhem, The Netherlands.

Hindmarsh, A.C., Brown, P.N., Grant, K.E., Lee, S.L., Serban, R., Shumaker, D.E., Woodward, C.S., 2005. SUNDIALS: Suite of nonlinear and differential/algebraic equation solvers. ACM Transactions on Mathematical Software (TOMS) 31, 363–396.

Hodges, M.S., Sanders, C.E., 2014. Nuclear criticality accident safety, near misses and classification. Progress in Nuclear Energy 76, 88–99.

Holmes, W.D., McLaughlin, T.P., 1994. Nuclear criticality safety guide for fire protection professionals in DoE nuclear facilities. Technical Report. U.S. Department of Energy.

Houston, W.N., Mahmoudand, H.H., Houston, S., 1993. Laboratory procedure for partial-wetting collapse determination. Proceedings of the 1993 ASCE National Convention and Exposition, Unsaturated Soils.

Hurwitz, H., J., Ehrlich, R., 1953. Multigroup Methods for Neutron Diffusion Problems. Report HECD-3595. General Electric Company - Knolls Atomic Power Laboratory. Schenectady, New York.

IAEA, 1960. The Agency's Health and Safety Measures. INFCIRC/18, International Atomic Energy Agency (IAEA), Vienna.

IAEA, 2003. IAEA Safeguards Glossary. Number 3 in International Nuclear Verification Series, Vienna.

IAEA, 2006. Fundamental Safety Principles. Number SF-1 in Safety Fundamentals, International Atomic Energy Agency (IAEA), Vienna.

IAEA, 2010. Safety of uranium and plutonium mixed oxide fuel fabrication facilities. Number SSG-7 in Specific Safety Guides, International Atomic Energy Agency (IAEA), Vienna.

IAEA, 2010. Safety of uranium fuel fabrication facilities. Number SSG-6 in Specific Safety Guidance, International Atomic Energy Agency (IAEA), Vienna.

IAEA, 2014. Criticality safety in the handling of fissile material. Number SSG-27 in Specific Safety Guides, International Atomic Energy Agency (IAEA), Vienna.

IAEA, 2017. Safety of nuclear fuel reprocessing facilities. Number SSG-42 in Specific Safety Guidance, International Atomic Energy Agency (IAEA), Vienna.

IAEA, 2020. Storage of spent nuclear fuel. Number SSG-15 in Specific Safety Guidance, International Atomic Energy Agency (IAEA), Vienna.

IAEA, 2021. Nuclear Power Reactors in the World. Number 2 in Reference Data Series, International Atomic Energy Agency (IAEA), Vienna.

ICRP, 1959. Recommendations of the International Commission on Radiological Protection (ICRP) Publication 1. Pergamon Press.

Imafuku, K., Wang, T.Y., Koide, K., Kubota, H., 1968. The behaviour of suspended solid particles in the bubble column. Journal of Chemical Engineering of Japan 1, 153–158.

Ingham, D.B., Pop, I., 2005. Transport Phenomena in Porous Media III. Pergamon.

Ingram, D.M., Causon, D.M., Mingham, C.G., 2003. Developments in Cartesian cut cell methods. Mathematics and Computers in Simulation 61, 561–572. Modelling 2001 - Second IMACS Conference on Mathematical Modelling and Computational Methods in Mechanics, Physics, Biomechanics and Geodynamics.

IRPCG, 2012. The Application of ALARP to Radiological Risk. Industry Radiological Protection Co-ordination Group (IRPCG).

Ivanova, T., Rouyer, V., Rozhikhin, Y., Tsiboulia, A., 2009. Towards validation of criticality calculations for systems with MOX powders. Annals of Nuclear Energy 36, 305–309. PHYSOR 2008.

Iwamoto, H., Nishihara, K., Yagi, T., Pyeon, C.H., 2017. On-line subcriticality measurement using a pulsed spallation neutron source. Journal of Nuclear Science and Technology 54, 432–443.

JAERI, 2001. Working Group on Nuclear Criticality Safety Data. Japan Atomic Energy Research Institute (JAERI). Nuclear Criticality Safety Handbook, Version 2.

James, M.F., 1969. Energy released in fission. Journal of Nuclear Energy 23, 517–536.

Janeczek, J., Ewing, R.C., Thomas, L.E., 1993. Oxidation of uraninite: Does tetragonal U_3O_7 occur in nature? Journal of Nuclear Materials 207, 177–191.

Janov, J., Alfredson, P., Vilkaitis, V., 1972. The influence of precipitation conditions on the properties of ammonium diuranate and uranium dioxide powders. Journal of Nuclear Materials 44, 161–174.

Jean, R.H., Tang, W.T., Fan, L.S., 1989. The sedimentation-dispersion model for slurry bubble columns. American Institute of Chemical Engineers Journal 35, 662–665.

Jeans, J.H., 1917. The Equations of Radiative Transfer of Energy. Monthly Notices of the Royal Astronomical Society 78, 28–36.

Ji, W., Dahmani, A., Ahlfeld, D.P., Lin, J.D., Hill III, E., 1993. Laboratory study of air sparging: Air flow visualization. Groundwater Monitoring & Remediation 13, 115–126.

Jo, D., 2016. Hydrodynamic model of interfacial area for trickling flow in a packed bed. Journal of

Mechanical Science and Technology 30, 171–178.

Jo, D., Revankar, S.T., 2011. Investigation of bubble breakup and coalescence in a packed-bed reactor part 2: Development of a new bubble breakup and coalescence model. International Journal of Multiphase Flow 37, 1003 – 1012.

Jones, G., Cooling, C., Williams, M., Eaton, M., 2022a. Wetting-induced volumetric collapse of UO_2 powder beds and the consequence on transient nuclear criticality excursions. Progress in Nuclear Energy 154, 104460.

Jones, G., Cooling, C., Williams, M., Eaton, M., 2023. Transient nuclear criticality excursion analysis of highly dispersed particulate three-phase fluidised systems. Annals of Nuclear Energy 180, 109453.

Jones, G.S., Winter, G.E., Cooling, C.M., Williams, M.M.R., Eaton, M.D., 2022b. Mathematical and computational models for simulating transient nuclear criticality excursions within wetted fissile powder systems. Annals of Nuclear Energy 169, 108796.

Kalinske, A.A., Pien, C.L., 1943. Experiments on eddy-diffusion and suspended-material transportation in open channels. Eos, Transactions American Geophysical Union 24, 530–536.

Kalshoven, J., 1962. An aqueous homogeneous zero-energy suspension reactor - IV: The measurement of the colloid chemical stability of suspensions. Journal of Nuclear Energy Parts A/B 16, 39–41.

Kastenberg, W.E., Peterson, P.F., Ahn, J., Burch, J., Casher, G., Chambre, P.L., Greenspan, E., Olander, D.R., Vujic, J.L., Bessinger, B., Cook, N.G.W., Doyle, F.M., Hilbert, L.B., 1996. Considerations of autocatalytic criticality of fissile materials in geologic repositories. Nuclear Technology 115, 298–310.

Kato, Y., Nishiwaki, A., Fukuda, T., Tanaka, S., 1972. The behaviour of suspended solid particles and liquid in bubble columns. Journal of Chemical Engineering of Japan 5, 112–118.

Keni, V.S., Ghosh, S.K., Ganguly, C., Majumdar, S., 1994. Development of AUC-based process at BARC for production of free-flowing and sinterable UO_2 powder. Report BARC/1994/E/010. Government of India Atomic Energy Commission. Bhabha Atomic Research Centre, Bombay, India.

Kerlin, T.W., Upadhyaya, B.R., 2019. Dynamics and Control of Nuclear Reactors. Academic Press.

Kersten, J., 1962. An aqueous homogeneous zero-energy suspension reactor - I: Experiments with a subcritical reactor, in which an aqueous suspension of UO_2 particles is circulating. Journal of Nuclear Energy Parts A/B 16, 15–27.

Kim, L.K., 2018. Uranium Mining and Milling. Report LLNL-TR-747582. Lawrence Livermore National Laboratory (LLNL).

Kips, R., Leenaers, A., Tamborini, G., Betti, M., Van den Berghe, S., Wellum, R., Taylor, P., 2007. Characterization of uranium particles produced by hydrolysis of UF_6 using SEM and SIMS. Microscopy and Microanalysis 13, 156164.

Knief, R.A., 1985. Nuclear Criticality Safety: Theory and Practice. American Nuclear Society, 555 North Kensington Avenue La Grange Park, Illinois 60526 U.S.A.

Knudsen, I.E., Hootman, H.E., Levitz, N.M., 1964. A fluid-bed process for the direct conversion of uranium hexafluoride to uranium dioxide. Nuclear Science and Engineering 20, 259–265.

Kobayashi, K., Nishihara, K., 2000. Definition of subcriticality using the importance function for the production of fission neutrons. Nuclear Science and Engineering 136, 272–281.

Koide, K., Yasuda, T., Iwamoto, S., Fukuda, E., 1983. Critical gas velocity required for complete suspension of solid particles in solid-suspended bubble columns. Journal of Chemical Engineering of Japan 16, 7–12.

Kojima, S., Cuttler, J.M., Shimura, N., Koga, H., Murata, A., Kawashima, A., 2018. Present and future prospects of radiation therapy using α-emitting nuclides. Dose-Response 16, 1559325817747387. PMID: 29383010.

Komoda, Y., 2019. Powder Technology Handbook. 4th ed.. CRC Press. chapter Viscosity of Slurry. p. 5.

Kudryavtsev, V.A., Zakhary, P., Easeman, B., 2020. Neutron production in (α,n) reactions. Nuclear Instruments and Methods in Physics Research Section A: Accelerators, Spectrometers, Detectors and Associated Equipment 972, 164095.

Kuroda, P.K., 1956. On the nuclear physical stability of the uranium minerals. The Journal of Chemical Physics 25, 781–782.

Kuwahara, F., Shirota, M., Nakayama, A., 2001. A numerical study of interfacial convective heat transfer coefficient in two-energy equation model for convection in porous media. International Journal of Heat and Mass Transfer 44, 1153 – 1159.

Kuznetsov, A.V., 1994. An investigation of a wave of temperature difference between solid and fluid phases in a porous packed bed. International Journal of Heat and Mass Transfer 37, 3030 – 3033.

Kwon, K.Y., Ahn, S.K., Ahn, S.H., 2018. Comparison on the IAEA safety requirements for nuclear fuel fabrication facility and the requirements for fuel cycle research and development facility, in: Transactions of the Korean Nuclear Society Spring Meeting, Jeju, Korea.

Lane, J.A., MacPherson, H.G., Maslan, F., 1958. Fluid Fuel Reactors. Addison-Wesley books in nuclear science and metallurgy. 1st ed., Addison-Wesley Pub. Co.

Larachi, F., Iliuta, I., Rival, O., Grandjean, B.P.A., 2000. Prediction of minimum fluidization velocity in three-phase fluidized-bed reactors. Industrial & Engineering Chemistry Research 39, 563–572.

Laramore, D., Pfeifer, M.P., Lindstrom, J., Bindra, H., 2018. Design and criticality analysis of colloidal slurry nuclear reactors. Annals of Nuclear Energy 111, 255–261.

Larsen, E.W., 1992. The asymptotic diffusion limit of discretized transport problems. Nuclear Science

and Engineering 112, 336–346.

Larsen, E.W., Keller, J.B., 1974. Asymptotic solution of neutron transport problems for small mean free paths. Journal of Mathematical Physics 15, 75–81.

Leinhard, J.H., Dhir, V.K., 1973. Extended hydrodynamic theory of the peak and minimum pool boiling heat fluxes. NASA, Report CR-2270.

Leppänen, J., 2015. Serpent-a Continuous-energy Monte Carlo Reactor Physics Burnup Calculation Code. Technical Report. VTT Technical Research Centre of Finland.

Leppänen, J., Pusa, M., Viitanen, T., Valtavirta, V., Kaltiaisenaho, T., 2015. The Serpent Monte Carlo code: Status, development and applications in 2013. Annals of Nuclear Energy 82, 142–150.

Levenspiel, O., Bischoff, K.B., 1959. Backmixing in the design of chemical reactors. Industrial & Engineering Chemistry 51, 1431–1434.

Levy, E.K., Caram, H.S., Dille, J.C., Edelstein, S., 1983. Mechanisms for solids ejection from gas-fluidized beds. AIChE Journal 29, 383–388.

Lewis, E.E., 1977. Nuclear Power Reactor Safety. American Nuclear Society (ANS), 555 N Kensington Ave, La Grange Park, IL 60526, United States.

Li, H., Prakash, A., 2000. Influence of slurry concentrations on bubble population and their rise velocities in a three-phase slurry bubble column. Powder Technology 113, 158 – 167.

Li, P., Vanapalli, S., Li, T., 2016. Review of collapse triggering mechanism of collapsible soils due to wetting. Journal of Rock Mechanics and Geotechnical Engineering 8, 256 – 274.

Li, X., Yortsos, Y.C., 1995. Theory of multiple bubble growth in porous media by solute diffusion. Chemical Engineering Science 50, 1427–1271.

Lichtenwalter, J.J., 2008. Absorption of water into uranium powder and implications to nuclear criticality safety. Transactions of the American Nuclear Society 99, 361–362.

Littlechild, J.E., Gillies, G.M., 1974. Production of uranium dioxide in rotary kiln. United States Patent 3,845,193.

Loss, R.D., De Laeter, J.R., Rosman, K.J.R., Benjamin, T.M., Curtis, D.B., Gancarz, A.J., Delmore, J.E., Maeck, W.J., 1988. The oklo natural reactors: cumulative fission yields and nuclear characteristics of reactor zone 9. Earth and Planetary Science Letters 89, 193–206.

Luewisutthichat, W., Tsutsumi, A., Yoshida, K., 1997. Bubble characteristics in multi-phase flow systems: Bubble sizes and size distributions. Journal of Chemical Engineering Japan 30, 461–466.

Markandya, A., Wilkinson, P., 2007. Electricity generation and health. The Lancet 370, 979–990.

Marshall, A.C., 2008. Space Nuclear Safety. 1st ed., Krieger Publishing.

Marsily, G.D., 1986. Quantitative Hydrogeology. 1st ed., Academic Press.

Mason, R., Martin, J., Smith, P., Turland, B., 2012. Comparison of a post-closure transient criticality model with the oklo natural reactors. Mineralogical Magazine 76, 3145–3153.

Mason, R.M., Smith, P.N., 2015. Modelling of consequences of hypothetical criticality: post-closure criticality consequence analysis for ILW, LLW and DNLEU Disposal. Technical Report. AMEC Report Radioactive Waste Management Ltd, RWM005140.

Mason, R.M., Smith, P.N., Sweet, D.W., Eaton, M.D., Goddard, A.J.H., Gomes, J.L.M.A., Pain, C.C., 2009. A summary of verification, validation, benchmarking, uncertainty and sensitivity for the FETCH, QSS and RTM computer models. Technical Report. Serco Report for the Nuclear Decommissioning Authority (NDA), SERCO/TAS/P3648/W001 Issue 2.

Massignon, D., 1979. 3. Gaseous diffusion. Springer Berlin Heidelberg, Berlin, Heidelberg. pp. 55–182.

Mather, D., Bickley, A., Prescott, A., Fouillaud, P., Giroud, P., Grivot, P., 2004. Criticality Accident Code Identification Sheets: POWDER. CEA.

Maubert, L., Poullot, G., Coutois, G., Gagnier, E., Barbry, F., Fouillaud, P., 1999. MARACAS program: Polyethylene reflected critical configurations with low enriched and low moderated uranium dioxide powder U(5)O_2, in: 6th International Conference on Nuclear Criticality Safety, ICNC'99, Versailles, France. p. 818.

McCaughey, D.A., Bidinger, G.H., 1988. Film effects of fire sprinklers on low-enriched-uranium storage systems. Transactions of the American Nuclear Society 56.

McLaughlin, T.P., Monahan, S.P., Pruvost, N.L., Frolov, V.V., Ryazanov, B.G., Sviridov, V.I., 2000. A Review of Criticality Accidents 2000 Revision. Report LA-13638.

Mudd, G.M., 2001. Critical review of acid in situ leach uranium mining: 1. USA and Australia. Environmental Geology 41, 390–403.

Muroyama, K., Fan, L.S., 1985. Fundamentals of gas-liquid-solid fluidization. American Institute of Chemical Engineers Journal 31, 1–34.

Murray, H., Schultz, D., Weaver, L., 1966. Stability of coupled core reactors by the second method of liapunov. Journal of Nuclear Energy 20, 729–734.

Narcy, J.L., 1994. An innovative jet boring mining method available for the high grade uranium ore underground deposits, in: Technical committee meeting on innovations in uranium exploration, mining and processing techniques, and new exploration target areas.

Naudet, R., 1991. Oklo: Des réacteurs nucléaires fossiles. Collection du Commissariat à l'énergie atomique. Série Synthèses, Eyrolles.

NEA, 2005. Evaluation of Proposed Integral Critical Experiments with Low-moderated MOX Fuel: Report from an Ad hoc Expert Group of the NEA Working Party on Nuclear Criticality Safety.

Technical Report. Nuclear Energy Agency (NEA).

NEA, IAEA, 2020. Uranium Resources, Production and Demand 2020. Organisation for Economic Co-Operation and Development (OECD).

Newlon, C.E., Mallett, A.J., 1966. Hydrogen moderation - A primary nuclear safety control for handling and transporting low-enrichment UF_6. USAEC Report K-1663. Oak Ridge Gaseous Diffusion Plant, Union Carbide Corporation.

Nielsen, P., Teakle, I.A.L., 2004. Turbulent diffusion of momentum and suspended particles: A finite-mixing-length theory. Physics of Fluids 16, 2342–2348.

Nordsieck, A., 1962. On numerical integration of ordinary differential equations. Mathematics of Computation 16, 22–49.

Nouri, A., Nagel, P., Soppera, N., Ahite, A., Taton, B., Patrouix, J., Lecompagnon, F., Cunin, C., Rioland, O., Deurveilher, L., 2002. JANIS: A new software for nuclear data services. Journal of Nuclear Science and Technology 39, 1480–1483.

Nuclear Installations Act, 1965. [Accessed 2022-03-29] Available from: https://www.legislation.gov.uk/ukpga/1965/57.

O'Connor, G., 2013. Criticality safety of enriched UF_6 cylinders, in: 17th International Symposium on the Packaging and Transportation of Radioactive Materials (PATRAM).

Odong, J., 2007. Evaluation of empirical formulae for determination of hydraulic conductivity based on grain-size analysis. The Journal of American Science 3, 54–60.

Office of Nuclear Energy, 2022. Funding opportunities. [Accessed 2022-03-22] Available from: https://www.energy.gov/ne/funding-opportunities.

Okajima, S., Yamane, Y., Takemoto, Y., Sakurai, T., 2000. A note on the diven factor in fast systems. Journal of Nuclear Science and Technology 37, 720–723.

Olander, D.R., 1978. The gas centrifuge. Scientific American 239, 37–43.

ONR, 2017. Licence Condition Handbook. Office for Nuclear Regulation (ONR).

ONR, 2020. Guidance on the Demonstration of ALARP (As Low As Reasonably Practicible). Office for Nuclear Regulation (ONR).

Ornstein, L., Uhlenbeck, G., 1937. Some kinetic problems regarding the motion of neutrons through paraffine. Physica 4, 478–486.

Orr, R., Godfrey, H., Broan, C., Goddard, D., Woodhouse, G., Durham, P., Diggle, A., Bradshaw, J., 2017. Kinetics of the reaction between water and uranium hydride prepared under conditions relevant to uranium storage. Journal of Alloys and Compounds 695, 3727 – 3735.

Pain, C.C., Goddard, A.J.H., de Oliveira, C.R.E., 1998. The status of the finite element transient crit-

icality code FETCH. verification and validation, in: Proceedings of the 2nd NUCEF International Symposium NUCEF'98. Safety and Research and Development of Base Technology on Nuclear Fuel Cycle.

Pain, C.C., Gomes, J.L.M.A., Eaton, M.D., Goddard, A.J.H., Tollit, B., Hadi, J., 2009. Modelling of granular materials in the FETCH coupled criticality code. Transactions of the American Nuclear Society 100, 331–334.

Pál, L., 1962. Statistical theory of the chain reaction in nuclear reactors I, II, III. From Central Scientific Research Institute for Physics of the Hungarian Academy of Sciences, Budapest, Translated from Russian by V. Shibayev, as UKAEA Harwell Research Group Report, HAP 31981.

Patemoster, R., Miyoshi, Y., Suzaki, T., Shiroya, S., Ohtani, N., Barbry, F., Santamarina, A., Voloshin, N., Ryazanov, B., Sviridov, V., Nikolaev, M., Tsiboulia, A., Glouchkov, Y., Gagarinski, A., Ponomarev-Stepnov, N., Cousinou, P., Poullot, G., McFarlane, H., Scaefer, R., Aumeier, S., Harms, G., Naito, Y., Okuno, H., Briggs, J.B., Dean, V., Scott, L., Szatmary, Z., Vidovsky, I., Nakajima, K., Itagaki, M., Perry, R., Houts, M., Casey, H., Golubev, A., Vorontsov, S., Vasilyev, A., Rutherford, D., Whitesides, G., 1999. Experimental Needs in Criticality Safety. Technical Report. Nuclear energy Agency and Organisation for Economic Co-Operation and Development.

Paxton, H.C., 1972. Criticality Control in Operations with Fissile Material. Los Alamos Scientific Laboratory (LASL), Report LA-3366.

Paxton, H.C., 1980. Historical perspective of criticality safety in the united states, in: Nuclear criticality safety topical meeting, Report LA-UR-80-856, El Paso, TX, USA.

Paxton, H.C., Pruvost, N.L., 1986. Critical Dimensions of Systems Containing ^{235}U, ^{239}Pu, and ^{233}U. Los Alamos National Laboratory (LANL), Report LA-10860-MS.

Peierls, R.E., 1940. Considerations regarding chain reactions. MS-1,2,3,4. Ministry of Supply, Great Britain.

Pemberton, S.T., Davidson, J.F., 1986. Elutriation from fluidized beds-I. Particle ejection from the dense phase into the freeboard. Chemical Engineering Science 41, 243–251.

Pereira, J.H.F., Fredlund, D.G., 2000. Volume change behaviour of collapsible compacted Gneiss soil. Journal of Geotechnical and Geoenvironmental Engineering 126, 907–916.

Peters, M.H., Prybylowski, D.L., 1983. Particle motion above the surface of a fluidized bed: Multiparticle effects. American Chemical Society Symposium Series 79.

Phillips, G.W., Nagel, D.J., Coffey, T., 2005. A Primer on the Detection of Nuclear and Radiological Weapons. Report. Center for Technology and National Security Policy National Defense University.

Poirot-Delpech, S., Raineau, L., 2016. Nuclear waste facing the test of time: The case of the french deep geological repository project. Science and Engineering Ethics 22, 1813–1830.

Provost, J.L., Schrader, M., Nomura, S., 2000. MOX fuel fabrication and utilisation in LWRs world-

wide. Report IAEA-CSP-3/P. International Atomic Energy Agency (IAEA). Vienna.

Putman, V.L., 1999. Criticality safety basics, a study guide. Idaho National Engineering and Environmental Laboratory (INEEL) Applied Engineering and Development Department, Report INEEL/EXT-98-00895.

Pyeon, C.H., 2021. Accelerator-Driven System at Kyoto University Critical Assembly . Springer Verlag.

Pál, L.I., 1958. On The Theory of Stochastic Processes in Nuclear Reactors. Nuovo Cimento, Supplement 7.

Pátek, J., Hrubý, J., Klomfar, J., Souková, M., Harvey, A.H., 2009. Reference correlations for thermophysical properties of liquid water at 0.1MPa. Journal of Physical and Chemical Reference Data 38, 21–29.

Pázsit, I., Pál, L., 2007. Neutron Fluctuations: A Treatise on the Physics of Branching Processes. Elsevier.

Quicker, G., Schumpe, A., Deckwer, W.D., 1984. Gas-liquid interfacial areas in a bubble column with suspended solids. Chemical Engineering Science 39, 179 – 183.

Raap, M.B., Heinrichs, D.P., McLaughlin, T.P., Morman, J.A., 2014. CSSG position on use of water for firefighting in light of criticality constraints for DoE facilities. Technical Report. U.S. Department of Energy, CSSG.

Radkowsky, A., 1964. Naval Reactors Physics Handbook Volume 1: Selected Basic Techniques. Naval Reactors, Division of Reactor Development, United States Atomic Energy Commission (USAEC).

Randall, C.H., 1963. Stochastic Models for Heterogeneous Materials - II (Basic Theory and Fine Structure). Knolls Atomic Power Lab, Schenectady, N.Y., Report KAPL-M-CHR-7.

Rao, S.M., Revanasiddappa, K., 2000. Role of matric suction in collapse of compacted clay soil. Journal of Geotechnical and Geoenvironmental Engineering 126, 85–90.

Rechard, R.P., 2015. Probability and consequences of nuclear criticality at a geologic repositoryii: Potential repository in volcanic tuff as an example. Nuclear Technology 190, 127–160.

Reed, S., Crowley, P., 1956. Sedimentation of thorium oxide slurries at elevated temperatures. Nuclear Science and Engineering 1, 511–521.

Reider, R., 1971. Early history of criticality safety. Report LA-4671. Los Alamos Scientific Laboratory.

Richards, L.A., 1931. Capillary conduction of liquids through porous media. Physics 1, 318–333.

Ronchi, C., Iosilevski, I.L., Yakub, E.S., 2004. Equations of State of Uranium Dioxide: Data Collection. 1 ed., Springer.

Roosevelt, S.E., Corapcioglu, M.Y., 1998. Air bubble migration in a granular porous medium: Exper-

imental studies. Water Resources Research 34, 1131–1142.

Ross, R.H., Honkonen, D.L., Salaymeh, S.R., 1991. Water Film Thickness Effects from Automatic Fire Sprinklers (U). Technical Report. Westinghouse Savannah River Company. Savannah River Site, Aiken, South Carolina, 29808.

Rossi, B., 1933. Über die eigenschaften der durchdringenden korpuskularstrahlung im meeresniveau. Zeitschrift für Physik 82, 151–178.

Rothe, R.E., Goebel, G.R., 1982. Critical Experiments on Low-Enriched Uranium Oxide Systems With H/U=2.03: Reference Critical Experiments. Report NUREG/CR-2500. Rockwell International Energy Systems Group.

Rothman, D.H., 1988. Cellularautomaton fluids: A model for flow in porous media. GEOPHYSICS 53, 509–518.

Rouyer, V., Duhamel, I., Poullot, G., Cousinou, P., Barbry, F., Fouillaud, P., Girault, E., 2003. IRSN projects for critical experiments 'low moderated MOX fuel project' and others, in: ICNC2003: Proceedings of the seventh international conference on nuclear criticality safety. Challenges in the pursuit of global nuclear criticality safety.

Rozain, J., Fouillaud, P., Barbry, F., Mather, D., Bickley, A., Prescott, A., 1991. Criticality excursions in wetted UO_2 powder. Transactions of the American Nuclear Society 63, 228.

Russel, W.B., Saville, D.A., Schowalter, W.R., 1989. Colloidal Dispersions. 1st ed., Cambridge University Press.

Sakai, M., Yamamoto, T., Murazaki, M., Miyoshi, Y., 2004. Effect of particulate behavior on criticality evaluation in agitating powder of nuclear fuel. Powder Technology 148, 67 – 71.

Sakai, M., Yamamoto, T., Murazaki, M., Miyoshi, Y., 2005. Development of a criticality evaluation method considering the particulate behavior of nuclear fuel. Nuclear Technology 149, 141–149.

Sanchez, R., Pomraning, G.C., 1991. A statistical analysis of the double heterogeneity problem. Annals of Nuclear Energy 18, 371–395.

Santana, D., Nauri, S., Acosta, A., García, N., Macías-Machín, A., 2005. Initial particle velocity spatial distribution from 2-D erupting bubbles in fluidized beds. Powder Technology 150, 1–8.

Santi, P., Miller, M., 2008. Reevaluation of prompt neutron emission multiplicity distributions for spontaneous fission. Nuclear Science and Engineering 160, 190–199.

Saracco, P., Ricco, G., 2009. Various operating regimes of a subcritical system as a function of subcriticality in one-group theory. Nuclear Science and Engineering 162, 167–177.

Savornin, J., Gibault, M., Berger, R., Kaluzny, Y., Wallard, H.E., Winter, D., 1989. Action taken by the french safety authorities for fire protection and fire fighting in basic nuclear plants, in: International symposium on fire protection and fire fighting in nuclear installations, Vienna, Austria.

Scharff-Goldhaber, G., Klaiber, G.S., 1946. Spontaneous emission of neutrons from uranium. Physical Review 70, 229.

Seale, R.L., Anderson, R.E., 1991. Intrinsic neutron source strengths in uranium solutions. Transactions of the American Nuclear Society 63, 226.

Sesonske, A., 1961. Hindered settling rates of concentrated suspensions of uranium dioxide in sodium. Report LAMS-2604. Los Alamos Scientific Laboratory.

Shahbunder, H., Pyeon, C.H., Misawa, T., Lim, J.Y., Shiroya, S., 2010. Subcritical multiplication factor and source efficiency in accelerator-driven system. Annals of Nuclear Energy 37, 1214–1222.

Shaw, J., 1969. Reactor Operation. Pergamon Press Ltd.

Shmakov, V.M., 1999. Model calculations of dispersed media criticality, in: Proceedings 6th international conference on nuclear criticality safety ICNC 1999, Versailles, France. pp. 486–494.

Shmakov, V.M., Lyutov, V.D., Dean, V.F., 2000. Effective cross-section for calculations of criticality of dispersed media, in: PHYSOR 2000, Pittsburgh, PA, USA. pp. 7–11.

Shultis, J.K., Faw, R.E., 2016. Fundamentals of Nuclear Science and Engineering. 3rd ed., CRC Press.

Smith, D.N., Ruether, J.A., 1985. Dispersed solid dynamics in a slurry bubble column. Chemical Engineering Science 40, 741–753.

Sovacool, B.K., Andersen, R., Sorensen, S., Sorensen, K., Tienda, V., Vainorius, A., Schirach, O.M., Bjørn-Thygesen, F., 2016. Balancing safety with sustainability: Assessing the risk of accidents for modern low-carbon energy systems. Journal of Cleaner Production 112, 3952–3965.

Spiegler, P., Bumpus, Jr, C.F., Norman, A., 1962. Production of Void and Pressure by Fission Track Nucleation of Radiolytic Gas Bubbles During Power Bursts in a Solution Reactor. Atomics International. Div. of North American Aviation, Inc., Canoga Park, California, Report NAA-SR-7086.

Spriggs, G.D., Busch, R.D., Sakurai, T., Okajima, S., 1997. Measurement of the equivalent fundamental-mode source strength. Los Alamos National Laboratory (LANL), Report LA-UR-97-259. United States.

Spriggs, G.D., Busch, R.D., Sakurai, T., Okajima, S., 1999. The equivalent fundamental-mode source. Annals of Nuclear Energy 26, 237–264.

Stacey, W.M., 2018. Nuclear Reactor Physics. 3rd ed., Wiley-VCH.

Stakebake, J.L., 1992. Plutonium Pyrophoricity. Report RFP-4517. EG and G Rocky Flats. Golden, Colorado.

Starks, J.B., 1977. The PUREX process. Report DPSPU 77-11-1. E. I. Du Pont de Nemours and Co.

Steele, L.R., Carson, D., Dryden, C.E., 1963a. Solution to the fission recoil energy deposition in a

slurry by a Monte Carlo technique. Nuclear Science and Engineering 15, 451–457.

Steele, L.R., Gordon, S., Dryden, C.E., 1963b. Water decomposition by fission fragment recoil energy in an aqueous slurry of uraniumthorium oxides. Nuclear Science and Engineering 15, 458–467.

Steinour, H.H., 1944a. Rate of sedimentation. Industrial & Engineering Chemistry 36, 840–847.

Steinour, H.H., 1944b. Rate of sedimentation. concentrated flocculated suspensions of powders. Industrial & Engineering Chemistry 36, 901–907.

Steinour, H.H., 1944c. Rate of sedimentation. nonflocculated suspensions of uniform spheres. Industrial & Engineering Chemistry 36, 618–624.

Sun, D.M., Li, X.M., Feng, P., Zang, Y.G., 2016. Stability analysis of unsaturated soil slope during rainfall infiltration using coupled liquid-gas-solid three-phase model. Water Science and Engineering 9, 183–194.

Sun, Y., Nozawa, T., Furusaki, S., 1988. Gas holdup and volumetric oxygen transfer coefficient in a three-phase fluidized bed bioreactor. Journal of Chemical Engineering of Japan 21, 15–20.

Sutton, A.H., Bishop, J.C., Stahman, K.J., Cohen, M.H., 1964. Reduction and hydrofluorination of uranium concentrates by fluid bed techniques, in: 53rd National meeting of the American Institute of Chemical Engineers. Symposium on nuclear plant experience with fluidized beds, Part I, Pittsburgh, PA, United States.

Sánchez, A.L., Williams, F.A., 2014. Recent advances in understanding of flammability characteristics ofăhydrogen. Progress in Energy and Combustion Science 41, 1–55.

Tadepalli, R., Fredlund, D.G., 1991. The collapse behaviour of a compacted soil during inundation. Canadian Geotechnical Journal 28, 477–488.

Tadepalli, R., Rahardjo, H., Fredlund, D.G., 1992. Measurements of matric suction and volume changes during inundation of collapsible soil. Geotechnical Testing Journal 15, 115–122.

Tadros, T., 2012. Dispersion of Powders in Liquids and Stabilization of Suspensions. 1st ed., Wiley.

Taylor, R.G., 1973. Monitoring for uranium accumulations, in: 19th Annual Meeting of the American Nuclear Society.

Terrell, J., 1957. Distributions of fission neutron numbers. Phys. Rev. 108, 783–789.

The Ionising Radiations Regulations, 2017. [Accessed 2022-03-29] Available from: https://www.legislation.gov.uk/uksi/2017/1075.

Thomas, A., Abbey, F., 1973. Calculational Methods for Interacting Arrays of Fissile Material. 1 ed., Pergamon Press.

Tichy, J., Douglas, W.J.M., 1972. Bed expansion in a mobile-bed contactor. The Canadian Journal of Chemical Engineering 50, 702–706.

Tsuchiya, K., Furumoto, A., Fan, L.S., Zhang, J., 1997. Suspension viscosity and bubble rise velocity in liquid-solid fluidized beds. Chemical Engineering Science 52, 3053 – 3066.

Tu, J., Yeoh, G.H., Liu, C., 2013. Computational Fluid Dynamics: A Practical Approach. 2nd ed., Butterworth-Heinemann.

Tuck, G., Oh, I., 1979. Benchmark Critical Experiments on Low-Enriched Uranium Oxide Systems with H/U=0.77. Report NUREG/CR-0674. Atomics International Division.

Tuya, D., Obara, T., 2017. Supercritical transient analysis in coupled fuel debris systems of symmetric and asymmetric geometry using integral kinetic model. Annals of Nuclear Energy 109, 113–119.

U.S. NRC, 2002. Event notification report for April 4, 2002. [Accessed 2022-04-05] Available from: https://www.nrc.gov/reading-rm/doc-collections/event-status/event/2002/20020404en.html.

U.S. NRC, 2016. The in situ uranium recovery process [illustration]. [Accessed 2022-04-04] Available from: https://www.nrc.gov/images/materials/uranium-recovery/extraction-methods/in-situ-uranium-recovery-large.jpg.

Ussachoff, L.N., 1955. Equation for the importance of neutrons, kinetics and the theory of perturbations, in: Proceedings international conference on peaceful uses of atomic energy, Geneva, pp. 503–510.

Verma, V.K., Katovsky, K., 2018. Spent Nuclear Fuel and Accelerator-Driven Subcritical Systems (Green Energy and Technology). 1st ed., Springer Verlag.

Versteeg, H., Malalasekera, W., 2007. An Introduction to Computational Fluid Dynamics. 2nd ed., Pearson Prentice Hall.

Wagner, G.L., Kinkead, S.A., Paffett, M.T., Rector, K.D., Scott, B.L., Tamasi, A.L., Wilkerson, M.P., 2015. Morphologic and chemical characterization of products from hydrolysis of UF_6. Journal of Fluorine Chemistry 178, 107–114.

Wakao, N., Kaguei, S., 1983. Heat and Mass Transfer in Packed Beds. Gordon and Breach Science Publishers.

Wallis, G.B., 1969. One-Dimensional Two-Phase Flow. 1st ed., McGraw-Hill.

Warrick, A.W., 2003. Soil Water Dynamics. Oxford University Press.

Went, J., Kersten, J., Hermans, M., Wolf, H., Zolingen, J., Wijker, H., 1964. The Aqueous Homogenous Suspension Reactor Project EURATOM-RCN-KEMA. Report EUR 1611.e. European Atomic Energy Community - EURATOM and Keuring Van Electrotechnische Materialen - KEMA.

Werner, C.J., Armstrong, J., Brown, F.B., Bull, J.S., Casswell, L., Cox, L.J., Dixon, D., Forster, R.A., Goorley, J.T., Hughes, H.G., Favorite, J., Martz, R., Mashnik, S.G., Rising, M.E., Solomon, C., Sood, A., Sweezy, J.E., Zukaitis, A., Anderson, C., Elson, J.S., Durkee, J.W., Johns, R.C.,

McKinney, G.W., McMath, G.E., Hendricks, J.S., Pelowitz, D.B., Prael, R.E., Booth, T.E., James, M.R., Fensin, M.L., Wilcox, T.A., Kiedrowski, B.C., 2018. MCNP6.2 Release Notes. Technical Report. Los Alamos National Laboratory (LANL), Report LA-UR-18-20808.

Whitesides, G.E., Westfall, R.M., Hopper, C.M., 2010. Criticality Safety Methods. Springer Netherlands, Dordrecht. pp. 355–373.

Wigner, E.P., 1942. On Variations of the Power Output in a Running Pile. Report CP-351. Chicago University, Metallurgical Laboratory. Chicago, Illinois.

Williams, M.M.R., 1974. Random Processes in Nuclear Reactors. 1st ed., Pergamon Press.

Williams, M.M.R., 2009. The forward equation of probability balance for neutrons in a medium with randomly time-varying properties: Space and angle dependence. Progress in Nuclear Energy 51, 689–694.

Williams, M.M.R., 2016. Burst wait-times in the Caliban reactor using the Gamma probability distribution function. Nuclear Science and Engineering 183, 116–125.

Williams, M.M.R., 2019. Mathematical and Phenomenological Models to Predict Nuclear Criticality Excursions in Wetted Powders, Sludges, Slurries and Suspensions. Imperial Consultants (ICON).

Williams, M.M.R., 2022. Infiltration and evaporation in multiplying porous media and associated criticality phenomena. Nuclear Science and Engineering 196, 1–28.

Williams, M.M.R., Eaton, M.D., 2016. A theory of low source start-up based on the Pál-Bell equations. Annals of Nuclear Energy 94, 655–671.

Wilson, K., Addie, R., Sellgren, A., Clift, R., 2006. Slurry Transport Using Centrifugal Pumps. 3 ed., Springer.

Wilson, W.B., Perry, R.T., Charlton, W.S., Parish, T.A., Shores, E.F., 2005. SOURCES: a code for calculating (α,n), spontaneous fission, and delayed neutron sources and spectra. Radiation Protection Dosimetry 115, 117–121.

Wilson, W.B., Perry, R.T., Shores, E.F., Charlton, W.S., Parish, T.A., Estes, G.P., Brown, T.H., Arthur, E.D., Bozoian, M., England, T.R., Madland, D.G., Stewart, J.E., 2002. SOURCES 4C : a code for calculating (α,n), spontaneous fission, and delayed neutron sources and spectra. Los Alamos National Report (LANL), Report LA-UR-02-1839.

Winter, G.E., 2019. Transient Nuclear Criticality Analysis of Aqueous Fissile Solutions Using Point Nuclear Reactor Kinetics and Phenomenological Thermal-Hydraulic Feedback Models. Imperial College London PhD Thesis.

Winter, G.E., Cooling, C.M., Williams, M.M.R., Eaton, M.D., 2018. Importance of parametric uncertainty in predicting probability distributions for burst wait-times in fissile systems. Annals of Nuclear Energy 119, 117–128.

Wozniak, M., 1977. Pressure-drop and effective interfacial area in a column with a mobile bed. International Chemical Engineering 17, 553–559.

WPNCS, 2006. Reference Values for Nuclear Criticality Safety. Working Party on Nuclear Criticality Safety (WPNCS).

Xinhua News Agency, 2021. Outline of the People's Republic of China 14th Five-Year Plan for national economic and social development and long-range objectives for 2035 (Etcetera Language Group, Inc., Trans.).

Yamamoto, T., Miyoshi, Y., Takeda, T., 2006. Extension of effective cross section calculation method for neutron transport calculations in particle-dispersed media. Journal of Nuclear Science and Technology 43, 77–87.

Yamane, Y., Yamamoto, T., Miyoshi, Y., 2003a. Development of numerical simulation codes for estimation of number of fission released at criticality accident of MOX powder system, in: International Conference on Supercomputing in Nuclear Applications, SNA'2003, CEA Saclay, 91 - Gif-sur-Yvette, Paris, France.

Yamane, Y., Yamamoto, T., Miyoshi, Y., Nakajima, K., 2003b. Development of criticality accident analysis code AGNES. Japan Atomic Energy Research Institute (JAERI), Kashiwa, Chiba (Japan), in: International conference on nuclear criticality safety (ICNC2003). Challenges in the pursuit of global nuclear criticality safety, Tokai, Ibaraki (Japan). pp. 740–745.

Yang, G.Q., Du, B., Fan, L.S., 2007. Bubble formation and dynamics in gas-liquid-solid fluidizationa review. Chemical Engineering Science 62, 2 – 27.

Yearwood, D., Clayton, E.D., Koponen, B.L., 1993. Anomalous effects of moderation in transportation and storage arrays - revisited, in: Proceedings of the Topical Meeting on Physics and Methods in Criticality Safety, Nashville, Tennessee.

Yeoh, G.H., Tu, J., 2019. Computational Techniques for Multiphase Flows. 2nd ed., Butterworth-Heinemann.

Yi-Ming, P., Che-Bao, M., Nien-Nan, H., 1981. The conversion of UO_2 via ammonium uranyl carbonate: Study of precipitation, chemical variation and powder properties. Journal of Nuclear Materials 99, 135–147.

Zafar, U., Vivacqua, V., Calvert, G., Ghadiri, M., Cleaver, J., 2017. A review of bulk powder caking. Powder Technology 313, 389–401.

Zeitoun, O., Shoukri, M., Chatoorgoon, V., 1994. Measurement of interfacial area concentration in subcooled liquid-vapour flow. Nuclear Engineering and Design 152, 243 – 255.

Zuber, N., Findlay, J.A., 1965. Average volumetric concentration in two-phase flow systems. Journal of Heat Transfer 87, 453–468.

Zurrón-Cifuentes, O., López-Márquez, J., Escandón-Ortiz, E., 2011. Fractionated Dosage of Hydro-

genated Additives in UO_2 Powder Blending Process. Technical Report. European Nuclear Society (ENS).